NANOSYSTEMS:

PHYSICS, CHEMISTRY, MATHEMATICS

NANOSYSTEMS:
PHYSICS, CHEMISTRY, MATHEMATICS

AIM AND SCOPE

The scope of the journal includes all areas of nano-sciences. Papers devoted to basic problems of physics, chemistry, material science and mathematics inspired by nanosystems investigations are welcomed. Both theoretical and experimental works concerning the properties and behavior of nanosystems, problems of its creation and application, mathematical methods of nanosystem studies are considered.

The journal publishes scientific reviews (up to 30 journal pages), research papers (up to 15 pages) and letters (up to 5 pages). All manuscripts are peer-reviewed. Authors are informed about the referee opinion and the Editorial decision.

CONTENT

The F-index and coindex of V-Phenylenic Nanotubes and Nanotorus and their molecular complement graphs

Mohammed S. Y. Alsharafi[1], Abdu Q. Alameri[2]

[1]Graduate School of Natural and Applied Sciences, Yildiz Technical University, Istanbul, Turkey

[2]Department of Biomedical Engineering, University of Science and Technology, Sana'a, Yemen

alsharafi205010@gmail.com, a.alameri2222@gmail.com

The forgotten topological index was defined to be used in the analysis of chemical structures which often appear in drug molecular graphs. In this paper, we studied the F-index and F-coindex for certain important physico chemical structures such as V-Phenylenic Nanotube $VPHX[m,n]$ and V-Phenylenic Nanotorus $VPHY[m,n]$ and their molecular complement graph. Moreover, we computed F-polynomial of the V-Phenylenic Nanotubes and Nanotorus. These explicit formulae can correlate the chemical structure of molecular graphs of Nanotubes and Nanotorus to information about their physicochemical structure.

Keywords: F-index, F-coindex, V-Phenylenic Nanotubes and Nanotori, molecular graph, molecular complement graph.

Received: 10 April 2021

Revised: 18 April 2021

1. Introduction

Chemical graph theory is a part of mathematical chemistry that uses graph theory for mathematically modeling chemical phenomena. Chemical graphs are models of molecules in which atoms are represented by vertices and chemical bonds by edges of a graph. The topological indices explain chemical compound structures and help to predict certain physicochemical properties such as entropy, boiling point, acentric factor, vaporization enthalpy, etc [1]. We denote the V-Phenylenic nanotubes and nanotorus by $VPHX[m,n]$, and $VPHY[m,n]$ respectively, where m and n are the number of atoms in rows and columns. Many well-known topological indices of the V-Phenylenic nanotubes and nanotorus have been computed. The forgotten index one of the most important topological indices which preserve the symmetry of molecular structures and provide a mathematical formulation to predict their physical and chemical properties [2]. In this article, in view of structure analysis and mathematical derivation, we find the F-index and coindex of certain molecular graphs nanotubes and nanotorus that are interesting molecular graphs and nano-structures. Since the forgotten topological index and coindex are considered among the most effective topological indices in analysis the QSPR/QSAR with high accuracy, so we intend to compute the F-index and F-coindex for some nanostructures such as V-Phenylenic Nanotube $VPHX[m,n]$ and V-Phenylenic Nanotorus $VPHY[m,n]$ and their polynomials which are useful for description of some characteristics of nanostructures. Topological indices are the molecular descriptors that describe the structures of chemical compounds and they help us to predict certain physicochemical properties [3]. The first and second Zagreb indices can be regarded as one of the oldest graph invariants which was defined in 1972 by Gutman and Trinajsti [4,5]. The first and second Zagreb indices defined for a molecular graph G as:

$$M_1(G) = \sum_{uv \in E(G)} [\delta_G(u) + \delta_G(v)], \qquad M_2(G) = \sum_{uv \in E(G)} \delta_G(u)\,\delta_G(v).$$

The first and second Zagreb coindices have been introduced by A. R. Ashrafi, T. Doslic, and A. Hamzeh in 2010 [6]. They are respectively defined as:

$$\overline{M}_1(G) = \sum_{uv \notin E(G)} [\delta_G(u) + \delta_G(v)], \qquad \overline{M}_2(G) = \sum_{uv \notin E(G)} \delta_G(u)\,\delta_G(v).$$

Furtula and Gutman in 2015 introduced forgotten index (F-index) [7] which defined as:

$$F(G) = \sum_{v \in V(G)} \delta_G{}^3(v) = \sum_{uv \in E(G)} \left(\delta_G{}^2(u) + \delta_G{}^2(v)\right)$$

N. De, S. M. A. Nayeem and A. Pal. in 2016 defined forgotten coindex (F-coindex) [8], which defined as:

$$\overline{F}(G) = \sum_{v \notin V(G)} \delta_G{}^3(v) = \sum_{uv \notin E(G)} \left(\delta_G{}^2(u) + \delta_G{}^2(v)\right).$$

Then, Farahani et al. [9–11] computed the first and second Zagreb, first and second Hyper-Zagreb and multiplicative and Redefined Zagreb indices of V-Phenylenic Nanotube $VPHX[m,n]$ and V-Phenylenic Nanotorus $VPHY[m,n]$ and their polynomials. Ashrafi et al. [12] studied the computing Sadhana polynomial of V-phenylenic nanotubes and nanotori. Alamian et al. [13] studied PI Polynomial of V-Phenylenic Nanotubes and Nanotori, Z. Ahmad et al. [14] presented new results on eccentric connectivity indices of V-Phenylenic nanotube, and there are a lot of researchers who have studied some topological indices on V-Phenylenic Nanotube $VPHX[m,n]$ and V-Phenylenic Nanotorus $VPHY[m,n]$ that cannot be all mentioned here. B. Furtula et al. [7] and De, Nilanjan et al. [8] defined the F-index and F-coindex and studied their of some special graph and graph operation. Nanotubes and Nanotorus play an important role in many applications such as Energy storage, Bioelectronics and Optoelectronics. Because of their unique structural, electrical, optical, and mechanical properties, graphene nanosheets drew dramatic attention of academic and industrial research [15] and as nanotubes introduced into graphene could be extremely useful and exploited to generate novel, innovative, and useful materials and devices. Here, we present the F-index and F-coindex and their topological polynomials of V-Phenylenic Nanotube $VPHX[m,n]$ and V-Phenylenic Nanotorus $VPHY[m,n]$ which are useful for surveying structure of nanotubes and nanotorus. Any unexplained terminology is standard, typically as in [16–21].

2. Preliminaries

In this section, we give some basic and preliminary concepts which we shall use later.

Proposition 2.1 [2,8]   Let G be a simple graph on n vertices and m edges. Then:
$$F(\overline{G}) = n(n-1)^3 - 6m(n-1)^2 + 3(n-1)M_1(G) - F(G),$$
$$\overline{F}(G) = (n-1)M_1(G) - F(G),$$
$$\overline{F}(\overline{G}) = 2m(n-1)^2 - 2(n-1)M_1(G) + F(G).$$

Theorem 2.2 [9,10]   The first and second Zagreb and Hyper-Zagreb indices of the V-Phenylenic Nanotubes $VPHX[m,n]$ and V-Phenylenic Nanotorus $VPHY[m,n](\forall m,n \in \mathbb{N} - \{1\})$ (Fig. 1,2) are given by:

$$M_1(VPHX[m,n]) = 54mn - 10m, \qquad M_1(VPHY[m,n]) = 54mn,$$
$$M_2(VPHX[m,n]) = 81mn + 3m, \qquad M_2(VPHY[m,n]) = 81mn,$$
$$HM(VPHX[m,n]) = 4m(81n - 20), \qquad HM(VPHY[m,n]) = 324mn,$$
$$HM_2(VPHX[m,n]) = 9m(81n - 29), \qquad HM_2(VPHY[m,n]) = 729mn.$$

3. Main results

In this section, we compute the forgotten topological index and coindex for certain important chemical structures such as line graphs of the V-Phenylenic Nanotubes $VPHX[m,n]$ and V-Phenylenic Nanotorus $VPHY[m,n]$ $(\forall m,n \in \mathbb{N} - \{1\})$ and their molecular complement graph. Here, we study also F-polynomial of V-Phenylenic Nanotubes and Nanotorus.

3.1.   F-index and coindex of the V-Phenylenic Nanotubes $VPHX[m,n](\forall m,n \in \mathbb{N} - \{1\})$

Theorem 3.1.1   The F-index of the V-Phenylenic Nanotubes $VPHX[m,n](\forall m,n \in \mathbb{N} - \{1\})$ (Fig. 1) is given by:
$$F(VPHX[m,n]) = 162mn - 38m.$$

Proof. By definition of the F-index $F(G) = \sum\limits_{uv \in E(G)} \left[\delta_G^2(u) + \delta_G^2(v)\right]$, and by replacing each G with $VPHX[m,n]$, which yield:
$$F(VPHX[m,n]) = \sum\limits_{uv \in E(VPHX[m,n])} \left[\delta_{VPHX[m,n]}^2(u) + \delta_{VPHX[m,n]}^2(v)\right].$$

And the partitions of the vertex set and edge set $V(VPHX[m,n])$, $E(VPHX[m,n])$, of V-Phenylenic nanotube are given in Table 1,2 respectively [9].

The edge set of $VPHX[m,n]$ is divided into two edge partitions based on the sum of degrees of the end vertices as:
$$E_5(VPHX[m,n]) = E_6^* = \{e = uv \in E(VPHX[m,n]) : \delta(u) = 2, \delta(v) = 3\},$$
$$E_6(VPHX[m,n]) = E_9^* = \{e = uv \in E(VPHX[m,n]) : \delta(u) = 3, \delta(v) = 3\}.$$
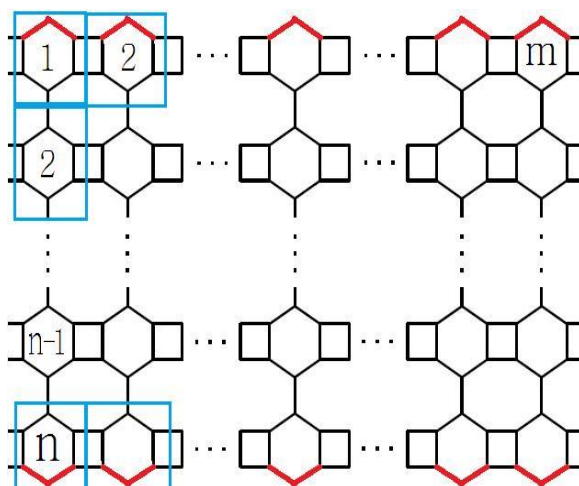
FIG. 1. The molecular graph of $VPHX[m, n]$ nanotube

TABLE 1. The edge partition of $VPHX[m, n]$ nanotubes

Edge partition	$E_5 = E_6^*$	$E_6 = E_9^*$
$Cardinality$	$4m$	$9mn - 5m$

TABLE 2. The vertex partition of $VPHX[m, n]$ nanotubes

Vertex partition	V_2	V_3
$Cardinality$	$m + m$	$6mn - 2m$

Thus:

$$
\begin{aligned}
F(VPHX[m,n]) &= \sum_{uv \in E(VPHX[m,n])} \left[\delta^2_{VPHX[m,n]}(u) + \delta^2_{VPHX[m,n]}(v) \right] \\
&= \sum_{uv \in E_6^*(VPHX[m,n])} \left[\delta^2_{VPHX[m,n]}(u) + \delta^2_{VPHX[m,n]}(v) \right] \\
&+ \sum_{uv \in E_9^*(VPHX[m,n])} \left[\delta^2_{VPHX[m,n]}(u) + \delta^2_{VPHX[m,n]}(v) \right] \\
&= 13|E_6^*(VPHX[m,n])| + 18|E_9^*(VPHX[m,n])| \\
&= 52m + 18[9mn - 5m] \\
&= 162mn - 38m. \quad \square
\end{aligned}
$$

Theorem 3.1.2 The F-polynomial of $VPHX[m, n]$ nanotube (Fig. 1) is given by:

$$
F(VPHX[m,n], x) = m\left[4x^{13} + [9n - 5]x^{18} \right].
$$

Proof. Since the F-polynomial of graph G is

$$
F(G, x) = \sum_{uv \in E(G)} x^{[\delta_G^2(u) + \delta_G^2(v)]}
$$

And, as Theorem 3.1.1, the partitions of the vertex set and edge set $V(VPHX[m,n])$, $E(VPHX[m,n])$, of V-Phenylenic nanotube are given in Table 1,2 respectively, we have:

$$
\begin{aligned}
F(VPHX[m,n],x) &= \sum_{uv \in E(VPHX[m,n])} x^{[\delta^2_{VPHX[m,n]}(u)+\delta^2_{VPHX[m,n]}(v)]} \\
&= \sum_{uv \in E_6^*(VPHX[m,n])} x^{[\delta^2_{VPHX[m,n]}(u)+\delta^2_{VPHX[m,n]}(v)]} \\
&+ \sum_{uv \in E_9^*(VPHX[m,n])} x^{[\delta^2_{VPHX[m,n]}(u)+\delta^2_{VPHX[m,n]}(v)]} \\
&= |E_6^*(VPHX[m,n])|x^{13} + |E_9^*(VPHX[m,n])|x^{18} \\
&= 4mx^{13} + [9mn - 5m]x^{18} \\
&= m\Big[4x^{13} + [9n-5]x^{18}\Big]. \quad \square
\end{aligned}
$$

We can also get the F-index of $VPHX[m,n]$ nanotube by derivating the relation F-polynomial of $VPHX[m,n]$ nanotube above as:

$$
\begin{aligned}
F(VPHX[m,n]) &= \frac{\partial Y(VPHX[m,n],x)}{\partial x}\Big|_{x=1} = \frac{\partial m\Big[4x^{13}+[9n-5]x^{18}\Big]}{\partial x}\Big|_{x=1} \\
&= 162mn - 38m.
\end{aligned}
$$

Corollary 3.1.3 The F-index of complement $VPHX[m,n]$ nanotube (Fig. 1) is given by:

$$
\begin{aligned}
F(\overline{VPHX[m,n]}) &= 6mn\Big[6mn-1\Big]^3 - 6(9mn-m)\Big[6mn-1\Big]^2 \\
&+ 3\Big[6mn-1\Big](54mn-10m) - (162mn-38m).
\end{aligned}
$$

Proof. By Proposition 2.1 we have

$$
F(\overline{G}) = n(n-1)^3 - 6m(n-1)^2 + 3(n-1)M_1(G) - F(G).
$$

And $F(VPHX[m,n]) = 162mn - 38m$ given in Theorem 3.1.1 above. $M_1(VPHX[m,n]) = 54mn - 10m$ and the partitions of the vertex set and edge set of $(VPHX[m,n])$ nanotubes are given in [9]:

$$
\sum |V(VPHX[m,n])| = 6mn, \qquad \sum |E(VPHX[m,n])| = 9mn - m
$$

Thus:

$$
\begin{aligned}
F(\overline{VPHX[m,n]}) &= \sum |V(VPHX[m,n])|\Big[\sum |V(VPHX[m,n])| - 1\Big]^3 \\
&- 6\sum |E(VPHX[m,n])|\Big[\sum |V(VPHX[m,n])| - 1\Big]^2 \\
&+ 3\Big[\sum |V(VPHX[m,n])| - 1\Big]M_1(VPHX[m,n]) - F((VPHX[m,n]) \\
&= 6mn\Big[6mn-1\Big]^3 - 6(9mn-m)\Big[6mn-1\Big]^2 \\
&+ 3\Big[6mn-1\Big](54mn-10m) - (162mn-38m). \quad \square
\end{aligned}
$$

Corollary 3.1.4 The F-coindex of $VPHX[m,n]$ nanotube (Fig. 1) is given by:

$$
\overline{F}(VPHX[m,n]) = 12m^2n(27n-5) - 24m(9n-2).
$$

Proof. By Proposition 2.1, we have $\overline{F}(G) = (n-1)M_1(G) - F(G)$, $F(VPHX[m,n]) = 162mn - 38m$ given in Theorem 3.1.1 and $M_1(VPHX[m,n]) = 54mn - 10m$ given in Theorem 2.2 above and since $n = \sum |V(VPHX[m,n])| = 6mn$. Then:

$$
\begin{aligned}
\overline{F}(VPHX[m,n]) &= \Big[\sum |V(VPHX[m,n])| - 1\Big]M_1(VPHX[m,n]) \\
&- F(VPHX[m,n]) \\
&= (6mn-1)(54mn-10m) - (162mn-38m) \\
&= 12m^2n(27n-5) - 24m(9n-2). \quad \square
\end{aligned}
$$

TABLE 3. Some topological indices values of $H = VPHX[m,n]$ nanotubes

m	n	$M_1(H)$	$M_2(H)$	$F(H)$	$HM(H)$	$HM_2(H)$	$\overline{F}(H)$
2	2	196	330	572	1136	2394	3.936×10^3
2	3	304	492	896	1784	3852	9.744×10^3
3	2	294	495	858	1704	3591	9.432×10^3
3	3	456	738	1344	2676	5778	22.824×10^3
4	4	824	1308	2440	4864	10620	75.840×10^3
5	5	1300	2040	3860	7700	16920	189.840×10^3

TABLE 4. The edge and vertex partitions of $VPHY[m,n]$ nanotorus

Edge partition	$E_6 = E_9^*$
Cardinality	$9mn$

Vertex partition	V_3
Cardinality	$6mn$

Corollary 3.1.5   The F-coindex of complement $VPHX[m,n]$ nanotube (Fig. 1) is given by:

$$\overline{F}(\overline{VPHX[m,n]}) = 2(9mn - m)\Big[6mn - 1\Big]^2 - 2\Big[6mn - 1\Big](54mn - 10m)$$
$$+ \; 162mn - 38m.$$

Proof.   By Proposition 2.1 we have

$$\overline{F}(\overline{G}) = 2m(n-1)^2 - 2(n-1)M_1(G) + F(G),$$

$F(VPHX[m,n]) = 162mn - 38m$ given in Theorem 3.1.1 and and $M_1(VPHX[m,n]) = 54mn - 10m$ given in Theorem 2.2 above and as Corollary 3.1.3 the partitions of the vertex set and edge set of $(VPHX[m,n])$ nanotubes. Then:

$$\overline{F}(\overline{VPHX[m,n]}) = 2\sum|E(VPHX[m,n])|\Big[\sum|V(VPHX[m,n])| - 1\Big]^2$$
$$- \; 2\Big[\sum|V(VPHX[m,n])| - 1\Big]M_1(VPHX[m,n]) + F(VPHX[m,n])$$
$$= \; 2(9mn - m)\Big[6mn - 1\Big]^2 - 2\Big[6mn - 1\Big](54mn - 10m)$$
$$+ \; 162mn - 38m. \quad \square$$

In Table 3 some index and coindex values of $VPHX[m,n]$ nanotubes. formulas reported in Theorem 2.2, Theorem 3.1.1 and Corollary 3.1.4 for the $VPHX[m,n]$ nanotube. In the table, it shows that values of first and second Zagreb indices, first and second Hyper-Zagreb indices, F-index and F-coindex are in increasing order as the values of m, n increase.

3.2.   F-index and coindex of the V-Phenylenic Nanotorus $VPHY[m,n](\forall m, n \in \mathbb{N} - \{1\})$

Theorem 3.2.1   The F-index of the V-Phenylenic Nanotorus $VPHY[m,n](\forall m, n \in \mathbb{N} - \{1\})$ (Fig. 2) is given by:

$$F(VPHY[m,n]) = 162mn.$$

Proof.   By definition of the F-index $F(G) = \sum\limits_{uv \in E(G)} \Big[\delta_G^2(u) + \delta_G^2(v)\Big]$, and by replacing each G with $VPHY[m,n]$, which yield to $F(VPHY[m,n]) = \sum_{uv \in E(VPHY[m,n])} \Big[\delta_{VPHY[m,n]}^2(u) + \delta_{VPHY[m,n]}^2(v)\Big]$, and the partitions of the vertex set and edge set $V(VPHY[m,n])$, $E(VPHY[m,n])$, of V-Phenylenic nanotorus are given in Table 4 respectively [9–11].

The edge set of $VPHY[m,n]$ have only one type of edges:

$E_6(VPHY[m,n]) = E_9^* = \{e = uv \in E(VPHY[m,n]) : \delta(u) = 3, \delta(v) = 3\},$
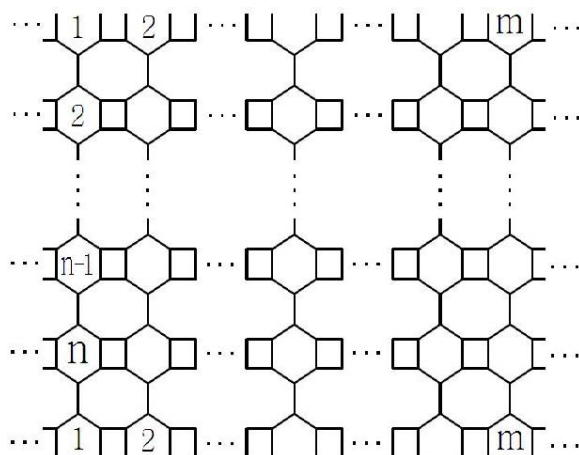
FIG. 2. The molecular graph of $VPHY[m,n]$ nanotorus

Thus:

$$
\begin{aligned}
F(VPHY[m,n]) &= \sum_{uv \in E(VPHY[m,n])} \left[\delta^2_{VPHY[m,n]}(u) + \delta^2_{VPHY[m,n]}(v) \right] \\
&= \sum_{uv \in E_9^*(VPHY[m,n])} \left[\delta^2_{VPHY[m,n]}(u) + \delta^2_{VPHY[m,n]}(v) \right] \\
&= 18|E_9^*(VPHY[m,n])| = 162mn. \quad \square
\end{aligned}
$$

Theorem 3.2.2 The F-polynomial of $VPHY[m,n]$ nanotorus (Fig. 2) is given by:

$$
F(VPHY[m,n], x) = 9mnx^{18}
$$

Proof. Since the F-polynomial of graph G

$$
F(G,x) = \sum_{uv \in E(G)} x^{[\delta_G^2(u) + \delta_G^2(v)]}
$$

And as Theorem 3.2.1 the partitions of the vertex set and edge set $V(VPHY[m,n])$, $E(VPHY[m,n])$, of V-Phenylenic nanotorus are given in Table 4 we have:

$$
\begin{aligned}
F(VPHY[m,n], x) &= \sum_{uv \in E(VPHY[m,n])} x^{[\delta^2_{VPHY[m,n]}(u) + \delta^2_{VPHY[m,n]}(v)]} \\
&= \sum_{uv \in E_9^*(VPHY[m,n])} x^{[\delta^2_{VPHY[m,n]}(u) + \delta^2_{VPHY[m,n]}(v)]} \\
&= |E_9^*(VPHY[m,n])|x^{18} = 9mnx^{18}. \quad \square
\end{aligned}
$$

We can also get the F-index of $VPHY[m,n]$ nanotorus by derivating the relation F-polynomial of $VPHY[m,n]$ nanotorus above as:

$$
F(VPHY[m,n]) = \frac{\partial F(VPHY[m,n], x)}{\partial x}\Big|_{x=1} = \frac{\partial [9mnx^{18}]}{\partial x}\Big|_{x=1} = 162mn.
$$

Corollary 3.2.3 The F-index of complement $VPHY[m,n]$ nanotorus (Fig. 2) is given by:

$$
F(\overline{VPHY[m,n]}) = 6mn\left[(6mn-1)^3 - 9(6mn-1)^2 + 27(6mn-2) \right].
$$

Proof. By Proposition 2.1 we have

$$
F(\overline{G}) = n(n-1)^3 - 6m(n-1)^2 + 3(n-1)M_1(G) - F(G),
$$

And $F(VPHY[m,n]) = 162mn$ given in Theorem 3.2.1 above. $M_1(VPHY[m,n]) = 54mn$ and the partitions of the vertex set and edge set of $(VPHY[m,n])$ nanotorus are given in [9].

$$
\sum |V(VPHY[m,n])| = 6mn, \qquad \sum |E(VPHY[m,n])| = 9mn
$$

TABLE 5. Some topological indices values of $G = VPHY[m,n]$ nanotorus

m	n	$M_1(G)$	$M_2(G)$	$F(G)$	$HM(G)$	$HM_2(G)$	$\overline{F}(G)$
2	2	216	324	648	1296	2916	4.320×10^3
2	3	324	486	972	1944	4374	10.368×10^3
3	2	324	486	972	1944	4374	10.368×10^3
3	3	486	729	1458	2916	6561	24.300×10^3
4	4	864	1296	2591	5184	11664	79.488×10^3
5	5	1350	2025	4050	8100	18225	197.100×10^3

Thus:

$$
\begin{aligned}
F(\overline{VPHY[m,n]}) &= \sum |V(VPHY[m,n])| \Big[\sum |V(VPHY[m,n])| - 1 \Big]^3 \\
&\quad - 6 \sum |E(VPHY[m,n])| \Big[\sum |V(VPHY[m,n])| - 1 \Big]^2 \\
&\quad + 3 \Big[\sum |V(VPHY[m,n])| - 1 \Big] M_1(VPHY[m,n]) - F((VPHY[m,n]) \\
&= 6mn \Big[(6mn-1)^3 - 9(6mn-1)^2 + 27(6mn-2) \Big]. \quad \square
\end{aligned}
$$

Corollary 3.2.4 The F-coindex of $VPHY[m,n]$ nanotorus (Fig. 2) is given by:

$$\overline{F}(VPHY[m,n]) = 54mn(6mn-4).$$

Proof. By Proposition 2.1 we have $\overline{F}(G) = (n-1)M_1(G) - F(G)$, $F(VPHY[m,n]) = 162mn$ given in Theorem 3.1.1 and $M_1(VPHY[m,n]) = 54mn$ given in Theorem 2.2 above and since $n = \sum |V(VPHY[m,n])| = 6mn$. Then:

$$
\begin{aligned}
\overline{F}(VPHY[m,n]) &= \Big[\sum |V(VPHY[m,n])| - 1 \Big] M_1(VPHY[m,n]) - F(VPHY[m,n]) \\
&= 54mn(6mn-4). \quad \square
\end{aligned}
$$

Corollary 3.2.5 The F-coindex of complement $VPHY[m,n]$ nanotorus (Fig. 2) is given by:

$$\overline{F}(\overline{VPHY[m,n]}) = 18mn \Big[(6mn-1)^2 - 36mn + 15 \Big].$$

Proof. By Proposition 2.1 we have

$$\overline{F}(\overline{G}) = 2m(n-1)^2 - 2(n-1)M_1(G) + F(G),$$

$F(VPHY[m,n]) = 162mn$ given in Theorem 3.2.1 and and $M_1(VPHX[m,n]) = 54mn$ given in Theorem 2.2 above and as Corollary 3.2.3 the partitions of the vertex set and edge set of $(VPHY[m,n])$ nanotorus. Then:

$$
\begin{aligned}
\overline{F}(\overline{VPHY[m,n]}) &= 2 \sum |E(VPHY[m,n])| \Big[\sum |V(VPHY[m,n])| - 1 \Big]^2 \\
&\quad - 2 \Big[\sum |V(VPHY[m,n])| - 1 \Big] M_1(VPHY[m,n]) + F(VPHY[m,n]) \\
&= 18mn \Big[6mn - 1 \Big]^2 - 108mn \Big[6mn - 1 \Big] + 162mn \\
&= 18mn \Big[(6mn-1)^2 - 36mn + 15 \Big]. \quad \square
\end{aligned}
$$

In Table 5 some index and coindex values of $VPHY[m,n]$ nanotorus formulas reported in Theorem 2.2, Theorem 3.1.1 and Corollary 3.2.5 for the $VPHY[m,n]$ nanotorus. Table 5 shows that values of first and second Zagreb indices, first and second Hyper-Zagreb indices, F-index and F-coindex are in increasing order as the values of m, n increase.

4. Conclusion

The forgotten index is one of the most important topological indices which preserves the symmetry of molecular structures and provides a mathematical formulation to predict their physical and chemical properties. The present study has computed the F-index and F-coindex of a physico chemical structure of V-Phenylenic Nanotube $VPHX[m, n]$ and V-Phenylenic Nanotorus $VPHY[m, n]$ and their molecular complement graphs. The study also has computed F-polynomial of V-Phenylenic Nanotube and V-Phenylenic Nanotorus. As the F-index and coindex can been used in QSPR/QSAR study and play a crucial role in analyzing some physico-chemical properties, the results obtained in our paper illustrate the promising prospects of application for nanostructures.

Acknowledgements

References

[1] Mondal S., Bhosale A., De N., Pal A. Topological properties of some nanostructures, *Nanosystems: Physics, Chemistry, Mathematics*, 2020, **11**(1),P. 14–24.

[2] Alsharafi M., Shubatah M., Alameri A. The forgotten index of complement graph operations and its applications of molecular graph. *Open Journal of Discrete Applied Mathematics*, 2020, **3**(3), P. 53–61.

[3] Alsharafi M., Shubatah M., Alameri A. The First and Second Zagreb Index of Complement Graph and Its Applications of Molecular Graph. *Asian Journal of Probability and Statistics*, 2020, **8**(3), P. 15–30.

[4] Gutman I., Trinajstic N. Graph theory and molecular orbitals. Total π-electron energy of alternant hydrocarbons. *Chem. Phys. Lett.*, 1972, **17**, P. 535–538.

[5] Khalifeh M., Yousefi-Azari H., Ashrafi A.R. The first and second Zagreb indices of some graph operations. *Discrete applied mathematics*, 2009, **157**(4), P. 804–811.

[6] Ashrafi A., Doslic T., Hamzeh A. The Zagreb coindices of graph operations. *Discret. Appl.Math*, 2010, **158**, P. 1571–1578.

[7] Furtula B., Gutman I. A forgotten topological index. *J. Math. Chem.*, 2015, **53**(4), P. 1184–1190.

[8] De., Nilanjan, Sk Md Abu Nayeem, and Anita Pal. The F-coindex of some graph operations. *SpringerPlus*, 2016, **5**(1), P. 221.

[9] Farahani M.R., Kumar R.P., Kanna M.R. First and second zagreb indices and polynomials of V-phenylenic nanotubes and nanotori. *Int. J. Pharm. Sci. Res.*, 2017, **8**(1), P. 330–333.

[10] Farahani M.R., Kanna M.R., Kumar R.P. On the Hyper-Zagreb indices of nano-structures. *Asian Academic Research Journal of Multidisciplinary*, 2016, **3**(1), P. 115–123.

[11] Farahani M.R., Wei Gao On Multiplicative and Redefined Version of Zagreb Indices of V-Phenylenic Nanotubes and Nanotorus. *BJMCS*, 2016, **13**(5), P. 1–8.

[12] Ashrafi A.R., Ghorbani M., Jalali M. Computing sadhana polynomial of V-phenylenic nanotubes and nanotori. *Ind. J. Chem.*, 2008, **47A**, P. 535–537.

[13] Alamian V., Bahrami A., Edalatzadeh B. PI Polynomial of V-Phenylenic Nanotubes and Nanotori. *Int. J. Mol. Sci.*, 2008, **9**, P. 229–234.

[14] Ahmad Z., Naseem M., Jamil M.K., Siddiquid M.K., Nadeemd M.F. New results on eccentric connectivity indices of V-Phenylenic nanotube. *Eurasian Chem. Commun.*, 2020, **2**, P. 663–671.

[15] Furtula B., Gutman I., Dehmer M. On structure-sensitivity of degree-based topological indices. *Appl. Math. Comput.*, 2013, **219**, P. 8973–8978.

[16] Jiang H., Sardar M.S., et al. Computing sanskruti index V-phenylenic nanotube and nanotori. *Int. J. Pure Appl. Math.*, 2017, **115**(4), P. 859–865.

[17] Alsharafi M., Shubatah M., Alameri A. On the Hyper-Zagreb coindex of some Graphs. *J. Math. Comput. Sci.*, 2020, **10**(5), P. 1875–1890.

[18] Alameri A., Shubatah M., Alsharafi M. Zagreb indices, Hyper Zagreb indices and Redefined Zagreb indices of conical graph. *Advances in Mathematics: Scientific Journal*, 2020, **9**(6), P. 3631–3642.

[19] Kwun Y.C., Munir M., Nazeer W., Rafique S., Kang S.M. M-Polynomials and topological indices of V-Phenylenic Nanotubes and Nanotori. *Scientific Reports*, 2017, **7**(1)P. 8756.

[20] Alsharafi M., Shubatah M. On the Hyper-Zagreb index of some Graph Binary Operations. *Asian Research Journal of Mathematics*, 2020, **16**(4), P. 12–24.

[21] Alsharafi M., Shubatah M., Alameri A. The hyper-Zagreb index of some complement graphs. *Advances in Mathematics: Scientific Journal*, 2020, **9**(6),P. 3631–3642.

Green's function method for time-fractional diffusion equation on the star graph with equal bonds

Z. A. Sobirov[1,2], K. U. Rakhimov[2], R. E. Ergashov[2]

[1]University of Geological Sciences, Olimlar str., 49, 100041, Tashkent, Uzbekistan

[2]National University of Uzbekistan, Universitet str., 4, 100174, Tashkent, Uzbekistan

z.sobirov@nuu.uz, kamoliddin_ru@inbox.ru

This work devoted to construction of the matrix-Green's functions of initial-boundary value problems for the time-fractional diffusion equation on the metric star graph with equal bonds. In the case of Dirichlet and mixed boundary conditions we constructed Green's functions explicitly. The uniqueness of the solutions of the considered problems were proved by the method of energy integrals. Some possible applications in branched nanostructures were discussed.

Keywords: Time-fractional diffusion equation, IBVP, PDE on metric graphs, Green's function.

1. Introduction

In this work we consider initial-boundary value problem (IBVP) for time fractional diffusion equation

$$D_{0,t}^{\alpha} u(x,t) = \frac{\partial^2}{\partial x^2} u(x,t) - f(x,t),$$

on the bounded star graph. Here $D_{0,t}^{\alpha} g(t)$ is the fractional derivative defined by:

$$D_{\eta,t}^{\alpha} g(t) = \frac{1}{\Gamma(1-\alpha)} \frac{d}{dt} \int\limits_{\eta}^{t} \frac{g(\xi)}{|t-\xi|^{\alpha}} d\xi, \quad 0 < \alpha < 1,$$

where $\Gamma(x)$ is the Gamma function.

It is known that the diffusion equation is widely used in many fields of science including physics, biology, mechanics, chemistry and others. In recent years, the theory of fractional calculus has been studied with great interest. In particular, in the work [1] Bartlomiej Dybiec and Ewa Gudowska-Nowak considered a long-time, scaling limit for the anomalous diffusion composed of the subordinated Levy-Wiener process. In [2] T. A. M. Langlands and B. I. Henry introduced mesoscopic and macroscopic model equations of chemotaxis with anomalous subdiffusion for modeling chemically directed transport of biological organisms. In [3], the fractional Fokker-Planck equation for subdiffusion in a general space and time-dependent force field was studied. In [4], the authors solved an asymptotic boundary value problem without initial conditions for diffusion-wave equation with time-fractional derivative and gave some applications in fractional electrodynamics. Igor Goychuk in [5], considered an alternative continuous time random walk and fractional Fokker-Planck equation description.

Naturally, such a powerful tool as a fractional derivative cannot stay away from nanoscience. In particular, this can be seen from the results in [6,7]. In [6] authors obtained solutions for the magnetohydrodynamic mixed convection problem of Maxwell fractional nanofluid. In [7] authors studied models with non-integer order derivatives to describe dynamics in nanofluids. In particular, it is noticed that the rate of heat transfer increases with increasing nanoparticle volume fraction and order of the time-fractional derivative.

It is known that the Green's function method is a powerful technique for solving boundary value problems. The Green's function method for fractional order equations was investigated by A. V. Pskhu in [8]. In [9] Green's function method was used to find numerical solution of boundary value problems for stationary and non-stationary differential equations in different dimensions.

Nowadays, differential equations are being investigated with great interest on the metric graphs. It is mostly due to the fact, that majority of physical systems demonstrate flows, e.g., flows through the branched nanotubes [10]. The Schrödinger equation on the metric graph are well studied (see [11–13] and references in them). In [14] the Schrödinger operator on the graph with varying edges was investigated. The Schrödinger equation on the metric graphs was also explored with Fokas unified transformation method in [15]. In [11] it was considered as scattering

problem on the quantum graph, which consists ring with two attached semi-infinite leads. In [16] authors proposed the model of time-dependent geometric graph for description of the dynamical Casimir effect. In [17], the authors used metric graph approximation for investigation of strong variation of the viscosity and density in cylindrical domains of the small radius. And paper [18] devoted to an explicitly solvable model for periodic chain of coupled disks. In [19–21] IBVP for time-fractional Airy equation on the star graphs are considered via method of potentials.

2. Formulation of the problems

In this paper we construct Green's function of two IBVPs on the metric star graph for the time-fractional subdiffusion equation. Motivation for the study of the fractional diffusion equations on metric graphs comes from such practically important problems as anomalous heat transport in mesoscopic networks, subdiffusion processes in nanoscale network structures, molecular wires, different lattices and discrete structures. In such discrete structures one has memory effect which leads, in particular, to time fractional equations. These problems, in particular, describe transport of nanofluids in branched structures [6, 7].

We consider the star graph which has $m = k + l$ bonds connected in one point O (Fig. 1). We define coordinates in the graph's edges by isometric mapping this bonds to the interval from 0 to L, such that in each edge the coordinate 0 corresponds to the vertex O. The bonds of the graph are denoted by $B_j, j = \overline{1, m}$.
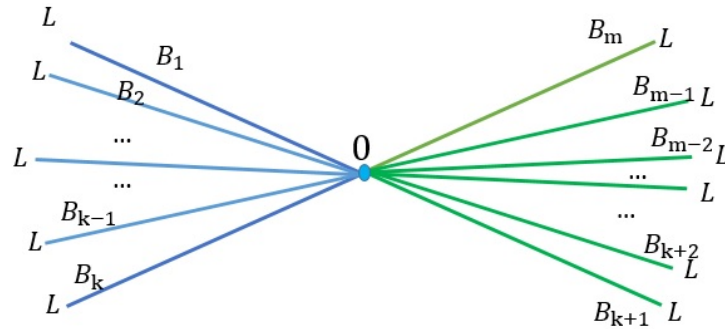
FIG. 1. Star graph with m bonds. We considered two cases of the boundary condition (BC): (a) Dirichlet BC at the all boundary vertices; (b) Dirichlet BC at the end points of the blue bonds and Neumann BC at the end points of the green bonds

On each bond B_j of the graph, we consider the time-fractional subdiffusion equation

$$D_{0,t}^\alpha u_j(x,t) = \frac{\partial^2}{\partial x^2} u_j(x,t) - f_j(x,t), \quad 0 < x < L, \, 0 < t < T, \, j = \overline{1, m}, \tag{1}$$

with the following initial conditions

$$\lim_{t \to 0} D_{0,t}^{\alpha-1} u_j(x,t) = \varphi_j(x), \quad 0 \le x \le L, \, j = \overline{1, m}. \tag{2}$$

At the inner vertex of the graph, we use the following gluing (Kirchhoff) conditions

$$u_1(0,t) = u_2(0,t) = ... = u_m(0,t), \tag{3}$$

$$\lim_{x \to 0} \left(\sum_{i=1}^m \frac{\partial}{\partial x} u_i(x,t) \right) = 0, \tag{4}$$

for all $t \in [0, T]$. These conditions ensure the local flow conservation at the branching point of the graph.

At the boundary vertices, we will use Dirichlet or Neumann boundary conditions (BC) given by

$$u_i(L,t) = \psi_i(t), \quad i = \overline{1, m}, \tag{5}$$

$$u_i(L,t) = \gamma_i(t), \quad i = \overline{1, k}, \tag{6}$$

$$\frac{\partial}{\partial x} u_j(L,t) = \gamma_j(t), \quad j = \overline{k+1, m}. \tag{7}$$

We suppose that the functions $f_j(x,t), j = \overline{1, m}$, initial and boundary data are smooth enough on the closure of their domains and the compatibility conditions on the boundary and branching points hold.

Problem 1. *Find regular solutions of equations (1) which satisfy conditions (2) — (5).*
Problem 2. *Find regular solutions of equations (1) which satisfy conditions (2) — (4), (6), (7).*

3. Uniqueness of solution

We put $u = (u_1, u_2, ..., u_m)^T$, $f = (f_1, ..., f_m)^T$, $\varphi = (\varphi_1, ..., \varphi_m)^T$. We define the norm of a vector function $v(x) = (v_1(x), ..., v_m(x))$ by $\|v\|^2 = \sum_{i=1}^{m} \int_0^L v_i^2(x)dx$.

$$D_{0,t}^{-\alpha}g(t) = \frac{1}{\Gamma(\alpha)} \int\limits_0^t \frac{g(\xi)}{|t-\xi|^{1-\alpha}}d\xi, \quad 0 < \alpha < 1,$$

is the time-fractional integral [22].

Lemma 1. *The problem 1 has at most one solution. Furthermore, if $\psi_i(t) \equiv 0, i = \overline{1, m}$, then the solutions satisfy the following a-priori estimate*

$$\|D_{0,t}^{\alpha-1}u\|^2 \leq E_\alpha(t^\alpha) \cdot \|\varphi\| + \Gamma(\alpha)E_{\alpha,\alpha}(t^\alpha)D_{0,t}^{-\alpha}\|D_{0,t}^{\alpha-1}f\|^2, \tag{8}$$

where $E_\alpha(z) = \sum_{n=0}^{\infty} z^n/\Gamma(\alpha n+1)$ and $E_{\alpha,\mu}(z) = \sum_{n=0}^{\infty} z^n/\Gamma(\alpha n+\mu)$ are the Mittag-Leffler functions.

Proof. Let $\psi_i(t) \equiv 0, i = \overline{1, m}$. We put $w(x,t) = D_{0,t}^{\alpha-1}u(x,t)$. It is clear, that the vector function $w(x,t) = (w_1(x,t), w_2(x,t), ..., w_m(x,t))^T$ satisfies the following equation:

$$\partial_{0,t}^{\alpha-1}w = w_{xx} + D_{0,t}^{\alpha-1}f(x,t), 0 < x < L, 0 < t < T, \tag{9}$$

with Caputo time-fractional derivative:

$$\partial_{\eta,t}^{\alpha}g(t) = \frac{1}{\Gamma(1-\alpha)} \int\limits_\eta^t \frac{g'(\xi)}{|t-\xi|^\alpha}d\xi, \quad 0 < \alpha < 1.$$

From [22], we have:

$$\int\limits_0^L w_j D_{0,t}^\alpha w_j dx \geq \frac{1}{2}D_{0,t}^\alpha \int\limits_0^L w_j^2 dx, \; j = 1, 2, ..., m. \tag{10}$$

Taking into account inequality (10), we multiply (9) by w^T from the left side, integrate the resulting relation with respect to x from 0 to L and use Cauchy's inequality:

$$\partial_{0,t}^\alpha \|w\|^2 + 2\|w_x\|^2 \leq \|w\|^2 + \|D_{0,t}^{\alpha-1}f\|^2.$$

Hence,

$$D_{0,t}^\alpha \|w\|^2 \leq \|w\|^2 + \|D_{0,t}^{\alpha-1}f\|^2. \tag{11}$$

From the analog of Gronwall-Bellman lemma (see [22]), in the case of Caputo type fractional derivative and the relation (11), we get:

$$\|w(\cdot,t)\|^2 \leq E_\alpha(t^\alpha)\|w(\cdot,0)\|^2 + \Gamma(\alpha)E_{\alpha,\alpha}(t^\alpha)D^{-\alpha}\|D_{0,t}^{\alpha-1}f(\cdot,t)\|.$$

So, we proved a-priory estimate (8). Uniqueness of the solution follows from this estimate.

Lemma 2. *The problem 2 has at most one solution. Furthermore, if $\gamma_i(t) \equiv 0, i = \overline{1, m}$, then the solutions satisfy the following a-priori estimate*

$$\|D_{0,t}^{\alpha-1}u\|^2 \leq E_\alpha(t^\alpha) \cdot \|\varphi\| + \Gamma(\alpha)E_{\alpha,\alpha}(t^\alpha)D_{0,t}^{-\alpha}\|D_{0,t}^{\alpha-1}f\|^2, \tag{12}$$

Proof. The proof is similar with the proof of the Lemma 1.

4.   Green's function of Problem 1

The following theorem directly follows from the theorem **4.3.1.** (see [8]). Let $E = \{(x,t)\colon 0 < x < L, 0 < t < T\}$ (where T is positive real number) and $E_t = \{(\xi, \tau)\colon 0 < \xi < L, 0 < \tau < t\}$.

Theorem 1. Let the $m \times m$ matrix function $V = V(x,t;\xi,\tau)$ satisfy following conditions:
1. The matrix function V is the solution for equation

$$V_{\xi\xi}(x,t;\xi,\tau) - D_{t,\tau}^{\alpha}V(x,t;\xi,\tau) = 0$$

on the fixed point $(x,t) \in E$;
2. For every $m \times 1$ vector function $h(x) \in C[0, L]$ holds

$$\lim_{\tau \to t} \int_0^L D_{t,\tau}^{\alpha-1}V(x,t;\xi,\tau)h(\xi)d\xi = h(x). \tag{13}$$

3. The matrix functions $V, V_\xi, V_{\xi\xi}, D_{0,t}^{\alpha-1}V$ are continuous on the $\overline{E} \times \overline{E_t}\backslash\{t = 0\}$ and for all points $(x,t) \in E$ and $(\xi,\tau) \in E_t$ holds inequality

$$|V_{ij}(x,t;\xi,\tau)| < (t - \tau)^{\alpha/2-1}.$$

If the function $u(x,t)$ is the solution of the equation (1) and satisfies the condition (2), then for all (x,t) is hold, that:

$$u(x,t) = \int_0^t (V(x,t;L,\tau)u_\xi(L,\tau) - V(x,t;0,\tau)u_\xi(0,\tau) - V_\xi(x,t;L,\tau)u(L,\tau)+$$

$$V_\xi(x,t;0,\tau)u(0,\tau))d\tau - \int_0^L V(x,t;\xi,0)\varphi(\xi)d\xi + \int_0^t\int_0^L V(x,t;\xi,\tau)f(\xi,\tau)d\xi d\tau.$$

Proof. The proof is similar to the proof of the theorem **4.3.1.** [8].

Taking into account the above theorem, we look for solution of **Problem 1** in the following form

$$u(x,t) = \int_0^t (G(x,t;L,\tau)u_\xi(L,\tau) - G(x,t;0,\tau)u_\xi(0,\tau) - G_\xi(x,t;L,\tau)u(L,\tau)+$$

$$G_\xi(x,t;0,\tau)u(0,\tau))d\tau - \int_0^L \varphi(t)G(x,t;\xi,\tau)d\xi - \int_0^t\int_0^L G(x,t;\xi,\tau)f(\xi,\tau)d\xi d\tau, \tag{14}$$

where:

$$G = \begin{pmatrix} G^{11} & G^{12} & ... & G^{1m} \\ G^{21} & G^{22} & ... & G^{2m} \\ ... & ... & ... & ... \\ G^{m1} & G^{m2} & ... & G^{mm} \end{pmatrix}$$

is a matrix-Green's function. Green's function satisfies the equation:

$$G_{\xi\xi} - D_{t,\tau}^{\alpha}G = 0,$$

for all $\xi \neq x, 0 < \tau < t$.

We look for Green's function in the following form

$$G = \sum_{n=-\infty}^{+\infty} \left(A_n\Gamma(x - \xi + 2nL, t - \tau) + B_n\Gamma(x + \xi + 2nL, t - \tau)\right), \tag{15}$$

where A_n and B_n are constant matrices of dimension $m \times m$ and $\Gamma(s,t)$ is:

$$\Gamma(s,t) = \frac{1}{2}t^{\alpha/2-1}e_{1,\alpha/2}^{1,\alpha/2}\left(-\frac{|s|}{t^{\alpha/2}}\right).$$

We have to find the matrices A_n and B_n.

Taking into account (14) and the conditions (2)—(4) we get the following conditions for matrix-Green's function:

$$G|_{\xi=L} = 0, \tag{16}$$

$$G^{i1}|_{\xi=0} = G^{i2}|_{\xi=0} = ... = G^{im}|_{\xi=0}, \quad i = \overline{1,m}, \tag{17}$$

$$G^{i1}_\xi|_{\xi=0} + G^{i2}_\xi|_{\xi=0} + ... + G^{in}_\xi|_{\xi=0} = 0, \quad i = \overline{1,m}. \tag{18}$$

Let

$$A_n = \begin{pmatrix} A_n^{11} & A_n^{12} & ... & A_n^{1m} \\ A_n^{21} & A_n^{22} & ... & A_n^{2m} \\ ... & ... & ... & ... \\ A_n^{m1} & A_n^{m2} & ... & A_n^{mm} \end{pmatrix} \quad \text{and} \quad B_n = \begin{pmatrix} B_n^{11} & B_n^{12} & ... & B_n^{1m} \\ B_n^{21} & B_n^{22} & ... & B_n^{2m} \\ ... & ... & ... & ... \\ B_n^{m1} & B_n^{m2} & ... & B_n^{mm} \end{pmatrix}.$$

From (16), we have:

$$A_n = -B_{n-1}. \tag{19}$$

From (17), we get:

$$A_n^{i1} - A_n^{im} = B_n^{im} - B_n^{i1}. \tag{20}$$

From (18), we obtain:

$$\sum_{j=1}^m A_n^{ij} = \sum_{j=1}^m B_n^{ij}, \quad i = \overline{1,m}. \tag{21}$$

We rewrite the relations (20) and (21) in the following matrix form $B_n = A_n M$, where:

$$M = \frac{1}{m}\begin{pmatrix} 2-m & 2 & ... & 2 \\ 2 & 2-m & ... & 2 \\ ... & ... & ... & ... \\ 2 & 2 & ... & 2-m \end{pmatrix}. \tag{22}$$

Combining (19), (20) and (21), we get:

$$\begin{cases} B_n = A_n M \\ A_{n+1} = -B_n \end{cases}.$$

And we find

$$A_{n+1} = -A_n M.$$

From the condition (13) follows that $A_0 = I$. So, we have

$$A_n = (-1)^n M^n, \quad B_n = (-1)^n M^{n+1}. \tag{23}$$

Substituting (23) into (15) we get matrix Green's function of the **Problem 1**:

$$G = \sum_{n=-\infty}^{+\infty} (-1)^n M^n \left(\Gamma(x - \xi + 2nL, t - \tau) + M\Gamma(x + \xi + 2nL, t - \tau) \right). \tag{24}$$

Taking into account **Lemma 1** we get following theorem.

Theorem 2. Let $\phi_i(t), \varphi_i(t) \in C[0,T]$ $(i = \overline{1,m}, T > 0)$, and $f(x,t) \in C^{0,1}\{(x,t) : 0 \le x \le L, 0 < t < T\}$. Then the **Problem 1** has unique solution in the form of:

$$u(x,t) = -\int_0^t G_\xi(x,t;L,\tau)u(L,\tau)d\tau - \int_0^L \varphi(\xi)G(x,t;\xi,\tau)d\xi - \int_0^t \int_0^L G(x,t;\xi,\tau)f(\xi,\tau)d\xi d\tau,$$

where $G(x,t;\xi,\tau)$ is given by (24).

5. Green's function of Problem 2

In this case, the Green's function has a form of:

$$G_1 = \sum_{n=-\infty}^{+\infty} \left(C_n \Gamma(x - \xi + 2nL, t - \tau) + D_n \Gamma(x + \xi + 2nL, t - \tau)\right), \tag{25}$$

where C_n and D_n are unknown constant matrices of dimension $m \times m$. We have to find the matrices C_n and D_n.

Taking into account (13) and conditions (2)—(4), (6), (7), we get following conditions for Green's function:

$$\begin{cases} G_1^{ij}|_{\xi=L} = 0, & i = \overline{1,k}, \ j = \overline{1,m}, \\ G_{1\xi}^{ij}|_{\xi=L} = 0, & i = \overline{k+1,m}, \ j = \overline{1,m} \end{cases}, \tag{26}$$

$$G_1^{i1}|_{\xi=0} = G_1^{i2}|_{\xi=0} = ... = G_1^{in}|_{\xi=0}, \quad i = \overline{1,m}, \tag{27}$$

$$G_{1\xi}^{i1}|_{\xi=0} + G_{1\xi}^{i2}|_{\xi=0} + ... + G_{1\xi}^{im}|_{\xi=0}, \quad i = \overline{1,m}. \tag{28}$$

Let

$$C_n = \begin{pmatrix} C_n^{11} & C_n^{12} & ... & C_n^{1m} \\ C_n^{21} & C_n^{22} & ... & C_n^{2m} \\ ... & ... & ... & ... \\ C_n^{m1} & C_n^{m2} & ... & C_n^{mm} \end{pmatrix} \quad \text{and} \quad D_n = \begin{pmatrix} D_n^{11} & D_i^{12} & ... & D_n^{1m} \\ D_n^{21} & D_i^{22} & ... & D_n^{2m} \\ ... & ... & ... & ... \\ D_n^{m1} & D_n^{m2} & ... & D_n^{mm} \end{pmatrix}.$$

Combining (26), (27) and (28), respectively, we get:

$$\begin{cases} C_n^{ij} = -D_{n-1}^{ij} & \text{for} \ i = \overline{1,k}, j = \overline{1,m}, \\ C_n^{ij} = D_{n-1}^{ij} & \text{for} \ i = \overline{k+1,m}, j = \overline{1,m}. \end{cases} \tag{29}$$

$$C_n^{i1} - C_n^{im} = D_n^{im} - D_n^{i1}, \quad i = \overline{1,m}. \tag{30}$$

$$\sum_{j=1}^{m} C_n^{ij} = \sum_{j=1}^{m} D_n^{ij}, \quad i = \overline{1,m}. \tag{31}$$

And we rewrite the relations (30) and (31) on the following matrix form:

$$C_n \begin{pmatrix} 1 & 1 & 1 & ... & 1 & 1 \\ -1 & 0 & 0 & ... & 0 & 1 \\ 0 & -1 & 0 & ... & 0 & 1 \\ ... & ... & ... & ... & ... & ... \\ 0 & 0 & 0 & ... & 0 & 1 \\ 0 & 0 & 0 & ... & -1 & 1 \end{pmatrix} = D_n \begin{pmatrix} -1 & -1 & -1 & ... & -1 & 1 \\ 1 & 0 & 0 & ... & 0 & 1 \\ 0 & 1 & 0 & ... & 0 & 1 \\ ... & ... & ... & ... & ... & ... \\ 0 & 0 & 0 & ... & 0 & 1 \\ 0 & 0 & 0 & ... & 1 & 1 \end{pmatrix}.$$

From this relation, we find $D_n = C_n M$ where: M given at the form (22). We find

$$C_{n+1} = \Phi D_n,$$

where

$$\Phi = \begin{pmatrix} -I_k & 0 \\ 0 & I_l \end{pmatrix}.$$

From the condition (13), we have that $C_0 = I$. (29) can be written as:

$$C_n = \Phi^n M^n, D_n = \Phi^n M^{n+1}, \tag{32}$$

where:

$$\Phi^n = \begin{pmatrix} (-1)^n I_k & 0 \\ 0 & I_l \end{pmatrix}.$$

Substituting (32) into (25) we get matrix Green's function of the **Problem 2**:

$$G_1 = \sum_{n=-\infty}^{+\infty} \Phi^n M^n \left(\Gamma(x - \xi + 2nL, t - \tau) + M\Gamma(x + \xi + 2nL, t - \tau)\right), \tag{33}$$

As a result, we get following theorem.

Theorem 3. Let $\beta_i(x) \in C[0,L], \gamma_i(t) \in C[0,T]$ and $f_i(x,t) \in C^{0,1}\{(x,t) : 0 \le x \le L, 0 < t < T,\}(i = \overline{1,m}, T > 0)$. Then the **Problem 2** has a unique solution in the form of:

$$u(x,t) = \int\limits_0^t \left(G_1^{(N)}(x,t;L,\tau)\frac{\partial u_N(\xi,\tau)}{\partial \xi}\bigg|_{\xi=L} - G_{1\xi}^{(D)}(x,L;t,\tau)u_D(L,\tau) \right)d\tau -$$

$$\int\limits_0^L \varphi(\xi)G_1(x,t;\xi,\tau)d\xi - \int\limits_0^t \int\limits_0^L G_1(x,t;\xi,\tau)f(\xi,\tau)d\xi d\tau,$$

where

$$G_1^{(D)} = \begin{pmatrix} G_1^{11} & G_1^{12} & ... & G_1^{1m} \\ ... & ... & ... & ... \\ G_1^{k1} & G_1^{k2} & ... & G_1^{km} \\ 0 & 0 & ... & 0 \\ ... & ... & ... & ... \\ 0 & 0 & ... & 0 \end{pmatrix}, \quad G_1^{(N)} = \begin{pmatrix} 0 & 0 & ... & 0 \\ ... & ... & ... & ... \\ 0 & 0 & ... & 0 \\ G_1^{k+1,1} & G_1^{k+1,2} & ... & G_1^{k+1,m} \\ ... & ... & ... & ... \\ G_1^{m1} & G_1^{m2} & ... & G_1^{mm} \end{pmatrix},$$

$u_D = (u_1, ..., u_k, 0, ..., 0)^T$, $u_N = (0, ..., 0, u_{k+1}, ..., u_m)^T$ and G_1 is on the form (33).

Conclusion

In this paper, we gave Green's function approach for IBVP to time-fractional diffusion equation with Neumann and Dirichlet boundary conditions. We constructed Green's functions of the considered problems in the form of matrix series. We notice that Green's functions for IBVP for time-fractional diffusive equation on metric graphs were firstly constructed in the present paper. Green's function on the case of line-interval for different IBVPs are constructed in [4].

It is well-known that Green's functions on metric graphs are closely related to scattering problem at the branching points [23]. In our case, the component $G_{ij}, (i \ne j)$ describes, for example, heat flow conduction from i-th bond to j-th bond, while G_{ii} describes heat flow reflection (thermal reflection) on i-th bond. Therefore, one can conclude that Green's functions constructed in the present paper can be considered as a powerful tool to investigate the conductivity (scattering) properties in sub-diffusive processes in nano-sized thin branched structures.

References

[1] Dybiec B., Gudowska-Nowak E. Anomalous diffusion and generalized Sparre-Andersen scaling. *Europhysics Letters Association*, 2009, **88**, P. 10003.

[2] Langlands T.A.M., Henry B.I. Fractional Chemotaxis Diffusion Equations. *Physics Review E*, 2010, **81**(5), P. 051102.

[3] Henry B.I., Langlands T.A.M., Starka P. Fractional Fokker-Planck Equations for Subdiffusion with Space-and-Time-Dependent Forces. *Physical Review Letters*, 2010, **105**, P. 170602.

[4] Pskhu A., Rekhviashvili S. Fractional Diffusion-Wave Equation with Application in Electrodynamics. *Mathematics*, 2020, **8**(2086), P. 1–13.

[5] Goychuk I. Fractional time random walk subdiffusion and anomalous transport with finite mean residence times: faster, not slower. *Physics Review E*, 2012, **86**(2), P. 021113.

[6] Aman S., Khan I., Ismail Z., Salleh M.Z., Tlili I. A new Caputo time fractional model for heat transfer enhancement of water based graphene nanofluid: An application to solar energy. *Results in Physics*, 2018, **9**, P. 1352–1362.

[7] Aman S., Khan I., Ismail Z., Salleh M.Z. Applications of fractional derivatives to nanofluids: exact and numerical solutions. *Mathematical Modelling of Natural Phenomena*, 2018, **13**(1), P. 1–12.

[8] Pskhu A.V. *Fractional partial differential equations*. Moscow, Nauka, 2005, 200 p.

[9] Mehdi D., Mohammad D., Mohsen J. Introduction to Green's Function and its Numerical Solution. *Middle-East Journal of Scientific Research*, 2012, **11**(7), P. 974–981.

[10] Chivilikhin S.A., Gusarov V.V., Popov I.Y. Charge pumping in nanotube filled with electrolyte. *Chinese Journal of Physics*, 2018, **56**(5), P. 2531–2537.

[11] Gerasimov D., Popov I., Blinova I., Popov A. Incompleteness of resonance states for quantum ring with two semi-infinite edges. *Analysis and Mathematical Physics*, 2019, **9**, P. 1287–1302.

[12] Kottos T., Smilansky U. Periodic Orbit Theory and Spectral Statistics for Quantum Graphs. *Annals of Physics*, 1999, **274**(1), P. 76–124.

[13] Gnutzmann S., Smilansky U. Quantum graphs: Applications to quantum chaos and universal spectral statistics. *Advances in Physics*, 2006, **55**(5-6), P. 527–625.

[14] Nikiforov D.S., Blinova I.V., Popov I.Y. Schrödinger and Dirac dynamics on time-dependent quantum graph. *Indian Journal of Physics*, 2019, **93**(7), P. 913–920.

[15] Khudayberganov G., Sobirov Z., Eshimbetov M. Unified transform method for the Schrodinger equation on a simple metric graph. *Journal of Siberian Federal University, Mathematics and Physics*, 2019, **12**(4), P. 412–420.

[16] Lobanov I.S., Nikiforov D.S., Popov I.Y., Trifanov A.I., Trifanova E.S. Model of time-dependent geometric graph for dynamical Casimir effect. *Indian Journal of Physics*, 2020, DOI: 10.1007/s12648-020-01866-5.

[17] Smolkina M.O., Popov I.Y., Blinova I.V., Milakis E. On the metric graph model for flows in tubular nanostructures. *Nanosystems: Physics, Chemistry, Mathematics*, 2019, **10**(1), P. 6–11.

[18] Grishanov E.N., Eremin D. A., Ivanov D.A., Popov I.Yu., Smirnov P.I. Periodic chain of disks in a magnetic field: bulk states and edge states. *Nanosystems: Physics, Chemistry, Mathematics*, 2015, **6**(5), P. 637–643.

[19] Sobirov Z.A., Rakhimov K.U. Cauchy problem for the Airy equation with fractional time-fractional on a star-shaped graph. *Institute of Mathematics Bulletin, Uzbekistan*, 2019, **5**, P. 40–49.

[20] Rakhimov K.U. The method of potentials for the Airy equation of fractional order. *Bulletin of National University of Uzbekistan: Mathematics and Natural Sciences*, 2020, **3**(2), P. 222–235.

[21] Rakhimov K.U., Sobirov Z.A. Jabborov N.M. The time-fractional Airy equation on the metric graph. *Journal of Siberian Federal University, Mathematics and Physics*, 2021, **14**(3), P. 376–388.

[22] Alikhanov A.A. A Priori Estimates for Solutions of Boundary Value Problems for Fractional-Order Equations. *Differential equations*, 2010, **46**(5), P. 658–664.

[23] Andrade F.M., Schmidt A.G.M., Vicentini E., Cheng B.K., M.G.E. da Luz. Green's function approach for quantum graphs: An overview. *Physics Reports*, 2016, **647**, P. 1–46.

Spectral characteristics of composite obtained by embedding of magnetic nanoparticles into polymer matrix

I. V. Pleshakov[1], A. V. Prokof'ev[1], E. E. Bibik[2], E. K. Nepomnyashchaya[3],
E. N. Velichko[3], T. A. Kostitsyna[3], D. M. Seliutin[3]

[1]Ioffe Institute, 26 Politechnicheskaya str., Saint Petersburg, 194021, Russia

[2]Saint Petersburg State Institute of Technology (Technical University), 26 Moskovsky ave.,
190013, Saint Petersburg, Russia

[3]Peter the Great Saint Petersburg Polytechnic University, 29 Polytechnicheskaya str.,
195251, Saint Petersburg, Russia

ivanple@yandex.ru

The transmission spectra of a composite material obtained by introducing magnetite nanoparticles into a polyvinyl alcohol matrix are studied. The samples were films on the glass substrate prepared by drying an aqueous solution of polymer and a ferrofluid. A number of them were made in a constant magnetic field, which led to the formation of extended aggregates. The features of these spectra and possible causes of their appearance are discussed.

Keywords: nanocomposite, magnetite nanoparticles, ferrofluid, polyvinyl alcohol.

1. Introduction

A composite, which is a polymer matrix with a nanodispersed filler, is a topic of interest both for basic science and for a wide variety of applications [1]. It is expected that among the plenty of such structures, in those where the integrated phase is a magnetically ordered compound, additional new properties, for example, the possibility to control their characteristics by an external field, may appear [2].

One of the simplest and most promising ways to produce a compound of this type is to prepare it from a mixture of a ferrofluid and a matrix-forming polymer dissolved in the same medium. This approach was used in the present work, where, on the basis of polyvinyl alcohol (PVA), the film samples with nanoparticles of magnetite (Fe_3O_4) were fabricated from an aqueous ferrofluid (FF) and PVA solution. These specimens, being transparent, were an optical material and their spectral properties were the subject of our study.

2. Experiment

2.1. Samples

The FF we used was a water-based magnetite colloid (the methods for producing such substances and their main properties are described in [3]). Its stabilization, i.e., preventing the nanoparticles adhesion, was performed by creating a double layer on the surface of Fe_3O_4, consisting of molecules with hydrophobic (inner) and hydrophilic (outer) portions, which are oleic acid salts. The diameter of the magnetite core was approximately 10 nm, and the total diameter of the particle together with the shell was about 15 nm (which is slightly larger than in those FFs where a single layer of surfactant is used). The concentration of the solid phase in the liquid was about 2 vol. %.

PVA solution was made by dissolution of its dry powder in deionized water (5 wt. % of PVA to water weight) at the temperature of 90°C. It was filtered through a cotton and then diluted with the heated to the same temperature FF in a ratio of 1 : 4 (FF volume to PVA solution volume). The mixture was thoroughly stirred and kept at 90°C for about an hour. Then it was left for two days in a hermetically sealed vessel, preventing evaporation. The resulting substance was a homogeneous liquid.

The samples were created by applying a drop of solution to a glass substrate, which, during drying at room temperature, formed a film with a thickness of 30–35 microns. In the same way, control samples of pure PVA films were made. The films with FF were dried both without a field and in a magnetic field with strength of H = 5 kOe applied in the film plane (for five hours). Visually, the samples differed: in the first case, they were a homogeneous,

fairly transparent material of a brownish color, and in the second – a material with a pronounced structure in the form of thin filamentous formations oriented along the field and separated by almost transparent areas.

Micrographs of the samples are shown in Fig. 1a depicts that, despite the external homogeneity, the composite prepared without a field comprises the droplets with the sizes of the order of ten micrometers. It is known that large aggregates of magnetic nanoparticles are formed in FF with certain additives [4–6], and, as it follows from our experiment, an aqueous solution of PVA produces the same effect. In the field, the agglomerates stretch out, forming a system of elongated objects, Fig. 1b. Their dimensions in thickness are tens of microns, which nearly corresponds to the data of other studies [5]. Note that along with the large prolate structural elements in Fig. 1b, the smaller ones are clearly visible, the precursors of which were, apparently, smaller droplets.
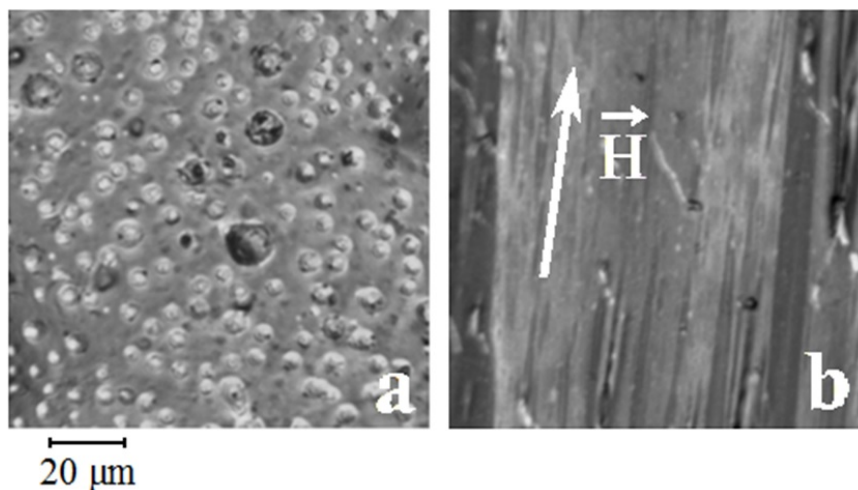
FIG. 1. Micrographs obtained for the samples prepared without field (a) and in the field H = 5 kOe (b)

To compare the experimental results obtained on the samples described above with the spectrum of a "pure" magnetic material in the solid phase, film obtained by drying highly concentrated (18 vol. % Fe_3O_4) FF on glass was also prepared.

2.2. Measurements

In our experiments we measured transmission spectra of the films in the wavelength (λ) range of 250–850 nm by a setup that included broadband light source L10290 (Hamamatsu) with deuterium and halogen lamps and spectrometer C10083MD (Hamamatsu) to detect the transmitted optical radiation. To apply the light to the sample, an optical fiber was used. The instrument function of the system was taken into account when processing the spectra.

The results of measurements on the composite materials were compared with the data obtained for pure PVA films on glass.

3. Results

Repeated experiments on recording the transmittance T of samples prepared at different times, carried out at different input optical radiation powers, gave qualitatively similar results. Figs. 1,2 exhibit typical data identifying the presence of peculiarity in the spectral characteristics of our composites.

Figure 2 shows the spectrum $T(\lambda)$ of the film obtained without the application of an external field, which is compared with the same characteristic of the FF in the liquid state. To measure the latter, a standard cuvette filled with a low-concentration (0.02 vol. % solid phase content) FF was used. A noticeable difference in these curves is apparent: in the liquid phase, the usual monotonic decrease in T in the range of 700–330 nm is observed (as an example, the similar data for kerosene-based FF can be found in [7]), in contrast to which the film with particle inclusions shows a significant increase in T at λ <450–500 nm. The sample obtained by drying of FF on a glass substrate did not display this feature. So, the behavior of the film spectrum must be related to the properties of the composite structure.

Figure 3 shows the transmission spectra of samples made with and without magnetic field (Fig. 3a), and also represents the spectrum of a sample with a pure PVA film (Fig. 3b). In general, the transmission of the film produced at the field action, increased (as expected due to the presence of transparent areas), while maintaining the feature of "enlarged translucence" at low λ. This may be perceived as the presence of a certain "peak", but a comparison of the
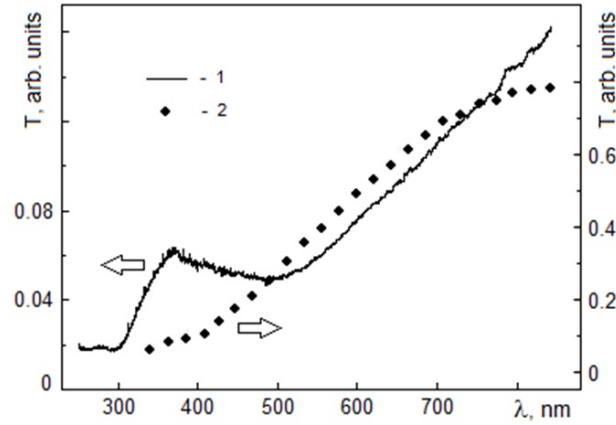
FIG. 2. Transmittance of the film prepared without field (1) compared with the transmittance of the liquid FF sample with solid phase concentration of 0.02 % (2)

data for composite films with $T(\lambda)$ in Fig. 3b shows that the glass with the PVA film acts as a kind of filter that cuts off light with $\lambda < 350$ nm. Thus, the corresponding curves may actually continue to increase at smaller wavelengths. However, the effect of material translucence at λ less than 450 nm remains unquestionable.
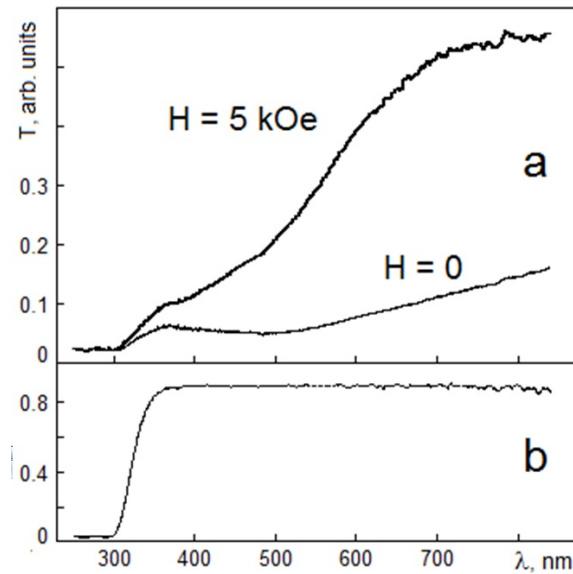
FIG. 3. Spectral characteristics of different samples: a – transmittance of the films prepared without magnetic field and in the field H = 5 kOe; b – transmittance of the film of pure PVA

4. Discussion

The light transmission of the FF solution is determined by processes of scattering and absorption on small particles of the material of solid phase. To separate these mechanisms may be difficult, but it is obvious that the smaller the λ, the greater the role of Rayleigh scattering on objects with a diameter of $d \sim 10$ nm, i.e., those that mainly make up the FF (the larger clusters also may exist in the solution, but their number can be regarded as insignificant [8]). The application of a magnetic field to such a medium leads to the formation of agglomerates, which affects its optical properties [9].

In our case, as shown in Fig. 1a, even a sample prepared in the absence of a magnetic field already contains large ($D \sim 10$ μm) droplet formations, which radically changes the scattering. Although scattering does not stop at $D \gg \lambda$, it takes on a different character [10]. Moreover, the number of scattering centers becomes many orders of magnitude smaller (the upper limit of it can be roughly estimated, assuming that all individual particles have entered to the drops,

and, consequently, the number of scatterers have become smaller by $(D/d)^3 \sim 10^9$ times). Drops in this situation will rather create a shadow effect. In fact, the part of the extinction that is associated with scattering turns out to be significantly weakened, which leads to the translucence of the sample in this range.

Samples manufactured in the magnetic field are much more transparent than those that were not exposed to the field (Fig. 3a), which is associated with a decrease in the shadow effect and with a decrease in the density of structural elements (Fig. 1b). An increase in the transmittance at $\lambda < 450$ nm was also observed here, which can presumably be explained by an additional decrease in the number of small scattering centers included in the extended magnetic nanoparticle aggregates formed by the field.

5. Conclusion

Thus, we performed a spectroscopic study of a nanostructured material containing magnetic particles. It is shown that a fundamental role in the analysis of the optical characteristics of this composite is played by taking into account the change in light scattering associated with both the peculiarities of the incorporation of nanoparticles into the polymer matrix and with the action of a magnetic field during sample preparation.

References

[1] Crosby A.J., Lee J.Y. Polymer nanocomposites: the "nano" effect on mechanical properties. *Polym. Rev.*, 2007, **47**(2), P. 217–229.

[2] McHenry M.E., Laughlin D.E. Nano-scale materials development for future magnetic applications. *Acta Mater.*, 2000, **1**, P. 223–238.

[3] Scherer C., Figueiredo Neto A.M. Ferrofluids: Properties and applications. *Braz. J. Phys.*, 2005, **35**(3A), P. 718–727.

[4] Zakinyan A.R., Dikansky Yu.I. Effect of microdrops deformation on electrical and rheological properties of magneticfluid emulsion. *J. Magn. Magn. Mat.*, 2017, **431**, P. 103–106.

[5] Prokof'ev A.V., Pleshakov I.V., Bibik E.E., Kuz'min Yu.I. An optical investigation of the geometric characteristics of aggregates formed by particles of magnetic fluid. *Tech. Phys. Lett.*, 2017, **43**(2), P. 194–196.

[6] Shlyagin M.G., Agruzov P.M., Pleshakov I.V., Prokofiev A.V., Bibik E.E. Incident-power-dependent refractive index of ferrofluid in magnetic field measured with a fiber optic probe. *Optik*, 2019, **186**, P. 418–422.

[7] Hoffmann B., Köhler W. Reversible light-induced cluster formation of magnetic colloids. *J. Magn. Magn. Mat.*, 2003, **262**(2), P. 289–293.

[8] Nepomnyashchaya E.K., Prokofiev A.V., Velichko E.N., Pleshakov I.V., Kuzmin Yu.I. Investigation of magneto-optical properties of ferrofluids by laser light scattering techniques. *J. Magn. Magn. Mat.*, 2017, **431**, P. 24–26.

[9] Mohapatra D.K., Philip J. Investigations on magnetic field induced optical transparency in magnetic nanofluids. *Opt. Mater.*, 2018, **76**, P. 97–105.

[10] Bohren C.F., Huffman D.R. *Absorption and scattering of light by small particles*. John Wiley & Sons, Inc., NY, 1998, 544 p.

Prooxidant potential of CeO$_2$ nanoparticles towards hydrogen peroxide

M. M. Sozarukova[1], E. V. Proskurnina[2], V. K. Ivanov[1]

[1]Kurnakov Institute of General and Inorganic Chemistry, Russian Academy of Sciences,
Leninsky Prospect, 31, Moscow, 119991, Russia

[2]Research Centre for Medical Genetics, Moskvorechie St, 1, Moscow, 115522, Russia

s_madinam@bk.ru, proskurnina@gmail.com, van@igic.ras.ru

The multifaceted enzyme-like activity of CeO$_2$ nanoparticles (CeNPs) expands the prospects for their potential biomedical applications. In this regard, there is a need for a comprehensive analysis of the redox behavior of CeO$_2$ nanoparticles in relation to key molecules of free radical homeostasis. Here, the prooxidant potential of CeNPs towards H$_2$O$_2$ was investigated to elucidate both prooxidant capacity and prooxidant activity of CeNPs. To describe the kinetics in the luminol–H$_2$O$_2$ system at pH 8.5 upon the addition of citrate-stabilized CeO$_2$ sol (3 nm), a numerical model of three reactions is proposed. The rate constants being a measure of prooxidant activity, were $k_1 = 9.0 \cdot 10^4$ μM^{-1}min^{-1}, $k_2 = 2.0 \cdot 10^{-6}$ μM^{-1}min^{-1}, $k_3 = 2.9 \cdot 10^{-5}$ μM^{-1}min^{-1}. The functionalization of CeO$_2$ nanoparticles surface with ammonium citrate increases their prooxidant capacity by two-fold, while modification with maltodextrin decreases it by six-fold. It was shown that the prooxidant capacity of citrate-stabilized CeO$_2$ sol in Tris-HCl is approximately four-fold higher than in phosphate buffer solution at pH 7.4.

Keywords: cerium dioxide nanoparticles, nanozymes, hydrogen peroxide, luminol, peroxidase, chemiluminescence, prooxidant, ammonium citrate, maltodextrin, mathematical modeling.

Received: 13 May 2021

1. Introduction

Cerium dioxide nanoparticles have a wide spectrum of nanozyme (enzyme-like) activities [1–6]. The ability to mimic the functions of a number of enzymes is due to the unique physicochemical properties of CeO$_2$ nanoparticles. The combination of the pro- and antioxidant properties of nanodisperse CeO$_2$ with its relatively low toxicity expands the field of its potential biomedical applications [7–11]. In turn, this makes it necessary to study the redox behavior of CeO$_2$ nanoparticles in relation to the key molecules of free radical homeostasis.

Among the types of enzyme-like activity of nanodisperse CeO$_2$, their functioning as peroxidase mimetics is important. Hydrogen peroxide is the most abundant reactive oxygen species and is involved in free radical metabolism [12]. Dismutation of superoxide anion radicals (SAR) catalyzed by superoxide dismutase (SOD) in biological tissues inevitably leads to the formation of H$_2$O$_2$ molecules that easily penetrate cell membranes. On the other hand, cerium dioxide nanoparticles exhibit SOD-like activity and, accordingly, the formation of hydrogen peroxide takes place when cerium dioxide acts as a SOD mimetic [1, 13, 14]. Thus, the study of the redox behavior of CeO$_2$ nanoparticles towards to hydrogen peroxide needs to be considered when analyzing SOD-like ceria activity. Currently, increasing attention is being paid not only to the cytotoxic function of H$_2$O$_2$ found in phagocytosis, mitochondrial and microsomal function, but also to its involvement in the regulation of cell signaling and transcription factors [15, 16]. Hydrogen peroxide plays an important role in cell proliferation [17], differentiation [18], migration [19] and apoptosis [20].

In this work, we analyzed the prooxidant potential of nanodisperse CeO$_2$ towards hydrogen peroxide according to the data of chemiluminescence analysis. Here, we consider prooxidant potential as a complex characteristic, combining both the prooxidant capacity (the number of formed reactive oxygen species per unit concentration of the prooxidant) and the prooxidant activity (the rate constant of the total reaction of the production of reactive oxygen species).

2. Materials and methods

2.1. Synthesis and physicochemical study of CeO$_2$ nanoparticles

An unstabilized aqueous colloidal solution of cerium dioxide nanoparticles (0.13 M) was prepared by thermohydrolysis of ammonium cerium(IV) nitrate (#215473, Sigma-Aldrich) [21]. Briefly, an aqueous solution of ammonium cerium(IV) nitrate (100 g/l) was kept for 24 h in an oven at 95°. The precipitate formed was separated by centrifugation and washed three times with isopropanol. To completely remove isopropanol, the resulting precipitate was redispersed in deionized water, followed by boiling for 1 h with constant stirring. The concentration of CeO$_2$ sol was determined

by the thermogravimetric method. Thus prepared colloidal solution of CeO_2 nanoparticles was stabilized with ammonium citrate ($C_6H_{14}O_7N_2$, disubstituted ammonium citrate, #247561, Sigma-Aldrich) or maltodextrin (#419672, dextrose equivalent 4.0–7.0, Sigma-Aldrich) in a molar ratio of 1 : 1 and 1 : 1.1, respectively.

X-ray diffraction patterns of nanodisperse CeO_2 samples were obtained using a Bruker D8 Advance diffractometer ($CuK\alpha$ radiation, geometry θ–2θ). The diffraction maxima were identified using the ICDD PDF2 database. The average hydrodynamic diameter of CeO_2 nanoparticles was estimated by dynamic light scattering using a Photocor Complex analyzer. The microstructure of the samples was studied by transmission electron microscopy on a Leo 912 AB Omega electron microscope at an accelerating voltage of 100 kV. UV-visible absorption spectra of CeO_2 sols were recorded using on OKB Spectr SF-2000 spectrophotometer.

3. The study of prooxidant activity in the chemiluminescent system luminol – H_2O_2

Luminol (5-amino-1, 2, 3, 4-tetrahydro-1, 4-pthalazinedione, 3-aminophthalic acid hydrazide, #A8511, Sigma-Aldrich) was used as a chemiluminescent probe (CL probe) sensitive to H_2O_2. A working solution with a concentration of 1 μM was prepared by dissolving a weighed amount of a CL probe in a 100 μM phosphate buffer solution (PBS, KH_2PO_4, #60220, Sigma-Aldrich), with further addition of KOH (#484016, Sigma-Aldrich) until the luminol was completely dissolved. After that, pH of the solution was adjusted to 7.4 using concentrated HCl (#320331, Sigma-Aldrich). Working solutions of hydrogen peroxide were prepared by diluting a stock solution of H_2O_2 (30%, #8.22287, Sigma-Aldrich). We also used a 100 μM buffer solution (pH 7.4) prepared from Tris hydrochloride (#10812846001, Merck).

Chemiluminescence (CL) was recorded on a 12-channel Lum-1200 chemiluminometer (DISoft) at room temperature. Aliquots of luminol (50 μM) and hydrogen peroxide (200 μM) were added to a plastic cuvette containing PBS. The analyzed sample was added to the luminol–H_2O_2 system 30–60 s after the start of the background emission recording. The total volume of the system was 1.000 ml. The light sum (area under the chemiluminescence curve) for 5 min was chosen as an analytical signal.

Mathematical simulation of chemiluminograms was carried out using the Kinetic Analyzer software (developed by D. Yu. Izmailov). As a result, the rate constants of the interaction of CeO_2 nanoparticles with the reaction substrate, which are a measure of prooxidant activity, were determined.

4. Results and discussion

Thermolysis of aqueous solution of ammonium cerium(IV) nitrate resulted in formation of electrostatically stabilized sol of nanodisperse cerium dioxide. The concentration of the CeO_2 sol, determined by the thermogravimetric method, was 23 g/l (0.13 M). The results of X-ray diffraction analysis indicated that the resulting sol contained single-phase cerium dioxide (PDF2 34-0394). The size of the obtained CeO_2 nanoparticles determined by Scherrer equation was found to be 3 nm. The data on the particle size and phase composition of the obtained CeO_2 samples were confirmed by transmission electron microscopy and electron diffraction.

According to the dynamic light scattering data, the average hydrodynamic diameters of CeO_2 nanoparticles without a stabilizer and those modified with ammonium citrate or maltodextrin were 11–12 nm, 16 nm and 17 nm, respectively. Insignificant changes in the hydrodynamic diameter upon interaction with stabilizers indicate approximately the same degree of particle aggregation in CeO_2 sols. The absorption spectra of the analyzed samples are shown in Fig. 1, the appearance of an absorption band in the region of 280–300 nm confirms the fact that the sols do contain nanodispersed cerium dioxide.

It is generally believed that the redox behavior of CeO_2 nanoparticles is determined by many factors, among which the pH of the reaction medium plays an important role. The effect of pH (4.0, 7.4, 8.5) on chemiluminescence in the luminol–H_2O_2 system was investigated upon the addition of nanodisperse cerium dioxide (Fig. 2).

For non-stabilized colloidal solution of cerium dioxide nanoparticles, as well as for the colloidal solution of CeO_2 nanoparticles stabilized with ammonium citrate, the highest CL response in the system was observed at pH 8.5. According to the existing data, a decrease in pH enhances the oxidative properties of Ce^{4+} ions [22]. A pronounced peroxidase-like activity of CeO_2 nanoparticles was reported at pH 4.0 [22]. In our study, neither the addition of CeO_2 nanoparticles nor the addition of Fe^{2+} ions to the system (hemoglobin solution, data not shown) caused any changes at this pH value. The mechanism of chemiluminescence during luminol oxidation in an aqueous solution has been extensively studied [23–25]. Hydroxyl and superoxide anion radicals are important intermediate products contributing to luminescence [23,24]. Since both $\cdot O_2^-$ and the luminol hydroperoxide anion participating in the luminol chain of transformations are stable in an alkaline medium only, the quantum yield of luminol-dependent CL increases dramatically with increasing pH [26]. In neutral and acidic media, the contribution of side reactions not accompanied by chemiluminescence seems to prevail [27].
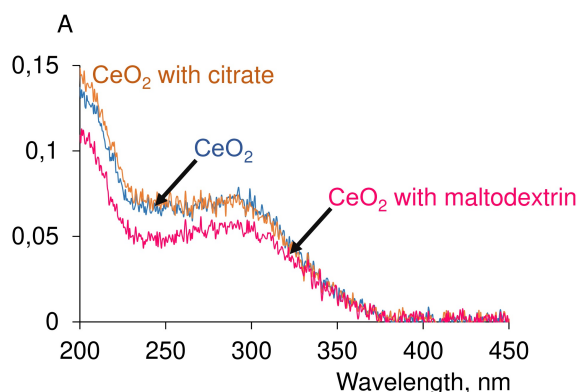
FIG. 1. Absorption spectra of CeO₂ sols (non-stabilized, citrate-stabilized and maltodextrin-stabilized)
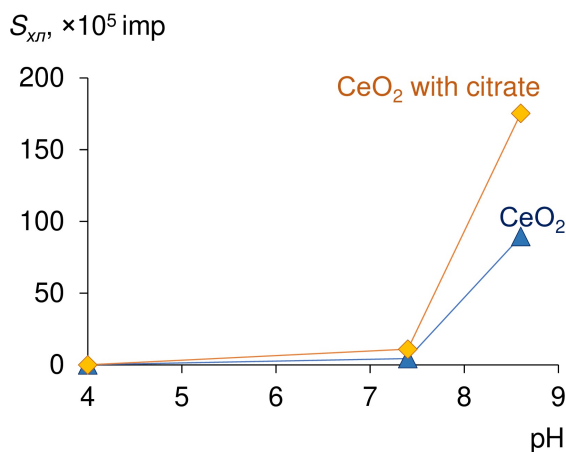
FIG. 2. Dependences of the CL light sum (S_{CL}, $\times 10^5$ imp) on pH (4.0; 7.4; 8.5) upon the addition of CeO₂ sols (both non-stabilized and citrate-stabilized) to the luminol–H₂O₂ system in 100 μM PBS. Conditions: 50 μM luminol, 500 μM H₂O₂, 1.0 μM CeO₂ sol

At pH 8.5 kinetic curves were recorded in the luminol–H₂O₂ system depending on the concentrations of both the citrate-stabilized CeO₂ sol (Fig. 3a) and the H₂O₂ substrate (Fig. 3c).

CL intensity increased with increasing concentration of citrate-stabilized CeO₂ sol added to the system (Fig. 3a) and hydrogen peroxide (Fig. 3c). Thus, CeO₂ nanoparticles in the luminol–H₂O₂ system exhibited prooxidant activity. As an analytical signal, we chose the CL light sum (S_{CL}, the area under the CL curve for 5 min), proportional to the concentration of free radicals formed in the system, which can serve as a measure of the prooxidant capacity of the analyzed sample. Fig. 3b,d show the dependences of the analytical signal on the concentration of citrate-stabilized CeO₂ sol and H₂O₂, respectively. In the absence of a catalyst, the reaction of luminol with H₂O₂ in alkaline medium proceeds relatively slowly and is characterized by weak CL.

Nanodispersed cerium dioxide exhibits multifaceted activity towards hydrogen peroxide [14]. At pH > 6.0, the peroxidase-like properties of nanodisperse CeO₂ are absent, since at high pH values CeO₂ nanoparticles act as catalase [22]. However, stoichiometric CeO₂ nanoparticles obtained by high-temperature treatment can exhibit peroxidase-like properties even at higher pH [28]. For example, at pH 7.2, due to the peroxidase-like activity, they accelerated the interaction of H₂O₂ with luminol and enhanced the luminescence of the latter [28]. Our data demonstrate the prooxidant function of citrate-stabilized CeO₂ sol towards H₂O₂ in the presence of luminol at pH > 6. The addition of CeO₂ nanoparticles leads to the high luminescence intensity with exponential type decay. Comparison of chemiluminograms of nanodispersed cerium dioxide and horseradish peroxidase showed a smooth increase in the luminescence intensity with a subsequent stationary luminescence level, confirming different mechanisms of processes occurring in these systems [29]. Thus, an assumption can be drawn that, in the luminol–H₂O₂ system, ceria nanoparticles act by a nonenzymatic mechanism. To support this assumption, the method of mathematical modeling was used
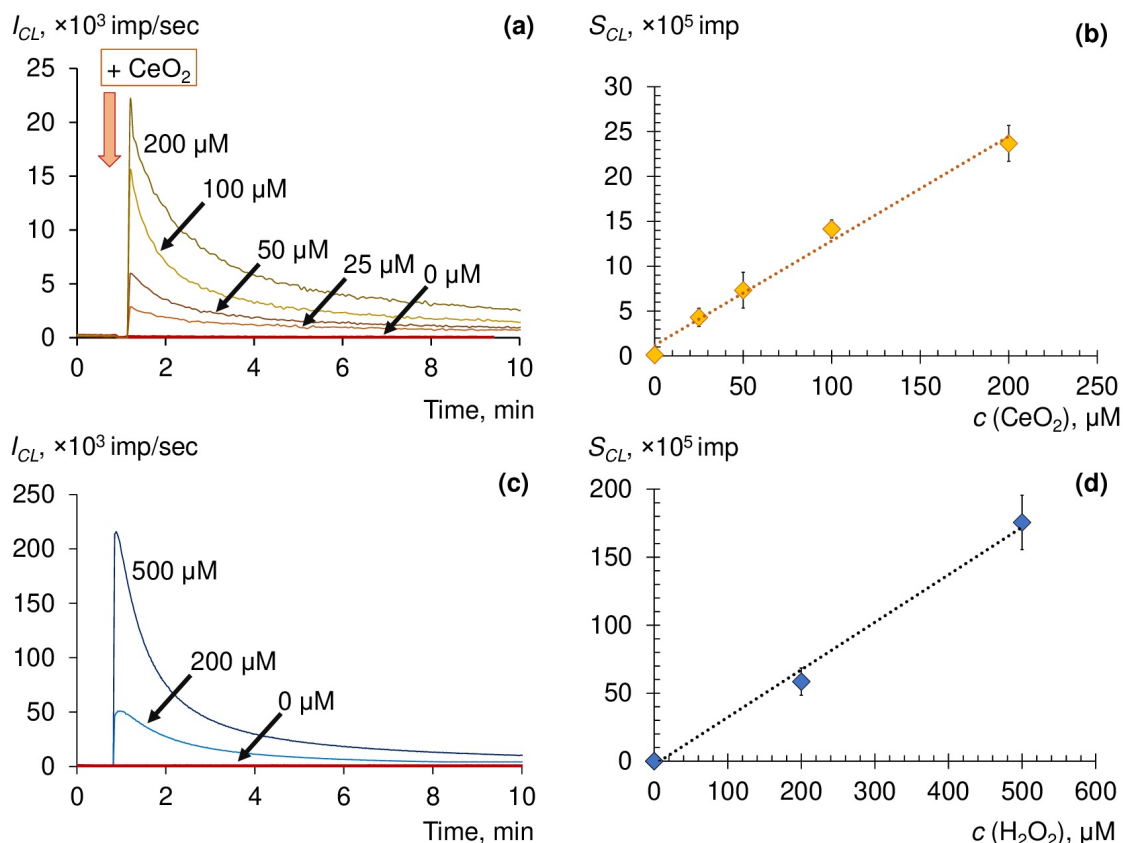
FIG. 3. Chemiluminograms for the luminol–H_2O_2 system in 100 μM PBS (pH 8.5) (a) with the addition of citrate-stabilized CeO_2 sol, (c) containing different concentrations of H_2O_2 with the addition of citrate-stabilized CeO_2 sol. The dependence of the light sum (S_{CL}, $\times$ 10^5 imp) on the concentration of (b) citrate-stabilized CeO_2 sol, (d) H_2O_2. Conditions: (a) 50 μM luminol, 200 μM H_2O_2, citrate-stabilized CeO_2 sol (concentrations are shown in the Figure), (b) 50 μM luminol, H_2O_2 (concentrations are shown in the Figure), 1 μM citrate-stabilized CeO_2 sol

our approach was based on developing a mathematical model of a system of chemical reactions and calculating their rate constants.

Studies of the peroxidase-like activity of nanodisperse cerium dioxide have previously shown that its action is similar to the mechanism of catalysis by other nanoparticles [30–34]. Constants were selected for reactions (1)–(6), which, according to the literature, describe the most probable mechanism of the redox behavior of CeO_2 nanoparticles towards H_2O_2 in the presence of luminol [22, 31, 33]:

$$H_2O_2 + OH^- \rightarrow HO_2^- + H_2O, \quad k_1 = 9.4 \cdot 10^{-14} \ \mu M^{-1}min^{-1}, \tag{1}$$

$$Lum + OH^- \rightarrow Lum^- + H_2O, \quad k_2 = 1.9 \cdot 10^{-15} \mu M^{-1}min^{-1}, \tag{2}$$

$$H_2O_2 + CeNPs \rightarrow 2OH\cdot, \quad k_3 = 7.9 \ \mu M^{-1}min^{-1}, \tag{3}$$

$$OH\cdot + HO_2^- \rightarrow O_2^- + H^+, \quad k_4 = 6.4 \cdot 10^{10} \quad \mu M^{-1}min^{-1}, \tag{4}$$

$$OH\cdot + Lum^- \rightarrow \cdot Lum^-, \quad k_5 = 2.4 \cdot 10^{-8} \quad \mu M^{-1}min^{-1}, \tag{5}$$

$$\cdot O_2^- + \cdot Lum^- \rightarrow 3APA*, \quad k_6 = 6.0 \cdot 10^{-15} \quad \mu M^{-1}min^{-1}, \tag{6}$$

$$3APA* \rightarrow 3APA + h\nu, \quad k_7 = 9.9 \cdot 10^{-1} \quad \mu M^{-1}min^{-1}, \tag{7}$$
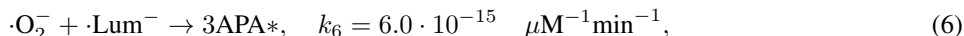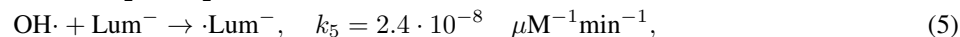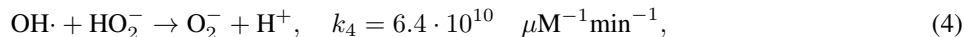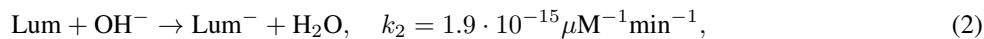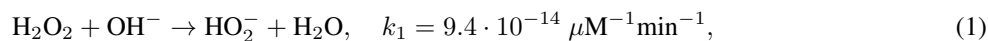
where Lum, Lum^- and $\cdot Lum^-$, 3APA$*$ refer to luminol, luminol anion, luminol radical and 3-aminophthalate anion, respectively.

Kinetic modeling of experimental data is shown in Fig. 4.

Kinetic behavior is similar to the chemiluminescence curves obtained for horseradish peroxidase [29], and significantly differs from the experimental data for CeO_2 sols obtained in the present study. The formation of 3-aminophthalate anions, hydroxyl and superoxide anion radicals plays a key role in the enhancement of CL induced
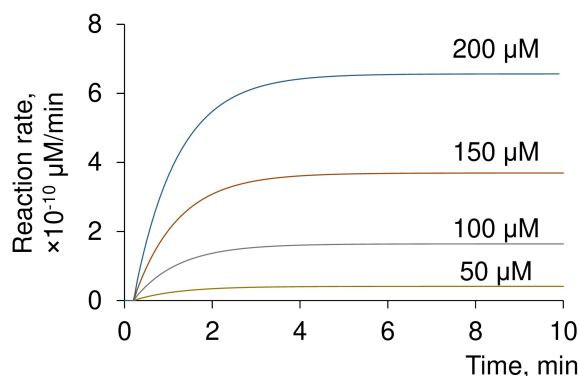
FIG. 4. Kinetic modeling of experimental data in the CL system luminol–H$_2$O$_2$ with CeO$_2$ nanoparticles. Conditions: 50 μM luminol, 200 μM H$_2$O$_2$, CeO$_2$ sol (concentrations are shown in the figure)

by the addition of CeO$_2$ nanoparticles as confirmed by analysis of absorption spectra (425 nm — absorption band of 3-aminophthalate) and inhibitory analysis using SOD (for enzymatic dismutation of SAR) and selective traps for hydroxyl radicals — *tert*-butanol, *n*-butanol, and mannitol [31]. Possible participation of oxygen dissolved in the reaction medium in the interaction with luminol and SAR radicals should be taken into account as demonstrated earlier in the experiments on deaeration with CuO nanoparticles [35]. In the same study, it was found that the enhancement factor of nanoparticles on luminol–H$_2$O$_2$ CL system for CuO is 400 [35], while for CeO$_2$ nanoparticles it is 22.5 [31].

We proposed the following simplified model as a possible mechanism for the prooxidant activity of CeO$_2$ nanoparticles towards H$_2$O$_2$:

$$\text{CeNPs} + \text{H}_2\text{O}_2 \rightarrow 2\text{OH}\cdot, \quad k_1 = 9.0 \cdot 10^4 \ \mu\text{M}^{-1}\text{min}^{-1}, \tag{8}$$

$$\text{Lum} + \text{OH}\cdot \rightarrow \text{Lum}*, \quad k_2 = 2.0 \cdot 10^{-6} \ \mu\text{M}^{-1}\text{min}^{-1}, \tag{9}$$

$$\text{Lum}* + \text{Lum}* \rightarrow \text{P} + \text{h}\nu, \quad k_3 = 2.9 \cdot 10^{-5} \mu\text{M}^{-1}\text{min}^{-1}, \tag{10}$$
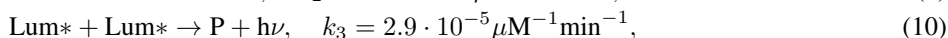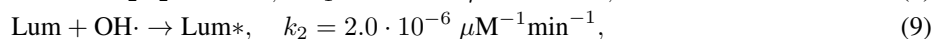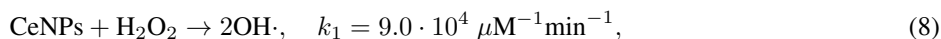
where Lum$*$ is luminol in an excited state, P is the CL reaction product.

For the given initial concentrations of the reactants the reaction rate constants were selected. Comparison of the experimental data for citrate-stabilized CeO$_2$ sol and fitting results is shown in Fig. 5.
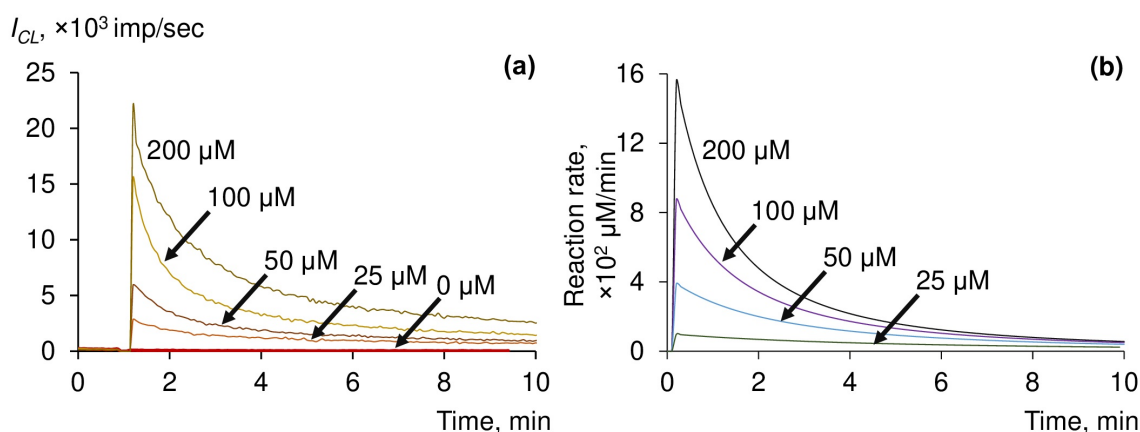

FIG. 5. Chemiluminescence of the luminol–H$_2$O$_2$ system in 100 μM PBS (pH 8.5) upon the addition of the citrate-stabilized CeO$_2$ sol (a), fitting of the experimental data (b). Conditions: 50 μM luminol, 200 μM H$_2$O$_2$, CeO$_2$ sol (concentrations are shown in the figure)

The proposed basic model agrees well with the experimental data. The rate constants of interaction of CeO$_2$ nanoparticles with the reaction substrate can be judged as a measure of their prooxidant activity.

The formation of highly reactive hydroxyl radicals in the presence of CeO$_2$ nanoparticles was confirmed and studied by various methods [36–38]. Some researchers associate the catalytic activity of CeO$_2$ nanoparticles with the formation of peroxide-like intermediates [39, 40]. Despite various assumptions regarding the mechanism of ceria enzyme-like activity, most researchers agree that the pro- and antioxidant properties of nanodispersed CeO$_2$ are

closely related to each other and are determined by several factors. According to the literature, the redox activity of nanodispersed cerium dioxide is influenced by the size and the shape of the particles, pH of the reaction medium, the presence of surface ligands, etc. Thus, in a recent study, a strong structure-sensitive peroxidase-mimetic activity of CeO_2 nanoparticles (nanocubes and nanorods) was revealed [40]. Two types of oxidants were identified in CeO_2/H_2O_2 systems: HO· and peroxidase-like intermediates, the formation of which strongly depends on pH and morphology of CeO_2 nanocrystals. The nature of the peroxidase-like activity of nanocrystalline cerium dioxide is mainly explained by formation of HO radicals under acidic conditions, while peroxide-like intermediates play an important role along with HO at neutral and basic pH values. In comparison with CeO_2 nanocubes, nanorods demonstrated higher peroxidase activity, due to the higher Ce^{3+} concentration and the concentration of oxygen vacancies [40].

Another factor influencing the redox activity of CeO_2 nanoparticles is surface functionalization. The prospects for biomedical applications of nanodispersed cerium dioxide necessitate the use of biocompatible ligands.

The effect of the stabilizer on the prooxidant potential of CeO_2 nanoparticles towards hydrogen peroxide in the presence of luminol was further analyzed. Kinetic curves and dependences of the analytical signal on the concentration were obtained for both non-stabilized CeO_2 nanoparticles and nanoparticles stabilized with ammonium citrate or maltodextrin (Fig. 6a,b).
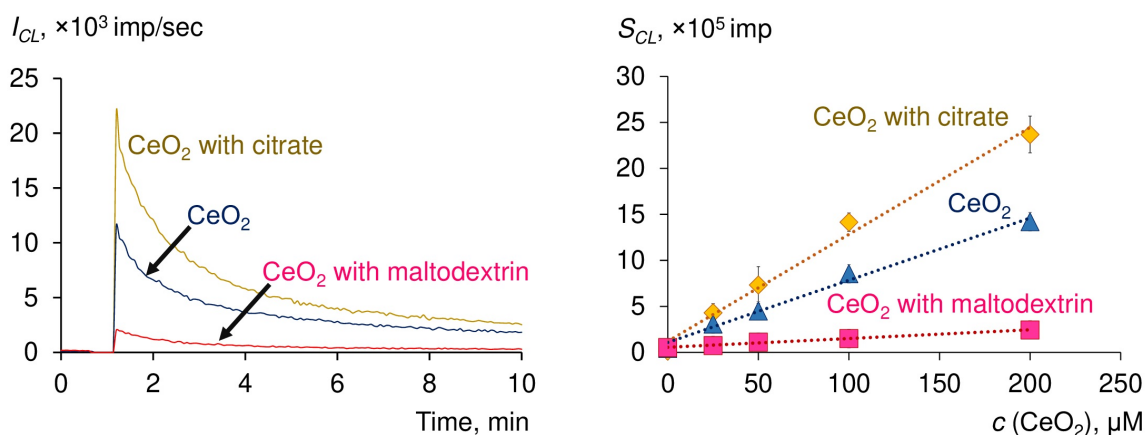
FIG. 6. Chemiluminescence of the luminol–H_2O_2 system in 100 μM PBS (pH 8.5) upon the addition of 200 μM non-stabilized colloidal solution of CeO_2 nanoparticles, citrate-stabilized CeO_2 sol or CeO_2 sol stabilized with maltodextrin in 100 μM PBS (pH 8.6) (a), the dependence of the light sum (S_{CL}, $\times 10^5$ imp) on the concentration of CeO_2 sols (b). Conditions: 50 μM luminol, 200 μM H_2O_2, CeO_2 sols (concentrations are shown in the figure)

It can be seen that citrate-stabilized CeO_2 sol has the most pronounced prooxidant activity in comparison with the non-stabilized sol and maltodextrin-stabilized sol. Taking the prooxidant capacity of non-stabilized CeO_2 sol (200 μM) as 1, it follows that functionalization of the surface with ammonium citrate increases prooxidant capacity by two-fold, while maltodextrin decreases it by 6-fold. These results are consistent with previously published data on the protective effect of maltodextrin-stabilized CeO_2 nanoparticles against H_2O_2 [41]. Maltodextrin is considered the most promising non-toxic non-ionic stabilizer. The use of such stabilizers in the synthesis of therapeutic nanoparticles makes it possible to purposefully regulate their size and, accordingly, the ratio of pro- and antioxidant properties. Importantly, the polymer stabilizer does not prevent cerium dioxide particles from participating in redox processes and performing enzymatic functions.

Finally, the prooxidant capacity of the citrate-stabilized CeO_2 sol was estimated in the presence of phosphate species at pH 7.4, under physiologically relevant conditions. It is known that phosphate ions inhibit the biochemical activity of cerium dioxide by being adsorbed on the surface of nanoparticles [42, 43]. Chemiluminograms, as well as the dependence of the number of formed radicals on the concentration of CeO_2 citrate sol in Tris-HCl medium and phosphate buffer solutions are shown in Fig. 7a,b.

It was found that the prooxidant capacity of the citrate-stabilized CeO_2 sol in Tris-HCl buffer exceeds that for the case of a phosphate buffer by four-fold, which agrees well with the literature data on a decrease in the biochemical activity of nanodispersed cerium dioxide in the presence of phosphates [42, 43].

FIG. 7. Chemiluminograms for the luminol–H$_2$O$_2$ system in 100 μM Tris-HCl and PBS (pH 7.4) (are shown in the figure) upon the addition of the citrate-stabilized CeO$_2$ sol (a), the dependence of the light sum (S$_{CL}$, $\times 10^5$ imp) on the citrate-stabilized CeO$_2$ sol (b). Conditions: 50 μM luminol, 200 μM H$_2$O$_2$, 200 μM the citrate-stabilized CeO$_2$ sol

5. Conclusion

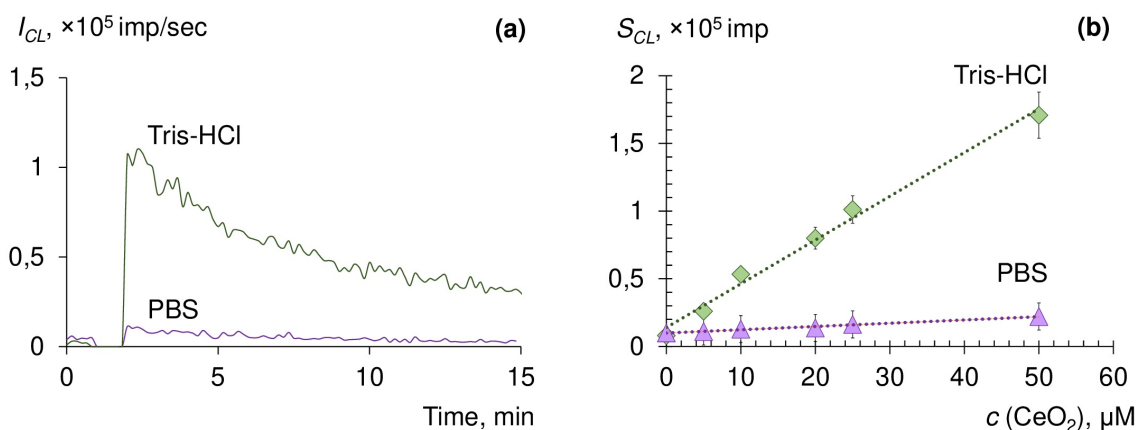A certain level of free radicals is constantly maintained in the body, which is necessary for normal life. Violations of the free radical balance inevitably lead to the development of diseases and pathological conditions. Special attention is currently paid to the search for drugs capable of regulating redox homeostasis. In this respect, CeO$_2$ nanoparticles are of particular interest, due to their multifaceted nanozyme activities, which makes it necessary to analyze the redox behavior of nanodispersed cerium dioxide with respect to key molecules involved in free radical reactions in the body.

In this work, to analyze the redox activity of CeO$_2$ nanoparticles, we used an approach that makes it possible to comprehensively assess their prooxidant potential towards hydrogen peroxide. Determination of the prooxidant capacity and prooxidant activity allows one not only to obtain quantitative characteristics for a comparative analysis of the enzyme-like activity of CeO$_2$ nanoparticles, but would allow further clarification of the mechanisms underlying this activity.

Acknowledgements

References

[1] Korsvik C., Patil S., et al. Superoxide dismutase mimetic properties exhibited by vacancy engineered ceria nanoparticles. *Chem. Commun. (Camb.)*, 2007, **10**, P. 1056–1058.

[2] Asati A., Santra S., et al. Oxidase-like activity of polymer-coated cerium oxide nanoparticles. *Angew. Chem. Int. Ed. Engl.*, 2009, **48**(13), P. 2308–2312.

[3] Pirmohamed T., Dowding J.M., et al. Nanoceria exhibit redox state-dependent catalase mimetic activity. *Chem. Commun. (Camb.)*, 2010, **46**(16), P. 2736–2738.

[4] Tian Z., Yao T., et al. Photolyase-Like Catalytic Behavior of CeO$_2$. *Nano Lett.*, 2019, **19**(11), P. 8270–8277.

[5] Xu F., Lu Q., et al. Nanoceria as a DNase I mimicking nanozyme. *Chem. Commun. (Camb.)*, 2019, **55**(88), P. 13215–13218.

[6] Yao T., Tian Z., et al. Phosphatase-like Activity of Porous Nanorods of CeO$_2$ for the Highly Stabilized Dephosphorylation under Interferences. *ACS Appl. Mater. Interfaces*, 2019, **11**(1), P. 195–201.

[7] Krysanov E.Y., Demidova T.B., et al. Synergetic action of ceria nanoparticles and doxorubicin on the early development of two fish species, *Danio rerio* and *Puntius tetrazona*. *Nanosystems: Phys. Chem. Math.*, 2019, **10**(3), P. 289–302.

[8] Thakur N., Prasenjit M., Das J. Synthesis and biomedical applications of nanoceria, a redox active nanoparticle. *J. Nanobiotechnol.*, 2019, **17**(1), P. 1–27.

[9] Hosseini M., Mozafari M. Cerium Oxide Nanoparticles: Recent Advances in Tissue Engineering. *Materials (Basel)*, 2020, **13**(14).

[10] Nyoka M., Choonara Y.E., et al. Synthesis of Cerium Oxide Nanoparticles Using Various Methods: Implications for Biomedical Applications. *Nanomaterials (Basel)*, 2020. **10**(2).

[11] Popova N.R., Andreeva V.V., et al. Fabrication of CeO$_2$ nanoparticles embedded in polysaccharide hydrogel and their application in skin wound healing. *Nanosystems: Phys. Chem. Math.*, 2020, **11**(1), P. 99–109.

[12] Rojkind M., Dominguez-Rosales J.A., et al. Role of hydrogen peroxide and oxidative stress in healing responses. *Cell. Mol. Life Sci.*, 2002, **59**(11), P. 1872–1891.

[13] Sozarukova M.M., Shestakova M.A., et al. Quantification of free radical scavenging properties and SOD-like activity of cerium dioxide nanoparticles in biochemical models. *Russ. J. Inorg.*, 2020, **65**, P. 597–605.

[14] Sozarukova M.M., Proskurnina E.V., et al. CeO$_2$ nanoparticles as free radical regulators in biological systems. *Nanosystems: Phys. Chem. Math.*, 2020, **11**(3), P. 324–332.

[15] Stone J.R., Yang S. Hydrogen peroxide: a signaling messenger. *Antioxid. Redox. Signal.*, 2006, **8**(3–4), P. 243–270.

[16] Sies H. Hydrogen peroxide as a central redox signaling molecule in physiological oxidative stress: Oxidative eustress. *Redox. Biol.*, 2017, **11**, P. 613–619.

[17] Geiszt M. Leto T.L. The Nox family of NAD(P)H oxidases: host defense and beyond. *J. Biol. Chem.*, 2004, **279**(50), P. 51715–51718.

[18] Li J., Stouffs M., et al. The NADPH oxidase NOX4 drives cardiac differentiation: Role in regulating cardiac transcription factors and MAP kinase activation. *Mol. Biol. Cell*, 2006, **17**(9), P. 3978–3988.

[19] Ushio-Fukai M. Localizing NADPH oxidase-derived ROS. *Sci. STKE*, 2006, **2006**(349), re8.

[20] Cai H. Hydrogen peroxide regulation of endothelial function: origins, mechanisms, and consequences. *Cardiovasc. Res.*, 2005, **68**(1), P. 26–36.

[21] Shcherbakov A.B., Teplonogova M.A., et al. Facile method for fabrication of surfactant-free concentrated CeO$_2$ sols. *Mater. Res. Express*, 2017, **4**(5), P. 055008.

[22] Jiao X., Song H., et al. Well-redispersed ceria nanoparticles: promising peroxidase mimetics for H$_2$O$_2$ and glucose detection. *Anal. Methods*, 2012, **4**(10), P. 3261–3267.

[23] White E.H., Zafiriou O., et al. Chemilunimescence of luminol: The chemcial reaction. *J. Am. Chem. Soc.*, 1964, **86**(5), P. 940–941.

[24] Merényi G., Lind J., Eriksen T.E. Luminol chemiluminescence: chemistry, excitation, emitter. *J. Biolumin. Chemilumin.*, 1990, **5**(1), P. 53–56.

[25] Khan P., Idrees D., et al. Luminol-based chemiluminescent signals: clinical and non-clinical application and future uses. *Appl. Biochem. Biotechnol.*, 2014, **173**(2), P. 333–355.

[26] Krasowska A., Rosiak D., et al. The antioxidant activity of BHT and new phenolic compounds PYA and PPA measured by chemiluminescence. *Cell. Mol. Biol. Lett.*, 2001, **6**(1), P. 71–82.

[27] Vladimirov Y.A., Proskurnina E.V. Free radicals and cell chemiluminescence. *Biochem. (Mosc.)*, 2009, **74**(13), P. 1545–1566.

[28] Li X., Zhang Z., et al. A chemiluminescence microarray based on catalysis by CeO$_2$ nanoparticles and its application to determine the rate of removal of hydrogen peroxide by human erythrocytes. *Appl. Biochem. Biotechnol.*, 2013, **171**(1), P. 63–71.

[29] Izmailov D.Y., Proskurnina E.V., et al. The effect of antioxidants on the formation of free radicals and primary products of the peroxidase reaction. *Biophysics*, 2017, **62**(4), P. 557–564.

[30] Zhang Z.F., Cui H., et al. Gold nanoparticle-catalyzed luminol chemiluminescence and its analytical applications. *Anal. Chem.*, 2005, **77**(10), P. 3324–3329.

[31] Li X., Sun Li, et al. Enhanced chemiluminescence detection of thrombin based on cerium oxide nanoparticles. *Chem. Commun.*, 2011, **47**(3), P. 947–949.

[32] Xu S., Chen F., et al. Luminol chemiluminescence enhanced by copper nanoclusters and its analytical application. *RSC Adv.*, 2014, **4**(30), P. 15664–15670.

[33] Wang R., Yue N., Fan A. Nanomaterial-enhanced chemiluminescence reactions and their applications. *Analyst*, 2020, **145**(23), P. 7488–7510.

[34] Guo J.-Z., Cui H., et al. Ag nanoparticle-catalyzed chemiluminescent reaction between luminol and hydrogen peroxide. *J. Photochem. Photobiol.*, 2008, **193**(2–3), P. 89–96.

[35] Chen W., Hong L., et al. Enhanced chemiluminescence of the luminol-hydrogen peroxide system by colloidal cupric oxide nanoparticles as peroxidase mimic. *Talanta*, 2012, **99**, P. 643–648.

[36] Lousada C.M., Yang M., et al. Catalytic decomposition of hydrogen peroxide on transition metal and lanthanide oxides. *J Mol. Catal. A-Chem.*, 2013, **379**, P. 178–184.

[37] Liu Q., Ding Y., et al. Enhanced peroxidase-like activity of porphyrin functionalized ceria nanorods for sensitive and selective colorimetric detection of glucose. *Mater. Sci. Eng. C*, 2016, **59**, P. 445–453.

[38] Alizadeh N., Salimi A., et al. Intrinsic Enzyme-like Activities of Cerium Oxide Nanocomposite and Its Application for Extracellular H$_2$O$_2$ Detection Using an Electrochemical Microfluidic Device. *ACS Omega*, 2020, **5**(21), P. 11883–11894.

[39] Grulke E., Reed K., et al. Nanoceria: factors affecting its pro-and anti-oxidant properties. *Environ. Sci. Nano*, 2014, **1**(5), P. 429–444.

[40] Wei X., Li X., et al. Morphology-and pH-dependent peroxidase mimetic activity of nanoceria. *RSC Adv.*, 2018, **8**(21), P. 11764–11770.

[41] Shcherbakov A.B., Zholobak N.M., et al. Synthesis and antioxidant activity of biocompatible maltodextrin-stabilized aqueous sols of nanocrystalline ceria. *Russ. J. Inorg.*, 2012, **57**(11), P. 1411–1418.

[42] Singh S., Dosani T., et al. A phosphate-dependent shift in redox stateof cerium oxide nanoparticles and its effects on catalytic properties. *Biomaterials*, 2011, **32**(28), P. 6745–6753.

[43] Singh R., Singh S. Role of phosphate on stability and catalase mimetic activity of cerium oxide nanoparticles. *Colloids Surf. B: Biointerfaces*, 2015, **132**, P. 78–84.

Fabrication of room temperature operated ultra high sensitive gas sensor based on mesoporous Ni doped WO$_3$ nanoparticles

M. S. Duraisami[1], D. Benny Anburaj[2], K. Parasuraman[1*]

[1]PG & Research Department of Physics, Poompuhar College (Autonomous) (Affiliated to Bharathidasan University, Tiruchirappalli), Melaiyur – 609107, Tamil Nadu, India

[2]PG & Research Department of Physics, D. G. Govt. Arts College (Affiliated to Bharathidasan University, Tiruchirappalli), Mayiladuthurai, Tamil Nadu, India

tharmamithran@gmail.com, bennyanburaj@rediffmail.com, *resphy21@gmail.com

Ultra high sensitive room temperature gas sensor based on Ni-doped WO$_3$ nanoparticles(hereafter NPs) has been reported here. The synthesis of pure and Ni-doped WO$_3$ NPs was done by facile precipitation route. XRD studies revealed the polycrystalline monoclinic structure of the prepared samples with the preferential growth orientation along (002) crystal plane. Analysis via SEM and FE–SEM was conducted, and the micrographs showed that the synthesized samples were found to have highly porous structure with excellent dispersibility. The successful incorporation of Ni^{2+} ions in to WO$_3$ lattice has been confirmed by XPS analysis. The highly improved room temperature gas sensing characteristics of WO$_3$ by Ni doping is also studied using a high sensitive electrometer. Compared to undoped WO$_3$, 3 mol. % Ni-doped WO$_3$ sensor showed nearly 20-fold greater sensitivity (2641 – 200 ppm ammonia, room temperature) with rapid response/recovery times of 40/97 s.

Keywords: Ni doped WO$_3$, gas sensor, precipitation, mesoporous, room temperature.

Received: 18 February 2021

Revised: 25 March 2021

1. Introduction

Over the past few decades, the rapid increase of air pollution due to harmful gases released from various industrial processes has become a labyrinthine concern, which poses a threat to our environment and serious health issues to human. Toxic gases are among the vital air pollutants and their short and long term exposure may cause deleterious health effects in human such as respiratory tract ailments, memory problems, fatigue, asthma and even lung cancer [1]. From a well-being perspective, the detection of toxic gases at their early stage is an urgent demand. Therefore, toxic gas detection has become a burning topic to monitor such lethal chemical compounds and set a norm for toxic emissions. It is worth mentioning that the metal oxide semiconductors (MOSs) serve as one of the potential candidates for detecting toxic gases owing to their distinctive sensing behaviors with lower operating temperatures, availability, cost-effectiveness and compatibility with micro-electronic processes [2].

WO$_3$ is one such important MOS, which attracts greater attention due to its unique structural, morphological, and optical properties, which have made it a suitable substance for many real time applications like gas sensors [3], catalysts [4] and energy storage systems [5]. Besides, transition–metal oxides like ZnO, WO$_3$ or TiO$_2$ with d^0 and d^{10} electronic configurations exhibit impressive physicochemical properties and stability which are beneficial for gas sensing applications [6]. The techniques employed for the synthesis of WO$_3$ nanostructures are also manifold. We have already reported in our previous work [7] that the precipitation method is a flexible technique for preparing monoclinic WO$_3$ NPs with optimal thermal treatment (823 K). Since pure WO$_3$ contributes to a limited extent; it is necessary to improve the sensing properties through various strategies. It is believed that doping of WO$_3$ with certain appropriate metal ions is one of the greatest possibilities to enhance the functional properties and sensing behavior of the base material.

WO$_3$ can also be effectively deployed as a nanocomposite along with other noble and transition metals. Liu et al. [8] have investigated the ethanol and methanol sensing properties of intrinsic and Pt-doped WO$_3$ nanorods at 220 °C. Qi et al. [9] have fabricated a NO$_2$ sensor based on Sb-doped WO$_3$ nanocomposites at low temperature. Chen et al. [10] have reported Ag decorated WO$_3$ nanopowder for NO gas detection at 250 °C. Li et al. [11] have prepared the Cr incorporated WO$_3$ nanofibers for xylene sensing. Pristine and Au-doped WO$_3$ nanostructures were employed as gas sensing material for enhanced H$_2$ sensing [12].

In this context, the present work is targeted to prepare nickel-doped WO$_3$ NPs through a well-engineered precipitation technique and investigate their gas sensing characteristics at room temperature. Nickel is considered as a suitable dopant material for WO$_3$ as its ionic radius (0.60 Å) is nearly equal to that of W (0.62 Å), which would also effectively

modify the structural and morphological properties of the base material (WO_3) [13]. As far as we know, only a very few reports are available for room temperature gas sensing properties of Ni-incorporated WO_3 NPs via precipitation method. The room temperature gas sensing behavior of the fabricated sensor was investigated systematically in terms of selectivity, transient response, repeatability and stability measurements.

2. Materials and methods

2.1. Synthesis of pristine WO_3 NPs

Pure WO_3 NPs were prepared according to our previous work [7], as well as the detailed preparation process has been explained as follows. In a facile precipitation technique, sodium tungstate dihydrate ($Na_2WO_4 \cdot 2H_2O$) and calcium chloride dihydrate ($CaCl_2 \cdot 2H_2O$) were used as a precursor. Initially, $Na_2WO_4 \cdot 2H_2O$ and $CaCl_2 \cdot 2H_2O$ were dissolved separately in 100 ml of de-ionized water (DI) to obtain 1.2 and 2 mM respectively. Later these two solutions were transferred to a beaker and stirred vigorously ($\sim$ 900 rpm) for 45 minutes using a magnetic stirrer at room temperature. Then the settled white precipitate ($CaWO_4$) was collected and washed several times with ethanol, acetone and DI. Subsequently the precipitate has been placed in hot air oven and dried at 333 K for 16 hours, followed by a soaking process in 50 ml of conc. nitric acid (HNO_3, Emplura, India) for 48 hours. At the end of soaking process, the colour of the precipitate was changed from white to rich yellow, which indicates the formation of tungstite ($WO_3 \cdot H_2O$) compound. Then the filtered precipitate was cleansed several times with ethanol, acetone and DI, and followed by a thermal calcination at 823 K for 2 hours, resulting in WO_3 NPs.

2.2. Synthesis of Ni-doped WO_3 NPs

The experimental procedure for the synthesis of Ni-doped WO_3 NPs is as follows: For the preparation of 1 mol. % of Ni-doped WO_3 samples, 100 ml of 0.01 M aqueous $NiCl_2 \cdot 6H_2O$ solution was added to 100 ml of 0.99 M precipitation precursor ($CaWO_4$) solution. These solutions were mixed under constant magnetic stirring for 45 minutes at room temperature. Then the precipitate was filtered, washed, dried and soaked in HNO_3 as described in Section 2.1. Finally, the substance was calcined at 823 K for 2 hours to obtain Ni-doped WO_3 samples. A similar procedure was followed to prepare 3 and 5 mol. % of Ni-doped WO_3 NPs. The WO_3 NPs synthesized using 0, 1, 3, and 5 mol. % of Ni dopants were named as WN0, WN1, WN3 and WN5 respectively.

2.3. Characterization techniques

XRD analysis (PANalytical X'pert–pro Diffractometer equipped with CuK_α radiation) was employed to determine the crystal structure of the prepared samples. The surface morphology behavior of the synthesized NPs was analyzed using SEM (ZEISS–SEM) and FE–SEM (FE–SEM, FEI Quanta 250 FEG–SEM) images. EDAX (Bruker) analysis was employed to reveal the elemental composition of the prepared samples. The surface chemistry of the prepared NPs has been investigated with the help of XPS (XPS-Thermo Fisher Scientific Inc., K Alpha, USA) spectra. The presence of functional groups in the NPs were determined using FTIR (Perkin–Elmer Spectrum Two, USA) spectra. The conventional BET and BJH methods (Nova 3200, Quantachrom Instrument Corporation, USA) were employed to measure the specific surface area and pore volume of the prepared samples respectively. The NPs were degassed at 150 °C for 3 h prior to the BET investigation. To disclose the defect states in the samples, PL spectra were recorded (room temperature, $\lambda_{ex} = 325$ nm) using fluorescence spectrophotometer (Varian Cary Eclipse, USA).

2.4. Gas sensing setupand measurements

The systematic evaluation of sensing performance of the prepared NPs was done using a customized gas sensing setup as described in our previous work [7]. In order to construct a sensing material the synthesized NPs were mixed with certain amount of isopropyl alcohol; subsequently dispersed on a glass substrate. In which a pair of copper electrodes were used to supply a DC potential of 10 V and the whole sensing process was achieved in an evaporation chamber of 1 Litre. Sensing measurements were taken using a computer controlled high resistance electrometer (Keithley 6517B, USA) towards various target gases at room temperature. The following relation is used to measure the sensitivity in terms of variation in sensor resistances.

$$S = \frac{R_a}{R_g} \quad (R_a \gg R_g). \tag{1}$$

Since R_a and R_g are the resistances of the fabricated sensor in air and gas respectively.

3. Results and discussion

3.1. Structural, morphological and elemental studies

X-ray diffraction (XRD) patterns of the pure and nickel-doped WO_3 NPs calcined at 823 K were displayed in Fig. 1(a). All the characteristic XRD peaks could be indexed according to the monoclinic (space group $P2_{1/n}(14)$) crystal structure and are agreed with the standard JCPDS card no. 043-1035. Three major diffraction peaks for pure WO_3 were obtained from (002), (020) and (200) crystal planes which correspond to the angles 2θ of 23.02, 23.61 and 24.25° with lattice parameters; $a = 7.297$, $b = 7.539$, $c = 7.688$ Å, and $\beta = 90.91°$. For Ni-doped samples, these high intense peaks were slightly shifted towards higher angles as shown in Fig. 1(b). This can be associated to the smaller size of dopant ion (0.60 Å for Ni^{2+}) as compared to the host W^{6+} ion (0.62 Å) [13]. It is also observed that, all the samples exhibited the preferential growth orientation along (002) plane. The average crystallite size of all the prepared NPs can be estimated by Debye–Scherrer relation as shown in Eq. (2) and the values are given in Table 1.
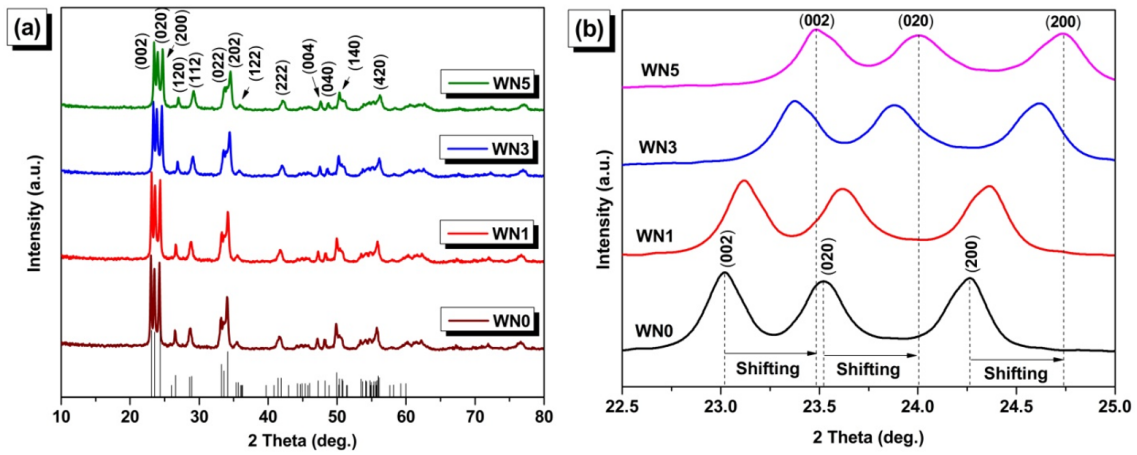
FIG. 1. (a) XRD patterns of the pure and Ni doped WO_3 NPs and (b) Magnified spectra of (002), (020) and (200) peaks

TABLE 1. Results obtained from XRD studies

Sample	2θ	FWHM (deg.)	Crystallite size (nm)
WN0	23.0230	0.2234	36.3
WN1	23.1231	0.2302	35.2
WN3	23.3731	0.2596	31.2
WN5	23.4731	0.2753	29.5

Average crystallite size

$$D = \frac{K \cdot \lambda}{\beta \cos \theta}, \tag{2}$$

where K is the Scherrer constant, λ is the wavelength (1.5406 Å), β is the full width at half–maximum and θ is the Bragg angle.

The average crystallite size was observed to be decrease with the increase of Ni dopants. This trend may be due to the effect of Ni doping, which leads to lattice distortion and associated crystal imperfections. Surprisingly, the XRD patterns of the Ni-doped WO_3 NPs exhibit no apparent peaks related to nickel oxides like NiO, NiO_2 and Ni_2O_3, or any WO_3/Ni ternary oxides were found, which confirms that there is no additional phase formation in the prepared samples and also indicated that Ni doping was within in the solubility limit.These results confirm the formation of nickel-doped WO_3 nanocrystallites without changing the monoclinic structure.

Figure 2 (a–d) illustrates the SEM images of the pristine and Ni-doped WO_3 samples. A significant morphological change influenced by Ni doping was observed. The presence of Ni ions can increase crystal defects in the host material and thus induce notable changes in morphology. A decreasing trend has been observed in grain size, which may be
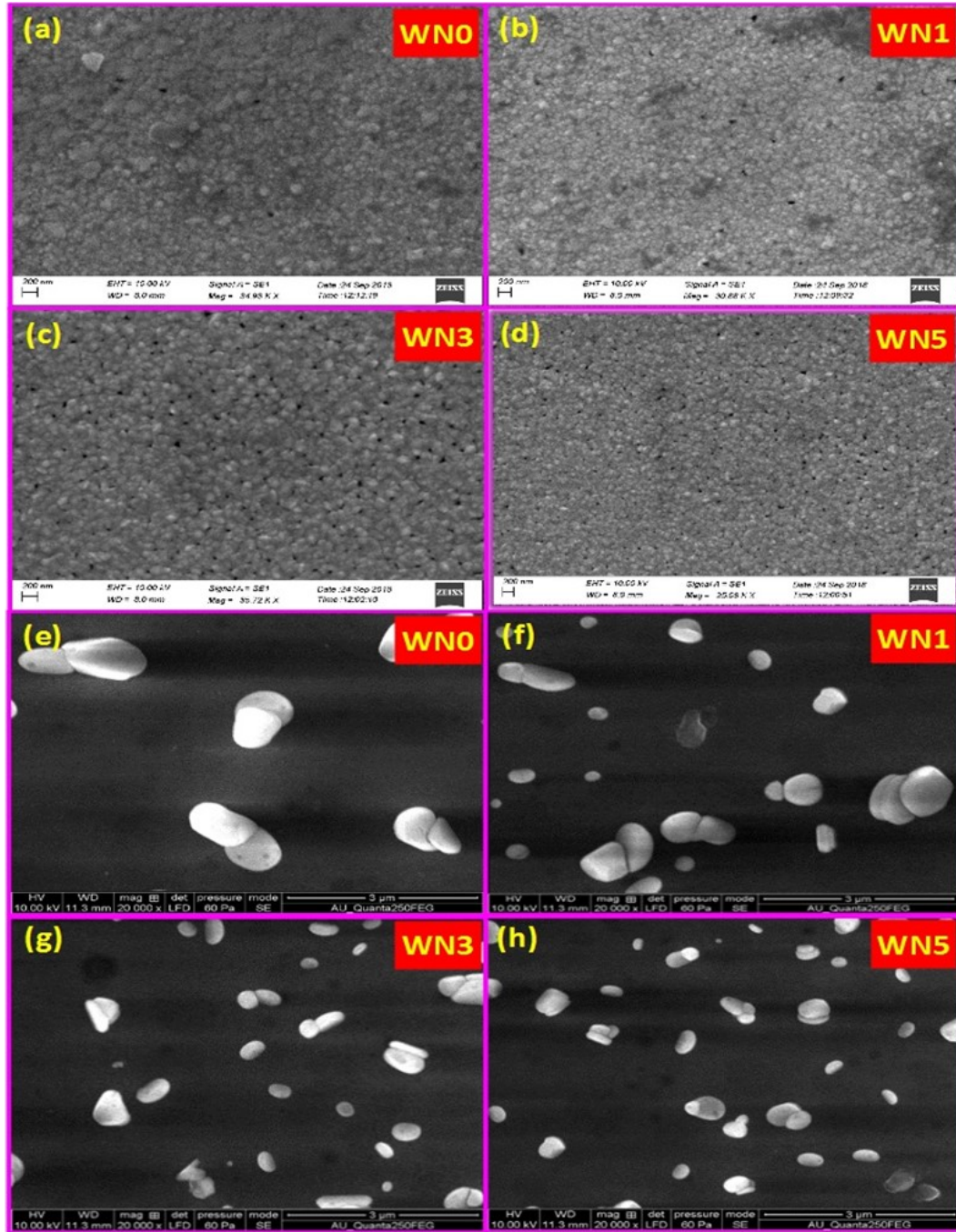
FIG. 2. (a – d) SEM images and (e – h) FE–SEM micrographs of the pristine and Ni doped WO₃ samples

ascribed to the grain growth inhibition nature of nickel ions [14]. A uniformly aligned nanogranular morphology with highly distributed pores were found in Ni-doped samples. In order to gain more insight into the surface morphology of the prepared NPs, FE–SEM analysis was conducted and the micrographs were displayed in Fig. 2(e–h). The obtained FE–SEM images clearly disclosed that the grains were distributed randomly with quasi-spherical shape and their dimension is further diminished upon Ni doping. We may also infer that the prepared samples have more open space with loosely packed structure. These observations are fairly consistent with the XRD studies.

The elemental composition of the prepared samples was identified through EDAX spectra as shown in Fig. 3. Fig. 3(a) reveals the presence of W and O atoms in the WN0 sample and also confirmed the formation of WO₃ NPs without any impurities. Fig. 3(b) depicts the EDAX spectrum of WN3 sample, which ascertains the co–existence of

Ni and W elements in the sample. In addition, a peak found at ~ 0.85 keV of the WN3 sample is attributed to the emitting energy level (L_α) of nickel atom, confirmed the successful incorporation of Ni species in WO_3 NPs.
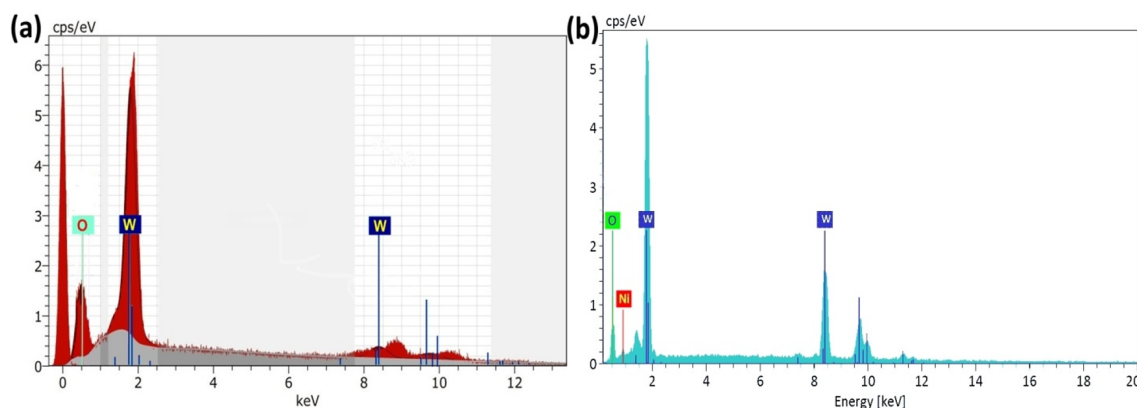
FIG. 3. EDAX spectra of (a) WN0 and (b) WN3 samples

3.2. Functional groups

To examine the vibrational modes on the surface of the NPs, FTIR spectra were recorded in the $400 - 4000$ cm^{-1} range as displayed in Fig. 4. The peak found at 431 cm^{-1} belongs to the W–O group. The stretching vibrational mode of O–W–O group is located at 607 cm^{-1} [15]. The other vibration modes appeared at 1381 and 1613 cm^{-1} are ascribed to W–OH bond and these bands have lower absorption intensities suggesting that a very small hydration of the synthesized samples. The peak found at $3300 - 3600$ cm^{-1} is due to the stretching vibrational mode of O–H groups in H_2O [15]. As a result of Ni doping, these peaks were slightly shifted to greater wave number which probably due to the fact that the change in size of the Ni-doped WO_3 NPs [16]. It is also observed from Fig. 4 that, no signal related to Ni or NiO were found, indicating the high purity of the synthesized NPs. These findings are corroborate well with the results received from XRD.
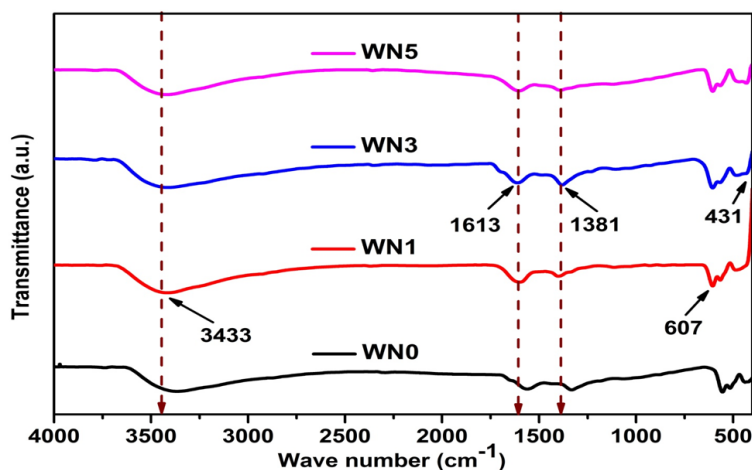
FIG. 4. FTIR spectra of the synthesized samples

3.3. Surface analysis

In order to disclose the chemical composition and metal ionic states in the prepared samples, XPS technique has been employed. Fig. 5 depicts the XPS spectra of WN0 and WN3 NPs. Fig. 5(a) shows the survey scan spectrum of WN0 and WN3 samples. The survey scan spectrum of WN0 confirms the presence of W, O and C elements in the sample. All the peaks of WN3 sample have been observed to be similar as identified for WN0 except the presence of Ni 2p peaks (encircled) [17]. The high resolution core level XPS spectrum of W4f has been shown in Fig. 5(b); as we can see the presence of two peaks related to W4f$_{7/2}$ (at 35.8 eV) and W4f$_{5/2}$ (at 38 eV) has demonstrated that the

existence of W^{6+} chemical state in the sample [18, 19]. Furthermore, the W4f peaks of the WN3 sample (Fig. 5(b)) were shifted toward lower binding energy and this may be due to the effect of electronegativity of Ni ions present in the sample [18, 19]. The doping of Ni ions was also responsible for the distribution of oxygen ions on the surface of WO_3 and the density change of oxygen vacancies in the sample [19, 20], which has a crucial effect on promoting the gas sensing properties.
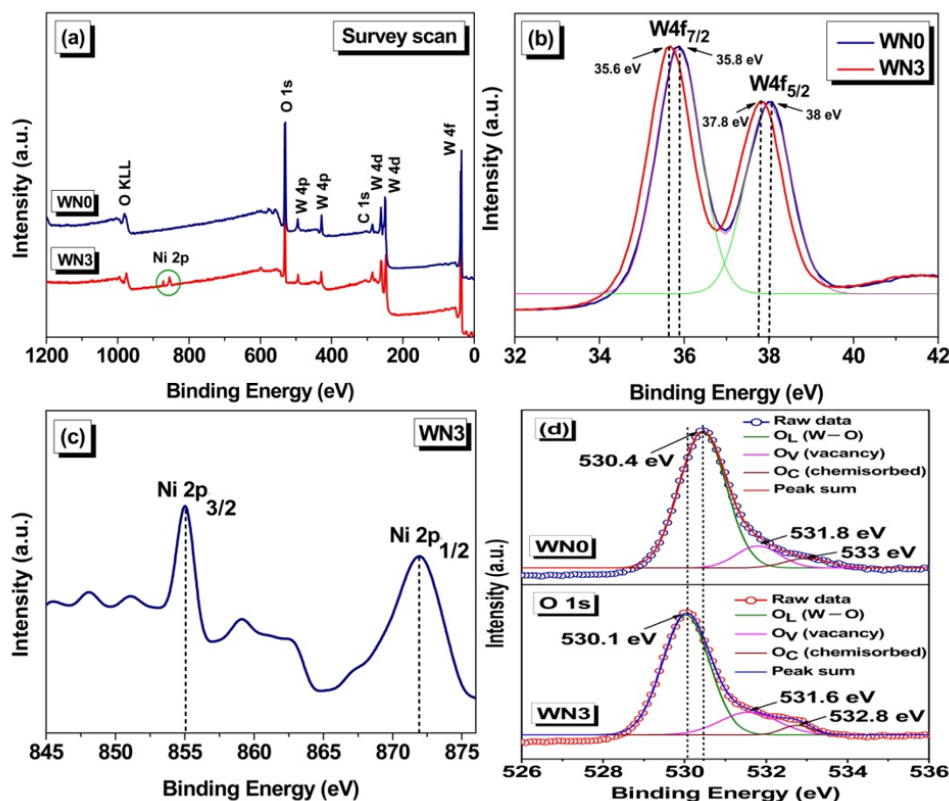
FIG. 5. (a) Survey scan spectrum of WN0 and WN3 samples (b) W4f spectra (c) XPS Ni 2p spectra and (d) O 1s spectra of WN0 and WN3 samples

The core level XPS spectrum of Ni could be fitted in to two characteristic peaks with binding energies at 872 and 855.1 eV, which correspond to Ni $2p_{1/2}$ and Ni $2p_{3/2}$, respectively (Fig. 5(c)). This result clearly demonstrates that Ni ions exist in the form of Ni^{2+} ionic state in the WO_3 sample [13, 19]. The O 1s spectra of WN0 and WN3 samples were displayed in Fig. 5(d) have been fitted with three peaks such as lattice oxygen (O_L peak at 530.4 eV), oxygen vacancy (O_V peak at 531.8 eV) and chemisorbed oxygen species (O_C peak at 533 eV) [21–24]. The O 1s peaks of WN3 NPs were shifted to lower binding energy, indicating the incomplete W–O binding via Ni addition or highly defective nature of the samples [25].

3.4. BET analysis

BET specific surface area (SSA) measurements and corresponding BJH pore size distribution of bare and Ni-doped WO_3 NPs were calculated using adsorption–desorption analysis and are depicted in Fig. 6(a–d). According to the IUPAC classification, it is observed that both pure and Ni-doped WO_3 NPs show a classical IV–type N_2 adsorption isotherm with a H3–type hysteresis loop confirming the formation of mesoporous structure. The determined SSA of 10.946, 14.631, 22.508 and 31.679 m^2/g with an average pore diameter of 33.981, 21.567, 16.687 and 11.28 nm are observed for the samples WN0, WN1, WN3 and WN5 respectively. It is very clear that the doping with Ni ions ultimately increases the SSA of WO_3 as well as make the pore-size distribution on the surface of the sample more uniform. This larger SSA with abundant pores may assist in increasing the active sites and enhance the adsorption of gas molecules which are advantageous for sensing process.
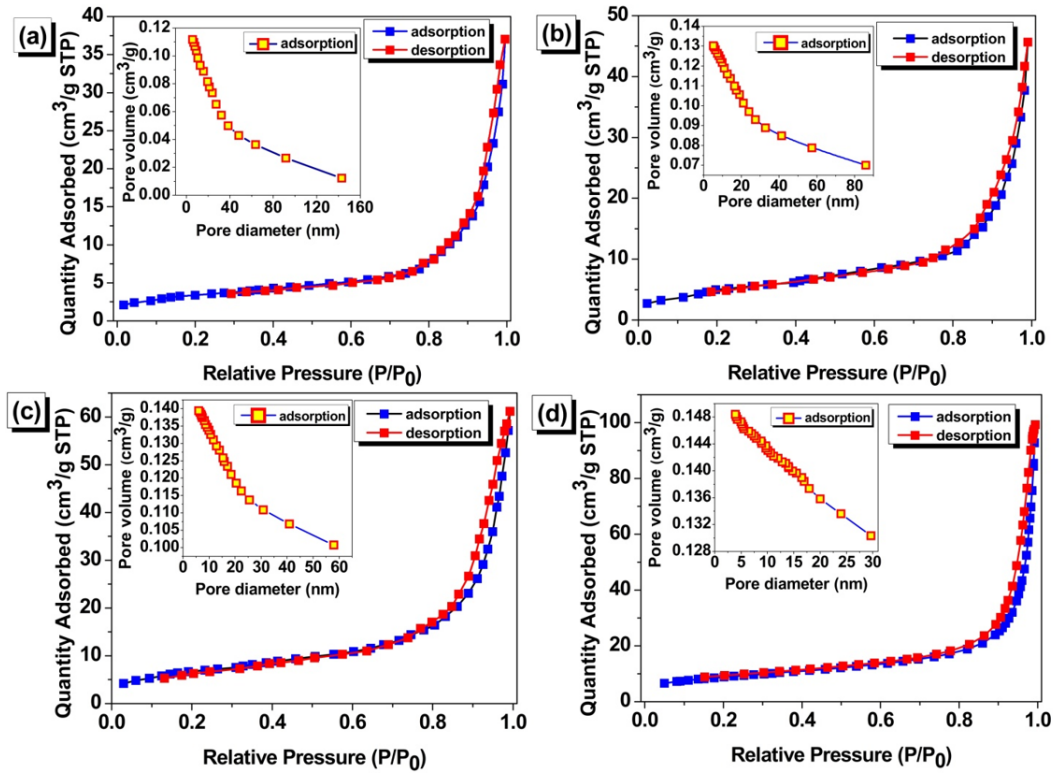
FIG. 6. N_2 adsorption and desorption isotherms of (a) WN0 (b) WN1 (c) WN3 (d) WN5 samples with their corresponding pore-size distribution (inset)

3.5. PL signatures

PL spectra were further employed to investigate the surface processes including photo-generated electron hole pairs. PL spectra of the synthesized NPs were displayed in Fig. 7. The recombination between the electron occupying the resonant defect state in conduction band and a hole in the valence band is related to the peak cited at 378 nm (NUV emission). The peak located at 411 nm may be due to the recombination of free excitons and is generally known as near band edge (NBE) emission. The rapid electron hole pair separation is associated with the peak found at 445 nm. The blue emission at 490 nm is attributed to oxygen vacancies accompanied with defect level in the band gap for its electron transition [26].
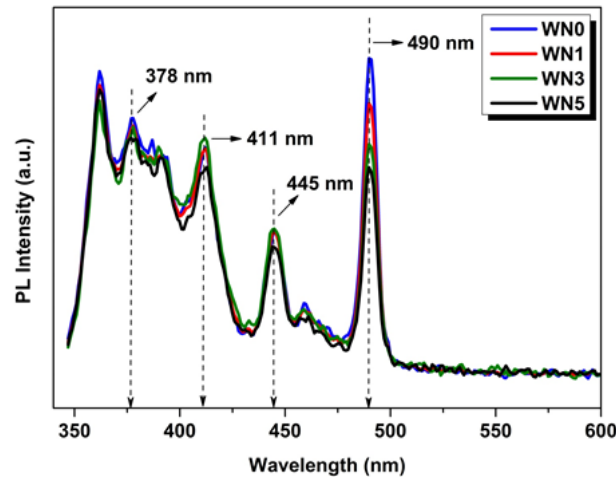
FIG. 7. Room temperature PL spectra of pure and Ni doped WO_3 NPs

Interestingly, no evidence for new PL phenomena can be found after the addition of Ni dopant to the host material. However, a decrease in excitonic PL intensity of WO_3 is observed which may be attributed to the electronic capture of Ni^{2+}. By capturing an electron, Ni^{2+} gets transformed to Ni^+ which is stable to some degree with a half–filled or full–filled outermost electronic configuration. Since, the capability in capturing the photo induced electrons is greater for Ni^{2+} than compared to surface oxygen vacancies and defects, therefore a degeneracy in the production of excitons is occurred [13]. This results lower the excitonic PL intensity of Ni-doped WO_3 samples and is ascribed to the lower recombination rate of the photo-generated electrons and holes, which is mainly affected by the greater defect density [13]. PL investigations were in glad agreement with the XPS results.

3.6. Gas sensing studies

Selectivity of the prepared samples was investigated in the presence of 200 ppm of acetone (C_3H_6O), formaldehyde (CH_2O), ammonia (NH_3), xylene (C_8H_{10}), ethanol (C_2H_5OH), acetaldehyde (C_2H_4O), toluene (C_7H_8) and n-butanol ($C_4H_{10}O$) gases at room temperature as shown in Fig. 8. An interesting phenomenon is noticed in Fig. 8; all the samples were highly selective towards NH_3 vapor and showed a lower sensitivity to other gases. However, a considerable sensitivity is observed for acetaldehyde ($S = 98$) and formaldehyde ($S = 66$) gases. It is also evident from Fig. 8, the sensitivity of the pure WO_3 NPs was found to be increased with further addition of Ni dopants and reaches a maximum value at WN3, indicating that the transition metal Ni remarkably improves the sensing properties of the WO_3 NPs. In addition, the WN3 sample showed ultra-high selective behavior towards ammonia vapor (200 ppm) and its sensitivity ($S = 2641$) is nearly 20 times higher than that of WN0 ($S = 137$) sample. Hence all the subsequent investigations were carried out with the WN3 sample.
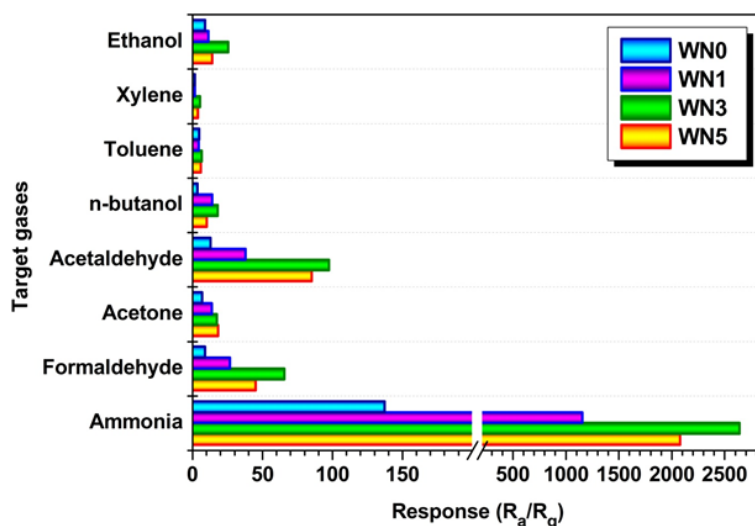
FIG. 8. Selectivity studies of the synthesized pristine and Ni doped WO_3 samples towards 200 ppm of different gases

Transient resistance response of WN3 sample was studied towards 5 – 200 ppm of NH_3 vapour at room temperature and is displayed in Fig. 9(a). It is worth mentioning that, WN3 sample shows outstanding responses to NH_3 even at lower concentrations. The sensing response values of the WN3 sensor are 50.4, 62.8, 416, 717, 1118.3, 1316.8, 1680.3 and 2641.3, respectively when it is exposed to 5, 10, 25, 50, 75, 100, 150 and 200 ppm NH_3. The sensor also exhibits a satisfying response trend towards varying concentrations of acetaldehyde and formaldehyde gases as depicted in Fig. 9(b). The WN3 sensor was tested in the range 5 – 1100 ppm of NH_3 and exhibited a linear response till 1000 ppm as shown in Fig. 10(a). Beyond 1000 ppm, there is no considerable improvement in sensitivity was observed. Therefore the WN3 sensor was saturated at 1100 ppm, and it could be attributed to the coverage of active sites by NH_3 species. Moreover, the sensor is almost insensitive below 0.5 ppm of NH_3, hence this concentration could be considered as lower detection limit of WN3 sample. It is noteworthy that, the sensor exhibits better sensitivity to lower concentration of NH_3 vapour even after exposure to 1100 ppm of NH_3, suggesting that the sensor has very good reversibility.

Figure 10 (b) shows the response and recovery trend of WN3 NPs towards 200 ppm of NH_3. The sensor resistance undergoes a dramatic decrease and reaches a saturation point (R_g) under NH_3 environment, and recovers almost to its initial baseline value (R_a) after the removal of NH_3 vapor. The response and the recovery time of WN3 sensor are
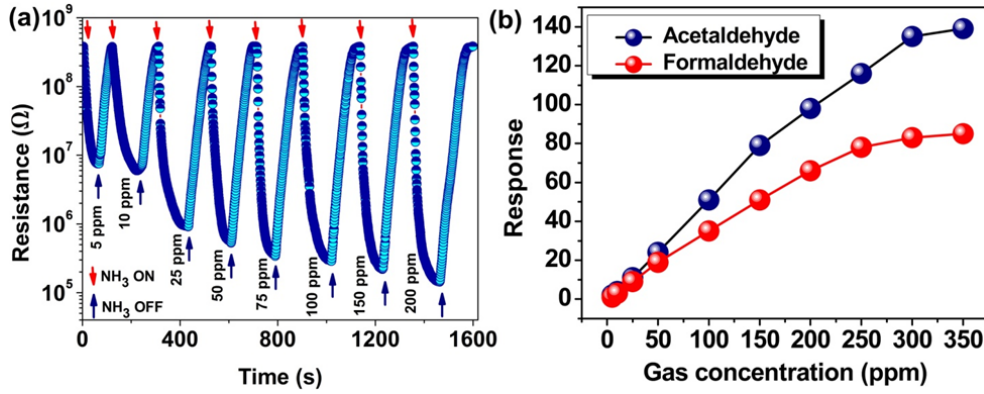
FIG. 9. (a) Transient resistance response of WN3 sample towards 5 – 200 ppm of NH_3 vapour at room temperature and (b) Transient response trend of WN3 sample towards varying concentrations of acetaldehyde and formaldehyde gases at room temperature
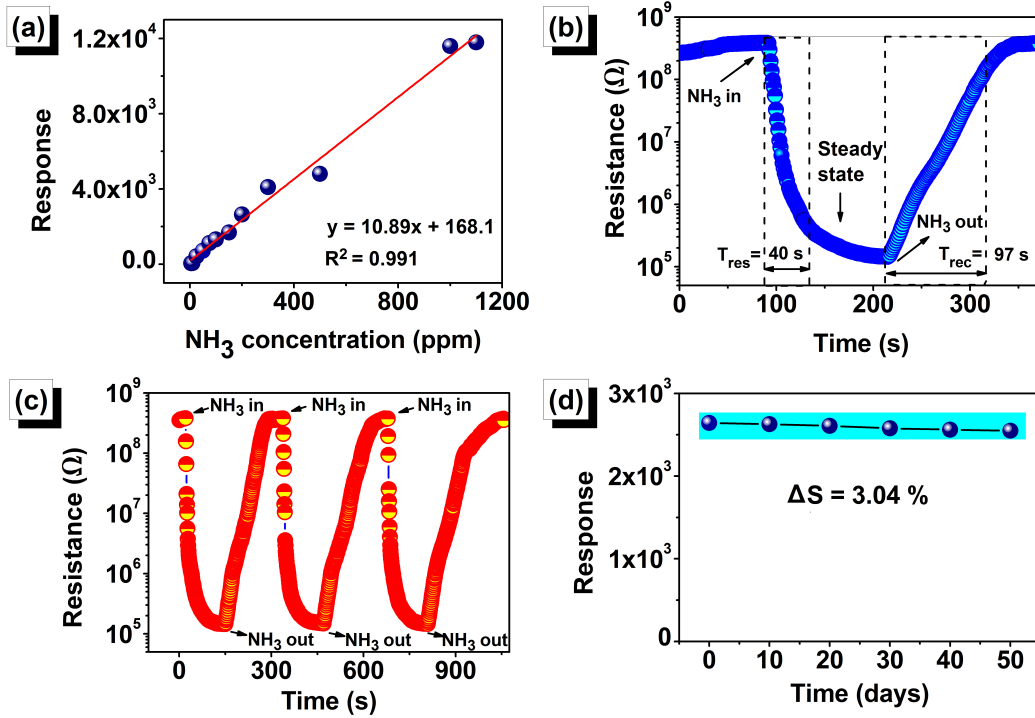
FIG. 10. (a) Response trend of WN3 sample towards different concentrations (5 – 1100 ppm) of NH_3 vapour at room temperature (b) Response-recovery profile of WN3 sample towards 200 ppm of NH_3 (c) Repeatability and (d) Stability of WN3 sample towards 200 ppm of NH_3 vapour at room temperature

evaluated as 40 and 97 s, respectively, which suggests that the rate of adsorption was faster than rate of desorption. Repeatability and long–time stability have been also measured at room temperature. The sensor shows a nearly constant signal over the three evaluation cycles towards 200 ppm of NH_3, confirming the good repeatability as shown in Fig. 10(c). The stability was found to be good towards 200 ppm of NH_3 over a period of 50 days in the interval of 10 days as displayed in Fig. 10(d). There was no significant drift found in the stability measurements and the change in sensitivity for the duration of 50 days was observed only 3.04 %, indicating that the high stability behavior of the sample.

Based on all the above considerations, the reported sensor has excellent figure of merits such as the capability of operating at room temperature, prompt sensing response to NH_3 with quick response/recovery times, higher active detection range and long–term stability.

3.7. Sensing mechanism

In general, the gas sensing behavior of MOSs especially n-type WO_3 sensor can be explained in terms of the interaction between the surface chemisorbed oxygen and the gas molecules to be detected. When WO_3 NPs were exposed to air, the oxygen molecules (O_2, below 100 °C) were chemisorbed on the sensing surface and form oxygen ions (O_2^-) by capturing the conduction band electrons as given in Eq. (3). This leads to the formation of a depletion region resulting in higher resistance (R_a) of the NPs. Whereas, under a reducing gas environment such as NH_3, the interaction between O_2^- and NH_3 molecules results in the liberation of electrons and are transported back to the conduction band of WO_3 as given in Eq. (4). This increases the electrical conductivity of the material and thus reduce the width of the depletion region. As a result of this reaction, the sensor reaches a steady state resistance (R_g) [7].

$$O_{2(\text{atmosphere})} + e^-_{(\text{WO}_3 \text{ surface})} \rightarrow O_2^-{}_{(\text{WO}_3 \text{ surface})}, \tag{3}$$

$$4NH_3 + 3O_2^-{}_{(\text{WO}_3 \text{ surface})} \rightarrow 2N_2 + 6H_2O + 6e^-. \tag{4}$$
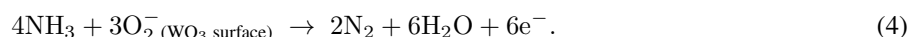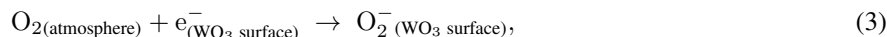
The high selective response behavior to NH_3 might be due to the following factors: (i) NH_3 has the least kinetic diameter (0.36 nm) than other vapors, lower bond dissociation enthalpy and ionization energy which might have supported the improved surface interactions [27]. (ii) Obviously, the electron donating behavior of NH_3 at effective surface regions (the areas in which the sensing layer can develop contacts with target gas) causes further increase in the density of free electrons to enhance the electrical conducting nature of the sensing material. This in-turn selective response towards NH_3 [28].

Compared to bare WO_3, the ultra high sensing response of Ni-doped WO_3 samples was probably due to various factors as follows, (i) The transition metal Ni is not only responsible for providing specific adsorption sites in the WO_3 matrix but typically most of the Ni^{2+} ions could also perform as catalysts. It is accepted that, the p-type behavior of Ni ions actively improve the rate of oxidation owing to greater oxygen adsorption and thus exhibit high catalytic activity to toxic gases, hence the sensing reaction is promoted. (ii) The Ni^{2+} ions were allowed to displace from the co-ordinate center to the oxygen vacancy along the z-axis. This phenomenon can induce a deformation in the host lattice (as discussed in Section 3.3). The imperfections and dislocations have greater strain energies, which accommodate more active sites for adsorption of O_2 and NH_3. (iii) The smaller crystallite size would also helped in greater oxygen adsorption onto the NPs surfaces. (iv) The Ni-doped WO_3 samples might have improved the inner grain interaction with analyte vapor resulting in notable switch-like change in the width of the depletion layer. (v) The large specific surface area facilitates more potential reaction sites on the surface of the sample thereby improving the performance of the sensor. (vi) Such a mesoporous structure of Ni-doped WO_3 samples (as observed from SEM and BET studies) may be helpful to enhance the target-receptor interface and be in favor for the diffusion of gas molecules during the gas sensing process, which are advantageous to enhance the sensing properties of Ni-doped WO_3 samples. Despite that, the excess amount of Ni dopants (WN5) will suppress the sensing characteristics of the sensor by reducing the available adsorption sites between the sensing surface and the analyte vapor [29]. Table 2 summarizes the NH_3 sensing performance of our WN3 sensor in the present work and those reported in the literatures [30–34].

TABLE 2. Comparison of various sensing performances of NH_3 gas sensors

Preparation technique	Dopant material	Response	Concentration (ppm)	Response time (s)	Recovery time (s)	Operating Temperature (K)	Ref.
Precipitation	Ni (3 mol.%)	2641^a	200	40	97	303	This work
Chemical method	PANI	4.75^b	1000	15	45	303	[30]
Hydrolysis	Ag (3 molar %)	25.1^a	10	150	600	303	[31]
Screen printing	Ru (0.37 wt.%)	386^b	1000	18	960	523	[32]
Screen printing	Mn (0.01M)	100^b	50	10	50	303	[33]
Hydrothermal	Pd (1 M)	45.7^a	50	3	9	623	[34]

$$^aS = \frac{R_a}{R_g}, \qquad ^bS = \frac{(R_a - R_g)}{R_a} \times 100.$$

4. Conclusion

In summary, pure and Ni-doped WO_3 NPs were successfully prepared by a facile precipitation technique. The XRD discloses a polycrystalline monoclinic crystal structure of the NPs. The SEM and FE–SEM images revealed that the samples composed of well-dispersed smaller grains with a mesoporous morphology. XPS study confirms the successful incorporation of Ni^{2+} ions into the WO_3 lattice. BET and BJH analyzes demonstrate that the Ni-doped samples contain large surface area and higher textural porosity. It could be inferred from the room temperature gas sensing investigations that, the Ni doping has remarkable impacts on enhancing the sensing properties of WO_3 NPs. However, the sensitivity of WO_3 NPs was highly improved with lower Ni doping level. Notably, the sensor fabricated based on WN3 sample (3 mol. % Ni/WO_3) exhibited a superior sensitivity ($S = 2641$ for 200 ppm NH_3) with a detection limit down to 0.5 ppm. Smaller grain size with huge surface area, abundant pores, rich adsorption sites, improved catalytic activity and excellent charge transport would make the Ni-doped WO_3 NPs as excellent sensing material for gas sensing applications and the WN3 sample can be a highly promising candidate for NH_3 detection in practice, particularly in medical diagnosis systems and food sectors.

Acknowledgements

Conflicts of interest

The authors declare no competing interests.

References

[1] Soni V., Singh P., Shree V., Goel V. (2018) Effects of VOCs on Human Health. In: Sharma N., Agarwal A., Eastwood P., Gupta T., Singh A. (eds) *Air Pollution and Control. Energy, Environment, and Sustainability*, Springer, Singapore, 2018, P. 119–142.

[2] Hahn Y.B., Ahmad R., Tripathy N. Chemical and biological sensors based on metal oxide nanostructures. *Chem. Commun.*, 2012, **48**, P. 10369–10385.

[3] Wu C.H., Zhu Z., Huang S.Y., Wu R.J. Preparation of palladium-doped mesoporous WO_3 for hydrogen gas sensors. *J. Alloys Compd.*, 2019, **776**, P. 965–73.

[4] Gu F., Cui Y., et al. Atomically dispersed Pt (II) on WO_3 for highly selective sensing and catalytic oxidation of triethylamine. *Appl. Catal. B Environ.*, 2019, **256**, P. 117809.

[5] Wang Z., Chiu H.C., et al. Lithium Photo-intercalation of CdS-Sensitized WO_3 anode for energy storage and photoelectrochromic applications. *Chem. Sus. Chem.*, 2019, **12**, P. 2220–30.

[6] Wang C., Yin L., et al. Metal oxide gas sensors: Sensitivity and influencing factors. *Sensors*, 2010, **10**, P. 2088–2106.

[7] Duraisami M.S., Parasuraman K. High sensitive room temperature ammonia sensor based on dopant free m-WO_3 nanoparticles: Effect of calcination temperature. *Nanosystems: Physics, Chemistry, Mathematics*, 2020, **11**, P. 578–589.

[8] Liu X., Zhang J., et al. Synthesis of Pt nanoparticles functionalized WO_3 nanorods and their gas sensing properties. *Sensors and Actuators B: Chemical*, 2011, **156**, P. 918–923.

[9] Qi J., Chen K., et al. Application of 3D hierarchical monoclinic-type structural Sb-doped WO_3 towards NO2 gas detection at low temperature. *Nanoscale*, 2018, **10**, P. 7440–7450.

[10] Chen L., Tsang S.C. Ag doped WO_3-based powder sensor for the detection of NO gas in air. *Sensors and Actuators B: Chemical*, 2003, **89**, P. 68–75.

[11] Li F., Ruan S., et al. Synthesis and characterization of Cr-doped WO_3 nanofibers for conductometric sensors with high xylene sensitivity. *Sensors and Actuators B: Chemical*, 2018, **265**, P. 355–364.

[12] Xiang Q., Meng G.F., et al. Au Nanoparticle Modified WO_3 Nanorods with Their Enhanced Properties for Photocatalysis and Gas Sensing. *The Journal of Physical Chemistry C*, 2010, **114**, P. 2049–2055.

[13] Faisal Mehmood, Javed Iqbal, Ismail M., Arshad Mehmood. Ni doped WO_3 nanoplates: An excellent photocatalyst and novel nanomaterial for enhanced anticancer activities. *Journal of Alloys and Compounds*, 2018, **746**, P. 729–738.

[14] Gattu K.P., Ghule K., et al. Bio-green synthesis of Ni-doped tin oxide nanoparticles and its influence on gas sensing properties. *RSC Adv.*, 2015, **5**, P. 72849.

[15] Delichere P., Falaras P., Froment M., Goff A.H.L. Electrochromism in anodic WO_3 films I: preparation and physicochemical properties of films in the virgin and coloured states. *Thin Solid Films*, 1988, **35**, P. 161.

[16] Abhudhahir M.H.S., Kandasamy J. Photocatalytic effect of manganese doped WO_3 and the effect of dopants on degradation of methylene blue. *J. Mater. Sci.: Mater. Electron.*, 2015, **26**, P. 8307–8314.

[17] Zhou J., Wei Y., et al. Electrochromic properties of vertically aligned Ni-doped WO_3 nanostructure films and their application in complementary electrochromic devices. *Journal of Materials Chemistry C*, 2016, **4**, P. 1613–1622.

[18] Wang Y., Liu B., et al. Low-temperature H_2S detection with hierarchical Cr-doped WO_3 microspheres. *ACS Appl. Mater. Interfaces*, 2016, **8**, P. 9674–9683.

[19] Dakhel A.A., Ashoor H. Synthesis of semi ferromagnetic Ni doped WO_3 nanoparticles by precipitation method: evaluation of effect of treatment in hydrogen gas. *Mater. Chem. Phys.*, 2019, **230**, P. 172–177.

[20] Grosvenor A.P., Biesinger M.C., Smart R.St.C., McIntyre N.S. New interpretations of XPS spectra of nickel metal and oxides. *Surf. Sci.*, 2006, **600**, P. 1771–1779.

[21] Bai S., et al. Gas sensing properties of Cd-doped ZnO nanofibers synthesized by the electrospinning method. *J. Mater. Chem. A*, 2014, **2**, P. 16697–16706.

[22] Lee Y.A., et al. Highly sensitive gasochromic H$_2$ sensing by nano-columnar WO$_3$–Pd films with surface moisture. *Sens. Actuators B*, 2017, **238**, P. 111–119.

[23] Tong M., et al. Facile preparation of amorphous carbon-coated tungsten trioxide containing oxygen vacancies as photocatalysts for dye degradation. *J. Mater. Sci.*, 2019, **54**, P. 10656–10669.

[24] Ta T.K.H., et al. Surface functionalization of WO$_3$ thin films with (3-Aminopropyl) triethoxysilane and succinic anhydride. *J. Electron. Mater.*, 2017, **46**, P. 3345–3352.

[25] Vuong N.M., Kim D., Kim H. Porous Au-embedded WO$_3$ nanowire structure for efficient detection of CH$_4$ and H$_2$S. *Sci. Rep.*, 2015, **5**, P. 11040.

[26] Kwangyeol Lee, Won Seok Seo, Joon T. Park. Synthesis and Optical Properties of Colloidal Tungsten Oxide Nanorods. *J. Am. Chem. Soc.*, 2003, **125**, P. 3408–3409.

[27] Nayak A.K., Ghosh R., et al. Hierarchical Nanostructured WO$_3$–SnO$_2$ for Selective Sensing of Volatile Organic Compounds. *Nanoscale*, 2015, **7**, P. 12460–12473.

[28] Mani G.K., Rayappan J.B.B. A highly selective room temperature ammonia sensor using spray deposited zinc oxide thin film. *Sensors Actuators, B Chem.*, 2013, **183**, P. 459–466.

[29] Yongjiao Sun, Lin Chen, et al. Synthesis of MoO$_3$/WO$_3$ composite nanostructures for highly sensitive ethanol and acetone detection. *J. Mater. Sci.*, 2017, **52**, P. 1561–1572.

[30] Shukla S.K., Singh N.B., Rastogi R.P. Efficient ammonia sensing over zinc oxide/polyaniline nanocomposite. *Indian J. Eng. Mater. Sci.*, 2013, **20**, P. 319–324.

[31] Haixin Liu, Wenhao Shen, Xiaoquan Chen. A room temperature operated ammonia gas sensor based on Ag-decorated TiO$_2$ quantum dot clusters. *RSC Adv.*, 2019, **9**, P. 24519–24526.

[32] Wagh M.S., Jain G.H., et al. Modified zinc oxide thick film resistors as NH$_3$ gas sensor. *Sens. Actuators B Chem.*, 2006, **115**, P. 128–133.

[33] Patil L.A., Sonawane L.S., Patil D.G. Room temperature ammonia gas sensing using MnO$_2$-modified ZnO thick film resistors. *J. Mod. Phys.*, 2011, **2**, P. 1215–1221.

[34] Yi Z., Zheng L., et al. Enhanced ammonia sensing performances of Pd–sensitized flowerlike ZnO nanostructure. *Sens. Actuators B Chem.*, 2011, **156**, P. 395–400.

Formation of cobalt ferrite nanopowders in an impinging-jets microreactor

K. I. Barashok[1], V. V. Panchuk[2], V. G. Semenov[2], O. V. Almjasheva[1,3,*], R. Sh. Abiev[4,5]

[1]Saint Petersburg State Electrotechnical University "LETI", Professora Popova St., 5,
Saint Petersburg, 197376, Russia

[2]Saint Petersburg State University, Universitetskaya emb., 7-9, Saint Petersburg, 199034, Russia

[3]Ioffe Institute Politekhnicheskaya St. 26, Saint Petersburg, 194021, Russia

[4]Saint Petersburg State Institute of Technology, Moskovsky Pr., 26, Saint Petersburg, 190013, Russia

[5]Institute of Silicate Chemistry RAS, Makarova emb., 2 Saint Petersburg, 199034, Russia

*almjasheva@mail.ru, rufat.abiev@gmail.com

The dependence of cobalt ferrite nanosized powder production process on the synthesis method and conditions was studied. The paper shows the possibility for producing nanocrystalline $CoFe_2O_4$ with an average particle size of 12 nm under conditions of an impinging-jets microreactor at room temperature. The influence exerted by the parameters of process implementation in the microreactor on phase formation in the $CoO–Fe_2O_3–H_2O$ system was analyzed.

Keywords: cobalt ferrite, nanosized powders, impinging jet microreactor.

1. Introduction

Nanocrystalline ferrite powders including cobalt ferrite powder are potentially widely used in medicine [1–8], catalysis [8–13], electronics, power industry and in other fields of engineering and technology [14–22]. For nanoparticles to be effectively used, as a rule, they should have not only small size but also quite narrow size distribution [3–5, 16, 23]. Therefore, it is of interest to study the formation processes of nanocrystalline cobalt-ferrite-based powder allowing the creation of slightly agglomerated crystalline nanoparticles with a narrow size distribution. Methods belonging to the group of "soft chemistry" techniques are often used for these purposes [13–19, 24–34]. A method for combined hydrothermal and microwave treatment of hydroxides [31–35] is one of the promising methods for the synthesis of nanosized powders; when this method is used, the hydrothermal medium is heated due to exposure to the microwave radiation. The earlier studies [35, 36] showed that $CoFe_2O_4$ nanocrystals were already formed within the first minute of synthesis at a temperature of 130 °C in the mode of microwave heating of co-precipitated cobalt and iron hydroxides. Such high rate of synthesis of nanocrystalline $CoFe_2O_4$ was associated with the formation of prenucleation cluster hydroxides with a structure, which was similar to that of cobalt ferrite, in the initial mixture [35, 36]. Another condition, in addition to the creation of nucleation clusters in the reaction medium, which provides a high rate of formation of the final product, is a decrease in the path length of the reagents and an increase in the rate of their transport in the reaction zone [37]. One of the ways to ensure the rapid course of chemical reactions is a high level of spatial contact of the initial components [24, 35, 36, 40, 41]. According to [42–44], it is possible to avoid spatial separation of the components during the synthesis of oxide nanoparticles resulting from the difference in pH values of hydroxide precipitation and variations in temperatures of their dehydration by using a method for microreactor synthesis with freely impinging jet-jets. Equipment of this type can provide for the rapid contact and micromixing of reagents, high level of reaction zone localization, and fast discharge of reaction products [42–49]. For example, the studies [43, 44] showed that the use of microreactor synthesis resulted in obtaining nanocrystalline cobalt ferrite with crystallite size of about 8 nm already at room temperature. Therefore, it is interesting to systematically study the influence exerted by the process parameters of synthesis in a freely impingingjet-jets microreactor on the formation process of nanocrystalline cobalt ferrite. In particular, it is interesting to analyze the influence of a pulsation mode of reagent supply, which showed the higher efficiency of microreactor synthesis in some cases [47].

2. Experimental

Cobalt ferrite was produced by coprecipitation from the mixture of aqueous solutions of 0.5 M iron (III) nitrate $(Fe(NO_3)_3$ (analytical reagent grade) and 0.25 M cobalt (II) nitrate $(Co(NO_3)_2$ (analytical reagent grade)) with 1.3 M sodium hydroxide (NaOH, (analytical reagent grade)) in a freely impinging jet-jets microreactor, the design of which was described in [44]. The alkali solution with the above concentration with the reagent supply rates use provides for a certain alkali excess in the interaction zone as compared to reaction stoichiometry, which is required for precipitation completeness.

The mixture of salt solutions (solution No. 1) and NaOH solution (solution No. 2) were supplied with the use of two Heidolph 5201 peristaltic pumps with a Quick-S five-roller head with constant flow rates to the microreactor unit through the nipples on the opposite sides (Fig. 1) [44]. The internal diameters of the nozzles (2, 3 – Fig. 1) were $520 - 540$ μm. The studies were performed in the microreactor made in two versions: without pulsations (Fig. 1a) and with pulsations with superposition of the pulsations on the liquid flow (Fig. 1b). In the second version, reagents were supplied to the interaction zone in the mode of reagent solution flows modulation, by coherent (with equal amplitude, frequency and phase) pulsations generated with the use of a pulsator 12 and two identical chambers with variable volume (bellows) 13. An idea of using the pulsation assembly when supplying the solutions to the reactor space consists in the fact that there takes place accelerated (as compared to uninterrupted supply of the solutions by the pumps) breaking up of jets to primary reagent drops 15, which, when moving from the opposite sides with equal velocities and colliding, form secondary microdrops 16 as a result of interfusion. Such mode allows implementing the interaction process of salt solutions and the precipitator in a limited space of microdrops 16 with diameter of about $1 -$ 2 mm. The drops of reagent solutions from the opposite nipples were formed simultaneously due to the coherence of the generated oscillations. The pulsation frequency was varied in the range of $4.26 - 13.9$ Hz.
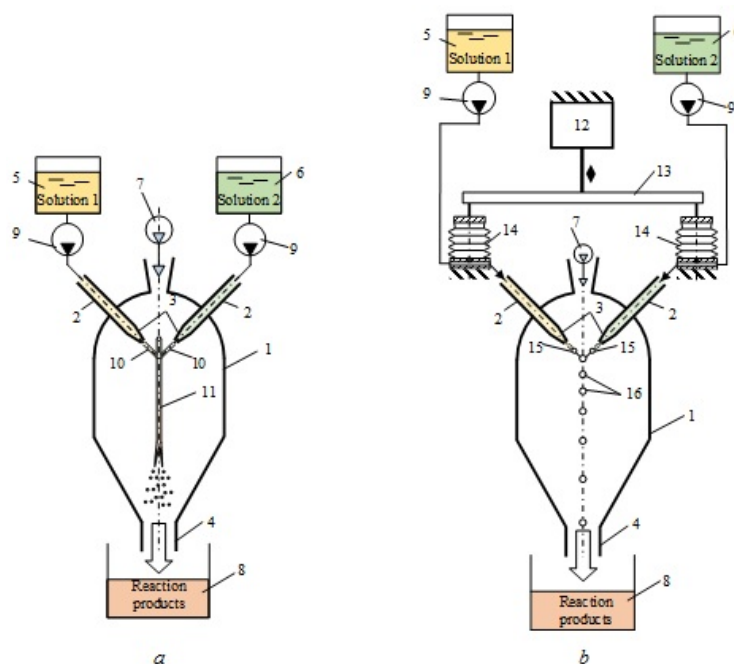
FIG. 1. Scheme of the microreactor unit: (a) – without the use of pulsations; (b) – with superposition of pulsations on the flow. 1 – cylinder-conic housing; 2 – nipples for supplying the initial components; 3 – nozzles; 4 – outlet for product discharge; 5,6 – vessels for solutions; 7 – purge gas blower; 8 – vessel for collecting the reaction products; 9 – pumps; 10 – jets; 11 – liquid sheet in free volume; 12 – drive of oscillation movements; 13 – crossbeam; 14 – chambers with variable volume (bellows); 15 – primary drops of individual solutions; 16 – secondary drops of the solution mixture

The precipitate obtained as a result of the solutions mixing was collected in a vessel under the microreactor unit, washed with distilled water to reach neutral pH and the absence of impurity ions, and dried at a temperature of 50 °C.

A material produced by the method for direct precipitation from the aqueous solution mixture of iron and cobalt salts with aqueous sodium hydroxide solution was used as the reference sample. NaOH solution was added at constant

mixing using a mechanical mixer until pH = 8 was reached. The obtained precipitate was washed also with distilled water and dried at a temperature of 50 °C.

The microstructure and elemental composition of the samples were determined using Quanta 200 scanning electron microscope (FEI Company) fitted out with EDAX X-ray spectral microanalysis attachment.

The phase composition of the samples was controlled by X-ray diffraction using SmartLab 3 X-ray diffractometer (CoK_α-radiation) (Rigaku Corporation). The peaks in the diffractogram were identified using PDWin 4.0 software complex and Crystallographica Search-Match package. The average crystallite size, i.e. the size of monocrystals, of which cobalt ferrite particles consisted, was determined as a value of the coherent scatter region, based on broadening of X-ray diffraction lines, using Scherrer formula.

The crystal size distribution was determined based on the data of X-ray diffraction of the samples using MAUD software.

Mössbauer spectra were recorded using a spectrometer by WISSEL in the permanent acceleration mode, at the room temperature. ^{57}Co in Rh-matrix with activity of 30 mCi was used as the source. The mathematical processing of the experimental spectra was performed using MOSSFIT software package [50]. The velocity scale of the spectrometer was calibrated using α-Fe foil in the room temperature. The values of chemical shifts are presented relative to α-Fe.

3. Results and discussion

According to elemental analysis data (Table 1), the Co:Fe ratio for all samples obtained both by direct precipitation and under conditions of microreactor synthesis, taking into account the method error, conforms to stoichiometry preset during the synthesis. Sodium is not detected in the sample within the sensitivity of X-ray spectral analysis, which evidences practically full removal of impurity solution components from the obtained powders.

X-ray diffractograms of the obtained samples are presented in Fig. 2. The X-ray diffractogram of the sample obtained by direct coprecipitation of iron and cobalt hydroxides with NaOH solution (Fig. 2, curve 1) shows broad X-ray maxima of low intensity which are evidence of the presence of Co–Fe-layered double hydroxide (LDH) [51,52], γ-Fe_2O_3 and cobalt ferrite ($CoFe_2O_4$) in the sample. At the same time, the analysis of X-ray diffraction line profile evidences of the fact that the sample is mainly in the X-ray amorphous condition.
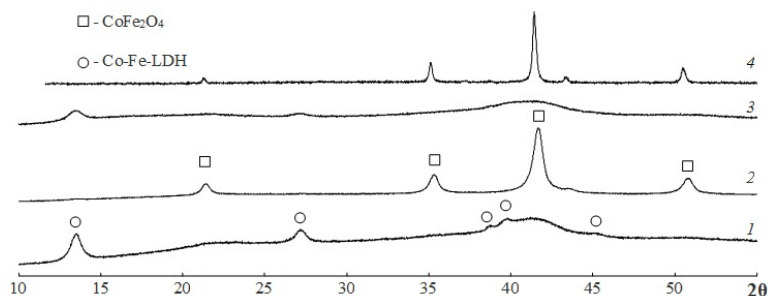
FIG. 2. X-ray diffractograms of the samples obtained in the process of 1 – direct precipitation; 2 – microreactor synthesis with continuously impinging-jets; 3 – microreactor synthesis in pulsation mode ($\nu = 13.9$ Hz); 4 – thermal treatment of the sample synthesized under conditions of a microreactor, in the pulsation mode ($\nu = 13.9$ Hz) at a temperature of 800 °C for 1 h

The analysis of X-ray diffractogram of the sample obtained using the microreactor without pulsation mode (Fig. 2, curve 2) is evidence of the fact that the interaction of reagents in the sheet being formed during jet collision results in production of nanocrystalline cobalt ferrite with the average crystallite size of about 12 nm. However, the analysis of the dependence presented in Fig. 3shows evidence of quite broad crystallite size distribution.

The use of the pulsation mode when supplying the reagents during the microreactor synthesis leads to the formation of a practically X-ray amorphous product. X-ray diffractograms of the samples obtained with different pulsation frequencies show only low-intensive halo in the region of maximal peaks corresponding to Co–Fe-layered double hydroxide and cobalt ferrite. The typical view of X-ray diffractogram of the samples 3 – 5 (see Table 1) is presented in Fig. 2 (curve 3).

The Mössbauer spectra of powders obtained both by the method for direct precipitation and with the use of microreactor synthesis is presented in Fig. 4. Fig. 4 shows also the results of the decomposition of the experimental spectra to components corresponding to iron atoms in different local surroundings. The Mössbauer parameters of iron-containing phases are presented in Table 1. The quantitative assessment of the relative iron content in different phases is performed within the accuracy of the difference in values of Mössbauer factor f_M.

FIG. 3. Size distribution of $CoFe_2O_4$ crystallites obtained by the method of microreactor synthesis with continuously impinging-jets

The Mössbauer spectrum for the sample obtained under conditions of microreactor synthesis without the pulsation mode is a superposition of sextets corresponding to the condition of iron atoms in octa- and tetra-p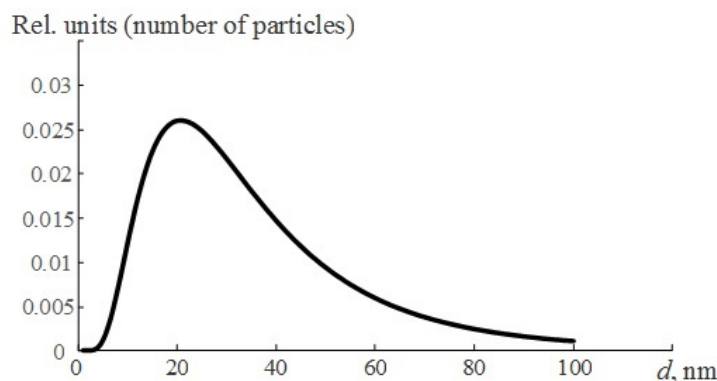ositions in cobalt ferrite structure. The values of magnetic hyperfine fields (H_{eff}) of these sextets depend not only on the differences in local surroundings of iron nuclei corresponding to them but also on magnetic crystal sizes. The value H_{eff} decreases when crystals pass to single-domain (superparamagnet) condition, in which magnet locking temperature depends on crystal size [53]. Moreover, the smaller the crystal size is, the lower the value H_{eff} is down to its full disappearance. Such behavior of H_{eff} occurs for magnet crystals, in which the rate of direction change of the total magnetic moment is much larger than the nucleus lifetime in the excited condition ($\tau \sim 10^{-9}$ s). This critical size for $CoFe_2O_4$ is about 6 nm [54, 55]. Thus, comparison of sextet parameters (Fig. 4, Table 1) with the data of [55] allows one to conclude that the maximum size of $CoFe_2O_4$ crystallites obtained by microreactor synthesis is less than 50 nm. In addition, the presence of a sextet with low H_{eff} (39.3 T) is explained by broad crystallite size distribution. These results are in good agreement with the X-ray diffraction data (Fig. 3).

The Mössbauer spectrum represents doublet superposition for all other samples obtained both by the method for direct precipitation and by using microreactor synthesis in the pulsation mode (Fig. 4, Table 1). The analysis of experimental spectra allows distinguishing a doublet corresponding to iron atom condition in the structure of Co–Fe-layered double hydroxide [48] and doublets evidencing the presence of small $CoFe_2O_4$ clusters with crystallite sizes corresponding to the superparamagnet condition [55].

According to the study [54], the critical size of superparamagnetism for $CoFe_2O_4$ is about 14 nm. In the [55] the authors observed two doublets with parameters $I_S(\text{tetr}) = 0.258$, $Q_S(\text{tetr}) = 1.943$ and $I_S(\text{tetr}) = 0.326$, $Q_S(\text{tetr}) = 0.653$ for cobalt ferrite with crystallite size of about 6 nm. The noticeable difference between the parameters of Mössbauer spectra presented in Table and the parameters in [55] may be associated with several factors, e.g., with significantly smaller size of clusters with cobalt ferrite structure as compared to the size of $CoFe_2O_4$ crystallites described in the study [55]. It is possible that these differences are caused by different population degree with cobalt and iron ions in the octa- and tetra-positions in the spinel structure, which can be explained, among other factors, by peculiarities of synthesis conditions.

Thus, the analysis of the presented data is evidence of the fact that when the methods for direct coprecipitation and microreactor synthesis in jet pulsation mode are used, formation of small clusters with cobalt ferrite structure with different population degree in octa- and tetra-positions is observed at the stage of mixing of the reagents (cobalt and iron nitrates solution with NaOH solution), which is confirmed by the deviation of quadrupolar splitting values from the data presented in [55]. At the same time, spatial component separation associated with the formation of the phase of Co–Fe-layered double hydroxide takes place, apparently, in the greater part of the system and, as a result, the mechanism of cobalt ferrite formation changes as compared to the mode of continuous mixing of reagent streams described in [51, 52].

The described difference in phase formation processes in the microreactor with continuously impinging-jets [43, 44] and when the pulsation mode is used can be associated with the fact that the sizes of colliding drops are about 1 mm and the energy dissipation rate in such case is significantly less than that when microjets collide with the formation of the liquid sheet with a thickness of about 20 μm. This difference results in the fact that it is not possible to implement hydrodynamic conditions leading to the formation of the microreactor in the pulsation mode [42, 43]. This leads, in its turn, to spatial separation of the reaction system components, and the formation of $CoFe_2O_4$ will take place not due to the coalescence of small clusters with cobalt ferrite structure as it was mentioned in [35, 36] but according to the
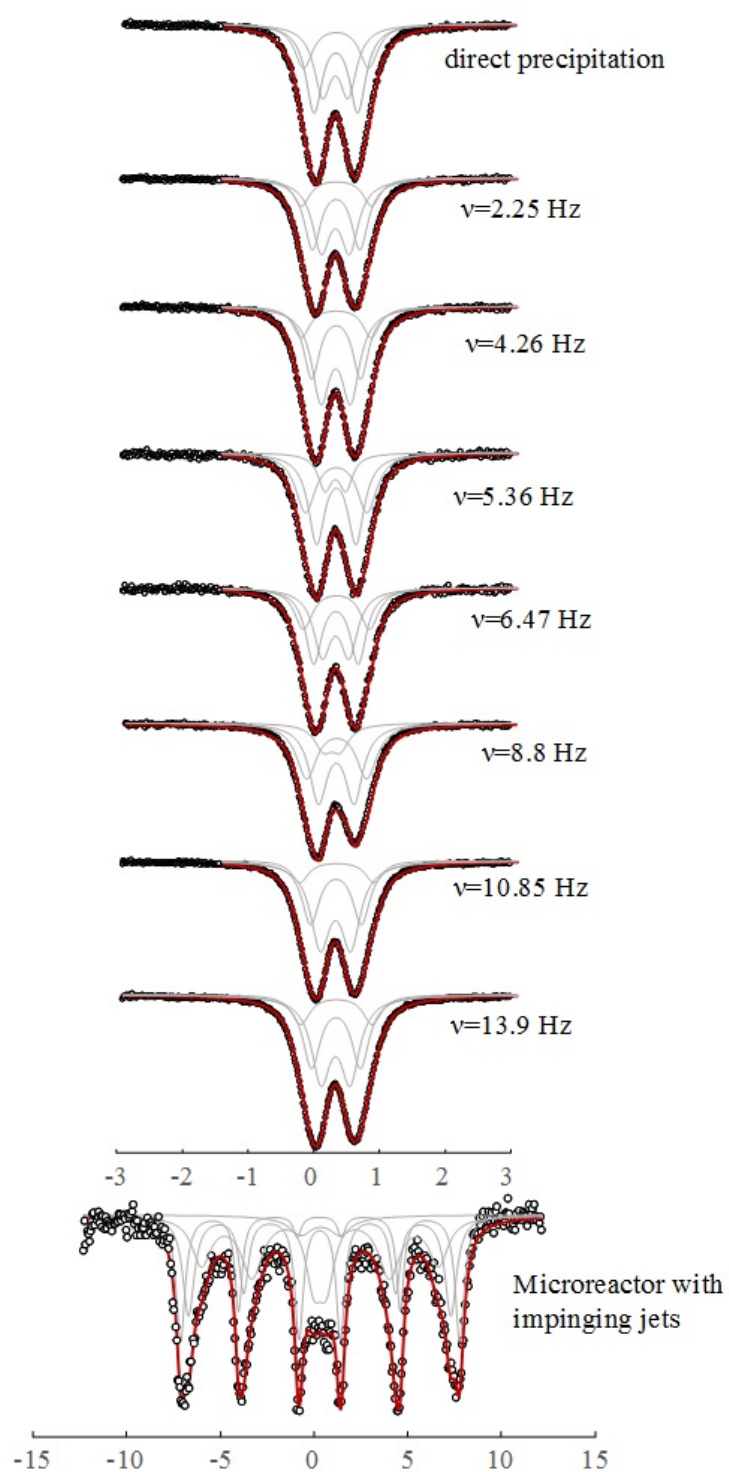
FIG. 4. Mössbauer spectra of the samples

TABLE 1. The parameters of Mössbauer spectra of the samples (determination error for $I_s \pm 0.002$ mm/s; $Q_s \pm 0.005$ mm/s; $H_{eff} \pm 0.1$ T)

Synthesis conditions	Fe/Co	Phases	Mössbauer parameters for iron atoms in various local environment				Identification of local environments of iron atoms
			I_S (mm/s)	Q_S (mm/s)	H_{eff} (T)	%	
Direct precipitation	2.05	Co–Fe–LDH, CoFe$_2$O$_4$	0.339	0.665	–	43.08	CoFe$_2$O$_4$
			0.343	0.994	–	23.43	
			0.330	0.388	–	33.50	Co–Fe–LDH
MS ($\nu = 0$)	2.03	CoFe$_2$O$_4$	0.307	−0.042	46.272	24.05	CoFe$_2$O$_4$
			0.303	0.004	43.462	34.53	
			0.337	0.031	39.302	29.46	
			0.322	0.674		11.96	
MS ($\nu = 4.26$)	2.13	am. ph., trace Co-Fe–LDH, CoFe$_2$O$_4$	0.340	0.746	–	35.63	CoFe$_2$O$_4$
			0.341	1.067	–	15.83	
			0.332	0.451	–	48.54	Co–Fe–LDH
MS ($\nu = 5.36$)	2.19	am. ph., trace Co-Fe–LDH, CoFe$_2$O$_4$	0.342	0.599	–	46.06	CoFe$_2$O$_4$
			0.341	0.936	–	38.00	
			0.327	0.317	–	15.94	Co–Fe–LDH
MS ($\nu = 6.47$)	2.01	am. ph., trace Co–Fe–CDG, CoFe$_2$O$_4$	0.336	0.678	–	40.32	CoFe$_2$O$_4$
			0.343	1.007	–	23.88	
			0.330	0.406	–	35.80	Co–Fe–LDH
MS ($\nu = 10.85$)	2.07	am. ph., trace Co–Fe–LDH, CoFe$_2$O$_4$	0.340	0.774	–	35.94	CoFe$_2$O$_4$
			0.354	1.125	–	12.26	
			0.332	0.463	–	51.80	Co–Fe–CDG
MS ($\nu = 13.90$)	2.03	am. ph., trace Co–Fe–LDH, CoFe$_2$O$_4$	0.338	0.744	–	38.36	CoFe$_2$O$_4$
			0.345	1.091	–	15.79	
			0.331	0.442	–	45.85	Co–Fe–LDH

Mossbauer parameters of comparison crystals CoFe$_2$O$_4$: *less 6 nm I_S(tetr) = 0.258, Q_S(tetr) = 1.943; I_S(octa) = 0.326, Q_S(octa) = 0.653 [55]; **nanocrystals I_S(A) = 0.24, Q_S(A) = 0.04; I_S(B) = 0.37, Q_S(B) = 0.03 [55]; ***Co–Fe–CDG I_S = 0.349, Q_S(tetr) = 0.497 [51,52]

mechanism of solid-phase interaction which is similar to the formation process of magnesium ferrite described in the study [40]. The implementation of such formation mechanism will require a stage involving long thermal treatment.

4. Conclusions

Thus, it is possible to conclude that the use of the method for microreactor synthesis with continuously impinging-jets allows one to obtain nanosized cobalt ferrite crystals at room temperature. The need to use the pulsation mode, at least in the form that was used in this work for the synthesis of CoFe$_2$O$_4$ nanoparticles, does not allow realization of the advantages of microreactor synthesis.

Acknowledgements

References

[1] Sharifi I., Shokrollahi H., Amiri S. Ferrite-based magnetic nanofluids used in hyperthermia applications. *Journal of Magnetism and Magnetic Materials*, 2012, **324**(6), P. 903–915.

[2] Amiri M., Akbari A., Ahmadi M., Pardakhti A., Salavati-Niasari M. Synthesis and in vitro evaluation of a novel magnetic drug delivery system; proecological method for the preparation of $CoFe_2O_4$ nanostructures. *Journal of Molecular Liquids*, 2018, **249**, P. 1151–1160.

[3] Amiri S., Shokrollahi H. The role of cobalt ferrite magnetic nanoparticles in medical science. *Materials Science and Engineering: C*, 2012, **33**(1), P. 1–8.

[4] Oh Y., Moorthy M.S., Manivasagan P., Bharathiraja S., Oh J. Magnetic hyperthermia and pH-responsive effective drug delivery to the sub-cellular level of human breast cancer cells by modified $CoFe_2O_4$ nanoparticles. *Biochimie*, 2017, **133**, P. 7–19.

[5] Drašler B., Drobne D., Novak S., et al. Effects of magnetic cobalt ferrite nanoparticles on biological and artificial lipid membranes. *International Journal of Nanomedicine*, 2014, **9**(1), P. 1559–1581.

[6] Guglielmo C.D., López D. R., Lapuente J. De., Llobet Mallafre J. M., Suàrez M. B. Embryotoxicity of cobalt ferrite and gold nanoparticles: A first in vitro approach. *Reproductive Toxicology*, 2010, **30**(2), P. 271–276.

[7] Sanpo N., Berndt C. C., Wen C., Wang J. Transition metal-substituted cobalt ferrite nanoparticles for biomedical applications. *Acta Biomaterialia*, 2013, **9**(3), P. 5830–5837.

[8] Sincai, M., Ganga, D., Bica, D., Vekas, L. The antitumor effect of locoregional magnetic cobalt ferrite in dog mammary adenocarcinoma. *Journal of Magnetism and Magnetic Materials*, 2001, **225**(1–2), P. 235–240.

[9] Amiri M., Salavati-Niasari M., Akbari A. A magnetic $CoFe_2O_4/SiO_2$ nanocomposite fabricated by the sol-gel method for electrocatalytic oxidation and determination of L-cysteine. *Microchimica Acta*, 2017, **184**(3), P. 825–833.

[10] Chen Y., Sun J., Zhang Y., Zheng S., Wang B., Chen Z., Xue Y., Chen M., Abbas M., Chen J. $CoFe_2O_4$ nanoarray catalysts for Fischer-Tropsch synthesis. *Journal of Fuel Chemistry and Technology*, 2017, **45**(9), P. 1082–1087.

[11] Chen H.D., Xu J.K., Wei J.Q., Wang P.F., Han Y.B., Xu J.C., Hong B., Jin H.X., Jina D.F., Peng X.L., Li J., Yang Y.T., Ge H.L., Wang X.Q. Mesoporous $CoFe_2O_4$ nanowires: Nanocasting synthesis, magnetic separation and enhanced catalytic degradation for ciprofloxacin. *Journal of Physics and Chemistry of Solids*, 2019, **132**, P. 138–144.

[12] Tan X., Wang X., Liu Q., Zhou J., Zhang P., Zheng S., Miao S. Bio-gel template synthesis of $CoFe_2O_4$ nano-catalysts and application in aerobic oxidation of cyclohexane. *International Journal of Hydrogen Energy*, 2107, **42**(30), P. 19001–19009.

[13] Huang Y., Yang W., Yu Y., Haov S. Ordered mesoporous spinel $CoFe_2O_4$ as efficient electrocatalyst for the oxygen evolution reaction. *Journal of Electroanalytical Chemistry*, 2019, **840**, P. 409–414.

[14] Xavier S., Thankachan S., Jacob B.P., Mohammed E.M. Effect of sintering temperature on the structural and magnetic properties of cobalt ferrite nanoparticles. *Nanosystems: Physics, Chemistry, Mathematics*, 2013, **4**(3), P. 430–437.

[15] Song N., Gu S., Wu Q., Li C., Jhou J. Facile synthesis and high-frequency performance of $CoFe_2O_4$ nanocubes with different size. *Journal of Magnetism and Magnetic Materials*, 2018, **451**, P. 793–798.

[16] Song N., Gu S., Zhou J., Xia W., Zhang P. Achieving a high cutting-off frequency in the oriented $CoFe_2O_4$ nanocubes. *Journal of Applied Physics Letter*, 2017, **111**, P. 133108.

[17] Karthick R., Ramachandran K., Srinivasan R. Study of faraday effect on $Co_{1-x}Zn_xFe_2O_4$ nanoferrofluids. *Nanosystems: Physics, Chemistry, Mathematics*, 2016, **7**(4), P. 624–628.

[18] Ojha Vibha H., Kant K. Mohan. Temperature dependent magnetic properties of superparamagnetic $CoFe_2O_4$ nanoparticles. *Physica B: Condensed Matter.*, 2019, **567**, P. 87–94.

[19] Lavela P., Tirado J.L. $CoFe_2O_4$ and $NiFe_2O_4$ synthesized by sol-gel procedures for their use as anode materials for Li ion batteries. *J. Power Sources.*, 2007, **172**(1), P. 379–387.

[20] Chauhan C.C., Jotania R.B. Structural and magnetic properties of $BaCo_{2-x}Ni_xFe_{16}O_{27}$ hexagonal ferrite prepared by a simple heat treatment method. *Nanosystems: Physics, Chemistry, Mathematics*, 2016, **7**(4), P. 595–598.

[21] Vasylenko I.V., Kazakevych M.L., Pavlishchuk, V.V. Design of ferrofluids and luminescent ferrofluids derived from $CoFe_2O_4$ nanoparticles for nondestructive defect monitoring. *Theoretical and Experimental Chemistry*, 2019, **54**(6), P. 365–368.

[22] Murugesan C., Perumal M., Chandrasekaran G. Structural, dielectric and magnetic properties of cobalt ferrite prepared using auto combustion and ceramic route. *J. Physica B: Condensed Matter.*, 2014, **448**, P. 53–56.

[23] Gofman I.V., Nikolaeva A.L., Khripunov A.K., Yakimansky A.V., Ivan'kova E.M., D.P. Romanov, Ivanova O.S., Teplonogova M.A., Ivanov V.K. Impact of nano-sized cerium oxide on physico-mechanical characteristics and thermal properties of the bacterial cellulose films. *Nanosystems: Physics, Chemistry, Mathematics*, 2018, **9**(6), P. 754–762.

[24] Gingasu D., Mindru I., Mocioiua O.C., Preda S., Stanica N., Patron L., Ianculescu A., Oprea O., Nita S., Paraschiv I., Popa M., Saviuc K., Bleotu C., Chifiriuc M.C. Synthesis of nanocrystalline cobalt ferrite through soft chemistry methods: A green chemistry approach using sesame seed extract. *Materials Chemistry and Physics*, 2016, **182**, P. 219–230.

[25] Popkov V.I., Almjasheva O.V. Formation mechanism of $YFeO_3$ nanoparticles under the hydrothermal condition. *Nanosystems: Physics, Chemistry, Mathematics*, 2014, **5**(5), P. 703–708.

[26] Nguen Anh Tien, Mittova I.Ya., Al'myasheva O.V. Influence of the synthesis conditions on the particle size and morphology of yttrium orthoferrite obtained from aqueous solutions. *Russian Journal of Applied Chemistry*, 2009, **82**(11), P. 1915–1918.

[27] Kim Y.I., Kim D., Lee C.S. Synthesis and characterization of $CoFe_2O_4$ magnetic nanoparticles prepared by temperature-controlled coprecipitation method. *Phys. B Condens. Matter.*, 2003, **337**, P. 42–51.

[28] Manova E., Kunev B., Paneva D., Mitov I., Petrov L., Estourns C., D'Orlans C., Rehspringer J.L., Kurmoo M. Mechano-synthesis, characterization, and magnetic properties of nanoparticles of cobalt ferrite $CoFe_2O_4$. *Chem. Mater.*, 2004, **16**(26), P. 5689–5692.

[29] Nguyen Anh Tien, Chau Hong Diem, Nguyen Thi Truc Linh, Mittova V.O., Do Tra Huong, Mittova I.Ya. Structural and magnetic properties of $YFe_{1-x}Co_xO_3$ ($0.1 \leq x \leq 0.5$) perovskite nanomaterials synthesized by co-precipitation method. *Nanosystems: Physics, Chemistry, Mathematics.*, 2018, **9**(3), P. 424–429.

[30] Saffari J., Ghanbari D., Mir N., Khandan-Barani K. Sonochemical synthesis of $CoFe_2O_4$ nanoparticles and their application in magnetic polystyrene nanocomposites. *J. Ind. Eng. Chem.*, 2014, **20**, P. 4119–4123.

[31] Kalpanadevi K., Sinduja C.R., Manimekalai R. A facile thermal decomposition route to synthesise CoFe$_2$O$_4$ nanostructures. *Mater Sci-Pol.*, 2014, **32**(1), P. 34–38.

[32] Meskin P.E., Gavrilov A.I., Maksimov V.D., Ivanov V.K., Churagulov B.P. Hydrothermal/microwave and hydrothermal/ultrasonic synthesis of nanocrystalline titania, zirconia, and hafnia. *Russian Journal of Inorganic Chemistry*, 2007, **52**(11), P. 1648–1656.

[33] Meng L.-Y., Wang B., Ma M.-G., Lin K.-L. The progress of microwave-assisted hydrothermal method in the synthesis of functional nanomaterials. *Materials Today Chemistry*, 2016, **1-2**, P. 63–83.

[34] Ivanov V.K., Polezhaeva O.S., Gil' D.O., Kopitsa G.P., Tret'yakov Yu.D. Hydrothermal microwave synthesis of nanocrystalline cerium dioxide. *Doklady Chemistry*, 2009, **426**(2), P. 131–133.

[35] Kuznetsova V.A., Almjasheva O.V., Gusarov V.V. Influence of microwave and ultrasonic treatment on the formation of CoFe$_2$O$_4$ under hydrothermal conditions. *Glass Physics and Chemistry*, 2009, **35**(2), P. 205–209.

[36] Almjasheva O.V., Gusarov, V.V. Prenucleation formations in control over synthesis of CoFe$_2$O$_4$ nanocrystalline powders. *Russ. J. Appl. Chem.*, 2016, **89**(6), P. 851–856.

[37] Gusarov V.V. Fast solid-phase chemical reactions. *Russ. J. Gen. Chem.*, 1997, **67**(12), P. 1846–1851.

[38] Gusarov V.V., Ishutina Zh.N., Malkov A.A., Malygin A.A. Solid-phase reaction of mullite formation in nanosized composite films. *Dokl. Phys. Chem.*, 1997, **357**(1–3), P. 360–363.

[39] Gusarov V.V., Malkov A.A., Ishutina Zh.N., Malygin A.A. Phase formation in a nanosize silicon oxide film on the surface of aluminum oxide. *Tech. Phys. Lett.*, 1998, **24**(1), P. 1–3.

[40] Komlev A.A., Panchuk V. V., Semenov V.G., Almjasheva O.V., Gusarov V.V. Effect of the sequence of chemical transformations on the spatial segregation of components and formation of periclase-spinel nanopowders in the MgO–Fe$_2$O$_3$–H$_2$O system. *Russ. J Appl. Chem.*, 2016, **89**(12), P. 1930–1936.

[41] Krasilin A.A., Almjasheva O.V., Gusarov V.V. Effect of the structure of precursors on the formation of nanotubular magnesium hydrosilicate. *Inorganic Materials*, 2011, **47**(10), P. 1111–1115.

[42] Proskurina O.V., Nogovitsin I.V., Il'ina T.S., Danilovich D.P., Abiev R.Sh., Gusarov V.V. Formation of BiFeO$_3$ nanoparticles using impinging jets microreactor. *Russian Journal of General Chemistry*, 2018, **88**(10), P. 2139–2143.

[43] Abiev R.S., Almyasheva O.V., Izotova S.G., Gusarov V.V. Synthesis of cobalt ferrite nanoparticles by means of confined impinging-jets reactors. *J. Chem. Tech. App.*, 2017, **1**(1), P. 7–13.

[44] Abiev R.Sh., Al'myasheva O.V., Gusarov V.V., Izotova S.G. Method of producing nanopowder of cobalt ferrite and microreactor to this end. RF Patent 2625981, Bull. 20, 20.07.2017. https://patents.google.com/patent/RU2625981C1/en.

[45] Ashgriz N., Brocklehurst W., Talley D. Mixing mechanisms in a pair of impinging jets. *J. Propul. Power.*, 2001, **17**(3), P. 736.

[46] *Handbook of Atomization and Sprays*. Ed. N. Ashgriz, Toronto, Springer Science Business Media, LLC, 2011. Ch. 30, P. 685.

[47] Erkoc E., Fonte C.P., Dias M.M., Lopes J.C.B., Santos R.J. Numerical study of active mixing over a dynamic flow field in a T-jets mixer – Induction of resonance. *Chem. Eng. Res. Design.*, 2016, **106**, P. 74.

[48] Ravi Kumar D.V., Prasad B.L.V., Kulkarni A.A. Impinging jet micromixer for flow synthesis of nanocrystalline MgO: role of mixing/impingement Zone. *Ind. Eng. Chem. Res.*, 2013, **52**, P. 17376.

[49] Kolodziej P., Yang W.P., Macosko C.W., Wellinghoff S.T. Impingement mixing and its effect on the microstructure of RIM polyurethanes. *J. Polymer Sci. B*, 1986, **24**(10), P. 2359.

[50] Semenov V.G., Moskvin L.N., Efimov A.A. Analytical potential of Mössbauer spectroscopy. *Russian Chemical Reviews*, 2006, **75**(4), P. 317–327.

[51] Gong C., Chen F., Yang Q., Luo K., Yao F., Wang S., Wang X., Wu J., Li X., Wang D., Zeng G. Heterogeneous activation of peroxymonosulfate by Fe–Co layered doubled hydroxide for efficient catalytic degradation of Rhoamdine B. *Chemical Engineering Journal*, 2017, **321**, P. 222–232.

[52] Carvalho D.C., Ferreira N.A., Filho J.M., Ferreira O.P., Soares J.M., Oliveira A.C. Ni–Fe and Co–Fe binary oxides derived from layered doublehydroxides and their catalytic evaluation for hydrogen production. *Catalysis Today*, 2015, **250**, P. 155–165.

[53] Lyubutin I.S., Starchikov S.S., Lin C.-R., Gervits N.E., Korotkov N.Yu., Bukreeva T.V. Structural and magnetic properties of iron oxide nanoparticles in shells of hollow microcapsules designed for biomedical applications. *Croat. Chem. Acta*, 2015, **88**(4), P. 397–403.

[54] Koch C.D. Structures and properties of anionic clay minerals. *Hyperfine Interactions*, 1998, **117**, P. 131–157.

[55] Vasundhara K., Achary S.N., Deshpande S.K, Babu P.D., Meena S.S., Tyagi A.K. Size dependent magnetic and dielectric properties of nano CoFe$_2$O$_4$ prepared by a salt assisted gel-combustion method. *J. Appl. Phys.*, 2013, **113**, P. 194101.

Ultraviolet and visible reflective TiO$_2$/SiO$_2$ thin films on silicon using sol-gel spin coater

S. Saravanan, R. S. Dubey

Advanced Research Laboratory for Nanomaterials & Devices, Department of Nanotechnology,
Swarnandhra College of Engineering & Technology, Narsapur-534 280, West Godavari (A.P.), India

shasa86@gmail.com

TiO$_2$/SiO$_2$ alternative thin films (stacks) were deposited on silicon substrates using sol-gel spin-coating techniques. The prepared samples had their corresponding optical properties analyzed by UV-Visible spectrophotometry (UV-Vis), X-ray diffractometry (XRD), a surface profilometer, and Raman spectroscopy. The optical and crystallization properties of thin films were varied and compared by changing the number of stacks. UV-Vis spectrum showed high reflectance and shifting towards the infrared region with effect of increased TiO$_2$/SiO$_2$ stacks. XRD spectra confirmed the existence of anatase TiO$_2$ and SiO$_2$ diffraction peaks. The multilayer film thickness was calculated at 109 and 151 nm at two and four stacks by a surface profilometer. The Raman spectra confirmed the Si–O–Si and TiO$_2$ stretching modes at 2600, 980, and 519 cm^{-1}. This investigation reveals the promising and effective UV-Visible reflective property of alternative TiO$_2$/SiO$_2$ thin films on a silicon substrate.

Keywords: Sol-gel, reflectance, multilayer, anatase, thickness.

Received: 12 November 2020

Revised: 20 March 2021

1. Introduction

Thin films could find a significant role in various semiconductor industrial applications. Numerous oxide combinations are extensively useful to improve optical (or surface) performance, such as TiO$_2$/SiO$_2$, Al$_2$O$_3$/SiO$_2$, ZnO/SiO$_2$ and ZnO/ZrO$_2$. In solar cells, the highest quantity of light absorption convert is possible by selecting a good combination of anti-reflection coatings materials and synthesis methods. Among the various materials, TiO$_2$/SiO$_2$ has been in demand due to its highest refractive index contrast, good passivity and providing conductive pathway [1, 2]. The formations of various metal oxide thin film and their stabilities determined by the selection of the materials [3]. The metallic coatings on multiple substrates are useful to obtain higher ultraviolet (UV), visible, infrared (IR) reflectance like silver (Ag), aluminium (Al), etc. But, the high maintenance and fabrication cost is a major issue with metallic coatings. The ultraviolet spectral region from 100 to 400 nm and reflection of this wavelength is of great importance to human life, causing the aging of skin, sunburn, etc [4]. The UV reflector is fabricated using atmospheric pressure physical vapor depositions (AP-PVD), sol-gel spin-coating, dip-coating, plasma-enhanced chemical vapor deposition (PECVD), and wet-chemical routes and multistep procedures [5–10]. This proposed work focused on UV and Visible wavelength reflective coatings of TiO$_2$/SiO$_2$ multilayers on a silicon substrate using sol-gel spin-coating methods. Sol-gel spin-coating is the easiest way to synthesize and fabricate One-dimensional photonic crystal (1DPC) layers by tuning the synthesis (precursor concentration, temperature) and fabrication (spin speed, calcined temperature, number of layers) parameters. Venkatesh Yepuri et al. (2020) addressed the process optimization of low-cost and rapid fabrication of TiO$_2$/SiO$_2$ reflectors with 100 % reflectivity. They summarized the desired reflection band of a selected wavelength range observed by changing various parameters such as the precursor concentrations, spin speed (rpm), annealing etc. Finally, the reflection window was observed from the visible to the near infrared region with 2.5 stacks [11]. Dubey et al. (2018) fabricated visible and near-IR wavelength TiO$_2$/SiO$_2$ reflectors using a sol-gel spin coater for various light trapping management applications. The homogeneous, uniform film thickness (56 – 94 nm) and cross-section of TiO$_2$/SiO$_2$ stacks were evidenced by field emission scanning electron microscopy (FESEM). Further, the elemental peaks (Ti, Si, O) and reflectance ($\sim$ 100 %) properties were studied using energy-dispersive X-ray spectroscopy (EDX) and UV-Visible spectrophotometer [12]. Sedrati et al. (2019) fabricated the TiO$_2$/SiO$_2$ Bragg reflectors using the sol-gel dip-coating process. The Raman spectrum confirmed the anatase phase. The UV-Vis-IR range shifted towards the more extended wavelength region with the effect of doping transition metals (copper, nickel, cobalt, and chromium). Also, doping TiO$_2$ showed enlarged stop-band of TiO$_2$/SiO$_2$ Bragg reflectors and enhanced optical properties [13]. Zhao et al. (2019) investigated the mesoporous SiO$_2$ and SiO$_2$-TiO$_2$ thin films prepared by the sol-gel method. The Raman spectrum confirmed the anatase TiO$_2$ phase, and the UV-vis reflectance spectrum shifted towards the more extended wavelength region with the effects of transition doped metals [14]. Dubey et al. (2017) fabricated TiO$_2$/SiO$_2$ Bragg reflectors for light trapping applications using a cost-effective and straightforward sol-gel spin coating method. UV-Vis spectrum showed 90 % reflectance at 617 nm using seven distributed Bragg reflectors

(DBR) stacks based structure, and the FESEM image confirmed alternative layers of one-dimensional TiO_2 and SiO_2 thin films. This DBR structure integrated solar cell design significantly enhanced light absorption [15].

This paper deals with the optical and structural properties of TiO_2 (anatase and rutile) and SiO_2 multilayers fabricated on silicon substrates using a sol-gel spin-coater. In the second section we describe the synthetic process and fabrication of thin-film TiO_2/SiO_2 structures. UV-Vis, XRD, Raman spectroscopy results are discussed in section third and summarized the work in the fourth section.

2. Experimental approach

Synthesis and fabrication procedural steps of TiO_2/SiO_2 thin films are shown in Fig. 1. Titanium butoxide (TBOT, $Ti(OBu)_4$), tetraethyl orthosilicate (TEOS, $Si(OC_2H_5)_4$), methanol (CH_3OH), acetic acid (CH_3COOH), and deionized water (DI) are the starting chemicals used without any additional purification. For the preparation of TiO_2 and SiO_2 solutions, $Ti(OBu)_4$: CH_3OH: CH_3COOH: DI and $Si(OC_2H_5)_4$:CH_3OH: CH_3COOH in the ratios of 1.2:20:1.7 and 1.5:20:2.3 respectively.
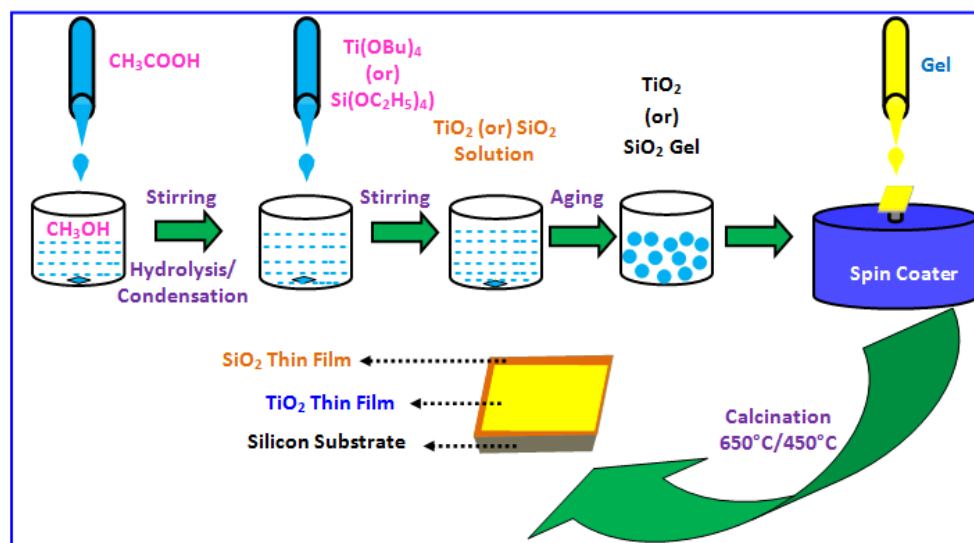

FIG. 1. The sol-gel synthesis of TiO_2 and SiO_2 thin film processing step

Initially, 1.2 ml acetic acid added in methanol (20 ml) and stirred for 5 minutes using a magnetic stirrer at room temperature. Titanium butoxide solution added drop-wise and stirring maintained for 90 minutes at room temperature (28 °C). Finally, TiO_2 solution (solution 'A') appears transparent color and was aged for 24 hrs. Next, 1.5 ml acetic acid was mixed with 20 ml methanol and stirred for five minutes with the continued dropwise addition of tetraethyl orthosilicate (2.3 ml) at 2 minutes intervals. The prepared SiO_2 solution was continuously stirred at 90 minutes (solution 'B') and aged 24 hrs. Before the deposition process, substrates were cleaned at room temperature by ultrasonication process using DI water, ethanol, and aqueous hydrofluoric (HF) acid. Using spin-coater, the alternative coating of TiO_2 and SiO_2 solution deposition coated on the glass substrates at 3000 rpm/30 sec. After the coating, thin film samples were calcined at 650 °C (TiO_2) and 450 °C (SiO_2) for 1 hour. Further, analyses were performed using the following instruments: X-ray diffractometer (XRD, Bruker D8 Advance), UV-visible spectrophotometer (UV-Vis, 1800 Shimadzu), and Surface Profilometer (SJ-301 Mitutoyo). Raman spectroscopy (micro Raman) was also used to study their optical properties.

3. Results and discussion

Figure 2 shows the reflectance spectra of 2-TiO_2/SiO_2 stacks (S1) and 4-TiO_2/SiO_2 stacks (S2) by UV-Visible spectrophotometry. Here, one alternating layer of TiO_2 and SiO_2 thin film is known as a stack. The obtained results show the high reflectance and shifted towards the longer wavelength region due to the increment of stacks. Similarly, Dubey et al. (2017) reported improved reflectance with the effect of an increased number of coating layers [15].

The enhanced reflectance could be possible in the whole UV-Visible spectrum due to the large refractive index contrast between TiO_2 and SiO_2 layers, as reported by Zhang et al. (2006) [16]. Significantly, the TiO_2 thin films could increase the reflectance in the visible and infra-red region as reported by Dalapati et al. (2015) [17]. Fig. 3 depicts
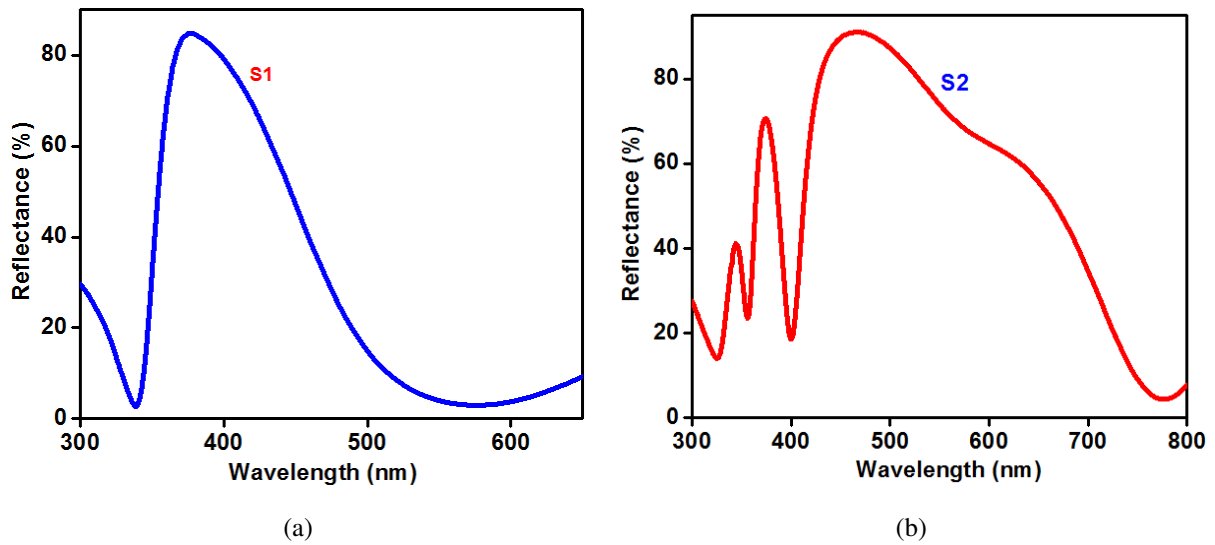
(a)   (b)

FIG. 2. Reflectance spectra of two (S1) and four (S2) stacks of TiO$_2$/SiO$_2$ thin films prepared on Si substrates

the reflectance (UV-visible) fullwidth half maximum (FWHM) of samples S1 and S2 corresponding enhancement 103 and 267 nm. Here, the FWHM enhancement $\sim$ 267 nm achieved by the highest deposition layers of silicon substrate. Saravanan et al. (2019) reported work revealed the enhanced FWHM concerning the increment of stacks, and this reflectance is mainly dependent on the thickness and surface of the structure [18]. Consequently, surface profilometer techniques revealed the sample thickness of 120 nm (S1) and 160 nm (S2).
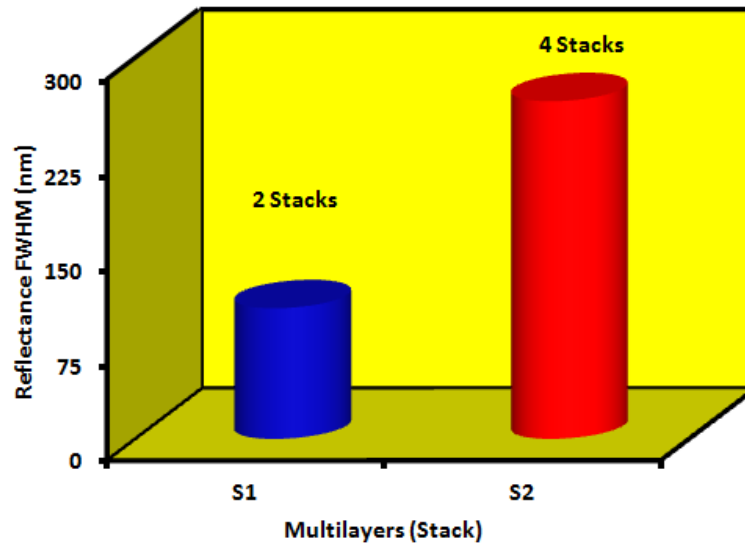
FIG. 3. Full-width half maximum (FWHM) of S1 (2 stacks) and S2 (4 stacks)

The XRD pattern can provide the structural parameters for TiO$_2$/SiO$_2$ thin films by varying the number of stacks (2-S1 and 4-S2), as shown in Fig. 4(a,b). At room temperature, thin films were fabricated which were attributed to the anatase and rutile mixed phase. The XRD patterns of the samples were noticed with the same nature. The obtained Bragg's diffraction peaks at $2\theta = 25.36°$ (A), $28.8°$ (R), $37.52°$ (A), $41.9°$ (A), $47.48°$ (A) and $53.99°$ (R) which is corresponding planes (101), (111), (004), (111), (200) and (211) respectively [11, 19]. Here, A and R are denoted as anatase and rutile peaks for our convenience. From both diffraction spectra, the intense diffraction peak noticed and confirmed the presence of anatase TiO$_2$ and well-matched with JCPDS#21-1272 [20–22]. The rutile diffraction can be assigned to the ICDD card #00-001-1292 and 01-072-4813. The highest TiO$_2$ thin film calcination temperature (650 °C) provides the rutile phase formation. Both XRD pattern, the broad and low intense peak envelope appeared

FIG. 4. XRD spectra of TiO_2/SiO_2 thin films (a) 2-stacks, S1 and (b) 4-stacks, S2

at $23°$, which is attributed to the existence of amorphous silica in the prepared samples [19, 23]. Finally, the impurities were not presented.

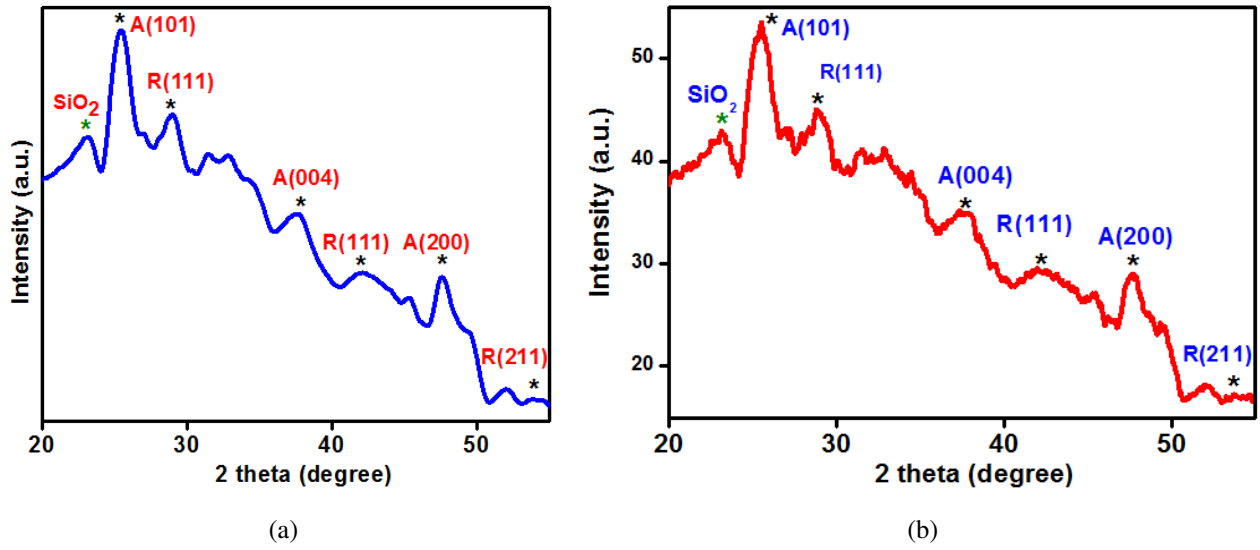Using the Debye–Sherrer formula, the crystalline size can be calculated, $(D = k\lambda/\beta\cos\theta)$, where D is the crystalline size, k is the numerical factor (0.9) referred to as the crystallite shape, λ is the X-ray incident wavelength (1.5406 Å), β is the full-width at half maximum (FWHM), and θ is the diffraction angles [24, 25]. Table 1 shows the calculated crystallite size of the samples.

TABLE 1. The crystallite size of TiO_2/SiO_2 multilayers on silicon

S.N.	Sample (TiO_2/SiO_2)	Peak positions (2θ) degree	FWHM (2θ)	Crystallite Size (nm)
1	S1 (Anatase-TiO_2)	61.75	0.1476	62.71
2	S2 (Anatase-TiO_2)	61.74	0.1476	62.70

Raman scattering is useful to identify (phase) the structural modification in 650 and 450 °C thermally treated thin film structures. Fig. 5 shows the Raman spectrum of the TiO_2/SiO_2 thin film with highest and broader intensity peaks within the range 0 to 3000 cm^{-1}. The micro Raman spectroscopy consists of the excitation wavelength, $\lambda = 785$ nm. Both spectral (S1 & S2) results showed the same nature of the spectrum by varying intensity of the peaks. First, the sharp peak at 519 cm^{-1} indicates the originating from the silicon (Si) substrate. For our convenience, Anatase, rutile, and silicon dioxide Raman modes were denoted as A, R, and S respectively. The vibrational bands of anatase TiO_2 material has centered at 137, 207, 414, 519 and 644.8 cm^{-1}, respectively, corresponding to the Raman active modes of Eg, Bg, B1g, A1g, and Eg as showed in inserted Fig. 5 [26, 27]. It can be concluded that strong anatase peak at 137 cm^{-1}. Accordingly, the normal vibrational mode of anatase bands is $\Gamma A = 2Eg + 2Bg + B1g + A1g$. The rutile TiO_2 phase identified at 238 (Eg), 450, 612. Similarly, silicon dioxide presented at 233, 333, 488 and 600 cm^{-1}. The Raman spectrum of SiO_2 had a weak peak ~ 980 cm^{-1} which was attributed to the bending of Si–O–Si symmetric bond stretching [28, 29]. Finally, the broad peak at 2600 cm^{-1} indicates the presence of SiO_2. This existence of broader peaks in the Raman spectrum attribute to the electronic Raman scattering mechanism [30–32].

4. Conclusions

TiO_2/SiO_2 thin films were deposited on silicon substrates using sol-gel and spin-coating techniques. The optical properties of thin films have been studied by UV-Vis, XRD and Raman spectroscopy. UV-Vis spectroscopy showed reflectance enhancement as an effect when increasing the number of stacks. XRD and Raman spectra revealed the presence of anatase TiO_2 and amorphous silica phase in both samples. Using a surface profilometer, the thin-film
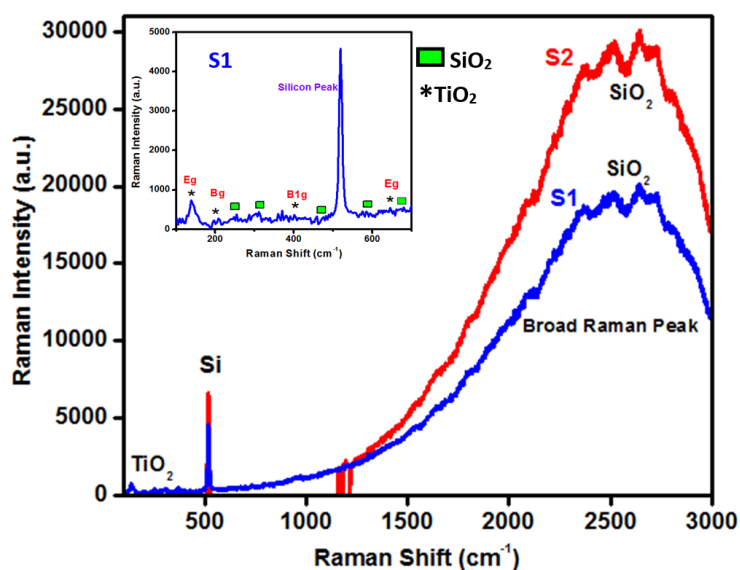
FIG. 5. Raman spectra of TiO$_2$/SiO$_2$ multilayer two stacks (S1) and four stacks (S2)

thickness of 120 nm (2 stacks) and 160 nm (4 stacks) calculated. Further, changing various parameters with optimization results will be useful for various novel applications, including solar cells, light-emitting diodes, the bandpass filters and lasers.

Acknowledgements

References

[1] Park N.G., van de Lagemaat J., Frank A.J. Comparison of dye-sensitized rutile- and anatase based TiO$_2$ solar cells. *J. Phys. Chem. D*, 2000, **104**, P. 8989–8994.

[2] Eframoktora R.G. Nelwan, Suliyandi M.M., Prastomo N. Fabrication of anti-reflection coating TiO$_2$-SiO$_2$ on silicon substrate with pulsed laser deposition method. *Proc. SPIE*, 2019, Third International Seminar on Photonics, Optics and Its Applications (ISPhoA 2018), 11044N.

[3] Kirillova S.A., Almjashev V.I., Gusarov V.V. Spinodal decomposition in the SiO$_2$-TiO$_2$ system and hierarchically organized nanostructures formation. *Nanosystems: Physics, Chemistry, Mathematics*, 2012, **3** (2), P. 100–115.

[4] Ortiz A.A., Yan B., D'Orazio J.A. Ultraviolet radiation, aging and the skin: Prevention of damage by topical cAMP manipulation. *Molecules*, 2014, **19** (5), P. 6202–6219.

[5] Chemin J.B., Bulou S., et al. Transparent anti-fogging and self-cleaning TiO$_2$/SiO$_2$ thin films on polymer substrates using atmospheric plasma. *Scientific Reports*, 2018, **8**, P. 1–8.

[6] Mao Q., Zeng D., Xu K., Xie C. Fabrication of porous TiO$_2$-SiO$_2$ multifunctional anti-reflection coatings by sol-gel coating method. *RSC Advances*, 2014, **101**, P. 58101–58107.

[7] Dembele A., Rahman M., et al. Deposition of hybrid organic-inorganic composite coatings using an atmospheric plasma jet. system. *J. Nanosci. Nanotechnol.*, 2011, **11**, P. 8730–8737.

[8] Liu F., Shen J., et al. In situ growth of TiO$_2$/SiO$_2$ nanospheres on glass substrates via solution impregnation for antifogging. *RSC Advances*, 2017, **7**, P. 15992–15996.

[9] Li X., He J. Synthesis of raspberry-Like SiO$_2$-TiO$_2$ nanoparticles toward antireflective and self-cleaning coatings. *ACS Appl. Mater. Interface*, 2013, **5**, P. 5282–5290.

[10] Saxena N., Naik T., Paria S. Organization of SiO$_2$ and TiO$_2$ nanoparticles into fractal patterns on glass surface for the generation of superhydrophilicity. *J. Phys. Chem. C*, 2017, **121**, P. 2428–2436.

[11] Venkatesh Y., Dubey R.S., Kumar B. Rapid and economic fabrication of dielectric approach of dielectric reflectors for energy harvesting applications. *Scientific Reports*, 2020, **10**, P. 1–9.

[12] Dubey R.S., Ganesan V. Visible and near-infrared wavelength-selective dielectric reflectors for light management applications. *Superlattices Microstruct.*, 2018, **122**, P. 228–234.

[13] Sedrati H., Benachour M.C., Dehdouh H., Bensaha R. Tuning of the stop-band position in the visible range of SiO$_2$/TiO$_2$ Bragg reflectors by doping TiO$_2$ with transition metals. *Optik*, 2019, **208**, 164098-1-6.

[14] Zhao W., Jia H., et al. Design and realization of antireflection coatings for the visible and the infrared based on mesoporous SiO$_2$ and SiO$_2$-TiO$_2$ hybrid materials. *Appl. Opt.*, 2019, **58** (9), P. 2385–2392.

[15] Dubey R.S., Ganesan V. Reflectance modulation using SiO$_2$/TiO-multilayer structures prepared by sol-gel spin coating process for optical applications. *Superlattices Microstruct.*, 2017, **111**, P. 1099–1103.

[16] Zhang X., Fujishima A., Jin M., Emeline A.V., Murakami T. Double-layered TiO$_2$-SiO$_2$ nanostructured films with self-cleaning and antireflective properties. *J. Phys. Chem. B*, 2006, **110**, P. 25142–25148.

[17] Dalapati G.K., Panah S.M., et al. Color tunable low cost transparent heat reflector using copper and titanium oxide for energy saving application. *Scientific Reports*, 2015, **6**, P. 1–14.

[18] Saravanan S., Dubey R.S. Fabrication and characterization of TiO$_2$/SiO$_2$ multilayers using sol-gel spin coating method. *Nanosystems: Physics, Chemistry, Mathematics*, 2019, **10** (1), P. 63–69.

[19] Wu Z.G., Jia Y.R., et al. Core-shell SiO$_2$/Ag composite spheres: synthesis, characterization and photocatalytic properties. *Materials Science – Poland*, 2016, **34** (4), P. 806–810.

[20] Venkatesh Y., Dubey R.S., Kumar B. Morphological and optical properties of dielectric multilayer structures prepared with distinct precursor concentrations. *Nanosystems: Physics, Chemistry, Mathematics*, 2019, **10** (3), P. 355–360.

[21] Dubey R.S., Krishnamurthy K.V., Singh S. Experimental studies of TiO$_2$ nanoparticles synthesized by sol-gel and solvothermal routes for DSSCs application. *Results in Physics*, 2019, **14**, 102390-1-6.

[22] Sedrati H., Bensaha R., et al. Correlation between structural and optical properties of SiO$_2$/TiO$_2$ multilayers processed by sol-gel technique and applied to Bragg reflectors. *Materials Science*, 2013, **9** (3), P. 113–118.

[23] Xue C., Zhang Q., et al. High photocatalytic activity of Fe3O4-SiO$_2$-TiO$_2$ functional particles with core-shell structure. *Journal of Nanomaterials*, 2013, 762423.

[24] Wardiyati S., Adi W.A., Deswita. Synthesis and characterization of microwave absorber SiO$_2$ by sol-gel method. *IOP Conf. Ser.: Mater. Sci. and Eng.*, 2017, **202**, P. 1–8.

[25] Monshi A., Foroughi M.R., Monsh M.R. Modified Scherrer equation of reaction of reaction to estimate more accurately nano-crystallite size using XRD. *World Journal of Nano Science and Engineering*, 2012, **2**, P. 154–160.

[26] Zhu X., Gu P., et al. Influence of substrate on structural, morphological and optical properties of TiO$_2$ thin films deposited by reaction magnetron sputtering. *AIP Advances*, 2017, **7**, 125326-1-8.

[27] Barimah E.K., Jones R.P., et al. Phase evolution, morphological, optical and electrical properties of femtosecond pulsed laser deposited TiO$_2$ thin films. *Scientific Reports*, 2020, **10**, P. 1–12.

[28] Lari N., Ahangarani S., Shanaghi A. Effect of different TiO$_2$-SiO$_2$ multilayer coatings applied by sol-gel method on antireflective property. *J. Mater. Eng.*, 2015, **24** (7), P. 2645–2652.

[29] Nezar S., Saoula N., et al. Properties of TiO$_2$ thin films deposited by RF reactive magnetron sputtering on biased substrates. *Appl. Surf.*, 2017, **395**, P. 172–179.

[30] Klein M.V. *Light Scattering in Solids I, Topics in Applied Physics*, Springer Berlin, Heidelberg, Germany 1983.

[31] Rosales A., Maury-Ramirez A., Det al. SiO$_2$-TiO$_2$ coating: synthesis, physical characterization and photocatalytic evaluation. *Coatings*, 2018, **8** (4), P. 1–13.

[32] Popovic D.M., Milosavljevic V., et al. Raman scattering analysis of silicon dioxide single crystal treated by direct current plasma discharge. *Appl. Phys. Lett.*, 2011, **98**, 051503-1-3.

Investigation of the effect of zinc precursors onto structural, optical and electrical properties of CBD deposited ZnS thin films

Rajeshkumar P Khatri[1], Amitkumar J Patel[2]

[1]Department of Physics, Gujarat Technological University, Ahmedabad 382424, Gujarat, India
[2]Department of Applied Science, Faculty of Physics, Government Engineering College, Godhra, Panchmahal 389001, Gujarat, India

rajukhatri_222@yahoo.co.in

Zinc sulfide (ZnS) thin films were deposited onto microscopic silica slides through the cost-effective chemical bath deposition (CBD) method. The optimized bath parameters were: 25 ml of 0.1 M zinc precursors ($ZnCl_2$, $Zn(CH_3COO)_2$, $ZnSO_4$), 25 ml of 1 M thiourea and 3 ml of 3.75 M triethanolamine (TEA). The effects of different zinc precursors ($ZnCl_2$, $Zn(CH_3COO)_2$, $ZnSO_4$) on the growth mechanism of ZnS thin film were investigated using thermal, structural, morphological, optical and electrical studies. The XRD pattern has shown Miller indexing peaks corresponding to the hexagonal phase of as-grown ZnS thin film with the estimated grain size of $22 - 27$ nm. The change in physical properties (weight loss) of ZnS powder as a function of temperature was recorded using thermogravimetry (TGA/DTA). Scanning electron microscopy (SEM) revealed the effect of $ZnCl_2$, $Zn(CH_3COO)_2$ and $ZnSO_4$ precursors on growth mechanism. UV/visible optical transmission/absorption spectra displayed the transmittance between 10 to 29 % of as-grown ZnS thin film with a band gap in the range of $4.10 - 4.25$ eV. Photoluminescence (PL) analyses demonstrated broad blue emission around ~ 459 nm was attributed to recombination of electron-hole pair from donor-acceptor trap levels to valance band. Raman spectra of ZnS powder prepared using different zinc precursors were also reported. The values of electrical parameters (resistivity, conductivity, activation energy, Hall coefficient, carrier concentration, mobility) were investigated using the two-point probe method and Hall-effect apparatus.

Keywords: ZnS thin films, chemical bath deposition, zinc precursors.

Received: 20 January 2021

Revised: 22 April 2021

Final revision: 26 May 2021

1. Introduction

Zinc sulfide (ZnS) is the most promising material in the field of sensors [1], solar cell [2] and bio-imaging [3]. It is a wide band gap semiconductor that serves as host materials for various kinds of dopant for luminescence application [4]. In view of the above technological importance, several researchers have made efforts to tailor the physical properties of ZnS thin films using variation in thickness [5], molar concentration [6], heat treatment [7], bath temperature [8] and other possible means. Earlier, M. Cao, et al. [9] and T. Liu, et al. [10] investigated the effect of different zinc salts on crystallographic, morphology and optical properties of CBD deposited ZnS thin films. In earlier reported literatures, there has not been enough investigation with the effect of zinc precursors on the physical properties of ZnS thin films.

ZnS thin film has been developed by various researchers using different chemical and physical deposition methods such as Thermal evaporation [11], Metal-organic chemical vapor deposition (MOCVD) [12], Successive ionic layer adsorption and reaction (SILAR) [13], Chemical bath deposition [14], etc. Among these deposition methods, CBD is simple, cost-effective and ideal for large scale deposition [15]. Using this CBD method, a thin film can be deposited nearly at room temperature through a controlled chemical reaction.

In the present work, authors have tried to deposit CBD-ZnS thin film using triethanolamine (TEA) as a complexing agent since it is a much safer alternative compare to hydrazine hydrate [16]. Moreover, the researchers have investigated the effect of different zinc precursors ($ZnCl_2$, $Zn(CH_3COO)_2$, $ZnSO_4$) on structural, morphological, optical and electrical properties of CBD deposited ZnS thin films.

2. Experimental method

All reagents were received from Fisher Scientific and used without further processing. A high-quality silica slide having dimensions $75 \times 26 \times 1$ mm^3 is used as substrate. The cleaning procedure and detailed process of film deposition are reported in our earlier literature [17]. The only difference in the present work is that we deposited three different samples using three different precursors instead of zinc chloride, as reported in earlier work. The optimized molar concentration and volume of precursors for the growth of ZnS thin films are listed in Table 1. The pre-cleaned silica substrate is inserted vertically into the reaction bath. The bath temperature was adjusted to 70 °C and deposition was carried for 2 hours. The simplified layout of the chemical bath deposition method is represented in Fig. 1.

TABLE 1. Molar concentration and volume of precursors for the growth of ZnS thin films by CBD method

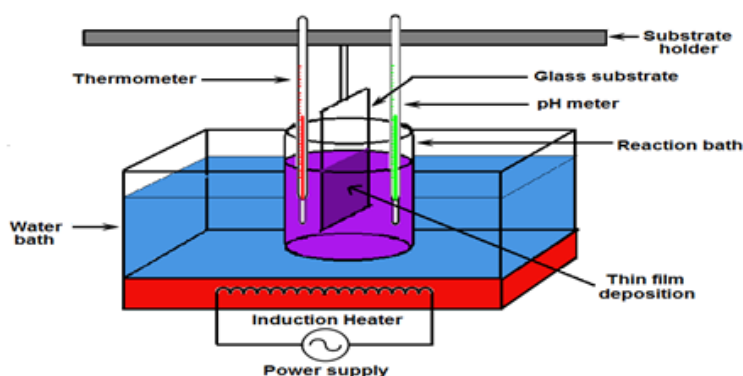| Thin film	Molar concentration and volume of precursors			
	zinc precursor	thiourea	Triethanolamine (TEA)	Ammonia
ZnS–Cl	25 ml of 0.1 M ZnCl$_2$	25 ml of 1 M	3 ml of 3.75 M	2 ml of 13.4 M
ZnS–Ac	25 ml of 0.1 M Zn(CH$_3$COO)$_2$	25 ml of 1 M	3 ml of 3.75 M	2 ml of 13.4 M
ZnS–SO	25 ml of 0.1 M ZnSO$_4$	25 ml of 1 M	3 ml of 3.75 M	2 ml of 13.4 M

FIG. 1. Simplified layout of Chemical Bath Deposition Method

After the deposition, the film is taken out from the bath and dipped into de-ionized water to remove loosely bound ZnS powder that adheres to the film. ZnS thin films deposited using ZnCl$_2$, Zn(CH$_3$COO)$_2$ and ZnSO$_4$ were labeled as ZnS–Cl, ZnS–Ac and ZnS–SO, respectively for the sake of analysis.

The deposited ZnS thin films were analyzed using various instruments without annealing treatment. The alteration in physical properties as a function of temperature was obtained using thermogravimetry (METTLER TOLEDO). The Miller indices (h k l) for diffracting planes for the given structure of the thin film was evaluated by grazing incident X-ray diffraction (GIXRD) spectrometer (PANalytical Empyrean) using CuKα radiations (wavelength = 0.15406 nm) for 2θ values over $20 - 60°$. X-ray was impinging at angle $0.5°$ and a detector was moving in the step of $0.01°$ with a collection time of 7 s. The surface morphology was characterized using the field emission scanning electron microscope (JEOL JSM-6010LA). The stoichiometric composition of films was analyzed by energy dispersive X-ray analysis (EDX) using an EDX detector which is available as an add-on attachment with the scanning electron microscope (JEOL JSM-5610LV) with Inca software. In order to find the permitting light wavelengths for thin films, transmission/reflectance spectra were recorded as a function of wavelengths using UV/VIS/NIR spectrophotometer (Perkin Elmer Lambda 19). The Raman scattering measurement (vibrational phonon modes) was investigated at room temperature using a Raman microscope (RENISHAW Invia) with 514 nm (20 mW) argon ion excitation source. Photoluminescence spectra were registered with Perkin Elmer spectro-fluoro-photometer using 280 nm excitation wavelength. A self-made two probe resistivity measurement equipment and Hall-effect apparatus were used to find the correlation between different electrical parameters.

3. Results and discussion

3.1. Thermal analysis

In order to perform thermal analysis of the obtained samples, the as-deposited ZnS powders are collected by scratching the surface of deposited silica substrates. The analysis of the thermal behavior of scratched as-deposited ZnS powders were carried out using differential thermal analysis (DTA) and thermogravimetric analysis (TGA) in an ambient environment with temperature in the range of 30 – 900 °C. During measurements, the temperature was increased at a rate of 30 °C/min. DTA and TGA curves for ZnS–Cl, ZnS–Ac, and ZnS–SO powder are shown in Fig. 2.
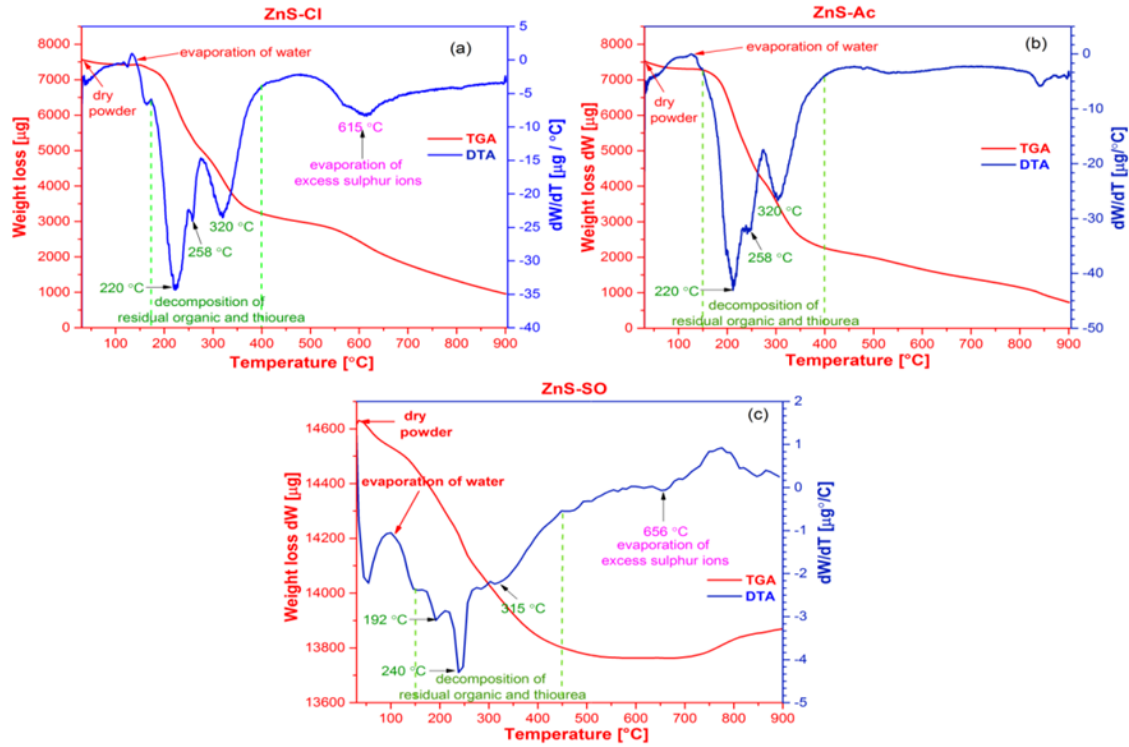

FIG. 2. TGA and DTA curves for ZnS powders grown by CBD method using different zinc precursors: (a) ZnS–Cl; (b) ZnS–Ac (c) ZnS–SO

The TGA curve indicates that all the as-grown samples of ZnS lose weight from 30 to 150 °C as a result of absorbed water vapor evaporation. The decomposition of residual organics and TEA leads to second weight loss between 150 – 450 °C. It is also confirmed by a series of endothermic peaks between temperature ranges 150–450 °C in DTA sketches, as shown in Fig. 2. The endothermic peak at 615 °C in the case of ZnS–Cl and 656 °C in the case of ZnS–SO could be attributed to the evaporation of excess residual sulfur ions from the sample [18].

3.2. Structural analysis

The structural information of ZnS thin film was obtained using grazing incident X-ray diffraction (GIXRD) with CuKα radiation with scan range 20 – 60°. GIXRD can reduce the signal contribution from the substrate and improve the signal from the thin film. X-ray diffractogram of as-grown ZnS thin film prepared using different zinc precursors (ZnCl$_2$, Zn(CH$_3$COO)$_2$ and ZnSO$_4$) are shown in Fig. 3.

The peaks at 2θ values 31.64°, 34.53°, 36.20°, 47.45° and 56.48° are diffraction angles for planes with Miller indices (1 0 4), (1 0 6), (0 0 10), (1 1 0) and (1 1 8) which satisfies Bragg's equation. The plane (0 0 10) consists more number of atoms resulted in the highest intensity peak. Comparing observed peaks with JCPDS card No. 39-1363 assures hexagonal phase of ZnS thin film.

The particle size of ZnS thin films deposited using different zinc precursors were calculated using the Debye–Scherrer formula as [19]:

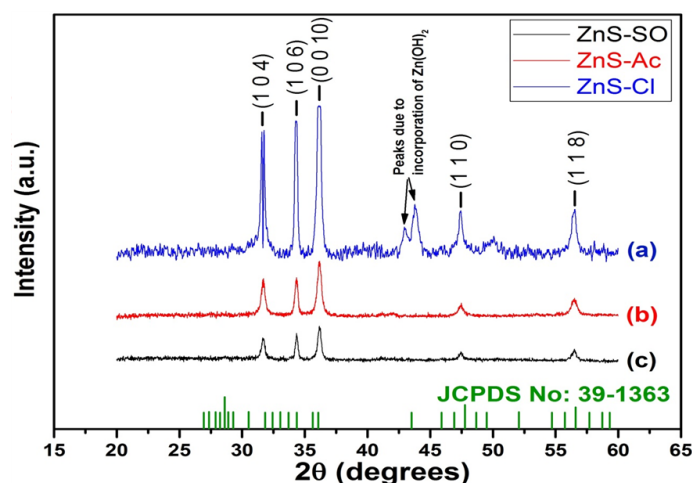$$D = \frac{0.94\lambda}{\beta \cos \theta}, \tag{1}$$

FIG. 3. X-ray diffractogram for as-grown ZnS thin films deposited using different zinc precursors:
(a) ZnS-Cl; (b) ZnS-Ac;(c) ZnS-SO

where D is particle size, λ is the wavelength of incident X-ray generally its value is 0.15406 nm for CuKα radiation, β is full width at half maximum (FWHM) for the peak of the plane with Miller indices (h k l) and θ is the angle between the incident beam and (h k l) plane. The particle sizes of as-grown ZnS thin film deposited using different zinc precursors onto the silica substrate are listed in Table 2. From X-ray diffractogram and particle size analysis, it is clearly observed that anions associated with zinc precursors play an important role in the growth chemistry of ZnS thin films. The intermolecular interactions between anions and intermediate complex precursors decide heterogeneous or homogenous growth mechanism for ZnS film growth [10]. In our case, the Cl$^-$ anions favor heterogeneous (ions by ions) growth mechanism and improve the crystallinity of ZnS thin films while SO$_4^{-2}$ and CH$_3$COO$^-$ anions follow homogeneous (clusters by clusters) or mixed growth mechanism for ZnS thin film formation on silica slide. Moreover, two extra peaks are observed in the case of ZnS–Cl thin film at 42.93 and 43.87$°$, which are likely due to the incorporation of Zn(OH)$_2$ into the film during the growth process [20, 21]. In this case, ZnS film could be formed by the decomposition of thiourea over the surface of intermediate hydroxide cluster Zn(OH)$_2$ rather than nucleate separately in the solution.

TABLE 2. Particle size, thickness, transmittance and band gap of as-grown ZnS thin films deposited using different zinc precursors

Thin film (ZnS thin film)	Particle size (nm)	Thickness (μm)	Avearge Transmittance T (%) ($\lambda > 350$ nm)	Band gap (eV)
ZnS–Cl	27	37 ± 0.2	29	4.10
ZnS–Ac	25	39 ± 0.3	25	4.17
ZnS–SO	22	41 ± 0.2	10	4.25

The thickness of ZnS thin films deposited using different zinc precursors was predicted using the transverse view of SEM images, which are presented in Fig. 4. The observed values of thickness are listed in Table 2. It is apparently clear that the thickness of ZnS thin films was greatly affected by growth rate and hence liberated anions from zinc precursors in solution during growth mechanism.

In order to investigate the effect of zinc precursors onto the surface morphology of as-grown ZnS thin film, micrographs of films were recorded using scanning electron microscope which is shown in Fig. 5. In general, the films deposited by chemical route have uncontrolled growth rate resulted in non-uniform surface.

In the present research, ZnS thin films acquire rough surfaces due to uneven grain growth in different directions. Fig. 5(a) shows ZnS–Cl film has a smooth, compact surface with reduced grain boundaries than other films. The reduction of grain boundaries has a considerable effect on the carrier drift velocity of materials [22]. Fig. 5(c) shows
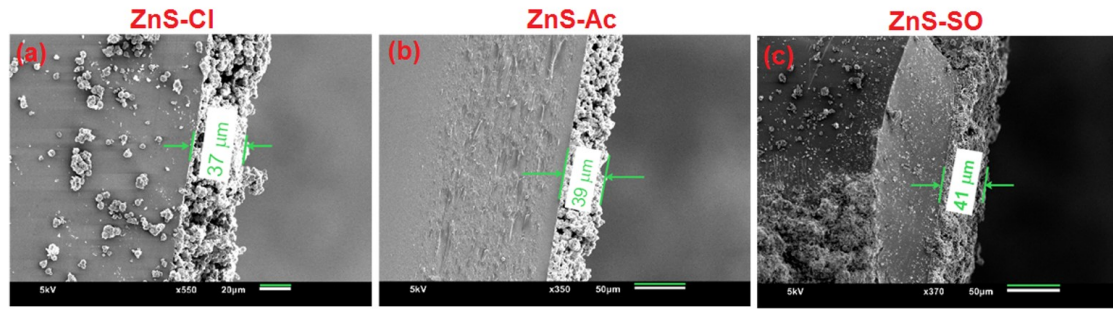
FIG. 4. Transverse view of SEM images for as-grown ZnS thin films deposited using different zinc precursors: (a) ZnS-Cl; (b) ZnS-Ac; (c) ZnS-SO
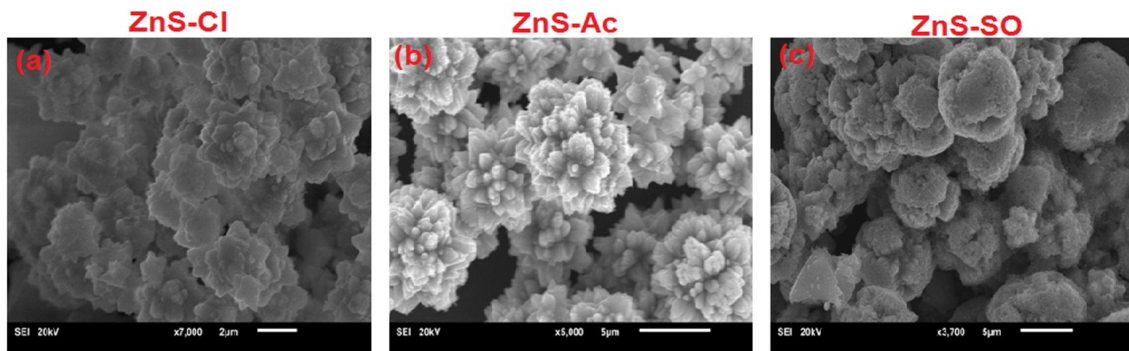

FIG. 5. SEM micrograph of as-grown ZnS thin films deposited using different zinc precursors: (a) ZnS-Cl; (b) ZnS-Ac; (c) ZnS-SO

ZnS–SO films formed by significant spherical clusters with relatively less dense morphology. The reason for this is SO_4^{-2} anions promote homogeneous (clusters by clusters) growth mechanism and ZnS clusters from solution adhere on a silica substrate. Fig. 5(b) shows ZnS–Ac film is relatively less compact than ZnS–Cl with flower-like morphology. In this case, CH_3COO^- anions promote a mixed growth mechanism in the solution for deposition of ZnS thin films.

3.3. Compositional analysis

The elemental composition of ZnS films deposited onto the silica substrate using different zinc precursors was analyzed using EDX spectra and is shown in Fig. 6. The obtained results are listed in Table 3. Because of the low thickness of films and high depth profile of EDX spectrometer, other elements from silica substrate such as O, Mg, Si, and Ca are also detected in the EDX spectra. As seen from Table 3, the atomic ratios of Zn/S are slightly higher than 1 which indicates that the obtained ZnS films are rich in zinc and deficient in sulfur. The difference in the Zn/S ratio is ascribed to different growth mechanisms involved during film formation. The presence of excess zinc in the case of ZnS–Cl films could be due to the presence of $Zn(OH)_2$ [9, 10], which is consistent with our XRD results.

TABLE 3. Elemental composition of as-deposited ZnS thin films from EDX spectra

Thin film	Zn (at %)	S (at %)	Other elements (at %)	Zn/S atomic ratio
ZnS–Cl	26.22	22.74	51.04	1.15
ZnS–Ac	25.38	22.58	52.04	1.12
ZnS–SO	24.71	22.45	52.84	1.10

FIG. 6. EDX spectra of as-grown ZnS thin films deposited using different zinc precursors: (a) ZnS-Cl; (b) ZnS-Ac; (c) ZnS-SO

3.4. Optical analysis

The thickness and uniformity of film play a vital role in controlling optical properties like transmittance, absorbance, refractive index, etc. [23]. A film with higher uniformity and the least thickness leads to the high transmission with a sharp absorption edge [24]. Moreover, the energy band gap of the film can be determined from transmission spectra [23].

In the direction to know the effect of zinc precursors on the optical behavior of as-grown ZnS thin films, transmittance and reflectance spectra were noted using UV/VIS/NIR spectrophotometer. Fig. 7 shows the percentage of transmittance and absorbance of CBD-deposited as-grown ZnS thin films with zinc precursor variation. The highest transmittance is observed in ZnS–Cl thin film and lowest in ZnS–SO thin film. It shows low absorption above 350 nm wavelength and abrupt absorption at $\sim$ 310 nm wavelength for all ZnS thin films.

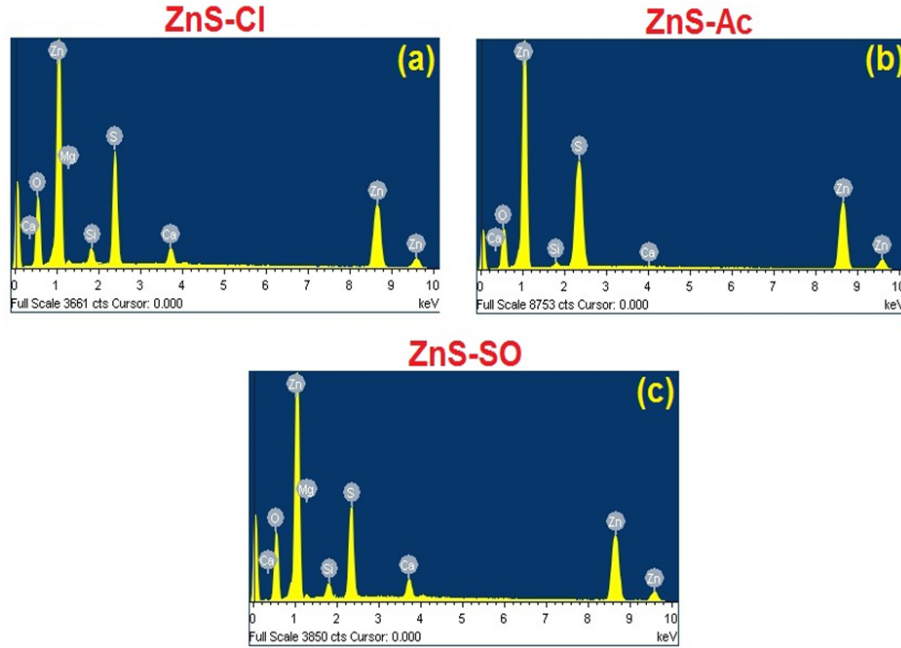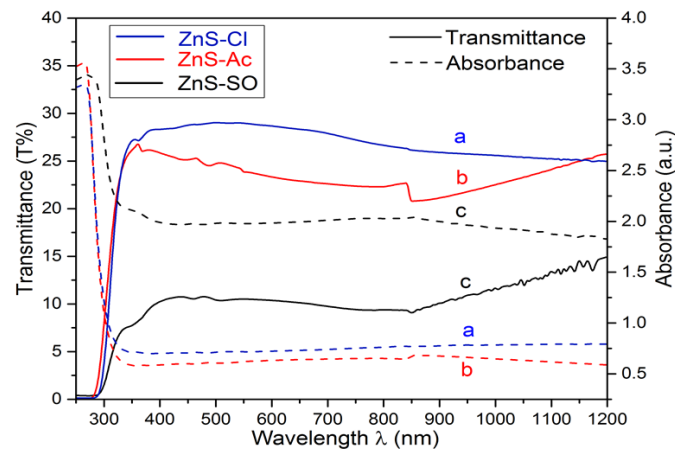FIG. 7. UV/visible transmittance and absorbance spectra of as-grown ZnS thin films deposited using different zinc precursors: (a) ZnS-Cl; (b) ZnS-Ac; (c) ZnS-SO

Once Transmission/Reflectance data were registered with respect to wavelength, the optical energy band gaps of thin films were evaluated with the help of the formula derived from the theory of inter-band transition of the

semiconductor. The absorption coefficient (α) was determined from absorbance (A) and film thickness (t) by using the relation [25, 26]:

$$\alpha = \frac{2.303 \cdot A}{t}. \tag{2}$$

The theory of inter-band transition shows that at the optical absorption edge, the absorption coefficient (α) varies with the photon energy hν according to [23]:

$$\alpha h\nu = A(h\nu - E_g)^n, \tag{3}$$

where E_g is the optically forbidden energy gap, A is constant and the exponential factor $n = 1/2, 1, 2, 3$ depending on the type of electronic transition in k-space [26]. For direct band gap semiconductor, the exponential factor has value 0.5 and for indirect band gap semiconductor, it has a value of 2. Since ZnS is a direct band gap material, the value of n becomes 0.5:

$$(\alpha h\nu)^2 = A^2(h\nu - E_g). \tag{4}$$

Figure 8 represents the plot of $(\alpha h\nu)^2$ versus $h\nu$ for as-grown ZnS thin film deposited from different zinc precursors. The film's band gap value is obtained by extrapolating the straight-line portion of curves to $\alpha h\nu = 0$ using a computer fitting program in which the intercept value of $h\nu$-axis is band gap value. The calculated band gaps (E_g) for as-grown ZnS films are listed in Table 2. The estimated band gap value of ZnS–Cl, ZnS–Ac and ZnS–SO thin films are found to be 4.10, 4.17 and 4.25 eV, respectively. The tabulated band gap values of ZnS thin films showed that the increase in particle size due to the presence of different anions during the growth mechanism lower the band gap values due to the quantum size effect. Further, the tabulated band gap values of all ZnS thin films are slightly higher than bulk ZnS, which is probably due to the quantum size effect as the grown polycrystalline thin films' grain size is small enough [10, 27].
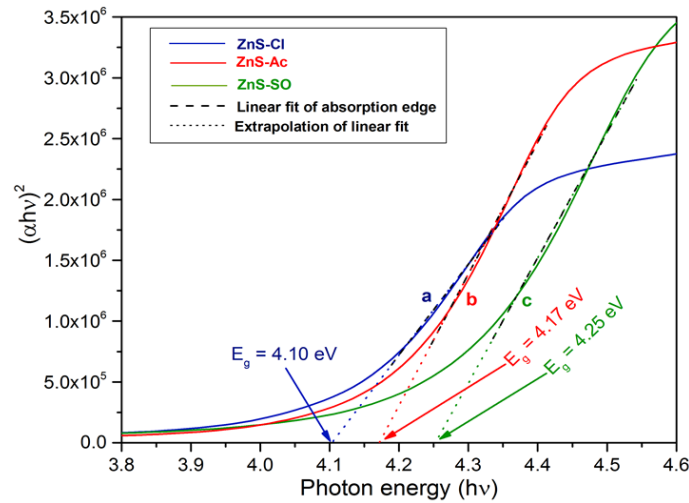
FIG. 8. Plot of $(\alpha h\nu)^2$ versus $h\nu$ for as-grown ZnS thin films deposited using different zinc precursors: (a) ZnS-Cl; (b) ZnS-Ac; (c) ZnS-SO

3.5. Photoluminescence study

The photoluminescence (PL) spectra of as-grown ZnS thin film grown using different zinc precursors under UV excitation is presented in Fig. 9. The intense emission with blue wavelength range is observed in all ZnS thin films, which could be attributed to the recombination of electron-hole pair from donor-acceptor trap levels to the valance band [28]. The stoichiometric difference of ZnS film during the growth mechanism is responsible for various kinds of defect formations. As per EDX analysis, the obtained ZnS films have a Zn/S ratio greater than 1. This stoichiometric deviation leads to excess zinc and a sulfur deficiency which could produce zinc interstitial (Zn_i) and sulfur vacancies (V_S) in ZnS thin film. The broadening of PL spectra around Zn_i was ascribed to various kinds of donor-acceptor pair transitions due to the formation of native defect states into the forbidden gap, which is depicted in Fig. 10.

In the present case, blue emission at ~ 459 nm signifies the involvement of interstitial zinc ions [28]. The spreading of emission spectra of ZnS thin film around blue wavelength is credited to different types of donor-acceptor transitions along with zinc interstitial [28]. The intensity of ZnS–SO is higher than other films and can be ascribed to the hindrance of diffusion of zinc complex precursors onto the silica substrate during growth of film and hence the
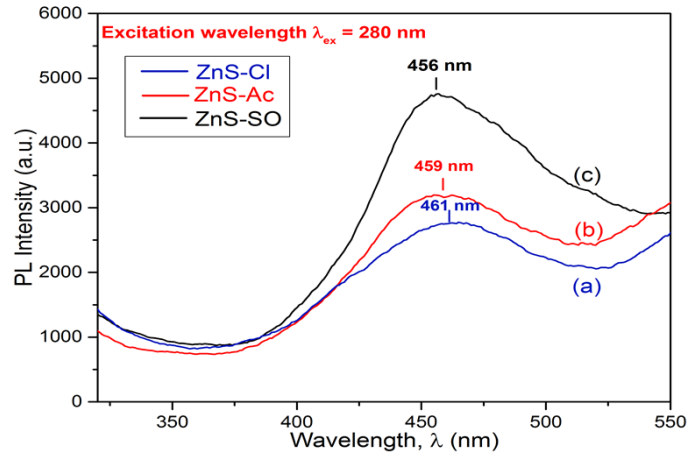
FIG. 9. Emission spectra of as-grown ZnS thin films deposited using different zinc precursors: (a) ZnS-Cl; (b) ZnS-Ac; (c) ZnS-SO
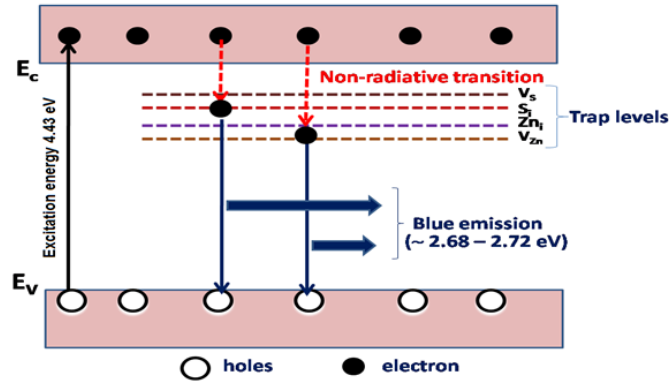

FIG. 10. Energy band diagram of the photoluminescence phenomenon in as-grown ZnS powder grown using different zinc precursors [28]

formation of native defect states. These indicate that anions play a crucial role in defect formation during the growth of thin films.

3.6. Raman study

For 514 nm excitation wavelength, ZnS thin film has low Raman scattering efficiency and is detectable only with film thickness 1 μm or higher [29]. Therefore, the Raman spectra of scratched as-grown ZnS powder (instead of ZnS thin films) prepared using different zinc precursors were recorded using 514 nm excitation wavelength (green excitation) shown in Fig. 11. The peak positioned at 348 cm^{-1} corresponds to the first-order longitudinal optical (LO) mode of ZnS materials. The second-order and third-order LO modes are observed at 697 and 1018 cm^{-1}, respectively. The obtained results are found consistent with the reviewed literature [29]. The intensity of the LO peak is highest for ZnS–Cl and that of the lowest for ZnS–SO. The peak due to the 2LO phonon is absent in ZnS–SO, while a slightly visible peak is observed in ZnS–Ac and ZnS–Cl with an increase in intensity, respectively. This could be due to anions present in zinc precursors affecting the defect chemistry of ZnS thin film during deposition, which influences the vibrational mode of ZnS thin films [29]. The increase in the sharpness of phonon peak represents an improvement in crystallinity [9] which is consistent with the above discussions.

3.7. Electrical measurements

The activation energy, electrical resistivity and conductivity of all ZnS thin films were determined using the two-point probe method. The relation for resistivity with temperature is denoted by [30]:

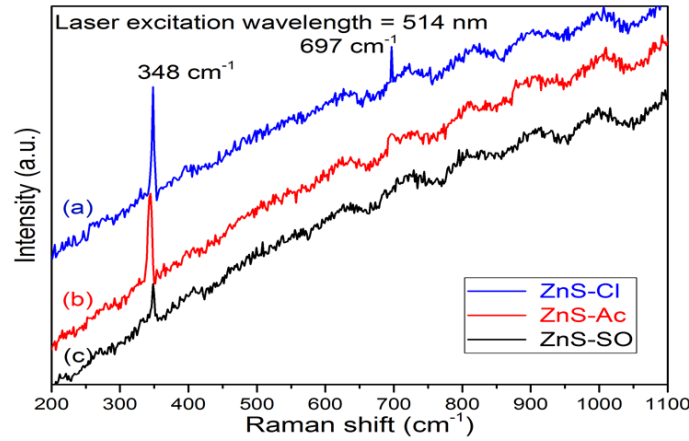$$\log \rho = \frac{E_a}{2.303 \cdot k_B} \left(\frac{1}{T} \right) + \log C, \tag{5}$$

FIG. 11. Raman spectra of as-grown ZnS powders prepared by different zinc precursors: (a) ZnS-Cl; (b) ZnS-Ac; (c) ZnS-SO

where ρ is resistivity (in $\Omega \cdot$cm), E_a is activation energy (in eV), k_B is Boltzmann constant (in eV/K), T is the temperature (in Kelvin) and $\log C$ is constant.

The Hall coefficient, carrier concentration and mobility of thin films were figured out using the relation given below [31]:

$$R_H = \frac{V_H \cdot t}{I \cdot B}, \qquad \eta = \frac{1}{R_H \cdot q}, \tag{6}$$

where R_H is Hall Coefficient (cm^3/C), V_H is Hall Voltage (in volt), I is probe current (in Ampere), t is the thickness (in meter), B is the magnetic field (in Gauss) and η is carrier concentration (in 1/cm^3).

The data for the resistivity measurements were recorded by raising the temperature from 35 to 190 °C. The plot for $\log \rho$ Vs $1000/T$ for ZnS thin film deposited using different zinc precursors is depicted in Fig. 12. The plot of $\log \rho$ versus $1000/T$ gives a straight line whose slope corresponds to E_a/k_B. The calculated values of resistivity, conductivity and activation energy is represented in Table 4. The shallow trap levels are responsible for low activation energy E_{a1} and the deep trap levels are responsible for the high value of activation energy E_{a2} in the case of ZnS–SO thin film [32].
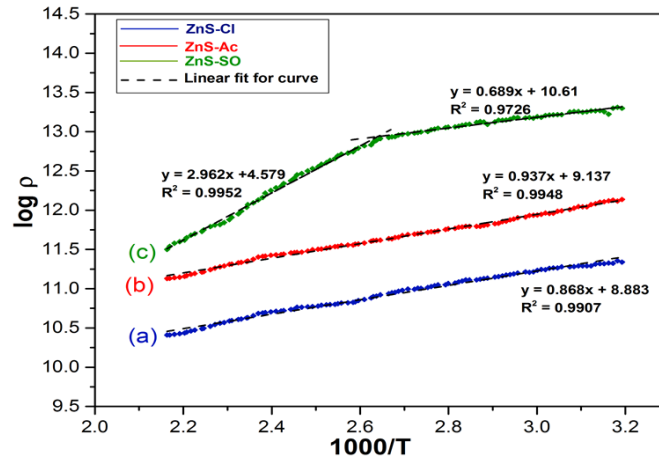
FIG. 12. Plot of $\log \rho$ versus $1000/T$ for as-grown ZnS thin films deposited using different zinc precursors

The Hall effect measurements were recorded by keeping probe current constant and varying magnetic field and measuring corresponding Hall voltage. The sketch for Hall voltage versus magnetic field is outlined in Fig. 13. The calculated values for the Hall coefficient, carrier concentration and mobility are listed in Table 4. The n-type conductivity was observed in all ZnS films irrespective of zinc precursors used. The tabulated values show that ZnS–SO thin film has a high charge density and low conductivity compared to other thin films. The explanation of the observed results is that native defect states are generated during the growth of film act as scattering centers

TABLE 4. Electrical parameter for as-grown ZnS thin films deposited using different zinc precursors: ZnS–Cl (a); ZnS–Ac (b); ZnS–SO (c)

Thin film	Activation energy (eV)		Resistivity ρ (Ω·cm)	Conductivity σ (Ω^{-1}·cm^{-1})	Hall Coefficient RH (cm^3/C)	Carrier concentration η (cm^{-3})	Mobility μ (cm^2/V$_s$)
	E_{a1}	E_{a1}					
ZnS–Cl	0.75	—	2.08×10^4	4.81×10^{-5}	3.48×10^3	1.79×10^{15}	1.68×10^{-1}
ZnS–Ac	0.81	—	1.63×10^4	6.14×10^{-5}	1.71×10^2	3.65×10^{16}	1.05×10^{-2}
ZnS–SO	0.59	2.55	8.52×10^4	1.17×10^{-5}	2.53×10^1	2.47×10^{17}	2.97×10^{-4}

for conduction electrons in the film.So defect chemistry and hence anions associated with zinc precursors play an important role in the electrical transport properties of ZnS thin films. Fig. 14 represents the comparative graph for carrier concentration, conductivity and mobility for ZnS thin films. It reveals from the graph that ZnS-Cl shows a considerable amount of conductivity compared to other samples even though its low carrier concentration. This is due to the high mobility offered by it.
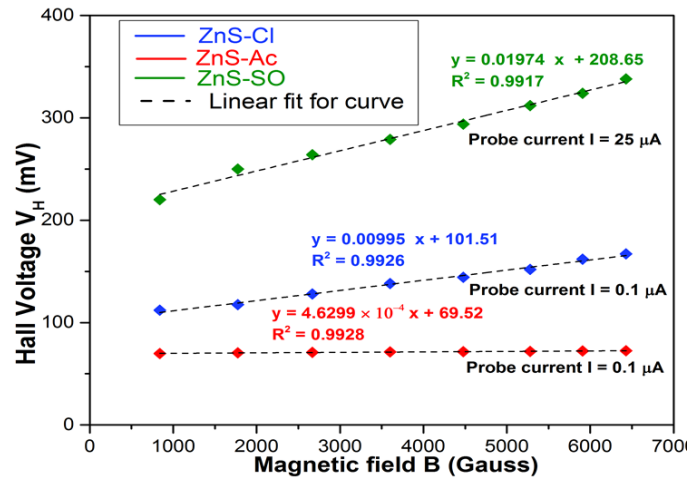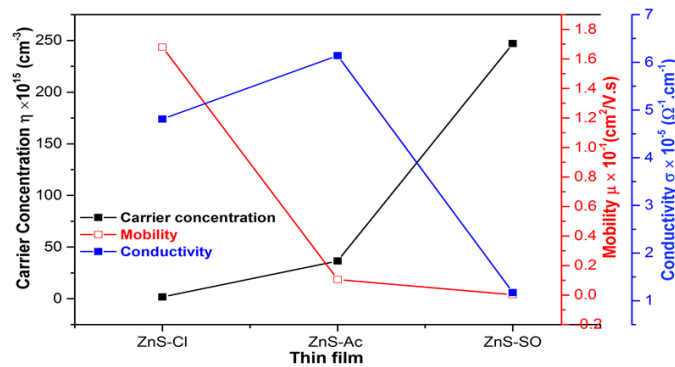

FIG. 13. Plot of Hall voltage VH versus magnetic field B for constant probe current of ZnS thin films deposited using different zinc precursors

FIG. 14. Comparative graph for carrier concentration, mobility and conductivity for as-grown ZnS thin films deposited using different zinc precursors

4. Conclusion

Good quality ZnS thin films have been deposited onto silica substrates using different zinc precursors, thiourea, non-toxic complexing agent triethanolamine (TEA) by optimizing bath parameters. The XRD confirms the hexagonal phase with maximum intensity peak along (0 0 10) plane of as-grown ZnS thin film prepared using different zinc precursors. SEM demonstrates the notable effect of anions of zinc precursors on the growth mechanism of ZnS thin film. Optical measurements demonstrate transmittance varies from 10 to 29 % in the visible region. The band gap increases with a decrease in particle size due to the quantum size effect. The ZnS thin film has higher band gap values than the counter bulk sample in the range of 4.10 – 4.25 eV. The blue emission at $\sim$ 459 nm was obtained by PL spectra under UV excitation. The first-order Raman shift was observed at 348 cm^{-1} in all ZnS films. The Hall-effect apparatus measures carrier concentration of order 10^{15} to 10^{17} e^{-}/cm^{3}, reflecting the semiconducting nature of ZnS thin film with n-type conductivity. The observed studies show the significant effect of zinc precursors on the transport properties of CBD-ZnS thin films. ZnS thin film deposited using ZnCl$_2$ as precursor material is found to have good carrier mobility amongst all films.

References

[1] Nemade K.R., Waghley S.A. Ultra-violet C absorption and LPG sensing study of zinc sulphide nanoparticles deposited by a flame-assisted spray pyrolysis method. *Journal of Taibah University for Science*, 2016, **10** (3), P. 437–441.

[2] Islam M.M., Ishizuka S., et al. CIGS solar cell with MBE-grown ZnS buffer layer. *Solar Energy Materials & Solar Cells*, 2009, **93**, P. 970–972.

[3] Bujňáková Z., Dutková E. Mechanochemistry of Chitosan-Coated Zinc Sulphide (ZnS) Nanocrystals for Bio-imaging Applications. *Nanoscale Research Letters*, 2017, **12**, 328.

[4] Ben Nasr T., Kamoun N., Guasch C. Structure, surface composition, and electronic properties of zinc sulphide thin films. *Materials Chemistry and Physics*, 2006, **96**, P. 84–89.

[5] Ubale A.U., Kulkarni D.K. Preparation and study of thickness dependent electrical characteristics of zinc sulfide thin films. *Bull. Mater. Sci.*, 2005, **28** (1), P. 43–47.

[6] Yu F-P., Ou S-L., et al. Structural, Surface Morphology and Optical Properties of ZnS Films by Chemical Bath Deposition at Various Zn/S Molar Ratios. *Journal of Nanomaterials*, 2014, **6**, P. 1–7.

[7] Gode F. Annealing temperature effect on the structural, optical and electrical properties of ZnS thin films. *Physica B*, 2011, **406**, P. 1653–1659.

[8] Zein R., Alghoraibi I. Influence of Bath Temperature and Deposition Time on Topographical and Optical Properties of Nanoparticles ZnS Thin Films Synthesized by a Chemical Bath Deposition Method. *Journal of Nanomaterials*, 2019, 1–13.

[9] Cao M., Zhang B.L., Li L. Huang J., et al. Effects of zinc salts on structural and optical properties of acidic chemical bath deposited ZnS thin films. *Materials Research Bulletin*, 2013, **48**, P. 357–361.

[10] Liu T., Ke H., et al. Effect of four different zinc salts and annealing treatment on growth, structural, mechanical and optical properties of nanocrystalline ZnS thin films by chemical bath deposition. *Materials Science in Semiconductor Processing*, 2014, **26**, P. 301–311.

[11] Gurin N.T., Sabitov O.Y., Afanas'ev A.M. Characteristics of surface states at the insulator-semiconductor interface in the thin-film electroluminescent structures based on ZnS:Mn. *Semiconductors*, 2010, **44** (4), P. 498–507.

[12] Migita M., Kanehisa O., Shiiki M. Yamamoto H. The Preparation of ZnS:Mn electroluminescent layers by MOCVD using new manganese sources. *Journal of Crystals Growth*, 1988, **93** (1–4), P. 686–691.

[13] Lindroos S., Kanniainen T. Leskela M., Rauhala E. Deposition of manganese-doped zinc sulfide thin films by the successive ionic layer adsorption and reaction (SILAR) method. *Thin Solid Films*, 1995, **263** (1), P. 79–84.

[14] Doña J. M., Herrero J. Process and film characterization of chemical-bath-deposited ZnS thin films. *Journal of The Electrochemical Society*, 1994, **141** (1), P. 205–210.

[15] Oladeji I.O., Chow L., et al. Comparative study of CdS thin films deposited by single, contineous, and multiple dip chemical processes. *Thin Solid Films*, 2000, **359** (2), P. 154–159.

[16] Liu J., Wei A., Zhao Y. Effect of different complexing agents on the properties of chemical-bath-deposited ZnS thin films. *Journal of Alloys and Compounds*, 2014, **588**, P. 228–234.

[17] Khatri R.P., Patel A.J. Effect of post annealing on CBD deposited ZnS thin films. *International Journal of Scientific Research and Reviews*, 2018, **7** (1), P. 374–384.

[18] Basha S.J., Khidhirbrahmendra V., et al. Structural, optical, magnetic and thermal investigations on Cr3+ ions doped ZnS nanocrystals by co-precipitation method. *Journal of Science: Advanced Materials and Devices*, 2019, **4**, P. 260–266.

[19] Cullity B.D., Stock S.R. *Element of X-ray Diffraction*, Addison-Wesley, Massachusetts, 1956, 99 p.

[20] Wang J., Hou S., et al. Ultra-rapid formation of ZnO hierarchical structures from dilution-induced supersaturated solutions. *Cryst. Eng. Comm.*, 2014, **16**, P. 7115–7123.

[21] The Materials Project. Materials Data on Zn(HO)$_2$ by Materials Project. United States, 2020. URL: https://doi.org/10.17188/1278479.

[22] Echendu O.K., Weerasinghe A.R., et al. Characterization of n-type and p-type ZnS thin layers grown by an electrochemical method. *Journal of Electronic Materials*, 2013, **42** (4), P. 692–700.

[23] Moholkar A.V., Agawane G.L., et al. Influence of deposition temperature on morphological, optical, electrical and opto-electrical properties of highly textured nano-crystalline spray deposited CdO:Ga thin films. *Applied Surface Science*, 2010, **257** (1), P. 93–101.

[24] Ruffner J.A., Himel M.D., et al. Effects of low substrate temperature and ion assisted deposition on composition, optical properties, and stress of ZnS thin films. *Applied Optics*, 1989, **28** (24), 5209.

[25] Ahn H., Um Y. Post-annealing effects on ZnS thin films grown by using CBD method. *Journal of Korean Physical Society*, 2015, **67** (6), P. 1045–1050.

[26] Nadeem M.Y., Ahmed W. Optical properties of ZnS thin films. *Turk. J. Phy.*, 2000, **24**, P. 651–659.

[27] Mendil R., Ben Ayadi Z., Ben Belgacem J., Djessas K. The properties of ZnS thin films prepared by rf-magnetron sputtering from nanoparticles synthesized by solvothermal/hydrothermal route. *J. Mater. Sci.: Mater. Electron.*, 2016, **27**, P. 444–451.

[28] Babu P., Reddy M., et al. Chemical bath deposition of Mn-doped ZnS thin films using greener complexing agents: Effect of Mn-doping on the optical properties. *Optik*, 2017, **130**, P. 608–618.

[29] Fairbrother A., Izquierdo-Roca V., et al. ZnS grain size effects on near-resonant Raman scattering: optical non-destructive grain size estimation. *Cryst. Eng. Comm.*, 2014, **16**, P. 4120–4125.

[30] Vishwakarma R. Effect of substrate temperature on ZnS films prepared by thermal evaporation technique. *J. Theor. Appl. Phys.*, 2015, **9**, P. 185–192.

[31] Shukla V., Patel A. Effect of doping concentration on optical and electrical properties of intrinsic n-type ZnO (i-ZnO) and (Cu,Na and K) doped p-type ZnO thin films grown by chemical bath deposition method. *Nanosystems: physıcs, chemıstry, mathematıcs*, 2020, **11** (4), P. 391–400.

[32] Göde F., Gümüş C. Influences of copper and manganese concentrations on the properties of polycrystalline ZnS:Cu and ZnS:Mn thin films. *Journal of Optoelectronics and Advanced Materials*, 2009, **11** (4), P. 429–436.

Comprehensive cytotoxicity analysis of polysaccharide hydrogel modified with cerium oxide nanoparticles for wound healing application

A. L. Popov[1,2], V. V. Andreeva[3], N. V. Khohlov[4], K. A. Kamenskikh[1], V. B. Gavrilyuk[1], V. K. Ivanov[2]

[1]Institute of Theoretical and Experimental Biophysics of the Russian Academy of Sciences, Institutskaya str., 3, Pushchino, 142290, Russia

[2]Kurnakov Institute of General and Inorganic Chemistry of the Russian Academy of Sciences, Leninskiy prosp., 31, Moscow, 119991, Russia

[3]Moscow Regional Research and Clinical Institute, Laboratory of Medical and Physics Research, Shchepkina str. 61/2, Moscow, 129110, Russia

[4]I. M. Sechenov First Moscow State Medical University, Bolshaya Pirogovskaya str., 19s1, Moscow, 119146, Russia

antonpopovleonid@gmail.com, viktoriaa@yandex.ru, nikolay.khokhlov@gmail.com, kristina.kamensk@mail.ru, vbg@mail.ru, van@igic.ras.ru

This paper is aimed at the experimental study (in animal models) of acute toxicity and irritating properties of polysaccharide hydrogel modified with cerium oxide nanoparticles. In the acute experiment, there were no indications of irritating action of the gel at the site of application when the hydrogel was administered intragastrically or epicutaneously. No lethal effects were registered during this experiment even at the highest concentration. The results obtained demonstrate the lack of acute toxicity and local irritability of the synthesized hybrid hydrogel, which allows to classify the developed hybrid hydrogel as the relatively low-risk drug.

Keywords: wound healing, hydrogel, cerium oxide nanoparticles, epicutaneous application, regeneration, cell proliferation.

Received: 13 May 2021

1. Introduction

Nanocrystalline cerium oxide has recently been proven to be a promising inorganic antioxidant and a key component of a wide range of biomedical products [1–4]. Its unique redox activity, high biocompatibility and low toxicity make it very different from many other nanomaterials [5–7]. The ability of CeO_2 nanoparticles to switch between Ce^{3+} and Ce^{4+} states allows them to inactivate a wide range of reactive oxygen species (ROS) and free radicals [8]. Previously, it has been shown that CeO_2 nanoparticles are capable of mimicking the activity of a number of endogenous enzymes, such as catalases and superoxide dismutases (SOD) [9]. The most significant feature of CeO_2 nanoparticles is their ability to recover their activity and to participate in redox reactions multiple times, thus making this compound one of the most advantageous nanomaterials in biomedical applications. Meanwhile, the catalytic activity of CeO_2 nanoparticles and their role (pro- or antioxidant) strongly depend on the nanoparticle's microenvironment [10–13]. Previously, it has been shown that CeO_2 nanoparticles under acidic conditions exhibit pro-oxidant properties, whereas in neutral or weakly alkaline media, they are strictly antioxidant [14]. Also, it has been shown that the catalytic activity of CeO_2 nanoparticles depends on the concentration of trivalent ions on the nanoparticle's surface; in this way, SOD-mimetic activity of CeO_2 increases with the increase in Ce^{3+} concentration [15]. Therefore, the microenvironment affects directly the physicochemical characteristics of CeO_2 nanoparticles thus controlling their catalytic and biological activity.

In this study, biocompatible citrate-stabilized CeO_2 nanoparticles were synthesized and were integrated into a polysaccharide hydrogel matrix for use as a wound healing agent. The choice of hydrogel matrix and the filler was based on the existing data on CeO_2 effect on the skin regeneration process. In particular, CeO_2 nanoparticles possess striking anti-inflammatory activity [6], affect immune cells [16], that could significantly shorten the Phase 2 of the regeneration process (inflammation phase), and thus accelerate the start of the Phase 3 – the proliferative phase of the regeneration process. As it has previously been demonstrated, CeO_2 nanoparticles are capable of accelerating the proliferation of fibroblasts, mesenchymal stem cells and osteoblasts [3, 17, 18]. It has also been previously shown that the integration of nanoparticles into various biopolymers [19] and scaffolds provides enhanced cell proliferation [20]. An additional advantage of using cerium oxide nanoparticles in the structure of wound-healing hydrogel is that they possess bacteriostatic [21] and bactericidal [22] action as well as antiviral activity [23]. Such multifaceted

biological activities provides an opportunity for cerium oxide nanoparticles to serve as a unique bioactive component in biomedical products design and development.

The polysaccharide hydrogel matrix allows one to not only provide a convenient application of the preparation onto the skin, but is also capable of providing prolonged release of nanoparticles from the matrix into the lesion, reducing inflammation and staving off infection, as well as stimulating proliferative fibroblast activity.

2. Materials and methods

2.1. Hydrogel synthesis

The hydrogels were made from citrate-stabilized cerium oxide nanoparticles prepared according to the previously reported protocol [24], using pectin, fucoidan, sodium alginate, water-soluble derivatives of cellulose (carboxymethyl cellulose) and purified water. Briefly, 1.0 g fucoidan, 1.0 g sodium alginate, 2.0 g pectin, 8.0 g carboxymethyl cellulose were dissolved in 100 ml distilled water. The mixture was mixed at 25°C and then left for 96 h at 4°C until the formation of a homogeneous gel. Then, 100 ml of the CeO_2 sol (2–4 nm CeO_2 nanoparticles; 10^{-2} M CeO_2 concentration) was added and the mixture was vigorously homogenized. Before application, the gel was sterilized in an autoclave at 120°C.

2.2. Laboratory animals

Experimental procedures were performed on Wistar white rats and outbred white mice of both genders. Rats and mice came from the breeding nursery of laboratory animals "Andreevka", Moscow region. Rats weighing 180–190 g at the age of 12–13 weeks and mice weighting 18–20 g at the age of 8–9 weeks were used.

Animal maintenance was carried out in accordance with the rules adopted by the European Convention for the Protection of Vertebrate Animals (Strasbourg, 1986). Rats and mice were kept in plastic cages, 10 individuals per each cage. The animals were fed twice a day. All-in-one feed for laboratory animals (PK-120-1) produced by Laboratorsnab LLC was filled ad libitum into the feed hopper at the top of the cage. Animals had unlimited access to water using special drinking bottles for rodents. Bacteriological analysis and sanitary chemical examination of water were performed initially. There was no contamination of the bedding, feed and water that could affect the results of the study.

2.3. Analysis of the effect ceria-containing polysaccharide hydrogel upon epicutaneous application

To study the effect of polysaccharide hydrogel modified with cerium oxide nanoparticles upon epicutaneous application, a day prior to the experiment, the square of 2.5×2.5 cm was depilated by trimming (plucking) of animal's dorsum. The hydrogel was preheated in a water bath to 38–40°C and then applied with a glass rod onto depilated area of rat's dorsum at ascending doses according to Litchfield-Wilcoxon method. Similar doses of petroleum jelly were administered to control animals in the same way. Thereafter, the animals were placed for 6 hours into special individual plexiglass containers to restrict locomotor activity and to prevent gel licking. After releasing the rats from the containers, the excess of the gel was removed from the skin with filter paper, and animals were placed for 14 days into check cages for observation. The acute toxicity testing was carried out at the maximum possible doses of gel on up to 20 g/kg by epicutaneous application.

2.4. Acute toxicity testing of polysaccharide hydrogel modified with cerium oxide nanoparticles

Acute toxicity of gels upon intragastric administration was assessed both in white rats and mice of both genders, and upon epicutaneous application in the mice only. Groups of 12 animals (6 males and 6 females) were used in the experiments. The absence of external symptoms (external manifestation of bacterial infections, physical activity, etc.) and homogeneity of groups by body weight (±10%) were considered as randomization acceptance criteria. To estimate acute toxicity characteristic values, polysaccharide hydrogel was administered intragastrically (i.g.) to white rats and mice of both genders in ascending doses (dosing accuracy is achieved by varying the volume of gel administered) according to Litchfield-Wilcoxon method. Upon oral administration, the gel was heated in a water bath to 38–40°C to a liquid state. An atraumatic metal gastric catheter was used for administration and it was inserted up to the stomach. Control animals were administered with similar volumes of petroleum jelly softened with warm water. Acute toxicity testing was carried out at the maximum possible doses of up to 25 g/kg by total gel weight. The mortality rate, lethal time for animals, symptoms of poisoning were recorded for 14 days, overall systemic condition and behavior were examined daily; the weight of the animals, food and water consumption were monitored. The dead animals were subjected to autopsy and macroscopic examination. After day 14, all the animals survived were euthanized in a CO_2-chamber and dissected. Hematologic studies, macroscopic description and the evaluation of mass coefficients of internal organs, histological studies were carried out.

2.5. List of recorded indicators of experimental animals

The animals were weighed just prior to administration of the hydrogel, on days 2 and 7, to control body weight dynamics, and just prior to euthanasia (day 14) to calculate the percentage of organ weight to body weight. To account for water and food consumption, rats were transferred to metabolic cages. All animals treated with the highest dose of tested hydrogel were selected for pathomorphological studies. The pathomorphological study included necropsy, macroscopic study, weighing and histological examination of internal organs. Necropsy was performed under the direct supervision of a pathologist. After euthanasia, the animals were carefully examined for the presence of external pathological signs. Examination of the gastrointestinal mucous membranes allowed us to estimate the local irritating effect of tested gel. The examination of overall state of the thoracic and abdominal cavities as well as a macro- and microscopic examination of the internal organs (heart, lungs with trachea, thymus, liver, spleen, kidneys, adrenal glands, brain, testicles or ovaries) was carried out.

2.6. The statistical evaluation of the effect

Statistical treatment of the results was performed using the STATISTICA 8.0 software. Data were presented as the sample mean M, the standard error of the mean m, and the achieved level of significance p. Lowest accepted significance level of differences was taken as $p \leq 0.05$. In some cases, especially when there was a natural drift of indicators (e.g. animal body weight gain over the observation period, etc.), the methods of dispersion analysis were used.

3. Results and discussion

Upon administering high doses of the gel (up to 25 g/kg), no mortality was noted among mice and rats. There were also no significant abnormalities in overall behavior and systemic condition of animals. The oral administration of high doses of the gel (more than 6 g/kg) showed limited retardation of animals, a reduction of feed intake on the first day and diarrhea on day 2 after gel administration. Similar reactions were observed in control animals that received large volumes of petroleum jelly. Limited retardation and reduction of feed intake on the first day occurred in the control group of animals, which were apparently not related to the toxic effect of polysaccharide hydrogel, but rather to the stressful effect of the oral administration procedure of large volumes. Such a discomfort was both due to mechanical troubles in the gastrointestinal tract due to large volumes of gel administered as well as to the nature of gelling agents (laxative effect could be caused by the presence of cellulose derivatives). The condition of the animals then started to normalize and after 24 hours their overall behavior and systemic condition did not differ from those in the control group and from the baseline status.

The dissection of the animals revealed a venous congestion of internal organs. There were no signs of gastrointestinal irritation. There were no gender differences during intoxication.

The results of animal body weight measurements are shown in Tables 1 and 2.

TABLE 1. The effect of acute intragastric administration of CeO_2-containing polysaccharide hydrogel on mice's body weight (g, M±m)

| Time, days | Experimental group and gender | | | |
| | Control | | Hydrogel | |
	M	F	M	F
Initially	18.7±0.4	19.3±0.2	19.2±0.3	18.8±0.3
2-nd day	18.4±0.3	19.2±0.1	19.1±0.2	18.9±0.2
7-th day	19.2±0.2	20.2±0.3	19.2±0.2	19.3±0.4
14-th day	20.1±0.4	20.4±0.2	19.9±0.1	19.7±0.2

On the second day after administration, a slight decrease was observed in the average body weight of all animals treated with CeO_2-containing gel. The same effect has been registered in the control group (though to a lesser extent), so it can be attributed to general stress. To exclude this effect (most likely caused by stress the associated with involvement of animals in an experimental procedure), weight changes relative to initial values were compared. The introduction of the hybrid hydrogel to animals did not lead to significant differences in the dynamics of water and food consumption (Tables 3,4).

TABLE 2. The effect of acute intragastric administration of CeO_2-containing polysaccharide hydrogel on rats' body weight (g, M±m)

Time, days	Experimental group and gender			
	Control		Hydrogel	
	M	F	M	F
Initially	176.5±3.4	179.1±2.4	180.1±4.6	181.4±3.4
2-nd day	176.4±3.2	180.2±3.0	176.2±4.3	179.6±3.1
7-th day	187.1±2.9	186.6±2.2	185.0±2.9	183.1±3.5
14-th day	196.3±3.1	198.5±3.3	195.8±4.8	194.7±2.4

TABLE 3. The effect of acute intragastric administration of CeO_2-containing polysaccharide hydrogel on water consumption dynamics (ml/day, M±m) by rats

Time, days	Experimental group and gender			
	Control		Hydrogel	
	M	F	M	F
Initially	18±0.6	15±0.7	19±0.6	16±0.6
2-nd day	17± 0.5	16±0.4	18±0.5	17±0.5
7-th day	18±0.8	18±0.5	20±0.3	19±0.6
14-th day	19±0.5	19±0.6	19±0.4	18±0.7

TABLE 4. The effect of acute intragastric administration of CeO_2-containing polysaccharide hydrogel on feed consumption dynamics (g/day, M±m) by rats

Time, days	Experimental group and gender			
	Control		Hydrogel	
	M	F	M	F
Initially	20.5±0.9	20.3±0.9	20.2±0.9	20.6±0.8
2-nd day	15.6±1.1*	16.2±1.0*	15.9±1.3*	17.1±1.4*
7-th day	19.9±1.6	24.2±1.9	23.9±2.3	22.1±2.0
14-th day	21.3±2.2	21.9±1.5	22.0±2.8	22.6±1.8

* – Significant difference from initial values (at $p < 0.05$)

Data analysis did not reveal any significant differences in body weight dynamics between the test and control animals. Slightly higher body weight gains in test groups compared with the control at the final stage of the study were not statistically significant.

No animal mortality was observed upon epicutaneous gel application. There were no external pathological manifestations that could be treated as the signs of intoxication. The condition and behavior of the test animals throughout the observation period were not different from that of the control groups, and, in all the groups, were consistent with that of intact animals. The dynamics of animal body weight in all test groups also did not differ from control (Table 5).

At the final stage of the experiment (dissection stage on the 14th day), there were no differences between the animals treated with CeO_2-containing polysaccharide hydrogel and the control group. Macroscopic studies did not reveal any species-specific or sex-specific differences, as well as the effect of the method of administration on the state of internal organs.

According to the visual inspection, the animal fur was shiny and tidy. No bald spots were observed. There were no excretions from animals. The front and hind limbs have not been altered and no deformation of the limbs has been observed. Teeth were preserved. Visible mucous membranes were pale, shiny, and smooth. Animal nutrition

TABLE 5. The effect of polysaccharide hydrogel on experimental animals' body weight upon application onto scarified skin (g, M±m)

Time, days	Experimental group and gender			
	Control		Hydrogel	
	M	**F**	**M**	**F**
Initially	180.2±4.6	178.3±2.5	176.3±3.0	179.6±2.4
2-nd day	181.5±4.4	179.3±3.1	178.2±3.3	178.1±2.0
7-th day	189.3±4.4	186.5±2.6	185.0±3.3	187.5±2.8
14-th day	198.8±4.8	197.9±2.5	199.7±3.1	198.1±2.4

was satisfactory. Examination of the thoracic and abdominal cavities did not reveal any irregularities in the internal organs. The submandibular lymph nodes and salivary glands had an oval or rounded shape, a homogeneous pinkish or yellowish color and a moderate density. The thyroid glands were tightly attached to the larynx, had the usual size and density, a pinkish-reddish color. The thymus had a triangular shape, a whitish color, and a moderately dense consistency. The size and shape of the heart was not altered. The heart muscle was brownish and dense.

The surface of the lungs had a pale pink color; the lungs collapsed when the breast was opened. The dissected tissue also had a homogeneous pale pink color. The mucous membrane of the extrapulmonary bronchi was smooth, shiny, and pale pink. The spleen had a dark cherry color, smooth surface and rather dense consistency. The pancreas was pale pink and lobular.

The size and shape of the liver did not represent any changes. The liver capsule was thin and transparent. Liver tissue had a brownish color and moderately dense consistency. The size and shape of the kidneys were not different from the control, the capsule was easily removed. The surface of the organ was smooth, had a homogeneous uniform brownish-grey color. In the section of the kidneys, the cortex and the medulla were clearly distinguished.

The shape, size and density of the adrenal glands, ovaries or testicles did not differ from the control. Cerebral meninges were thin and transparent. The brain matter had moderate density, and there were no enlargements of the brain's ventricles. Intragastric administration of the polysaccharide hydrogel modified with cerium oxide nanoparticles or petroleum jelly did not reveal visible abnormalities in the gastrointestinal tract. The esophageal mucosa was shiny, smooth, and pale in color. The size and shape of the stomach did not represent any changes. There was no hyperemia, erosion, hemorrhage, indicating the irritating effect of the gel. The duodenum lumen did not show any changes, and the intestinal mucosa was shiny, smooth, pale pink. The small intestine mucosa was pale pink, shiny, smooth as well. The colon mucosa had a slightly greyish tint and was smooth and shiny.

Epicutaneous administration of polysaccharide hydrogel modified with cerium oxide nanoparticles or petroleum jelly, did not lead to any observed local abnormalities, i.e. irritation, inflammation, hyperemia. In all the groups there was a normal process of fur restoration in the depilated areas. The application of polysaccharide hydrogel modified with cerium oxide nanoparticles onto animal skin was not accompanied by any signs of irritation. To analyze possible irritation, after placing animals into special chambers their tails for 2/3 were placed into test tubes filled with a gel. One hour after the completion of the gel application, no tail skin edema was observed.

Morphologically, the skin of the tails did not show any changes. Epidermis and skin appendages were intact. Epidermis layers were clearly expressed, the basal membrane was preserved. Epithelial cells of hair follicles of outer and inner root sheaths and connective tissue bag were well expressed.

Tables 6,7 show group-averaged mass coefficients of mice's and rats' internal organs.

Analysis of the mass coefficient values did not reveal any significant differences both in the groups of animals treated with polysaccharide hydrogel modified with cerium oxide nanoparticles, and in the control group. Upon epicutaneous application of polysaccharide hydrogel modified with cerium oxide nanoparticles the mass distribution of the internal organs in the groups was consistent with the normal values for intact animals.

Thus, the use of biologically active nanomaterials for the modification of various hydrogels and scaffolds gives them new functional properties which are applicable in biomedical applications [25–27].

4. Conclusions

Experimental data obtained suggest that single oral administration or application of ceria-containing polysaccharide hydrogel onto scarified skin of rats and mice of both genders does not cause changes in behavior and overall

TABLE 6. Mass coefficients of white mice's internal organs upon an acute intragastric administration of high doses of polysaccharide hydrogel modified with cerium oxide nanoparticles (g/kg body weight)

Organ	Experimental group and gender			
	Control		Hydrogel	
	M	F	M	F
Heart	3.2±0.2	3.3±0.2	3.5±0.1	3.1±0.3
Lungs with a trachea	6.2±0.2	6.4±0.1	6.3±0.1	6.5±0.1
Thymus	0.87±0.03	0.86±0.07	0.88±0.02	0.87±0.06
Liver	38.1±0.7	35.9±1.3	39.6±2.5	38.2±2.2
Spleen	2.9±0.2	3.0±0.1	3.3±0.1	3.1±0.2
Kidney (left)	4.2±0.2	4.3±0.3	4.3±0.3	4.5±0.1
Adrenal gland	0.17±0.01	0.15±0.01	0.17±0.01	0.16±0.01
Brain	15.5±0.5	15.6±0.4	15.5±0.4	15.9±0.4
Testicles or ovaries	3.6±0.2	0.21±0.02	3.4±0.3	0.18±0.02

TABLE 7. Mass coefficients of white rats' internal organs upon an acute intragastric administration of high doses of polysaccharide hydrogel modified with cerium oxide nanoparticles (g/kg body weight)

Organ	Experimental group and gender			
	Control		Hydrogel	
	M	F	M	F
Heart	3.9±0.3	3.8±0.2	4.1±0.2	4.0±0.2
Lungs with a trachea	7.5±0.2	7.3±0.4	7.4±0.1	7.6±0.3
Thymus	1.39±0.11	1.25±0.08	1.36±0.06	1.27±0.11
Liver	37.9±1.4	36.7±1.9	36.6±1.9	35.4±1.3
Spleen	3.9±0.5	3.9±0.1	3.9±0.2	4.1±0.3
Kidney (left)	4.4±0.1	4.2±0.2	4.5±0.1	4.3±0.2
Adrenal gland	0.09±0.02	0.08±0.01	0.08±0.02	0.09±0.02
Brain	8.6±0.2	8.9±0.2	8.9±0.2	8.6±0.1
Testicles or ovaries	12.2±0.1	0.26±0.02	12.2±0.1	0.25±0.02

systemic condition of animals, do not cause any changes in mass coefficients of organs compared with control animals, as well as do not cause any macroscopic changes in the brain, internal and endocrine organs of test animals.

In acute experiments, polysaccharide hydrogel application did not lead to irritating effects at the site of application.

Thus, our toxicology study performed 14 days after acute administration as well as necropsy data allow ranking the polysaccharide hydrogel modified with cerium oxide nanoparticles as the Schedule VI of relatively low-risk drug ($LD_{50} > 25$ g/kg, rats, per os) [28].

It can be concluded that a polysaccharide hydrogel modified with cerium oxide nanoparticles can be considered as a safe and effective substances for the treatment of skin damage with various etiologies [29].

Acknowledgements

References

[1] Bellio P., Luzi C., Mancini A., Cracchiolo S., Passacantando M., Di Pietro L., Perilli M., Amicosante G., Santucci S., Celenza G. Cerium oxide nanoparticles as potential antibiotic adjuvant. Effects of CeO$_2$ nanoparticles on bacterial outer membrane permeability. *Biochim. Biophys. Acta Biomembr.*, 2018, **1860**, P. 2428–2435.

[2] Popov A., Popova, N., Gould D., Shcherbakov A., Sukhorukov G., Ivanov V. Ceria nanoparticles-decorated microcapsules as a smart drug delivery/protective system: Protection of encapsulated P. *pyralis* luciferase. *ACS Appl. Mater. Interfaces*, 2018, **10**(17), P. 14367–14377.

[3] Rocca A., Mattoli V., Mazzolai B., Ciofani G. Cerium Oxide Nanoparticles Inhibit Adipogenesis in Rat Mesenchymal Stem Cells: Potential Therapeutic Implications. *Pharm. Res.*, 2014, **31**, P. 2952–2962.

[4] Sridharan P., Vinothkumar G., Pratheesh P., Suresh Babu K. Biomimetic potential of cerium oxide nanoparticles in modulating the metabolic gene signature in GBM-derived cell lines. *J Mater Sci.*, 2020, **55**, P. 11622–11636.

[5] Zhou D., Fang T., Lu L.-Q., Yi L. Neuroprotective potential of cerium oxide nanoparticles for focal cerebral ischemic stroke. *J. Huazhong Univ. Sci. Technol.*, 2016, **36**, P. 480–486.

[6] Hirst S.M., Karakoti A.S., Tyler R.D., Sriranganathan N., Seal S., Reilly C.M. Anti-inflammatory properties of cerium oxide nanoparticles. *Small*, 2009, **5**(24), P. 2848–2856.

[7] Celardo I., Pedersen J.Z., Traversa E., Ghibelli L. Pharmacological potential of cerium oxide nanoparticles. *Nanoscale*, 2011, **3**(4), P. 1411–1420.

[8] Malyukin Y., Maksimchuk P., Seminko V., Okrushko E., Spivak N. Limitations of Self-Regenerative Antioxidant Ability of Nanoceria Imposed by Oxygen Diffusion. *J. Phys. Chem. C*, 2018, **122**(28), P. 16406–16411.

[9] Seminko V., Maksimchuk P., Grygorova G., Malyukin Y.V. Mechanism and Dynamics of Fast Redox Cycling in Cerium Oxide Nanoparticles at High Oxidant Concentration. *J. Phys. Chem. C*, 2021, **125**(8), P. 4743–4749.

[10] Seminko V., Maksimchuk P., Grygorova G., Avrunin O., Semenets V., Klochkov V., Malyukin Y. Catalytic Decomposition of Hypochlorite Anions by Ceria Nanoparticles Visualized by Spectroscopic Techniques. *J. Phys. Chem. C*, 2019, **123**(33), P. 20675–20681.

[11] Klochkov V.K., Sedyh O.O., Grygorova G.V., Viagin O.G., Opolonin A.D., Malyukin Yu.V. Induction and inhibition of free radicals by the GdVO$_4$:Eu^{3+} and CeO$_2$ nanoparticles under X-ray irradiation. *Funct. Mater.*, 2018, **25**(2), P. 294–299.

[12] Klochkov V.K., Malyukin Yu.V., Grygorova G.V., Sedyh O.O., Kavok N.S., Seminko V.V., Semynozhenko V.P. Oxidation-reduction processes in CeO$_{2-x}$ nanocrystals under UV irradiation. *J. Photochem. Photobiol. A*, 2018, **364**, P. 282–287.

[13] Malyukin Y., Klochkov V., Maksimchuk P., Seminko V., Spivak N. Oscillations of cerium oxidation state driven by oxygen diffusion in colloidal nanoceria (CeO$_{2-x}$). *Nanoscale Res. Lett.*, 2017, **12**(1), P. 566.

[14] Alpaslan E., Yazici H., Golshan N.H., Ziemer K.S., Webster T.J. pH-Dependent Activity of Dextran-Coated Cerium Oxide Nanoparticles on Prohibiting Osteosarcoma Cell Proliferation. *ACS Biomater. Sci. Eng.*, 2015, **1**(11), P. 1096–1103.

[15] Ivanov V.K., Shcherbakov A.B., Usatenko A.V. Structure-sensitive properties and biomedical applications of nanodispersed cerium dioxide. *Russ. Chem. Rev.*, 2009, **78**(9), P. 855–871.

[16] Lord M.S., Jung M., Teoh W.Y., Gunawan C., Vassie J.A., Amal R., Whitelock J.M. Cellular uptake and reactive oxygen species modulation of cerium oxide nanoparticles in human monocyte cell line U937. *Biomaterials*, 2012, **33**(31), P. 7915–7924.

[17] Ciofani G., Genchi G.G., Liakos I., Cappello V., Gemmi M., Athanassiou A., Mazzolai B., Mattoli V. Effects of cerium oxide nanoparticles on PC12 neuronal-like cells: Proliferation, differentiation, and dopamine secretion. *Pharm Res.*, 2013, **30**, P. 2133–2145.

[18] Niu J., Azfer A., Rogers L.M., Wang X., Kolattukudy P.E. Cardioprotective effects of cerium oxide nanoparticles in a transgenic murine model of cardiomyopathy. *Cardiovasc. Res.*, 2007, **73**, P. 549–559.

[19] Chen S., Hou Y., Cheng G., Zhang C., Wang S., Zhang J. Cerium oxide nanoparticles protect endothelial cells from apoptosis induced by oxidative stress. *Biol. Trace Elem. Res.*, 2013, **154**, P. 156–166.

[20] Lu B., Zhu D.-Y., Yin J.-H., Xu H., Zhang C.-Q., Ke Q.-F., Gao Y.-S., Guo Y.-P. Incorporation of cerium oxide in hollow mesoporous bioglass scaffolds for enhanced bone regeneration by activating the ERK signaling pathway. *Biofabrication*, 2019, **11**(2), P. 025012.

[21] Alpaslan E., Geilich B.M., Yazici H., Webster T.J. pH-Controlled Cerium Oxide Nanoparticle Inhibition of Both Gram-Positive and Gram-Negative Bacteria Growth. *Sci. Rep.*, 2017, **7**, P. 45859.

[22] Agarwal C., Aggrawal S., Dutt D., Mohanty P. Cerium oxide immobilized paper matrices for bactericidal application. *Mater. Sci. Eng. B*, 2018, **232–235**, P. 1–7.

[23] Mohamed H.E.A., Afridi S., Khalil A.T., Ali M., Zohra T., Akhtar R., Ikram A., Shinwari Z.K., Maaza M. Promising antiviral, antimicrobial and therapeutic properties of green nanoceria. *Nanomedicine*, 2020, **15**(5), P. 467–488.

[24] Popov A.L., Popova N.R., Selezneva I.I., Akkizov A.Y., Ivanov V.K. Cerium oxide nanoparticles stimulate proliferation of primary mouse embryonic fibroblasts in vitro. *Mater. Sci. Eng. C*, 2016, **68**, P. 406–413.

[25] Thoniyot P., Tan M.J., Karim A.A., Young D.J., Loh X.J. Nanoparticle–Hydrogel Composites: Concept, Design, and Applications of These Promising, Multi Functional Materials. *Adv. Sci.*, 2015, **2**, P. 1400010.

[26] Dannert C., Stokke B.T., Dias R.S. Nanoparticle-Hydrogel Composites: From Molecular Interactions to Macroscopic Behavior. *Polymers*, 2019, **11**(2), P. 275.

[27] Almjasheva O.V., Garabadzhiu A.V., Kozina Yu.V., Litvinchuk L.F., Dobritsa V.P. Biological effect of zirconium dioxide-based nanoparticles. *Nanosyst. Phys. Chem. Math.*, 2017, **8**(3), P. 391–396.

[28] Gosselin R.E., Hodge H., Smith R.P., Gleason M.N. *Clinical Toxicology of Commercial Products: Acute Poisoning*. Williams and Wilkins, Baltimore, 1976, 332 p.

[29] Popova N.R., Andreeva V.V., Khohlov N.V., Popov A.L., Ivanov V.K. Fabrication of CeO$_2$ nanoparticles embedded in polysaccharide hydrogel and their application in skin wound healing. *Nanosyst. Phys. Chem. Math.*, 2020, **11**(1), P. 99–109.

Synthesis of core-shell titanium dioxide nanoparticles with water-soluble shell of poly(methacrylic acid)

E. L. Krasnopeeva[1,2], E. Yu. Melenevskaya[1], O. A. Shilova[2], A. M. Nikolaev[2], A. V. Yakimansky[1]

[1]Institute of Macromolecular Compounds, Russian Academy of Sciences, St. Petersburg, Russia
[2]Grebenshchikov Institute of Silicate Chemistry, Russian Academy of Sciences, St. Petersburg, Russia

opeeva@gmail.com

The article is devoted to the covalent modification of the surface of titanium dioxide nanoparticles with polymethacrylic acid using the method of controlled atom transfer radical polymerization. For the first time, core-shell titanium dioxide nanoparticles with water-soluble shell of poly(methacrylic acid) were obtained.

Keywords: modification of nanoparticles, titanium dioxide, controlled radical polymerization, polymethacrylic acid, core-shell nanoparticles.

1. Introduction

In the recent years, nanosized titania and titania-based nanocomposites have become increasingly popular materials in the industrial-scale manufacturing of many products, agriculture, environmental science, and power engineering due to their photocatalytic [1–6], photoluminescent [7,8], semiconductor [9–11], pigment [12], and biological [13–15] properties. In particular, titanium dioxide nanoparticles are widely used in agriculture for the photocatalytic decomposition of pesticides [16–31], solar energy-assisted photocatalytic water purification (review [16] and references therein), plant disease control [32–34]. One of the most important application areas of TiO_2 nanoparticles in agriculture is treatment of crop seeds aimed at accelerating seed germination and crop vegetation [35–40]. The possibility of this practical application of titanium dioxide is related to its capability for photocatalytic activation of oxygen, which yields reactive oxygen species such as peroxide and hydroxide radicals and ions. As a result, stress tolerance of seeds is enhanced, their ability to absorb water and oxygen increase [36]. Besides, treatment of seeds with titanium dioxide nanoparticles leads to enhanced nitrogen binding by plants, increase in chlorophyll and protein contents in plants [38].

In order to increase efficiency of TiO_2-based photocatalytic systems, it is necessary to use this substance in the form of stabilized aqueous dispersions (which are generated, for instance, upon interaction with triethanolamine [41]), or in the form of core-shell nanoparticles with TiO_2 core and a water-soluble shell. The most promising synthetic method for these core-shell structures consists in modifying titanium dioxide nanoparticle surfaceswith covalently grafted chains of water-soluble hydrophilic polymers. To date, a relatively large number of works devoted to modification of TiO_2 nanoparticles with various polymers have been published. The most common method is controlled atom transfer radical polymerization (ATRP) of vinyl monomers involving α-Br-ester groups immobilized on nanoparticle surface [42–54]. In most cases, this immobilization is preceded by modification of TiO_2 surface with amino groups in the process of treatment of nanoparticles with 3-aminopropyltriethoxysilane [42, 48–51, 53] or dopamine [43]. Then, the obtained nanoparticles are treated with bromoanhydrides of 2-bromopropionic or 2-bromo-isobutyric acids [42, 43, 48–51, 53], which results in immobilization of ATRP-initiating α-Br-ester groups on nanoparticle surface. In some cases, TiO_2 nanoparticles are immediately treated with 2-Br-isobutyroyl bromide [44].

It should be noted that there are virtually no literature data on modification of TiO_2 nanoparticle surfaces with water-soluble polymers. A small number of published papers report the synthesis of titanium dioxide and zinc oxide nanoparticles modified with poly(N,N-diethylaminoethyl methacrylate), which were used as nanocontainers for anti-cancer preparations [44]. Titanium dioxide nanoparticles modified with ionized poly(styrene sulfonic acid) were used as ion exchangers for Ag^+; the products were intended for applications as TiO_2/Ag binary nanocomposite photocatalysts [45] and one of components of proton-conducting membranes [54]. There are also papers reporting the synthesis of TiO_2 nanoparticles modified with poly(oligoethylene glycol) methacrylate [47] and poly(N-isopropyl acrylamide); the latter demonstrate self-flocculation in aqueous medium at temperatures above low critical solution temperature of poly(N-isopropyl acrylamide) [51,52]. In addition, block copolymers of styrene and acrylic acid were used as micellar nanoreactors for the synthesis of TiO_2 nanoparticles and stabilization of TiO_2 aqueous dispersions [55].

In the present work, we synthesized core-shell TiO_2 nanoparticles modified with water-soluble poly(methacrylic acid) for the first time. The two-stage grafting method described above was used for immobilization of 2-Br-isobutyrate groups on the surface of titanium dioxide; the method involved successive treatment of nanoparticles with 3-aminopropyltriethoxysilane and 2-Br-isobutyroyl bromide. Then, the obtained TiO_2-based macroinitiators were used for polymerization of *tert*-butyl methacrylate (TBMA) by ATRP. The prepared core-shell TiO_2@PTBMA nanoparticles with grafted PTBMA chains were subjected to acidic hydrolysis; ester groups of the grafted chains were converted to carboxylategroups, and TiO_2@PMAA core-shell nanoparticles with poly(methacrylic acid) shells were obtained. In order to determine lengths of the grafted chains, they were isolated by selective alkaline hydrolysis of ester bonds that connect polymer chains to TiO_2 surface; molecular masses and molecular mass distributions were estimated by size exclusion liquid chromatography (SEC).

The structure of nanoparticles at all stages of synthesis was confirmed by IR spectroscopy and solid state ^{13}C NMR spectroscopy.

2. Experimental: materials

3-Aminopropyltriethoxysilane (99 %, Acros Organics), N,N-dimethylformamide (DMF) (reagent grade, Vekton, Russia), and *N*, *N*, *N'*, *N''*, *N''*-pentamethyldiethylenetriamine (PMDETA) (99 %, Aldrich) were used without additional purification. Methylene chloride (reagent grade, Vekton, Russia) and toluene (analytical grade, Vekton, Russia) were dried by heating over anhydrous calcium hydride (99.9 %, Aldrich), then distilled under vacuum. The ionic liquid (1-butyl-3-methylimidazolium chloride (BMIMCl) ($\geq$98.0 % (Aldrich)), glacial acetic acid (reagent grade, Vekton, Russia), trifluoroacetic acid (99 %, Aldrich), copper (I) bromide (99.999 %, Aldrich), 2-bromo-isobutyroyl bromide (98 %, Aldrich) were used without additional purification. *Tert*-butyl methacrylate (TBMA) (98 %, Aldrich) was twice distilled under vacuum before use, commercial TiO_2 rutile nanopowder (Plasmotherm) was used for the modification.

3. Experimental: methods

3.1. TiO_2 nanoparticles

SEM image of particles is presented in Fig. 1. According to these data, the particles have the size of 100 – 300 nm, being characterized by the specific surface area (SSA) of $\sim$ 13 m^2/g and specific pore volume of 0.044 cm^3/g [56].

X-Ray diffraction of particles is presented in Fig. 2.
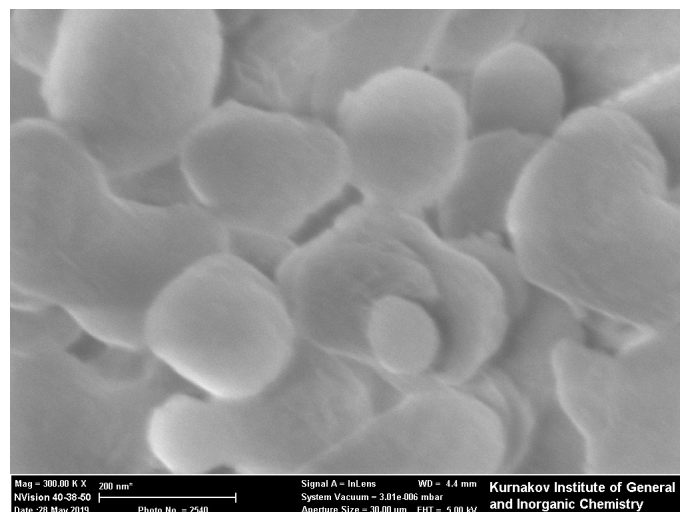

FIG. 1. SEM image of TiO_2 nanoparticles

3.2. Synthesis of TiO_2 nanoparticles modified with 3-aminopropyltriethoxysilane (APTES)

Titanium dioxide particles (0.73 g) were annealed under vacuum at 120 °C for 4 h in order to remove physically adsorbed water [57]. Then the product was cooled down to room temperature, and DMF (10 mL) was recondensed into the reaction vessel, and the mixture was subjected to ultrasound treatment for 30 min. Then the mixture was degassed thrice, and argon was passed through the system; APTES (0.5 mL) was added at cooling in an ice bath and at constant stirring. The mixture was left to stand for 24 h at constant agitation under anargon atmosphere at room temperature.
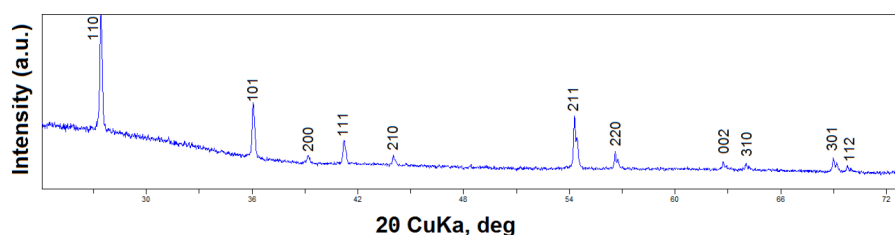
FIG. 2. X-Ray diffractogram of the TiO$_2$

The particles were isolated by centrifugation, washed thrice with DMF and thrice with methylene chloride. Yield: 0.74 g.

3.3. Synthesis of TiO$_2$-APTES-BiB macroinitiators based on TiO$_2$-APTES

Titanium dioxide nanoparticles modified with APTES (TiO$_2$-APTES, 0.5 g) were heated at 110 °C under vacuum for 2 h. Dry toluene (25 mL) was recondensed into the reaction flask; the mixture was degassed thrice, andargon was passed through the system; then 2-bromo-isobutyroyl bromide (BiB, 2 mL) was added. The reaction mixture was exposed at room temperature and constant stirring for 24 h. The product was precipitated into deionized water and washed thrice with subsequent centrifugation. The final product was obtained in the form of white powder. Yield: 0.83 g.

3.4. Synthesis of TiO$_2$-APTES-BiB-PTBMA core-shell nanoparticles with poly(*tert*-butylmethacrylate) (PTBMA) shells

The initiator (0.2 g) was put into the reaction flask together with 10 g of the ionic liquid (butyl-methyl imidazolium chloride), heated to 80 °C at constant stirring, degassed and subjected to ultrasound treatment for 30 min. Then, argon was passed through the flask; CuBr (0.063 g) and PMDETA (0.7 mL) were added. Then preliminarily distilled TBMA was added in the amounts indicated below. The mixture was exposed at 80 °C with constant agitation for 24 h. The synthesized particles were precipitated into excess distilled water and dried in air. The final product was obtained in the form of white powder.

The following samples containing various amounts of PTBMA were synthesized by addition of 7.5, 2.5, and 1 mL of TBMA: TiO$_2$-APTES-BiB-PTBMA-1, TiO$_2$-APTES-BiB-PTBMA-2, and TiO$_2$-APTES-BiB-PTBMA-3, respectively.

3.5. Elimination of grafted PTBMA chains by alkaline hydrolysis of TiO$_2$-APTES-BiB-PTBMA core-shell nanoparticles

The particles were put into 2 wt. % solution of KOH in methanol at 65 °C and exposed for 16 h. Linear PTBMA was precipitated into the methanol:water mixture and dried until constant weight was achieved.

3.6. Synthesis of TiO$_2$-APTES-BiB-PMAA core-shell nanoparticles with poly(methacrylic acid) (PMAA) shells

The synthesized TiO$_2$-APTES-BiB-PTBMA-1, TiO$_2$-APTES-BiB-PTBMA-2, and TiO$_2$-APTES-BiB-PTBMA-3 samples were dissolved in minimal amount of methylene chloride; trifluoroacetic acid (small excess) was added, then the mixture was exposed for 24 h at room temperature and constant stirring. The formed precipitate was washed with dichloromethane until neutral pH was reached, and then dried in air. Titanium dioxide particles modified with water-soluble poly(methacrylic acid) chains of various lengths (TiO$_2$-APTES-BiB-PMAA-1, TiO$_2$-APTES-BiB-PMAA-2, and TiO$_2$-APTES-BiB-PMAA-3) were obtained.

3.7. X-Ray diffraction

X-Ray diffraction was carried out using Rigaku MiniFlexII diffractometer with CuKα radiation in the 2θ range $5 - 75$ °, with step $0.02°$ at 5 °/min speed. Crystal scattering domain (CSD) length was calculated with Debye–Scherrer formula using 110 reflections.

3.8. IR spectroscopy

IR Fourier transform spectra were obtained with the aid of an IRAffinity-1S spectrometer (Shimadzu) equipped with a Quest attenuated total reflectance attachment (Specac) (diamond prism, spectral range $7800 - 400$ cm^{-1}).

3.9. NMR spectroscopy

Solid state ^{13}C NMR spectra were recorded using a Bruker Avance 400 SB instrument (1H: 400 MHz).

3.10. Size exclusion chromatography

The samples were analysed with the aid of an Agilent-1260 Infinity chromatography setup equipped with two columns packed with PLgel MIXED-C sorbent (column dimensions: 7.5×300 mm; sorbent particle size: 5 μm). Elution proceeded in isocratic regime; dimethylformamide was used as an eluent. Molecular masses and polydispersity parameters were measured by multidetector gel permeating chromatography. Characteristics of polymers were determined from the data of refractometric and viscosimetric detectors used in combination with a light scattering detector, which makes it possible to manage without calibration standards.

3.11. Scanning electron microscopy

The SEM studies were performed with the aid of a Carl Zeiss N Vision 40 instrument at an accelerating voltage of 1 kV and magnification of up to $\times 300000$.

3.12. Thermogravimetry

A DTG-60 setup (Shimadzu, Kyoto, Japan) was used for thermogravimetric (TGA) analysis to determine the amount of OH-groups chemically bound to the surface of TiO_2 nanoparticles, the samples being heated to 600 $^\circ$C at a rate of 5 $^\circ$C/min in air flow (80 mL/min).

4. Results and discussion

TiO_2 nanoparticles were studied by the TGA method in order to determine the amount of surface OH-groups bound covalently to Ti atoms. According to the procedure described in [57], the following equation was used to this aim:

$$\#OH/nm^2 = 0.625 \times \frac{2\left(\Delta W_{T_1 \to T_2}\right) N_A}{SSA \times MW_{H_2O}},\qquad(1)$$

where $\Delta W_{T_1 \to T_2}$ is the weight loss fraction upon heating the sample from $T_1 = 120$ $^\circ$C (the annealing temperature at which physically adsorbed water is removed) to $T_2 = 600$ $^\circ$C (the temperature at which no chemically bound OH-groups remain on the surface of titania nanoparticles [57]), N_A is Avogadro number, MW_{H_2O} is the molecular weight of water. As may be found from the TGA curve presented in Fig. 3, $\Delta W_{T_1 \to T_2} \approx 0.0092$. Then, according to formula (1) with $SSA = 13$ m^2/g, the surface density of chemically bound OH-groups, $\#OH/nm^2 = 29.4$ nm^{-2}. This value corresponds to $\sim 3.822 \cdot 10^{20}$ chemically bound surface OH-groups per 1 g of TiO_2 nanoparticles.
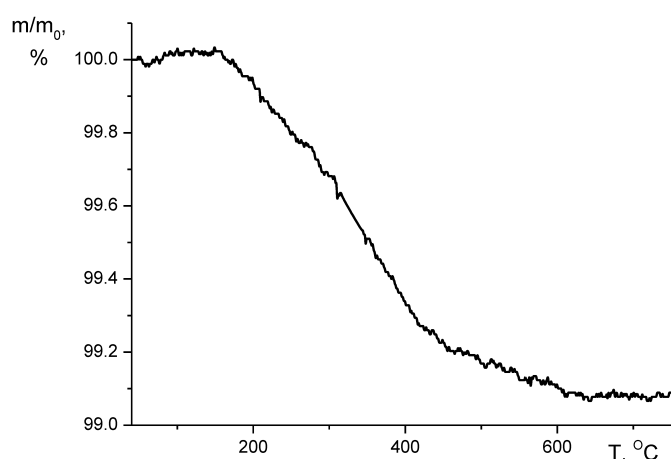

FIG. 3. TGA curve of the powder of TiO_2 nanoparticles

The scheme of the synthesis of TiO_2-APTES-BiB-PMAA core-shell particles with titanium dioxide cores and poly(methacrylic acid) shells included several stages; the synthesis scheme is presented in Fig. 4.

At the first stage, titanium dioxide nanoparticles were treated with APTES in order to graft primary amino groups onto nanoparticles' surface. The taken amount of APTES (0.5 g) corresponds to an approximately 5-fold molar excess
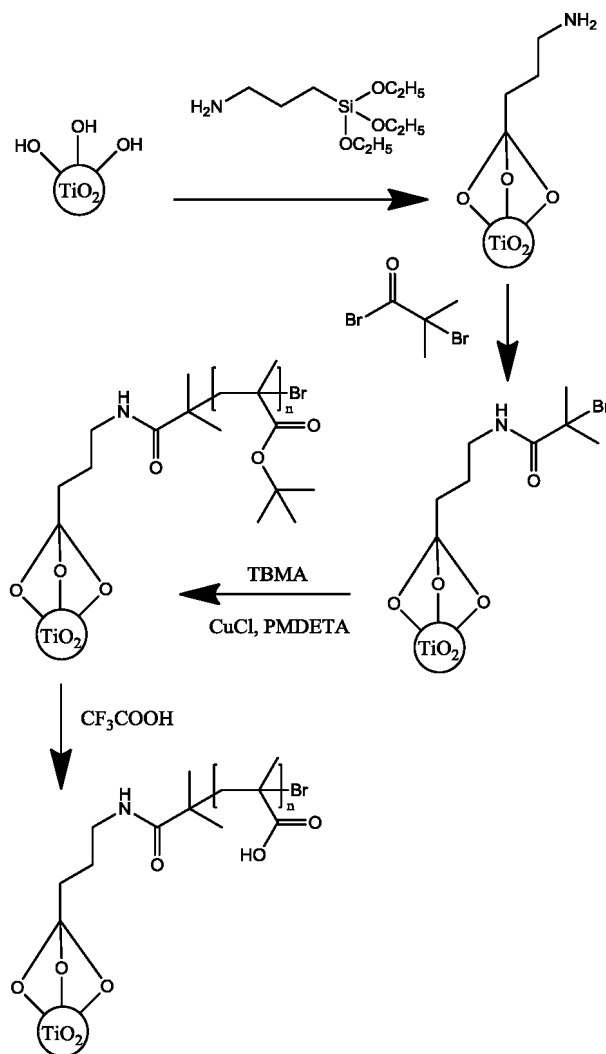
FIG. 4. Scheme of the synthesis of TiO_2-APTES-BiB-PMAA core-shell particles with titanium dioxide cores and poly(methacrylic acid) shells

of APTES with respect to chemically bound surface OH-groups in the taken amount of annealed TiO_2 nanoparticles (0.73 g). The presence of amino groups on the surface of the synthesized particles is confirmed by comparison of ^{13}C NMR spectra of the initial titanium dioxide nanoparticles (Fig. 5a) and the nanoparticles treated with APTES (Fig. 5b). The spectrum of the initial nanoparticles presented in Fig. 5a indicates that they have pure surface, i.e. there are no carbon-containing groups or compounds on TiO_2.

Meanwhile, the spectrum of TiO_2-APTES nanoparticles contains the signals attributed to carbon atoms of amino-propyl groups near 10, 25 and 45 ppm. In addition, the presence of surface amino groups is confirmed by comparison of IR spectra of the initial TiO_2 nanoparticles before and after treatment with APTES (Fig. 6). The following bands appear in the spectra of APTES derivatives: (i) wide bands in the region 1560 – 1570 cm^{-1} attributed to deformation vibrations of primary amino groups [58]; (ii) C–N stretching vibration band of APTES at 1323 cm^{-1} [58]; (iii) the bands near 1140 cm^{-1} assigned to valence vibrations of C–N bond in primary amines [59].

At the second stage, surface amino groups of TiO_2-APTES nanoparticles were acylated with 2-bromo-isobutyroyl bromide to graft 2-bromo-isobutyrate groups onto nanoparticles' surface; these fragments are able to initiate controlled atom transfer radical polymerization. ^{13}C NMR spectrum of the resulting TiO_2-APTES-BiB nanoparticles is presented in Fig. 5c. Comparison of this spectrum with NMR spectrum of TiO_2-APTES (Fig. 5b) demonstrates that the former-contains new signals attributed to methyl carbon atoms (32 ppm), quaternary carbon atoms (52 ppm), and carbonyl atoms in 2-bromo-isobutyrate fragments (170 – 180 ppm). Thus, the ^{13}C NMR spectroscopy data confirm successful preparation of TiO_2-APTES-BiB nanoparticles with surface 2-bromo-isobutyrate groups.
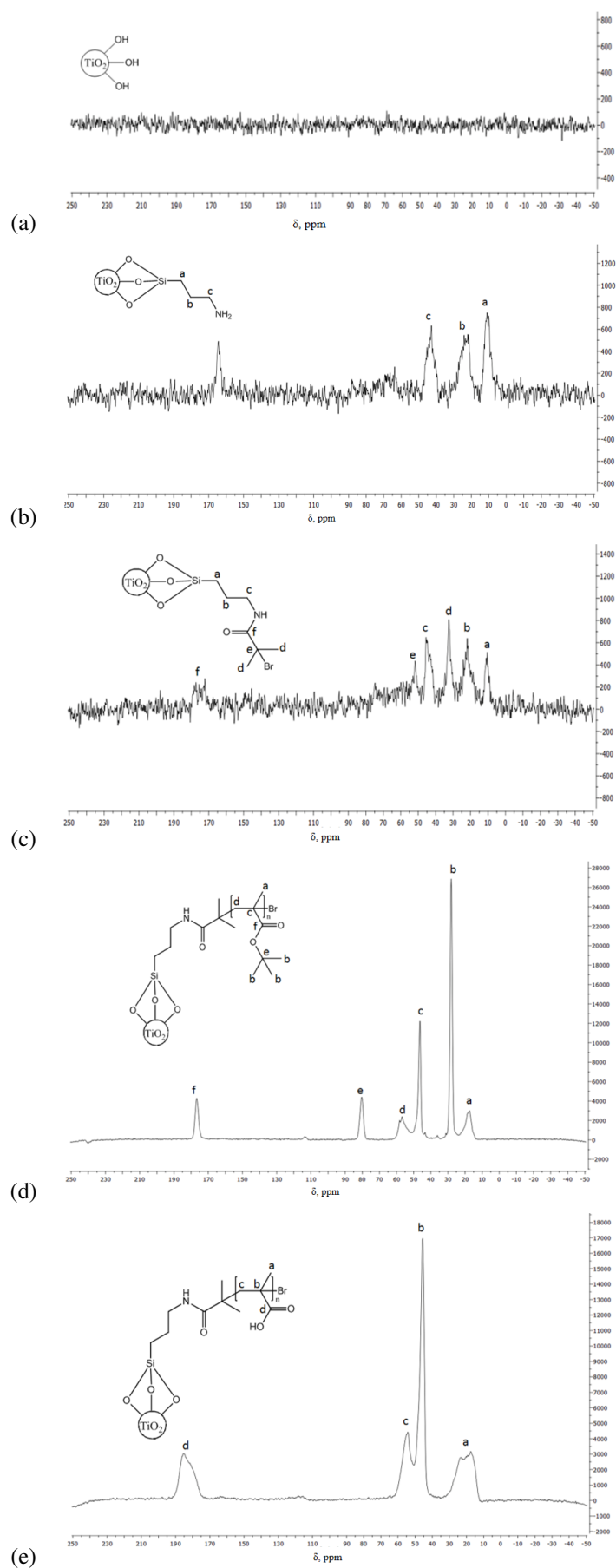
FIG. 5. Solid state ^{13}C NMR spectra of the initial titanium dioxide (a), TiO$_2$-APTES (b), TiO$_2$-APTES-BiB (c), TiO$_2$-APTES-BiB-PTBMA (d) and TiO$_2$-APTES-BiB-PMAA particle (e)
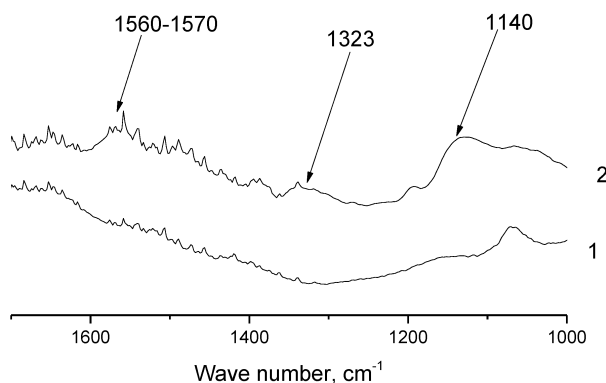
FIG. 6. IR spectra of the initial titanium oxide (1) and TiO$_2$-APTES nanoparticles (2)

The synthesized TiO$_2$-APTES-BiB nanoparticles were used in polymerization of *tert*-butyl methacrylate according to ATRP mechanism. The TiO$_2$-APTES-BiB-PTBMA nanoparticles were synthesized; their ^{13}C NMR spectrum (Fig. 5d) virtually coincides with that of poly(*tert*-butyl methacrylate). It includes signals related to all PTBMA carbon atoms: methylene group (~ 55 ppm) and α-carbon atom (~ 45 ppm) of PTBMA backbone, methyl group at α-carbon (~ 18 ppm), signals of carbonyl atoms (~ 180 ppm), quaternary carbon atoms (~ 80 ppm) and methyl carbon atoms (~ 28 ppm) of side ester groups. It should be noted that signals of TiO$_2$-APTES-BiB macroinitiator cannot be registered due to its extremely low amount in TiO$_2$-APTES-BiB-PTBMA samples.

The grafted PTBMA chains were eliminated from TiO$_2$-APTES-BiB-PTBMA nanoparticles in the process of alkaline hydrolysis, which destructs the ester bonds connecting polymer chains to macroinitiator fragments. Conditions of alkaline hydrolysis were selected so as to prevent transformation of side ester fragments of PTBMA [60]. The isolated linear PTBMA was analyzed by multidetector size exclusion liquid chromatography with the so-called triple detection (a combined analysis of the data provided by refractometric, viscosimetric and light scattering detectors [61]). It was found that the isolated PTBMA chains have the following characteristics: $M_n = 70000$, $M_w = 120000$, $M_w/M_n = 1.7$. Thus, the PTBMA chains grafted onto the surface of titanium dioxide nanoparticles are long (polymerization degree about 500) and have relatively narrow molecular mass distributions.

At the last synthesis stage, TiO$_2$-APTES-BiB-PTBMA nanoparticles were subjected to "dry" acidic hydrolysis that affected side ester groups of PTBMA chains. Hydrolysis proceeded under the action of anhydrous trifluoroacetic acid and was accompanied by release of gaseous isobutylene and transformation of ester groups into carboxylic fragments. As a result, we obtained TiO$_2$-APTES-BiB-PMAA nanoparticles with water-soluble poly(methacrylic acid) shells, their polymerization degree being the same as that of the initial PTBMA chains. ^{13}C NMR spectrum of these nanoparticles given in Fig. 5e confirms the presence of poly(methacrylic acid) in the shell. Thus, the spectrum contains the signals attributed to methylene group atoms (~ 55 ppm) and α-carbon atoms(~ 45 ppm) of PMAA backbone, the signals of methyl group at α-carbon atom (~ 20 ppm) and carboxylic carbon atom (~ 185 ppm). At the same time, there are no peaks related to quaternary carbon atoms and methyl carbon atoms of side ester groups, which indicates complete transformation of TiO$_2$-APTES-BiB-PTBMA into TiO$_2$-APTES-BiB-PMAA.

According to the polymerization degree of ~ 500 of PMAA chains in the shell of TiO$_2$-APTES-BiB-PMAA particles, the shell is ~ 125 nm thick, taking into account that the monomer unit length of PMAA side chains is ~ 0.25 nm. The UV spectrum of the synthesized TiO$_2$-APTES-BiB-PMAA nanoparticles in water solution is presented in Fig. 7.

As seen from Fig. 7, the spectrum shows a typical absorption of TiO$_2$ cores below 400 nm [62].

5. Conclusions

Modification of nanoparticles surface with polymers is of great interest for various practical applications. The obtained TiO$_2$-APTES-BiB-PMAA core-shell nanoparticles with a water-soluble shell can be used, in particular, for treatment of agricultural crop seeds with the purposes of enhancing their germination and increasing growth rate. Each nanoparticle contains photocatalytically active core of titanium dioxide that increases photosynthesis efficiency and poly(methacrylic acid) shell providing solubility of the product in water. It should be noted that the synthesis of titanium dioxide nanoparticles with grafted poly(methyl methacrylate) chains has been described in the literature [63]. However, water-soluble shells of poly(methacrylic acid) were grafted onto the surface of TiO$_2$ nanoparticles for the first time.
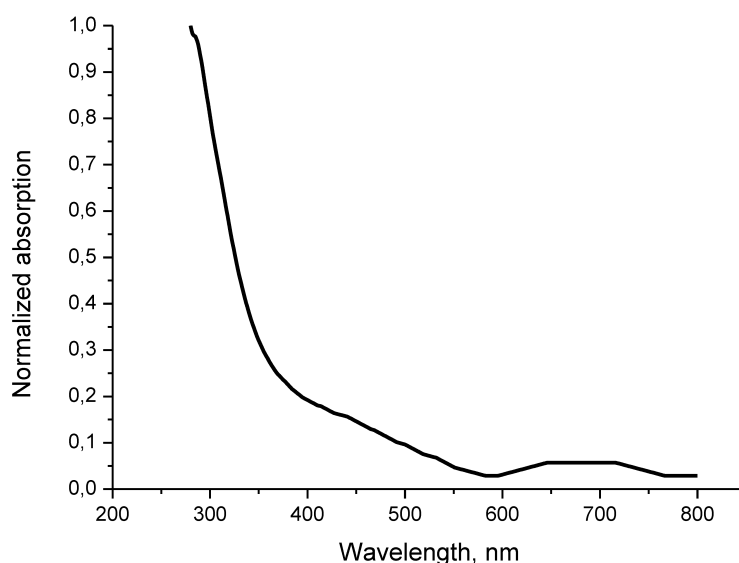
FIG. 7. UV spectrum of TiO_2-APTES-BiB-PMAA nanoparticles in water

Acknowledgements

References

[1] Byrne C., Subramanian G., Pillai S.C. Recent advances in photocatalysis for environmental applications. *Journal of Environmental Chemical Engineering*, 2018, **6**, P. 3531–3555.

[2] Colmenares J.C., Varma R.S., Lisowski P. Sustainable hybrid photocatalysts: titania immobilized on carbon materials derived from renewable and biodegradable resources. *Green Chemistry*, 2016, **18**, P. 5736–5750.

[3] Krasilin A.A., Bodalyov I.S., et al. On an adsorption/photocatalytic performance of nanotubular $Mg_3Si_2O_5(OH)_4$/TiO_2 composite. *Nanosystems: Physics, Chemistry, Mathematics*, 2018, **9**, P. 410–416.

[4] Kolesnik I.V., Lebedev V.A., Garshev A.V. Optical properties and photocatalytic activity of nanocrystalline TiO_2 doped by 3d-metal ions. *Nanosystems: Physics, Chemistry, Mathematics*, 2018, **9**, P. 401–409.

[5] Kozlov D.A., Lebedev V.A., et al The microstructure effect on the Au/TiO_2 and Ag/TiO_2 nanocomposites photocatalytic activity. *Nanosystems: Physics, Chemistry, Mathematics*, 2018, **9**, P. 266–278.

[6] Szanyi J., Kwak J.H., Photo-catalytic oxidation of acetone on a TiO_2 powder: An in situ FTIR investigation. *Journal of Molecular Catalysis A: Chemistry*, 2015, **406**, P. 213–223.

[7] Ulyanova E.S., Zamyatin D.A., Kolosov V.Yu., Shalaeva E.V. Visible light photoluminescence in TiO_2/CdS nanopowders synthesized by sol-gel route: effect of gel aging time. *Nanosystems: Physics, Chemistry, Mathematics*, 2020, **11**, P. 480–487.

[8] Zavialova A.Yu., Bugrov A.N., et al Structure and photoluminescent properties of TiO_2:Eu^{3+} nanoparticles synthesized under hydro and solvothermal conditions from different precursors. *Nanosystems: Physics, Chemistry, Mathematics*, 2019, **10**, P. 361–373.

[9] Wang Y., Sun C.,et al. The Application of Nano-TiO_2 Photo Semiconductors in Agriculture. *Nanoscale Research Letters*, 2016, **11**, 529.

[10] Morozova P.A., Petukhov D.I. Preparation of Au/TiO_2/Ti memristive elements via anodic oxidation. *Nanosystems: Physics, Chemistry, Mathematics*, 2017, **8**, P. 823–829.

[11] Ganeshraja A.S., Anbalagan K. Participation of nanocrystalline TiO_2 Surface in the electron transfer between semiconductor solid and adsorbed cobalt(III)-RPY complex. *Nanosystems: Physics, Chemistry, Mathematics*, 2013, **4**, P. 276–287.

[12] Gazquez M.J., Bolivar J P., Garcia-Tenorio R., Vaca F. A review of the production cycle of titanium dioxide pigment. *Materials Sciences and Applications*, 2014, **5**, P. 441–458.

[13] Dimkpa C.O. Can nanotechnology deliver the promised benefits without negatively impacting soil microbial life. *Journal of Basic Microbiology*, 2014, **54**, P. 889–904.

[14] Peller J., Wies O., Kamat P.V. Hydroxyl Radical's Role in the Remediation of a Common Herbicide, 2,4-Dichlorophenoxyacetic Acid (2,4-D). *Journal of Physical Chemistry A*, 2004, **108**, P. 10925–10933.

[15] Hou J., Wang X., et al. Toxicity and mechanisms of action of titanium dioxide nanoparticles in living organisms. *Journal of environmental sciences (China)*, 2019, P. 7540–7553.

[16] Guan H.N., Chi D.F., Yu J., Li X.C. A novel photodegradable insecticide: preparation, characterization and properties evaluation of nano-Imidacloprid. *Pesticide Biochemistry and Physiology*, 2008, **92**, P. 83–91.

[17] Ahmed S., Rasul M.G., Brown R., Hashib M.A. Influence of parameters on the heterogeneous photocatalytic degradation of pesticides and phenolic contaminants in wastewater. *J. Environ. Manage*, 2011, **92**, P. 311–330.

[18] Parida K.M., Sahu N., et al. Preparation, characterization, and photo-catalytic activity of sulfate-modified titania for degradation of methyl orange under visible light. *J Colloid Interface Sci.*, 2008, **318**, P. 231–237.

[19] Aragay G., Pino F., Merkoç I.A. Nanomaterials for sensing and destroying pesticides. *Chemical Reviews*, 2012, **112**, P. 5317–5338.

[20] Lee K., Ku H., Pak D. OH radical generation in a photocatalytic reactor using TiO$_2$ nanotube plates. *Chemosphere*, 2016, **149**, P. 114–120.

[21] Devipriya S., Yesodharan S. Photocatalytic degradation of pesticide contaminants in water. *Solar Energy Materials & Solar Cells*, 2005, **86**, P. 309–348.

[22] Rabindranathan S., Devipriya S., Yesodharan S. Photocatalytic degradation of phosphamidon on semiconductor oxides. *Journal of Hazardous Materials*, 2003, **102**, P. 217–229.

[23] Lhomme L., Brosillon S., Wolbert D. Photocatalytic degradation of pesticides in pure water and a commercial agricultural solution on TiO$_2$ coated media. *Chemosphere*, 2008, **70**, P. 381–386.

[24] Marien C.B.D., Cottineau T., Robert D., Drogui P. TiO$_2$ nanotube arrays: influence of tube length on the photocatalyticdegradation of Paraquat. *Applied Catalysis B: Environmental*, 2016, **194**, P. 1–6.

[25] Bzdon S., Goralski J., et al. Radiation-induced synthesis of Fe-doped TiO$_2$: characterization and catalytic properties. *Radiation Physics and Chemistry*, 2012, **81**, P. 59–63.

[26] Attarchi N., Montazer M., Toliyat T. Ag/TiO$_2$/β-CD nano composite: preparation and photo catalytic properties for methylene blue degradation. *Applied Catalysis A: General*, 2013, **467**, P. 107–116.

[27] Zhang X., Wu F., et al. Photocatalytic degradation of 4,4'-biphenol in TiO$_2$ suspension in the presence of cyclodextrins: a trinity integrated mechanism. *Journal of Molecular Catalysis A: Chemistry*, 2009, **301**, P. 134–139.

[28] Ramos-Delgado N.A., Gracia-Pinilla M.A., et al. Solar photocatalytic activity of TiO$_2$ modified with WO3 on the degradation of an organophosphorus pesticide. *Journal of Hazardous Mater*, 2013, **263**, P. 36–44.

[29] Vamathevan V., Amal R., et al. Silver metallization of titania particles: effects on photoactivity for the oxidation of organics. *Journal of Gastrointestinal Surgery*, 2015, **19**, P. 1–6.

[30] Behnajady M.A., Modirshahla N., Hamzavi R. Kinetic study on photocatalytic degradation of C.I. acid yellow 23 by ZnO photocatalyst. *Journal of Hazardous Materials*, 2006, **133**, P. 226–232.

[31] Leghari S.A.K., Sajjad S., Chen F., Zhang J. WO3/TiO$_2$ composite with morphology change via hydrothermal template-free route as an efficient visible light photocatalyst. *Chemical Engineering Journal*, 2011, **166**, P. 906–915.

[32] Yao K.S., Wang D.Y., et al. Photocatalytic bactericidal effect of TiO$_2$ thin film on plant pathogens. *Surface & Coatings Technology*, 2007, **201**, P. 6886–6888.

[33] Yao K.S., Wang D.Y., et al. Photocatalytic disinfection of phytopathogenic bacteria by dye-sensitized TiO$_2$ thin film activated by visible light. *Surface & Coatings Technology*, 2007, **202**, P. 1329–1332.

[34] Cui H.X., Yang G.C., et al. Biological effects of PAS TiO$_2$ sol on disease control and photosynthesis in cucumber (Cucumis sativus L). *Australian Journal of Crop Science*, 2013, **7**, P. 99–103.

[35] Shilova O.A., Khamova T.V., et al. Synthesis and Research of Functional Layers Based on Titanium Dioxide Nanoparticles and Silica Sols Formed on the Surface of Seeds of Chinese Cabbage. *Russian Journal of Applied Chemistry*, 2020, **93** (1), P. 25–34.

[36] Khot L.R., Ehsani R., et al. Applications of nanomaterials in agricultural production and crop protection. A review. *Crop Protection*, 2012, **35**, P. 64–70.

[37] Zheng L., Hong F., Lu S., Liu C. Effect of nano-TiO$_2$ on strength of naturally aged seeds and growth of spinach. *Biological Trace Element Research*, 2005, **104**, P. 83–91.

[38] Song G., Gao Y., et al. Physiological effect of anatase TiO$_2$ nanoparticles on Lemna minor. *Environmental Toxicology and Chemistry*, 2012, **31**, P. 2147–2152.

[39] Yang F., Liu C., et al. The improvement of spinach growth by nano-anatase TiO$_2$ treatment is related to nitrogen photoreduction. *Biological Trace Element Research*, 2007, **119**, P. 77–88.

[40] Raliya R., Biswas P., Tarafdar J.C., TiO$_2$ nanoparticle biosynthesis and its physiological effect on mung bean (Vigna radiata L). *Biotechnology Reports*, 2015, **5**, P. 22–26.

[41] Palmqvist N.G.M., Bejai S., et al. Nano titania aided clustering and adhesion of beneficial bacteria to plant roots to enhance crop growth and stress management. *Scientific Reports*, 2015, **5**, 10146.

[42] Wang Y., Liu L., et al. Synthesis of Modified TiO$_2$ Nanoparticles with Polyacrylonitrile and Poly(hydroxyethyl acrylate) via ATRP. *Chemistry Select*, 2020, **5**, P. 4695–4700.

[43] Kopec M., Spanjers J., et al. Surface-initiated ATRP from polydopamine-modified TiO$_2$ nanoparticles. *European Polymer Journal*, 2018, **106**, P. 291–296.

[44] Ensafi A.A., Khoddami E., Nabiyan A., Rezaei B. Study the role of poly(diethyl aminoethyl methacrylate) as a modified and grafted shell for TiO$_2$ and ZnO nanoparticles, application in flutamide delivery. *Reactive & Functional Polymers*, 2017, **116**, P. 1–8.

[45] Park J.T., Lee C.S., Park C.H., Kim J.H. Preparation of TiO$_2$/Ag binary nanocomposite as high-activity visible-light-driven photocatalyst via graft polymerization. *Chemical Physics Letters*, 2017, **685**, P. 119–126.

[46] Maeda S., Fujita M., et al. Preparation of Transparent Bulk TiO$_2$/PMMA Hybrids with Improved Refractive Indices via an in Situ Polymerization Process Using TiO$_2$ Nanoparticles Bearing PMMA Chains Grown by Surface-Initiated Atom Transfer Radical Polymerization. *ACS Applied Materials & Interfaces*, 2016, **8**, P. 34762–34769.

[47] Mai T.B., Tran T.N., et al. Synthesis and characterization of poly(oligoethyleneglycol methacrylate)-g-TiO$_2$ nanocomposites via surface-initiated ARGET ATRP. *Molecular Crystals and Liquid Crystals*, 2014, **602**, P. 118–125.

[48] Liu L., Chen H., Yang F. Enhancing membrane performance by blending ATRP grafted PMMA-TiO$_2$ or PMMA-PSBMA-TiO$_2$ in PVDF. *Separation and Purification Technology*, 2014, **133**, P. 22–31.

[49] Zhang G., Lu S., et al. Novel polysulfone hybrid ultrafiltration membrane prepared with TiO$_2$-g-HEMA and its antifouling characteristics. *Journal of Membrane Science*, 2013, **436**, P. 163–173.

[50] Cui W.-W., Tang D.-Y., Gong Z.-L. Electrospun poly(vinylidene fluoride)/poly(methyl methacrylate) grafted TiO$_2$ composite nanofibrous membrane as polymer electrolyte for lithium-ion batteries. *Journal of Power Sources*, 2013, **223**, P. 206–213.

[51] Gong Z.-L., Tang D.-Y., Guo Y.-D. The fabrication and self-flocculation effect of hybrid TiO$_2$ nanoparticles grafted with poly(N-isopropylacrylamide) at ambient temperature via surface-initiated atom transfer radical polymerization. *Journal of Materials Chemistry*, 2012, **22**, P. 16872–16879.

[52] Chen H., Pan S., et al. Preparation of thermo-responsive superhydrophobic TiO$_2$/poly(N-isopropylacrylamide) microspheres. *Applied Surface Science*, 2012, **258**, P. 9505–9509.

[53] Xiong L., Liang H., Wang R., Chen L. A novel route for the synthesis of poly(2-hydroxyethyl methacrylate-co-methyl methacrylate) grafted titania nanoparticles via ATRP. *Journal of Polymer Research*, 2011, **18**, P. 1017–1021.

[54] Park J.T., Koh J.H., et al. Proton-conducting nanocomposite membranes based on P(VDF-co-CTFE)-g-PSSA graft copolymer and TiO$_2$-PSSA nanoparticles. *International Journal of Hydrogen Energy*, 2011, **36**, P. 1820–1827.

[55] Akpolat L.B., Cakir B.A., Topel O., Hoda N. Synthesis of TiO$_2$ nanoparticles by self-assembling reverse micelle cores of PS-b-PAA for functional textile applications. *Materials Research Bulletin*, 2015, **64**, P. 117–122.

[56] Shilova O.A., Panova G.G., et al. Properties, and Phytoprotective Functions of Titanium Dioxide Nanopowders and Their Aqueous Suspensions. *Russian Journal of Inorganic Chemistry*, 2021, **66**, P. 765–772.

[57] Mueller R., Kammler H.K., Wegner K., Pratsinis S.E. OH Surface Density of SiO$_2$ and TiO$_2$ by Thermogravimetric Analysis. *Langmuir*, 2003, **19**, P. 160–165.

[58] Ou B., Li D., et al. Functionalized TiO$_2$ nanoparticle containing isocyanate groups. *Material Chemistry and Physics*, 2012, **135**, P. 1104–1107.

[59] Zhao J., Milanova M., Warmoeskerken M.M.C.G., Dutschk V. Surface modification of TiO$_2$ nanoparticles with silane coupling agents. *Colloids and Surfaces A: Physicochemical and Engineering Aspects*, 2012, **413**, P. 273– 279.

[60] Yakimansky A.V., Meleshko T.K., et al. Novel Regular Polyimide-graft-Poly(methacrylic acid) Brushes: Synthesis and Possible Applications as Nanocontainers of Cyanoporphyrazine Agents for Photodynamic Therapy. *Journal of Polymer Science, Part A: Polymer Chemistry*, 2013, **51**, P. 4267–4281.

[61] Kashina A.V., Meleshko T.K., et al. Synthesis of Pentablock Copolymers of the Mixed Linear-Brush Topology by Controlled Radical Polymerization and Ring-Opening Polymerization Reactions. *Polymer Science, Series C*, 2019, **61**, P. 174–185.

[62] Pugachevskii M.A. Ultraviolet absorption spectrum of laser-ablated titanium dioxide nanoparticles. *Technical Physics Letters*, 2013, **39**, P. 36–38.

[63] Raghuraman G.K., Rühe J., Dhamodharan R. Grafting of PMMA brushes on titania nanoparticulate surface via surface-initiated conventional radical and "controlled" radical polymerization (ATRP). *Journal of Nanoparticle Research*, 2008, **10**, P. 415–427.

Catalytic fullerenol action on Chlorella growth in the conditions of limited resource base and in the conditions of oxidation stress

L. V. Gerasimova[1], N. A. Charykov[1,2], K. N. Semenov[1,3], V. A. Keskinov[1], A. V. Kurilenko[1],
Zh. K. Shaimardanov[4], B. K. Shaimardanova[4], N. A. Kulenova[4], D. G. Letenko[5], Ayat Kanbar[1]

[1]Saint Petersburg State Technological Institute (Technical University), Moskovsky prospect, 26,
Saint Petersburg, 190013, Russia

[2]Saint Petersburg Electrotechnical University "LETI", ul. Professora Popova 5, 197376,
Saint Petersburg, Russia

[3]Saint Petersburg State University, 7/9 Universitetskaya emb., Saint Petersburg, 199034, Russia

[4]D. Serikbayev East Kazakhstan state technical university, A. K. Protozanov Street, 69,
UstKamenogorsk city, 070004, The Republic of Kazakhstan

[5]Saint Petersburg State University of Architecture and Civil Engineering (SPSUACE),
2nd Krasnoarmeiskaya St. 4, 190005, Saint Petersburg, Russia

keskinov@mail.ru

Catalytic fullerenol $C_{60}(OH)_{24}$ action on Chlorella Vulgaris growth in the conditions of limited resource growth base and in the conditions of oxidative stress are reported. Chlorella growth or oppression were investigated in open transparent in the visible area cylindrical polystyrene test tubes at room temperature under illumination by standard incandescent lamp for the period 9 days. Catalyst concentration were varied in the range $0.01 - 1.0$ g/dm^3. Oxidative stress was organized by the addition of hydrogen peroxide with the concentration 1.0 g/dm^3. Chlorella Vulgaris concentrations were determined by the method of turbidimetry – by the determination of optical density of scattered light in the direction of propagation of the incident beam at wavelength 664 nm. Obtained kinetic data were processed by the method of formal classical kinetics. The pseudo-order of the process Chlorella Vulgaris growth in the conditions of limited resource, according to Chlorella, is -2; the curve of the dependence of Chlorella concentration against time is concave at all fullerenol concentrations. The pseudo-order of the process Chlorella Vulgaris suppression in the conditions of oxidative stress, according to Chlorella, is $+2$, the curve of the dependence of Chlorella concentration against time is convex at all fullerenol concentrations. The kinetics of Chlorella Vulgaris growth in the conditions of limited resource was also processed by model Verhulst equation of logisitic growth, and this equation describes the kinetics as accurately and adequately as possible. The authors have established, that in the case of the conditions of limited resource, fullerenol at low concentrations (less than 0.1 g/dm^3) catalyzes-accelerates Chlorella growth and at higher concentrations ($0.1 - 1.0$ g/dm^3) inhibits Chlorella growth. For the conditions of oxidative stress, authors have established, that at all fullerenol concentrations, it considerably inhibits suppression-depopulation of Chlorella processes, so fullerenol proves enough strong anti-oxidant action. It was demonstrated, that Verhulst equation maybe satisfactory used for the description of different natural process.

Keywords: fullerenol, catalyst, inhibitor, hydrogen peroxide, Chlorella growth, suppression.

Received: 13 March 2021

Revised: 17 May 2021

1. Introduction

Light fullerenes (C_{60} and C_{70}) may be more or less effectively used in different fields of science and technics, but its application is sufficiently limited by practically complete insolubility and incompatibility with water and aqueous solutions. Covalent functionalization is the most reliable way to obtain systems based on fullerenes which are suitable for biomedical applications. It deals with the structures of such molecules can be precisely determined (using X-ray crystallography), and their pharmacokinetic and dynamic behavior is better understood. This belongs also to the most of the light fullerene derivatives (halogen, amino, hydro and others). Meanwhile, water soluble fullerenes may be used in more wide ranges of applications: machinery, building, medicine, pharmacology (as the result of compatibility with water, physiological solutions, blood, lymph, liquor, gastric juice), agriculture, crop production, cosmetics. Poly-hydroxylated fullerenes (fullerenols) and adducts of light fullerenes C_{60} and C_{70} with carboxylic acids and amino-acids are the perspective bioactive fairly water-soluble fullerene derivatives.

This article continues the series of articles investigating the synthesis, identification and properties of fullerenols. Some articles are devoted to the investigation of the influence of water-soluble fullerene derivatives on plants growth and development and common bioactivity (for example [1–11]). The common conclusion in the part, related to the bio-activity of water soluble adducts of light fullerenes on plant is the following – these derivatives have a beneficial

effect on grow and development of plants, in any case when using not very high concentrations of the latter – $n \cdot 10^2$ – $n \cdot 10^3$ g/dm^3.

The question of toxicity of fullerenes themselves, and water soluble fullerenes in particular, is closely related with bio-activity. Toxicity of fullerenes and their derivatives were investigated and discussed widely. In one of the last works [12, 13] a detailed and complete overview is given. A bibliography on the theme of fullerene toxicity [14–40] covers quite an extensive number of works over the 20 last years. The main conclusions are the following:

- Numerous further studies have also not shown any adverse or toxic effects of fullerene on organism. According to the Toxicological classification of substances exhibiting toxicity at doses above 1 g/kg, belong to the class of non-toxic substances. A long experiment was conducted in rats the diet of which added fullerene in the form of solution in olive oil [16]. The experiment lasted 5.5 years, as a control diet with the addition of just olive oil and water. Fullerene almost doubled the life expectancy of rats. Different diets did not affect the dynamics of animal weight, which also indicates the absence of toxic effects in.
- It is shown in [14] that fullerene in the form of water colloidal dispersion also does not show toxic proper-ties, but only shows the properties of antioxidant. This conclusion is based on more than ten years of biological tests of fullerene dispersion in various experiments in vitro and in vitro. It did not reveal any toxic effects (at concentrations from 10^{-9} to 10^{-4} mol/dm^3 and at total doses up to 25 mg/kg).
- The toxicology of water-soluble derivatives of fullerene has been the subject of many discussions, but the vast majority of works have shown their toxicity is low. So, water-soluble fullerene derivatives do not exhibit acute toxicity in vivo, even at sufficiently high doses. For example, the value for fullerenol in intraperitoneal mice is 1.2 g/kg [38, 39]. Parenteral administration of the amino-acid derivative to mice at a dose of 80 mg/kg had no effect on the behavior and viability of mice for 6 months [16].
- In [12] it was shown, that water solutions of octo-adduct C_{60} with arginine are characterized by acceptable (i.e., low) toxicity and the only one most concentrated solution (with concentration 0.25 g/dm^3) can be char-acterized by moderate toxicity (at the lower limit).
- Research [41] showed water solubility solutions of C_{60} no toxicity in in vitro experiments on Chinese hamster V79 cell lines.
- The cytotoxicity of C_{60} in water solution was noted in the research [42]. It showed that the cytotoxicity of water-soluble fullerene species is a sensitive function of surface derivatization; in two different human cell lines, the lethal dose of fullerene changed over 7 orders of magnitude with relatively minor alterations in fullerene structure.
- Authors [43] showed that $C_{60}(OH)_{24-26}$ did not show acute or chronic toxic effects in model organisms from four different kingdoms. There was evidence of increased growth and increased life expectancy that could have profound effects in environmental research.
- The antioxidant ability of $C_{60}(OH)_{24}$ has been shown to modulate the cytotoxic effects of the chemothera-peutic agent, doxorubicin (DOX), which causes ROS-mediated oxidative stress [44–46].
- The biological activity of a number of fullerenols with a different number of hydroxyl groups: $C_{60}(OH)_{12-14}$, $C_{60}(OH)_{18-24}$, $C_{60}(OH)_{30-38}$, was studied [47]: $C_{60}(OH)_{12-14}$, was insoluble in water and did not show biological activity when introduced into cell cultures in the form of suspensions. While $C_{60}(OH)_{18-24}$ was soluble and had maximum antiviral and protective activity.
- Fullerenols used in this work [48] demonstrated negligible toxicity even at high concentrations as a result of a specifically developed manufacturing process.

The following property of water soluble fullerene derivatives, which is closely connected with bio-activity is anti-oxidant activity, which was investigated in many works, in particular [3, 49–64]. The antioxidant properties of fullerenols were previously investigated. Several mechanisms for the antioxidant activity of fullerenol nanoparticles have been proposed [4]. All authors note very strong anti-oxidant activity of all water soluble fullerene derivatives. However, authors [49, 51] determined this bulk anti-oxidant activity weaker one in comparison with such classical anti-oxidant agents as ascorbic acid. But these derivatives possess one very rare and useful property, namely – the ability to reversible absorption of oxidant particles, or to multiple sorption-desorption oh the last ones.

In the present article, we report about the investigation of fullerenol of light fullerene $C_{60}(OH)_{24}$ in bio-testing, using as test micro-organism "Chlorella vulgaris beijer" – a very popular alga for laboratory studies. We shall re-port about the kinetics in the system: chlorella vulgaris beijer (bio-component)-fullerenol (catalyst-inhibitor)-water (solvent) in the presence of light (visional region wavelength) and CO_2 (dissolved in water solution).
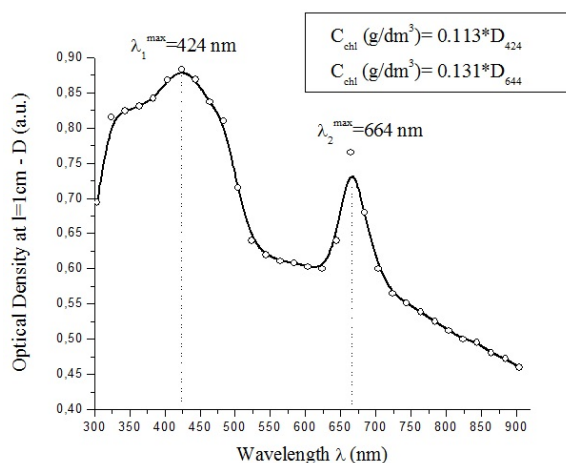
FIG. 1. Electronic spectrum of water suspension of Chlorella Vulgaris with concentration $C_{chl} = 1$ g/dm^3 without fullerenol

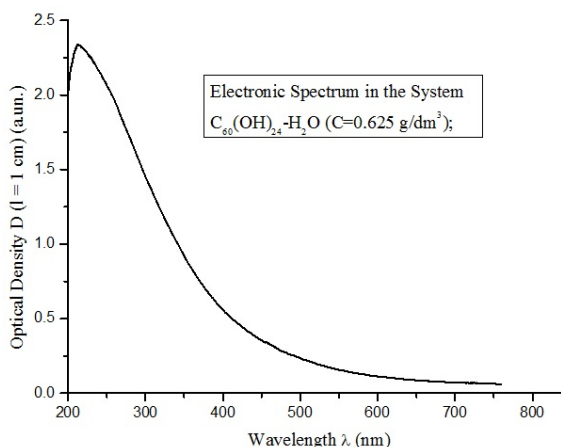FIG. 2. Electronic spectrum of $C_{60}(OH)_{24}$ water solution (concentration of $C_{60}(OH)_{24}$ – $C_{fullerenol} = 0.625$ g/dm^3)

2. Materials and experimental methods

In the investigations we used a suspension of Chlorella Vulgaris "Detox Urban Drink" Belive Organic (Saint Petersburg, Russia) with chlorella content 1 g/dm^3, recalculated on solids. Also we used fullerenol $C_{60}(OH)_{24}$, which was synthesized from Br-derivative - $C_{60}Br_{24}$, according to previous method [63,64]. $C_{60}(OH)_{24}$ was synthesized by the treatment of these product by boiling water-dioxane mixture with the dissolved NaOH. Then sodium fullerenes forms $C_{60}(OH)_{24-\delta}(ON\alpha)_\delta$ were neutralized and washed in the Soxlet-extractor.

Chlorella growth or suppression were investigated in open transparent in the visible area cylindrical polystyrene test tubes at room temperature under illumination by standard incandescent lamp (Phillips E27 – 40 Wt) for the period of 9 days. Catalyst concentrations were varied in the range $0.01 – 1.0$ g/dm^3. Oxidative stress was organized by the addition of hydrogen peroxide with the concentration 1.0 g/dm^3.

Chlorella Vulgaris concentrations were determined by the method of turbidimetry – by the determination of optical density of scattered light in the direction of propagation of the incident beam at wavelength $\lambda = 664$ nm $-D_{664}$. The spectrum was obtained relative to the comparison solution – water solution of $C_{60}(OH)_{24}$ with the same concentraion, that was in test suspension without fullerenol (fullerenol was not consumed during the growth of Chlorella). All suspensions were thoroughly shaken before turbidimetric determination.

A typical spectrum of chlorella water solution is represented in Fig. 1. We used the following formula to calculate chlorella concentration in suspensions:

$$C_{chl}(\text{g/dm}^3) = 0.131\, D_{664} \quad \text{(at the width of optical cell } l = 1 \text{ cm).} \tag{1}$$

We do not use wavelength $\lambda = 424$ nm, because the second component of the suspension substantially strengthen light absorb, when one transfers from yellow-green light to blue-violet one (Fig. 2).

The second reason of preferences of $\lambda = 664$ nm is in the fact, that this peak is considerably less diffusional (see, differential electronic spectrum in Fig. 3).

3. Kinetics of Chlorella Vulgaris growth described by formal kinetics method

Data on the dependence of chlorella concentration – C_{chl} against time of observation (t) are represented in Fig. 4.

One can see, that all graphics $C_{chl}(t)$ are concave, i.e. the velocity of chlorella growth decreases with chlorella concentration increases (at the same time concentration of significant participants in the process: fullerenols, visional photons, dissolved CO_2 are stationary). So, the order of the reaction is negative and chlorella should be self-inhibitor of its own growth. This is atypical for standard chemical reactions, but more often is realized in some other processes, such our now, for example.

Let us determine the order of chlorella growth according to chlorella, constructed graphics for orders $n = 2, 1, -1, -2$ order for the suspension without fullerenol – Fig. 5 (graphics for $n = 0$ is represented in Fig. 4).
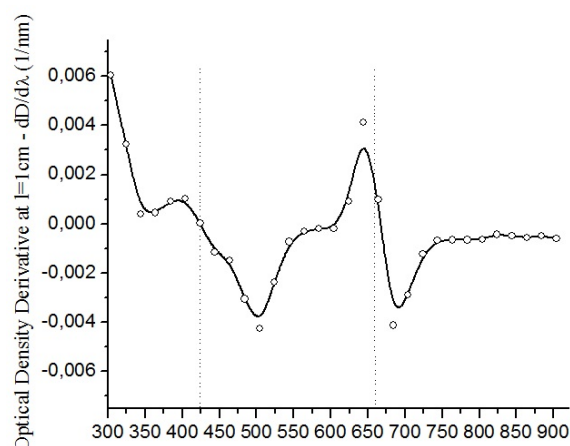
FIG. 3. Differential electronic spectrum of water suspension of Chlorella Vulgaris with concentration $C_{chl} = 1$ g/dm^3 without fullerenol
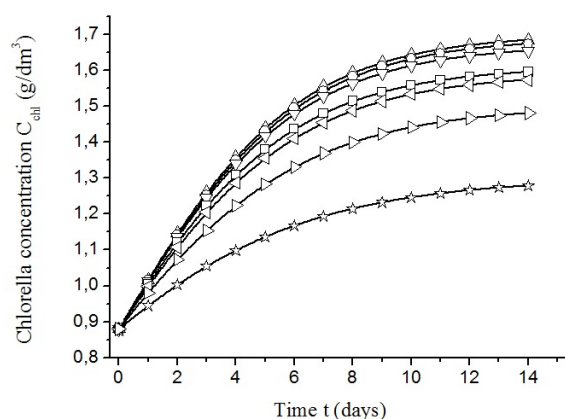

FIG. 4. Dependence of chlorella concentration – C_{chl} against time of observation – t for different fullerenol concentrations $C_{fullerenol} = 0.000$ g/dm^3 (triangles with base down); 0.010 (circles); 0.0625 (triangles with base down); 0.125 (squares); 0.250 (triangles with base on right); 0.500 (triangles with base left); 1.000 (stars). Initial concentration in all cases: $C_{chl} = 0.88$ g/dm^3

From Fig. 5 one can see, that pseudo-order of process is really nearly $n = -2$. Absolutely the same is realized in the presence of catalyst – fullerenol with all concentrations. So differential and integral kinetic equations at all fullerenol concentrations are as follows:

$$\frac{\mathrm{d}C_{chl}}{\mathrm{d}t} = KC_{chl}^{-2}, \tag{2}$$

$$\frac{1}{3}(C_{chl}^3 - C_{chl-0}^3) = Kt. \tag{3}$$

So, we determined velocity constant for the suspensions with the different fullerenol content – Table 1 and in Fig. 6.

From Fig. 6, one can see, that at low fullerenol concentrations $C_{fullerenol} < 0.1$(g/dm^2) it is the catalyst of chlorella growth process, but at higher concentration it is inhibitor of this process.

Unfortunately the authors are not satisfied by the presented higher calculation, because the presented experimental and calculated (according to $n = -2$) curves have no convex regions, where the velocity of growth increases with chlorella concentration growth. But, according to physical sense such region at low chlorella concentrations should be. In our experiment these regions were not investigated, but even if this were the case, the model of formal kinetics with the order $n = -2$ would not be able to describe this in principle.

The fact of pseudo-order $n = -2$ is not inexplicable in the conditions of limiting resources of growth, where competition between the participants of growth exists. Really:

- Dissolved CO_2 is distributed evenly between chlorella and the available concentration is inversely proportional to C_{chl};
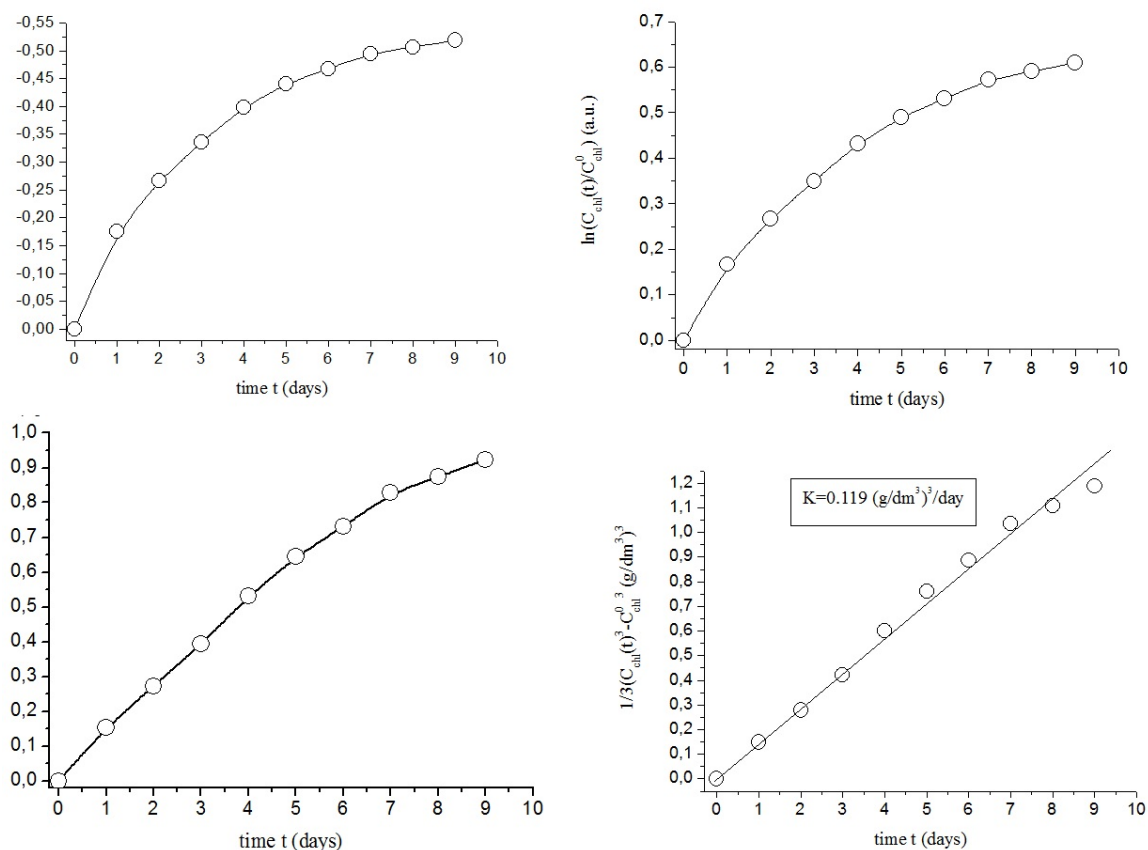
FIG. 5. Kinetic curves $F(C_{chl})(t)$ for different orders n of the process of chlorella growth for the solution without catalyst – fullerenol (from top to bottom: $n = 2$ (left-top), 1 (right-top), -1 (left-bottom), -2 (right-bottom))

TABLE 1. Velocity constants, formal integral and formal differential fullerenol activity in the process of chlorella growth (reaction of pseudo -2 order)

Fullerenol concentration $C_{fullerenol}$ (g/dm^3)	Velocity constant – K (g$_{chl}$/dm^3)^3/day	formal integral catalyst fullerenol activity $A_{fullerenol} =$ $= K - K_0$ (g$_{chl}$/dm^3)^3/day	formal differential catalyst fullerenol activity $a_{fullerenol} = (K - K_0)/C_{fullerenol}$ (g$_{chl}$/dm^2)^3/($g_{fullerenol}$·day)
0.000	0.119	0.000	–
0.010	0.121	0.002	0.200
0.0625	0.127	0.008	0.128
0.125	0.103	-0.016	-0.128
0.250	0.093	-0.026	-0.104
0.500	0.073	-0.046	-0.092
1.000	0.041	-0.078	-0.078

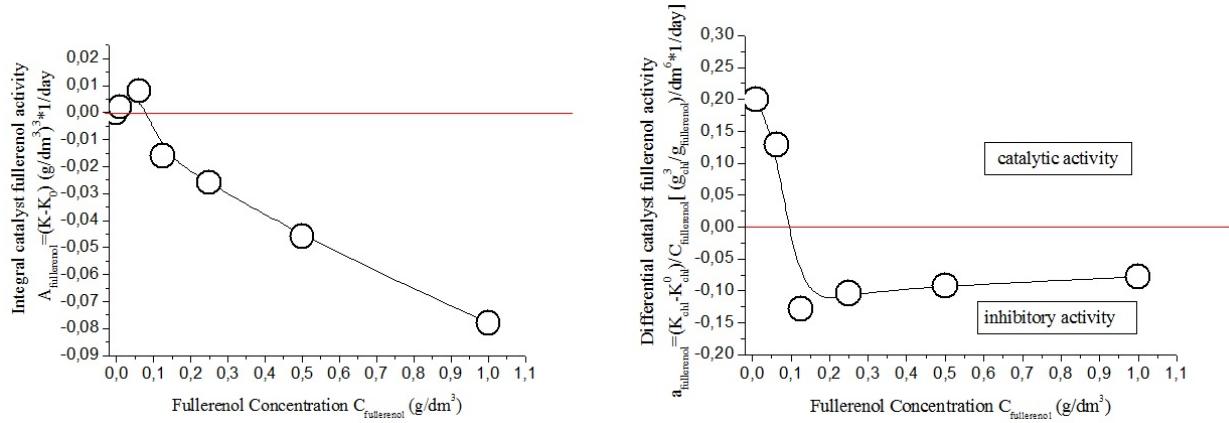K_0 – is velocity of chlorella growth without fullerenol.

FIG. 6. Integral (left) and differential (right) catalyst fullerenol activity against fullerenol concentration

- Tested suspensions in experiments are nearly opaque for visible light (optical density at $\lambda = 664$ nm and width of optical cell in experiment $l = 2$ cm is $D_{664} = 1.5 - 2.0$ a.u.), so from 100 photons $95 - 99$ photons are absorbed in the suspension. Thus, competition between chlorella for the photons also exist, and number of photons, absorbed by one chlorella also inversely proportional to C_{chl}.

4. Kinetics of Chlorella Vulgaris growth, described by Verhulst equation of logistic growth

The Verhulst model of logistic growth [65,66] was elaborated for the description of population growth in the conditions of resource constraints. Here under the term population we understand bio-mass of animals, plants, viruses, bacteria, fungi. Under limited resources we understand restricted access to food, territorial resources, access to individuals of the opposite sex for bisexual organisms, oppression or depopulation as a result of poisoning by products of metabolism. As a result, the Verhulst model describes population growth in the conditions of intraspecific competition.

The Verhulst equation has the following form:

$$X(t) = \frac{X_{max} X_0 e^{rt}}{X_{max} - X_0 + X_0 e^{rt}}. \tag{4}$$

Where X – some function, characterizing population or bio-mass, for example number of organisms, or their concentration in some normalized scale, t – current time from the moment of observation start $t = 0$. It is possible to extrapolate t in negative zone $t < 0$ or for the time before observation start, and predict, for example time of population origin. Equation contains 3 parameters:

$P_1 = X_{max}$ – maximal population or bio-mass, corresponds to $t \to \infty$;

$P_2 = X_0$ – population the moment of observation start $t = 0$. Here and everywhere further we shall not consider the case, when $X_{max} < X_0$, although this case maybe realized, for example in the case of sharp changes in the terms of experience;

$P_3 = r$ – initial velocity of population growth, when resource constraints are insignificant.

Two parameters X_{max}, r (as a rule are fitting ones), the third parameter – X_0 may be fitting and may be fixed (it depends on the accuracy of it's determination). If somebody wants to describe growth curve without extrapolating, possessing experimental data in whole time range, only a single parameter, r, may be varied.

Mathematically, the Verhulst curve is a bi-asymptotic monotonically increasing convex-concave curve with an inflection point.

Two horizontal asymptotes are the following:

$$\lim_{t \to \infty} X(t) = X_{max}, \quad \lim_{t \to -\infty} X(t) = X_0. \tag{5}$$

First derivative or growth velocity may be calculated as:

$$V = \frac{dx}{dt} = \frac{X_0 X_{max} r e^{rt}(X_0 - X_{max})}{(X_{max} - X_0 + X_0 e^{rt})^2}. \tag{6}$$

The second derivative or growth acceleration may be calculated as:

$$A = \frac{d^2 x}{dt^2} = \frac{(X_0 X_{max} r^2 e^{rt}(X_0 - X_{max}))(X_{max} - X_0 + X_0 e^{rt})}{(X_{max} - X_0 + X_0 e^{rt})^2}. \tag{7}$$

This second derivative turns to 0, at the following inflection time – t_{inf}:

$$t_{inf} = \frac{\ln \frac{x_{max} - x_0}{x_0}}{r}. \tag{8}$$

We processed obtained data C_{chl} at different catalyst – fullerenol concentrations with the help of Verhulst equation. Obtained Verhulst parameters are represented in Table 2 and I Fig. 7.

TABLE 2. Parameters of Verhulst equation of logistic growth: $C_{chl-max}(t) = \dfrac{C_{chl-max} C_{chl-0} e^{rt}}{C_{chl-max} C_{chl-0} + C_{chl-0} e^{rt}}$

Fullerenol concentration $C_{fullerenol}$(g/dm^3)	Verhulst equation parameter $C_{chl-max}$(g/dm^3)	Verhulst equation parameter $r(\frac{1}{\text{day}})$	Correlation factor of approximation $R^2(a.u.)$
0.000	1.70	0.328	0.998
0.010	1.69	0.324	0.982
0.0625	1.67	0.323	0.998
0.125	1.61	0.321	0.993
0.250	1.59	0.308	0.995
0.500	1.50	0.285	0.991
1.000	1.30	0.240	0.999

One can see, that the Verhulst equation quite successfully and with very low standard deviation describes dependencies $C_{chl}(t)$ at different fullerenol concentrations. The dependencies of Verhulst parameters on fullerenol concentration is practically linear (Fig. 8) and may be approximated as:

$$C_{chl-max} = 1.70 - 0.40 C_{fullerenol}(\text{g/dm}^3); \quad r = 0.328 - 0.088 C_{fullerenol}(\text{g/dm}^3). \tag{9}$$

So, now we can calculate the dependencies $C_{chl}(t)$ and $V = \dfrac{dC_{chl}(t)}{dt}$, according to Verhulst equation with parameters from Table 2 – Fig. 9,10.

One additional moment remains. Classical Verhulst curve is bi-asymptotic convex-concave curve with inflection point. One cannot see even second asymptotes, convex parts of curves (only concave), inflection points in all curves in Fig. 9. This fact can be explained easily if we take into account the fact, that we have chosen in the experiment a very high initial concentration of chlorella $C_{chl-0} = 0.88$ g/dm^3 comparable to maximal chlorella concentrations $C_{chl-max} = 1.3 - 1.7$ g/dm^3 in dependence of fullerenol concentration (Table 2). So, convex parts of the curves should correspond to lower values C_{chl}. Let us recalculate Verhulst curve into negative times (formally before start of observation) and we shall get absolutely classical Verhulst curves – Fig. 11,12.

We also calculate Verhulst integral ($A_{fullerenol}$) and differential fullerenol catalyst activity ($a_{fullerenol}$) in the process of chlorella growth:

$$A_{fullerenol} = V - V_0; \quad a_{fullerenol} = \frac{V - V_0}{C_{fullerenol}}. \tag{10}$$

Calculations we provided in the form of the dependencies of fullerenol catalyst activity on time at different fullerenol concentrations and on fullerenol concentration (at fixed time of observation) – can be seen in Figs. 13,14.

From the last two figures, one can see, that fullerenol has negative catalytic activity or inhibitor activity on chlorella growth, with exception of the cases of low concentrations ($C_{fullerenol}$ is hundredths or less than 0.1(g/dm^3) – see, for example Fig. 14. For these cases, fullerenol possesses real positive catalyst activity. Moreover, for the longer the observation time, positive catalyst fullerenol activity manifests stronger. This fact corresponds to results installed previously – Fig. 6.
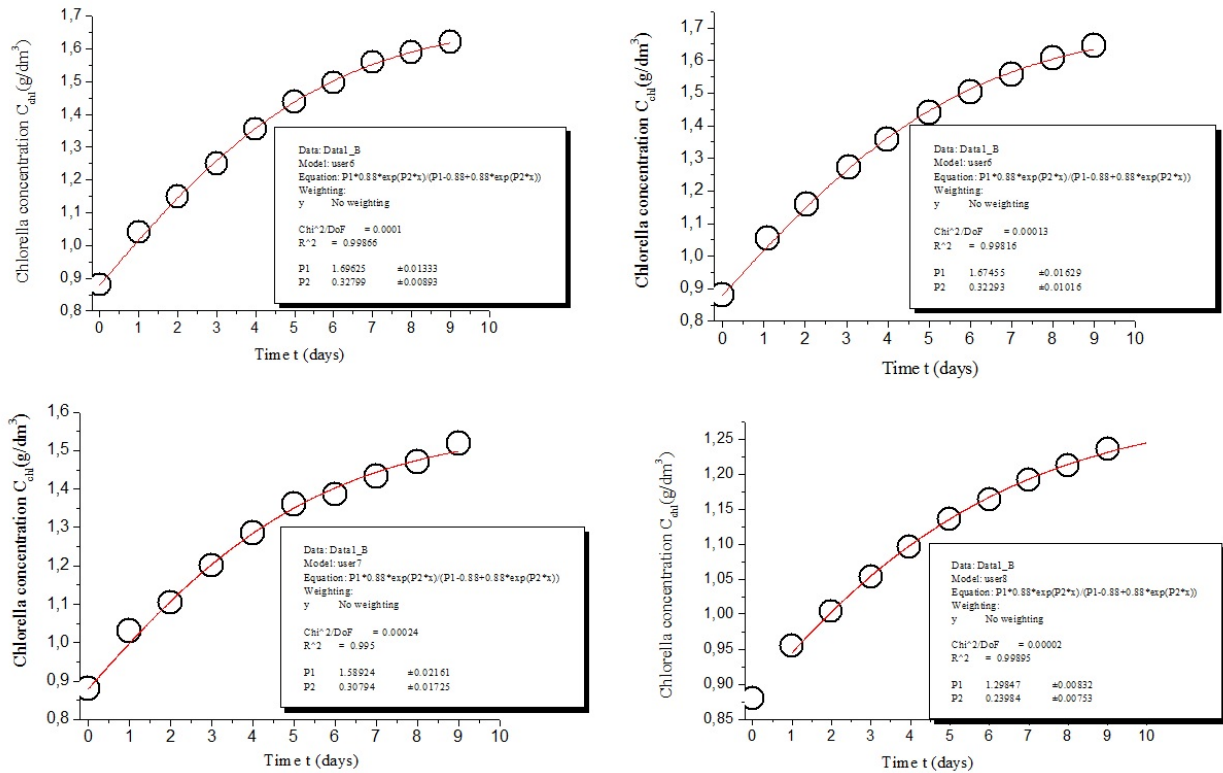
FIG. 7. Kinetic curves $C_{chl}(t)$ and Verhulst equation approximation (red lines) for different fullerenol concentrations as an example [from top to bottom: $C_{fullerenol} = 0.0$ (left-top), 0.0625 (right-top), 0.25 (left-bottom), 1.00 g/dm^3 (right-bottom)], $C_{chl-0} = 0.88$ g/dm^3
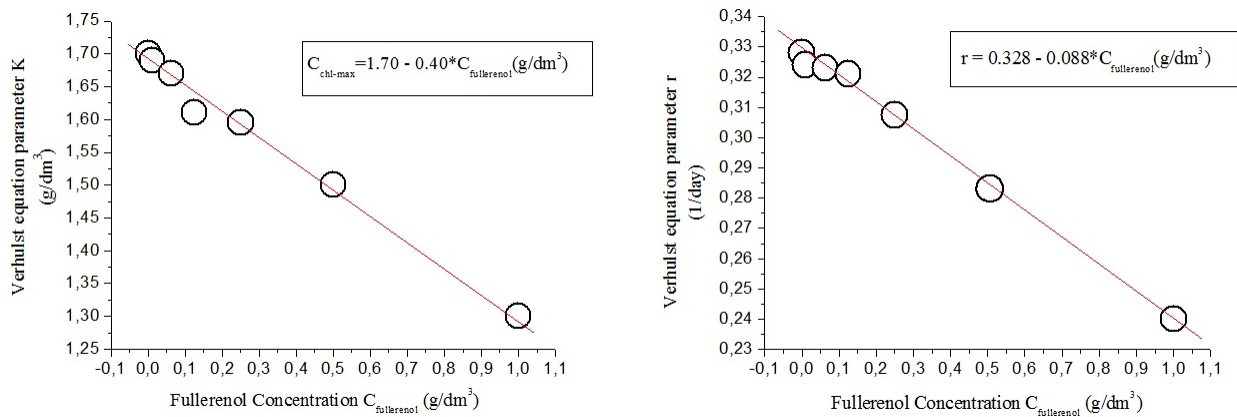

FIG. 8. Dependencies of Verhulst parameters on fullerenol concentration: $C_{chl-max}$ (left), r (right)

5. Kinetics of Chlorella Vulgaris growth in the conditions of oxidation stress

Oxidative stress on the chlorella population was organized by the use of a H_2O_2 solution with a concentration $C_{H_2O_2} = 0.1$(g/dm^3) as a breeding medium for chlorella. The process of chlorella population development in this case with the use of catalyst – fullerenol, should be more complex, because there are simultaneously several multidirectional affects on this process, namely:

- Oxygen – O_2 (maybe free radical – O: also), generated by H_2O_2 decomposition, itself is the product of chlorella metabolism, and so should inhibit chlorella population growth, or maybe cause chlorella depopulation;
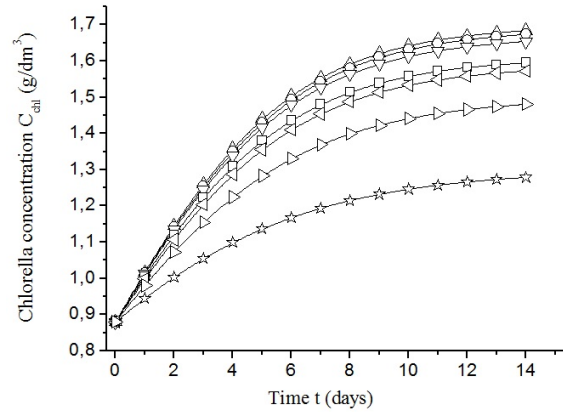
FIG. 9. Verhulst dependencies $C_{chl}(t)$ at different fullerenol concentrations $C_{fullerenol}$(g/dm^3) = 0.000 (triangles with base down); 0.010 (circles); 0.0625 (triangles with base down); 0.125 (squares); 0.250 (triangles with base on right); 0.500 (triangles with base left); 1.000 (stars)

FIG. 10. Verhulst dependencies $V = \dfrac{\mathrm{d}C_{chl}(t)}{\mathrm{d}t}$ at different fullerenol concentrations $C_{fullerenol}$(g/dm^3) = 0.000 (triangles with base down); 0.010 (circles); 0.0625 (triangles with base down); 0.125 (squares); 0.250 (triangles with base on right); 0.500 (triangles with base left); 1.000 (stars)
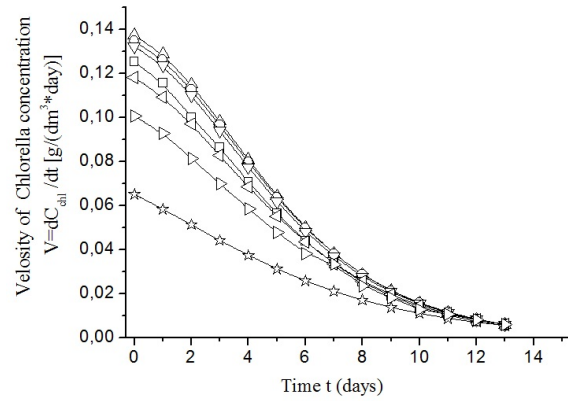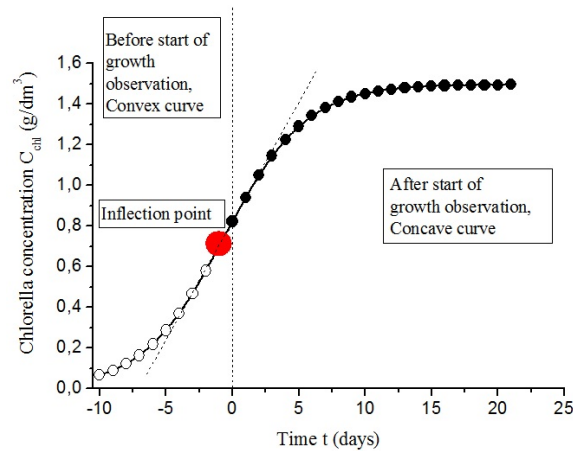

FIG. 11. Verhulst equation of logisitic growth approximation curve $C_{chl}(t)$ (at $C_{fullerenol}$(g/dm^3) = 0.000) with the extrapolation to the previous time

FIG. 12. Verhulst equation of the velocity of logisitic growth approximation curve $\dfrac{dC_{chl}(t)}{dt}$ (at $C_{fullerenol}$(g/dm^3) = 0.000) with the extrapolation to the previous time
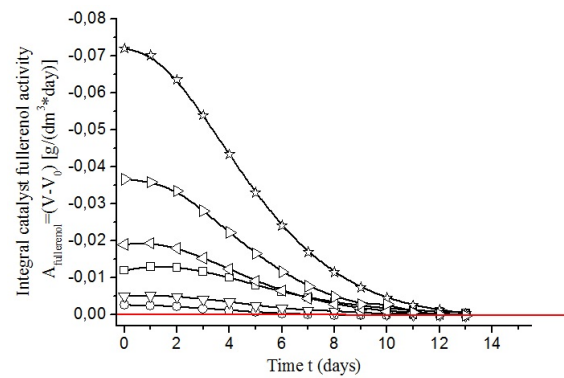
FIG. 13. Integral fullerenol catalyst activity in the process of chlorella growth at different fullerenol concentrations $C_{fullerenol}$(g/dm^3) = 0.000 (red line); 0.010 (circles); 0.0625 (triangles with base down); 0.125 (squares); 0.250 (triangles with base on right); 0.500 (triangles with base left); 1.000 (stars) against time of observation
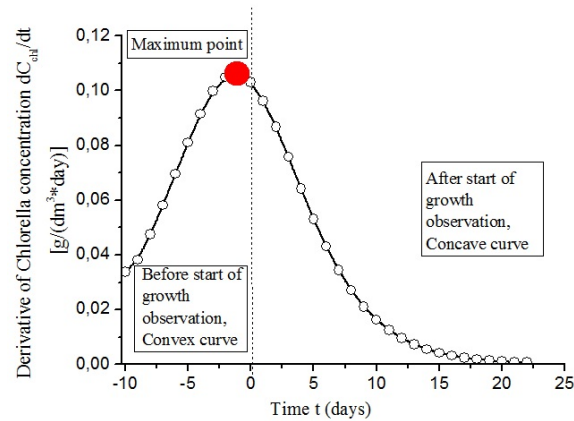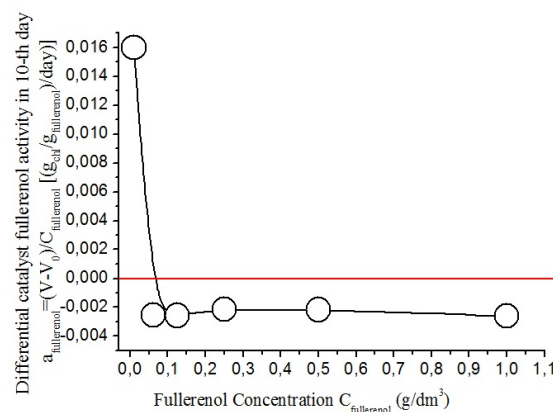

FIG. 14. Differential fullerenol catalyst activity in the process of chlorella growth on the 10-th day of observation

- Fullerenol in low concentrations catalyzes chlorella population growth, and in higher concentrations inhibits it;
- Fullerenol at all concentrations neutralize the inhibitory action of O_2, because it possesses strong antioxidant activity.

The graphics of the dependencies $C_{chl}(t)$ at $C_{H_2O_2} = 1.0(g/dm^3)$ and different $C_{fullerenol}$ are in Fig. 15.
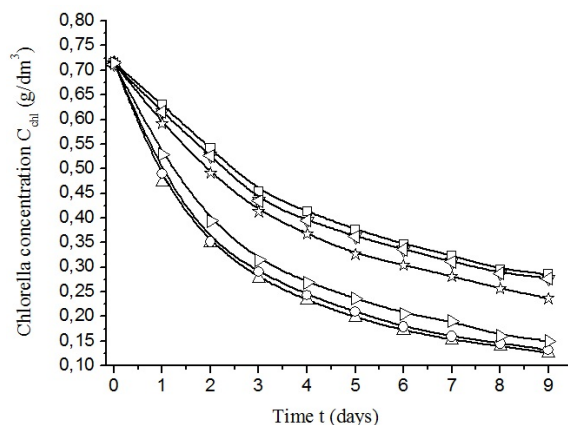

FIG. 15. Dependence of chlorella concentration – C_{chl} against time of observation – t in the conditions of oxidation stress for different fullerenol concentrations $C_{fullerenol}$(g/dm^3) = 0.000 (triangles with base down); 0.010 (circles); 0.0625 (triangles with base down); 0.125 (squares); 0.250 (triangles with base on right); 0.500 (triangles with base on left); 1.000 (stars). Initial concentration in all cases: C_{chl-0}(g/dm^3) = 0.715, $C_{H_2O_2} = 1.0$(g/dm^3).

One can see, that in all cases curves $C_{chl}(t)$ are monotonously decreasing, convex ones. So, we see chlorella depopulation and the order of this process should be n > 1. To determine n we have construct the curves for $n = 1$, $n = 2$ – see Fig. 16, as an example (the case $n = 0$ is represented in Fig. 15).
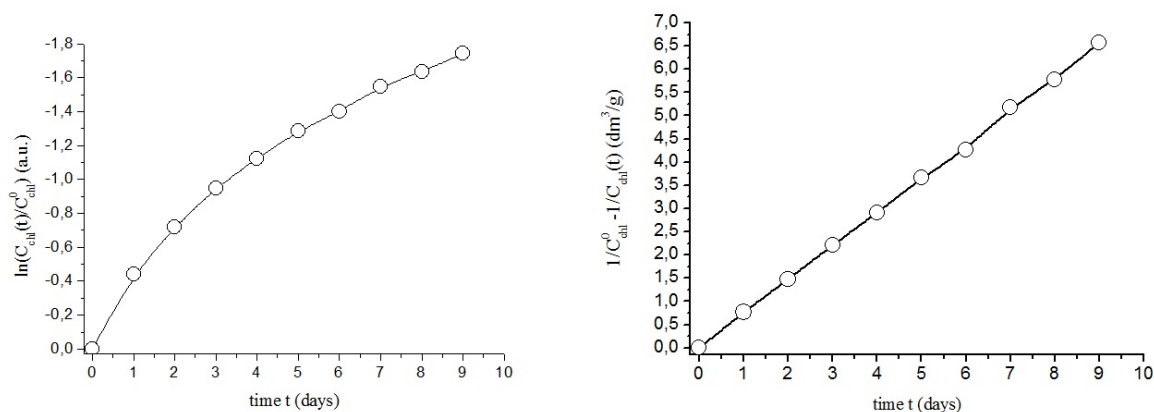
FIG. 16. Kinetic curves $F(C_{chl}(t))$ for different orders (n) of the process of chlorella growth for the solution with H$_2$O$_2$ and without catalyst – fullerenol ($n = 1$ (left), 2 (right))

Absolutely the same is in case of catalyst – fullerenol use. So, $n = 2$, and differential and integral kinetic equation at all fullerenol concentrations are the following:

$$-\frac{dC_{chl}}{dt} = KC_{chl}^2, \tag{11}$$

$$\left(\frac{1}{C_{chl}} - \frac{1}{C_{chl-0}}\right) = Kt. \tag{12}$$

In Fig. 17 we demonstrate how accurately eq. (12) describes the kinetics of the process at different $C_{fullerenol}$ concentrations. Calculated velocity constants for the process are represented in Table 3.
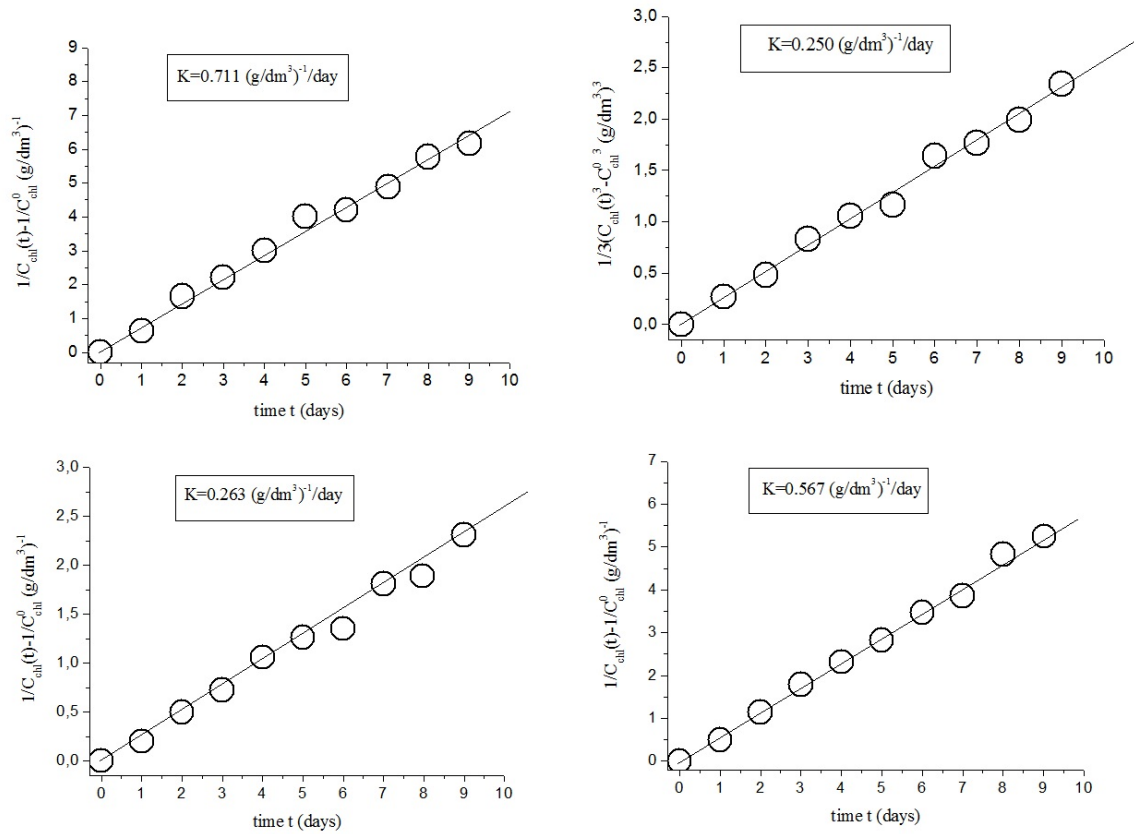
FIG. 17. Kinetic curves $\dfrac{1}{C_{chl}} - \dfrac{1}{C_{chl-0}} = f(t)$ for the solution with H_2O_2 and with different cat-
alyst – fullerenol concentrations $C_{fullerenol}$(g/dm^3): 0.01 (left-top), 0.125 (right-top), 0.250 (left-
bottom), 1.000 (right-bottom)
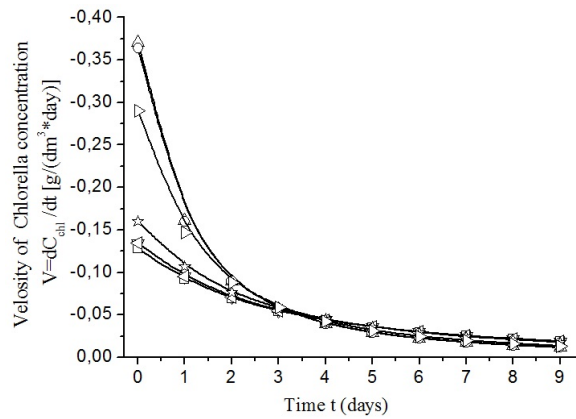
FIG. 18. Dependencies of the velocities of the process against time for different fullerenol concen-
trations $C_{fullerenol}$(g/dm^3) = 0.000 (triangles with base down); 0.010 (circles); 0.0625 (triangles
with base down); 0.125 (squares); 0.250 (triangles with base on right); 0.500 (triangles with base on
left); 1.000 (stars). Initial concentration in all cases: $C_{chl-0} = 0.715$(g/dm^3), $C_{H_2O_2} = 1.0$(g/dm^3)

TABLE 3. Velocity constants of the process of chlorella growth for the solution with H_2O_2 and with catalyst – fullerenol

Fullerenol concentration $C_{fullerenol}$(g/dm^3)	0.000	0.010	0.0625	0.125	0.250	0.500	1.000
Velocity constant K(g$_{chl}$/dm^3)$^{-1}$/day	0.725	0.711	0.263	0.253	0.625	0.313	0.567
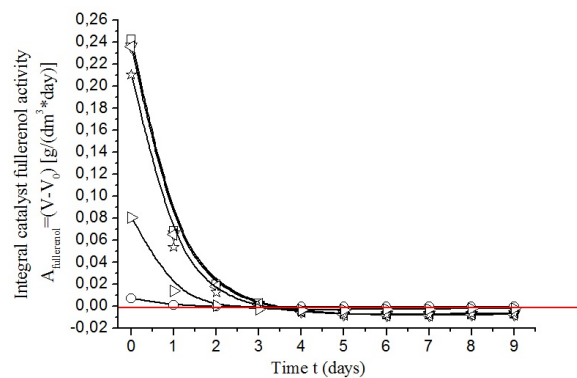
FIG. 19. Dependencies of the integral catalyst fullernol activities of the process against time for different fullerenol concentrations $C_{fullerenol}$(g/dm^3) = 0.000 (base red line); 0.010 (circles); 0.0625 (triangles with base down); 0.125 (squares); 0.250 (triangles with base on right); 0.500 (triangles with base on left); 1.000 (stars). Initial concentration in all cases: $C_{chl-0} = 0.715$(g/dm^3), $C_{H_2O_2} = 1.0$(g/dm^3)
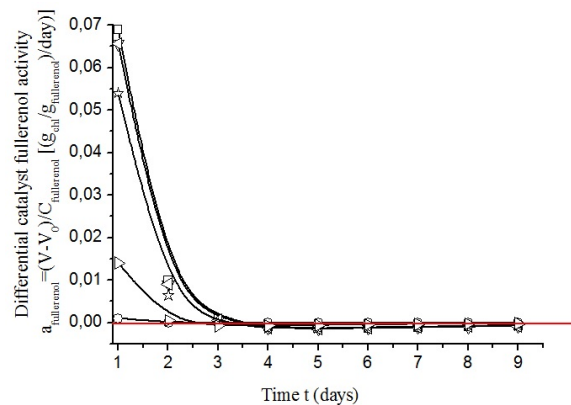
FIG. 20. Dependencies of the differential catalyst fullerenol activities of the process against time for different fullerenol concentrations $C_{fullerenol}$(g/dm^3) = 0.000 (base red line); 0.010 (circles); 0.0625 (triangles with base down); 0.125 (squares); 0.250 (triangles with base on right); 0.500 (triangles with base on left); 1.000 (stars). Initial concentration in all cases: $C_{chl-0} = 0.715$(g/dm^3), $C_{H_2O_2} = 1.0$(g/dm^3)
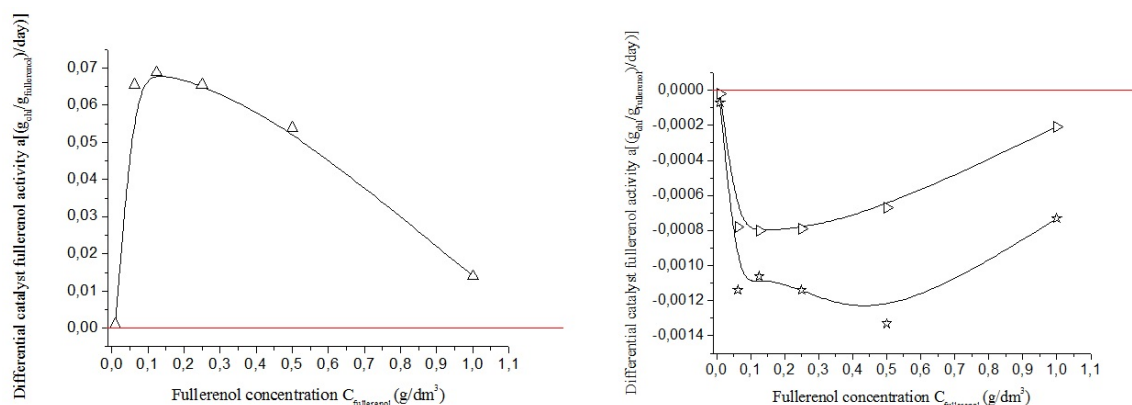
FIG. 21. Dependencies of the differential catalyst fullerenol activities of the process against fullerenol concentrations at different observation time (in days): 1-st (left); 4-th (right: triangles with base on left); 9-th (right: stars)

One can see that dependence $K(C_{fullerenol})$ is non-monotonic and passes through the minimum, which reflects the fact, that two or more oppositely directed tendencies are acting, which increasing and decreasing of the velocity of chlorella depopulation processes. In Fig. 18 we represent the graphics of the dependencies of the velocities of the process against time for different chlorella concentrations $V = \dfrac{dC_{chl}}{dt} = f(t)$. Obviously the dependencies $V(C_{fullerenol})$ are non-monotonic and also pass through the minimum, as $K(C_{fullerenol})$ at $C_{fullerenol} \approx 0.10(\text{g/dm}^3)$. We also calculated integral catalyst activity and differential catalyst activity in depopulation chlorella processes in the conditions of oxidation stress, according to eq. (10). Data are represented in Fig. 19,20, correspondingly. From Fig. 19,20, one can see, that at low observation times $0-2 \sim 3$ days fullerenol at all concentrations has an effect, inhibiting=protecting the process of chlorella depopulation, and after that – at times $2 \sim 3-9$ days this the effect is leveled and fullerenol starts catalyze=accelerate the process of chlorella depopulation.

Noticeably, it is more revealing to calculate the dependencies of differential catalyst fullerenol activities against fullerenol concentration at different fixed times of observation – see Table 4 and Fig. 21 for 1-st, 4-th and 9-th days.

TABLE 4. Integral ($A_{fullerenol}$) and differential $a_{fullerenol} = \dfrac{V - V_0}{C_{fullerenol}}$ catalyst fullerenol activity in 1-st, 4-th and 9-th day

Fullerenol concentration $C_{fullerenol}$ (g/dm^3)	1-st day $A_{fullerenol}$ (g/dm^3·day)	1-st day $a_{fullerenol}$ $\left(\frac{g_{chl}}{g_{fullerenol}}\right)$ /day	4-th day $A_{fullerenol}$ (g/dm^3·day)	4-th day $a_{fullerenol}$ $\left(\frac{g_{chl}}{g_{fullerenol}}\right)$ /day	9-th day $A_{fullerenol}$ (g/dm^3·day)	9-th day $a_{fullerenol}$ $\left(\frac{g_{chl}}{g_{fullerenol}}\right)$ /day
0.000	0.000	–	0.000	–	0.000	–
0.010	0.0010	0.0010	−0.00026	−0.00007	−0.00014	−0.00002
0.0625	0.0655	0.0655	−0.00456	−0.00114	−0.00700	−0.00078
0.125	0.0688	0.0688	−0.00422	−0.00106	−0.00723	−0.00080
0.250	0.0655	0.0655	−0.00456	−0.00114	−0.00700	−0.00079
0.500	0.0539	0.0539	−0.00532	−0.00133	−0.00607	−0.00067
1.000	0.0140	0.0140	−0.00294	−0.00073	−0.00187	−0.00021

From Fig. 21, one can see, that at the time of exposition 1 day (2, 3 also) fullerenol has an effect, inhibiting = protecting the process of chlorella depopulation, and after that – at times $2\sim3-9$ days fullerenol starts catalyze = accelerate the process of chlorella depopulation. At the same time positive fullerenol inhibitory activity at the first days according to the absolute value is 1-2 orders of magnitude greater than the negative fullerenol catalyst activity subsequently. Maximal positive fullerenol inhibitory activity corresponds to $C_{fullerenol} = 0.1(\text{g/dm}^3)$. With further increase common catalyst or inhibitory activities both quickly decreasing.

6. Conclusions

Catalytic fullerenol $C_{60}(OH)_{24}$ action on Chlorella Vulgaris growth in the conditions of limited resource growth base and in the conditions of oxidation stress were investigated. The kinetics of Chlorella Vulgaris growth in the conditions of limited resource growth, maybe adequately described by the equation of formal kinetics with a second order (inhibitory process) or Verhulst equation of logistic growth of bio-masses. It was demonstrated, that the Verhulst equation maybe satisfactorily used for the description of different natural process. The kinetics of Chlorella Vulgaris depopulation in the conditions of oxidation stress, maybe adequately described by the equation of formal kinetics of a second order. It was shown, that in the case of limited resource growth, low fullerenols concentrations $C_{fullerenol} < 0.1(g/dm^3)$ catalyzes or accelerate Chlorella growth, but higher concentrations suppress or inhibit the growth. Under conditions of oxidative stress in the first $2-3$ days, fullerenols protect chlorella or inhibit depopulation; after this time, the fullerenols catalyze or accelerate chlorella depopulation. Positive fullerenol depopulation inhibitory activity at the first days according to the absolute value $1-2$ orders of magnitude greater than the negative fullerenol catalyst activity in subsequent days. Maximal positive fullerenol inhibitory activity corresponds to $C_{fullerenol} \approx 0.1(g/dm^3)$. With further increase common catalyst or inhibitory activities both quickly decreasing.

Acknowledgements

References

[1] Sidorov L.N., Yurovskaya M.A., et al. *Fullerenes*. Moscow, Ekzamen, 2005, 688 p. (in Rus).

[2] Cataldo F., Da Ros T. Carbon Materials. *Chemistry and Physics: Medicinal Chemistryand Pharmacological Potential of Fullerenes and Carbon Nanotubes*. Springer, 2008.

[3] Piotrovskii L.B., Kiselev O.I. *Fullerenes in Biology*. Rostok, Saint-Petersburg, 2006, 335 p. (in Rus).

[4] Djordjevic A., Bogdanovic G., Dobric S. Fullerenes in biomedicine. *Journal of B.U.ON.: official journal of the Balkan Union of Oncology*, 2006, **11**(4), P. 391–404.

[5] Semenov K.N., Meshcheriakov A.A., et al. Physico-chemical and biological properties of C_{60} – L-hydroxyproline water solutions. *RSC Advances*, 2017, **7**. P. 15189–15200.

[6] Panova G.G., Ktitorova I.N., et al. Impact of polyhy-droxy fullerene (fullerol or fullerenol) on growth and biophysi-cal characteristics of barley seedlings in favourable and stressful conditions. Plant Growth Regulation. *International Journal on Plant Growth and Development*, 2016, **79**(3), P. 309–318.

[7] Panova G.G., Semenov K.N., et al. Water soluble fullerene derivatives and silica nano-compositions as perspec-tive nanomaterials in plant growing. *Agro-physics*, 2015, **4**, P. 37–48. (in Rus).

[8] Panova G.G., Kanash E.V., et al. Fullerene deriva-tives stimulate production process, growth and stability to oxidation stress for wheat and barley plants. *Agricultural Biology*, 2018, **53**(1), P. 38–49. (in Rus).

[9] Shevchenko D.S., Rakhimova O.V., Charykov N.A., Semenov K.N., Keskinov V.A., Vorobiev A.L., Kulenova N.A., Onalbaeva Zh.S. Synthesis, identification and biotesting of water soluble octo-adduct of fullerene C_{60} and arginine $C_{60}(C_6H_{12}NaN_4O_2)_8H_8$. *Rep. SPbGTI(TU)*, 2018, **45**, P. 77–81.

[10] Panova G.G., Serebryakov E.B., Semenov K.N., Charykov N.A., Shemchuk O.S., Andrusenko E.V., Kanash E.V., Khomyakov Y.V., Shpanev A.M., Dulneva L.L., Podolsky N.E., Sharoyko V.V. Bioactivity Study of the C_{60}-L-Threonine Derivative for Potential Application in Agriculture. *Journal of Nanomaterials*, 2019, P. 1-13.

[11] Pochkaeva E.I., Podolsky N.E., Zakusilo D.N., Petrov A.V., Charykov N.A., Vlasov T.D., Penkova A.V., Vasina L.V., Murin I.V., Sharoyko V.V., Semenov K.N. Fullerene derivatives with amino acids, peptides and proteins: From synthesis to biomedical application. *Progress in Solid State Chemistry*, 2020, **57**, P. 100255.

[12] Shevchenko D.S., Rakhimova O.V., Podolsky N.E., Charykov N.A., Semenov K.N., Keskinov V.A., Shaimardanov Zh.K., Shaimardanova B.K., Kulenova N.A., Onalbaeva Zh.S. Toxicity of water soluble octo-adduct of fullerene C_{60} and arginine $C_{60}(C_6H_{12}NaN_4O_2)_8H_8$. *Rep. SPbGTI(TU)*, 2019, **49**(75), P. 96–101.

[13] Andrievsky G., Klochkov V., Derevyanchenko L. Is the C_{60} fullerene molecule toxic?! *Fullerenes, Nanotubes, and Carbon Nanostructures*, 2005, **13**(4), P. 363–376.

[14] Aschberger K., Johnston H.J., Stone V., et al. Review of fullerene toxicity and exposure – appraisal of a human health risk assessment, based on open literature. *Regulatory Toxicology and Pharmacology*, 2010, **58**(3), P. 455–473.

[15] Andreev S.M., Babakhin A.A., Petrukhina A.O., Romanova V.S., Parnes Z.N., Petrov R.V. Immuno-henic and allergenic properties of conjugates of fullerenes with amino-acids. *Rep. Rus. Acad. of Sciences*, 2000, **370**(2), P. 387–399.

[16] Baati T., Bourasset F., Gharbi N., et al. The prolongation of the lifespan of rats by repeated oral administration of [60] fullerene. *Biomaterials*, 2012, **33**(19), P. 4936–4946.

[17] Baker G.L., Gupta A., Clark M.L., et al. Inhalation toxicity and lung toxicokinetics of C_{60} fullerene nanoparticles and microparticles. *Toxicological sciences*, 2008, **101**(1), P. 122–131.

[18] Costa C.L.A., Chaves I.S., Ventura -Lima J., et al. In vitro evaluation of coexposure of arsenicum and an organic nanomaterial (Fullerene C_{60}) in zebrafish hepatocytes. *Comparative Biochemistry and Physiology Part C: Toxicology & Pharmacology*, 2012, **155**(2), P. 206–212.

[19] Jia G., et al. Cytotoxicity of carbon nanomaterials: singl -wall nanotube, multi-wall nanotube, and fullerene. *Environmental science & technology*, 2005, **39**(5), P. 13780–1383.

[20] Jung H., Wang C. U., Jang W. Nano-C$_{60}$ and hydroxylated C$_{60}$: Their impacts on the environment. *Toxicology and vironmental Health Sciences*, 2009, **1**(2), P. 132–139.

[21] Gao J., Wang H.L., Shreve A., Iyer R. Fullerene derivatives induce premature senescence: A new toxicity paradigm or novel biomedical applications. *Toxicology and applied pharmacology*, 2010, **244**(2), P. 130–143.

[22] Horie M., Nishio K., Kato H., et al. In vitro evaluation of cellular responses induced by stable fullerene C$_{60}$ medium dispersion. *Journal of biochemis-try*, 2010, **148**(3), P. 289–298.

[23] Hendrickson O.D., Zherdev A.V., Gmoshinskii I.V., Dzantiev B.B. Fullerenes: in vivo stud-ies of biodistribution, toxicity, and biological action. *Nanotechnologies in Russia*, 2014, **9**(11-12), P. 601–617.

[24] Hendrickson O.D., Morozova O.V., Zherdev A.V., et al. Study of distribution and biological effects of fullerene C$_{60}$ after single and multiple intragastrical administrations to rats. *Fullerenes, Nanotubes and Car-bon Nanostructures*, 2015, **23**(7), P. 658–668.

[25] Kolosnjaj J., Szwarc H., Moussa F.Toxicity studies of fullerenes and derivatives. *Bio-Applications of nanoparticles*, 2007, P. 168–180.

[26] Kyzyma E.A., et al. Structure and toxicity of aqueous fullerene C$_{60}$ solutions. *Journal of Surface Investigation. X-ray, Synchrotron and Neutron Tech-niques*, 2015, **9**(1), P. 1-5.

[27] Moussa F., Chretien P., et al. The influence of C$_{60}$ powders on cultured human leukocytes. *Full. Sci. Technol.*, 1995, **3**, P. 333–342.

[28] Moussa F., Trivin F., Ceolin R., et al. Ear-ly effects of C$_{60}$ Administration in Swiss Mice: A Preliminary Account for In Vivo C$_{60}$ Toxicity. *Fullerene Science and Technology*, 1996, **4**(1), P. 21–29.

[29] Orlova M.A., Trofimova T.P., Orlov A.P., et al. Fullerene derivatives as modulators of cell proliferation and apoptosis. New directions in medicine science. *Onco-hematology*, 2012, **4**, P. 7–10.

[30] Prylutska S.V., Matyshevska O.P., Golub A. at. al. Study of C$_{60}$ fulllerenes and C$_{60}$ – containing composites cytotoxicity in vitro. *Materials Science and Engineering: C*, 2007, **7**(5), P. 1121–1124.

[31] Piotrovskiy L.B. Fullerenes in the design of medicinal substancies. *Russian Nanotechnologies*, 2007, **2**(7-8). P. 6-18.

[32] Rajagopalan P., Wudl F., Schinazi R.F., Boudinot F.D. Pharmacokinetics of a water-soluble fuller-ene in rats. *Antimicrobial agents and-chemotherapy*, 1996, **40**(10), P. 2262–2265.

[33] Sayes C.M., Marchione A.A., Reed K.L., Warheit D.B. Comparative pulmonary toxicity assessments of C$_{60}$ water suspensions in rats: few differences in fullerene toxicity in vivo in contrast to in vitro profiles. *Nano letters*, 2007, **7**(8), P. 2399–2406.

[34] Trpkovic A., Todorovic, Markovic B., Kleut D., et al. Oxidative stress-mediated hemolytic activity of solvent exchange -prepared fullerene (C$_{60}$) nanoparticles. *Nanotechnology*, 2010, **21**(37), P. 37510.

[35] Trpkovic A., Todorovic, Markovic B., Trajkovic V. Toxicity of pristine versus functionalized fullerenes: mechanisms of cell damage and the role of oxida-tive stress. *Archives of toxicology*, 2012, **86**(12), P. 1809–1827.

[36] Yamago S., Tokuyama H., Nakamura E., et al. In vivo biological behavior of a water-miscible fullerene: 14 C labeling, absorption, distribution, excretion and acute toxicity. *Chemistry & biology*, 1995, **2**(6), P. 385–389.

[37] Ueng T.H., Kang J.J., Wang H.W., et al. Suppression of microsomal cytochrome P450-dependent monooxygenases and mitochondrial oxida-tive phosphorylation by fullerenol, a polyhydroxylated fullerene C$_{60}$. *Toxicology letters*, 1997, **93**(1), P. 29–37.

[38] Shipelin V.A., Arianova E.A., Trushina E.N., et al. Hygienic characteristic of fullerene C$_{60}$ while it's introducing into gastrointestinal tract of rats. Hygiene and sanitation, 2012, **2**, P. 90–94.

[39] Shipelin V.A., Avreneva L.I., Guseva G.V., et al. Characteristic of oral toxicity of fullerene C$_{60}$ for rats in 92-days experiment. *Nutrition issues*, 2012, **81**(5), P. 20–27.

[40] Vengerovich N.G., Tyunin M.A., Antonenkova E.V., et al. Biological activity of nano-bio-composites fullerene C$_{60}$. *Immunology*, 2012, **12**, P. 161–177.

[41] Kyzyma E.A., Tomchuk A.A., Bulavin L.A., Petrenko V.I., Almasy L., Korobov M.V., Volkov D.S., Mikheev I.V., Koshlan I.V., Koshlan N.A., Blaha P., Avdeev M.V., Aksenov V.L. Structure and toxicity of aqueous fullerene C$_{60}$ solutions. *J. Surf. Invest.: X-ray, Synchrotron Neutron Tech.*, 2015, **9**(1), P. 1–5.

[42] Sayes C.M., Fortner J.D., Guo W., Lyon D., Boyd A.M., Ausman K.D., Tao Y.J., Sitharaman B., Wilson L.J., Hughes J.B., West J.L., Colvin V.L.. The differential cytotoxicity of watersoluble fullerenes. *Nano Lett.*, 2004, **4**(10), P. 1881–1887.

[43] Gao J., Wang Y., Folta K.M., Krishna V., Bai W., Indeglia P., Georgieva A., Nakamura H., Koopman B., Moudgil B. Polyhydroxy fullerenes (fullerols or fullerenols): beneficial effects on growth and lifespan in diverse biological models. *PLoS ONE*, 2011, **6**(5), P. 1–8.

[44] Djordjevicand A., Bogdanovic G. Fullerenol: anewnanopharmaceutic? *Arch. Oncol.*, 2008, **16**(3–4), P. 42–45.

[45] Srdjenovic B., Milic-Torres V., Grujic N., Stankov K., Djordjevic A., Vasovic V. Antioxidant properties of fullerenol C$_{60}$(OH)$_{24}$ in rat kidneys, testes, and lungs treated with doxorubicin. *Toxicol. Mech. Method*, 2010, **20**(6), P. 298–305.

[46] Jacevic V., Djordjevic A., Srdjenovic B., Milic-Tores V., Segrt Z., Dragojevic-Simic V., Kuca K. Fullerenol nanoparticles prevents doxorubicin-induced acute hepatotoxicity in rats. *J. Experimental and Molecular Pathology*, 2017, **3**.

[47] Eropkin M.Yu., Melenevskaya E.Yu., Nasonova K.V., Bryazzhikova T.S., Eropkina E.M., Danilenko D.M., Kiselev O.I. Synthesis and biolog-ical activity of fullerenols with various contents of hydroxyl groups. *Pharm. Chem. J.*, 2013, **47**(2), P. 87–91.

[48] Golomidova I., Bolshakova O., Komissarov A., Sharoyko V., Slepneva E., Slobodina A., Latypova E., Zherebyateva O., Tennikova T., Sarant-seva S. The neuroprotective effect of fullerenols on a model of Parkinson's disease in Drosophila melanogaster. *J. Biochemical and Biophysical Research Communications*, 2019,P. 1-6.

[49] Tyurin D.P., Kolmogorov F.S., Cherepkova I.A., Charykov N.A., Semenov K.N., Keskinov V.A., Safyannikov N.M., Pukharenko Yu.V., Letenko D.G., Segeda T.A., Shaimardanov Z. Antioxidant properties of fullerenol-d. *Nanosystems: Physics, Chemistry, mathematics*, 2018, **9**(6), P. 798–810.

[50] Podolsky N.E., Marcos M.A., Cabaleiro D., Semenov K.N., Lugo L., Petrov A.V., Charykov N.A., Sharoyko V.V., Vlasov T.D., Murin I.V. Physico-chemical properties of C$_{60}$(OH)$_{22-24}$ water solutions: density, viscosity, refraction index, isobaric heat capacity and antioxidant activity. *J. of Mol. Liq*, 2019, **278**, P. 342–355.

[51] Tyurin D.P., Kolmogorov S.F., Cherepkova I.A., Charykov N.A., Semenov K.N., Keskinov V.A., Saf'yannikov N.M., Pukharenko Yu.V., Letenko D.G., Shaimardanov Zh.K., Shaimardanova B.K. Anti-oxidant properties of octo-adduct of fullerene C$_{60}$ and L-arginine (C$_{60}$(C$_6$H$_{13}$N$_4$O$_2$)$_8$H$_8$). *Rep SPbGTI(TU)*, 2019, **49**(75), P. 70–78.

[52] Grigoriev V.V., Petrova L.N., et al. Antioxidant properties of water soluble amino acid derivatives of fullerenes and their role in the inhibition of herpes virus infection. *Rus. Chem. Bull. Int. Ed.*, 2011, **60**, P. 1172–1176.

[53] Mirkov S.M., Djordjevic, A.N., et al. Nitric oxidescavenging activity of polyhydroxylated fullerenol, $C_{60}OH_{24}$. *Nitric Oxide*, 2004, **11**, P. 201–207.

[54] Anderson R., Barron A.R. Reaction of hydroxyfullerene with metal salts: a route to remediation and immobilization. *J. Am. Chem. Soc.*, 2005, **127**(30), P. 10458–10459.

[55] Djordjevic A., Srdjenovic B., et al. Review of Synthesis and Antioxidant Potential of Fullerenol Nanoparticles. *Journal of Nanomaterials*, 2015, P. 567073(15).

[56] Lao F., Chen L., Li W., et al. Fullerene nanoparticles selectively enter oxidationdamaged cerebral microvessel endothelial cells and inhibit JNKrelated apoptosis. *ACS Nano*, 2009, **3**(11), P. 3358–3368.

[57] Yin J.J., Lao F., Fu P.P., et al. The scavenging of reactive oxygen species and the potential for cell protection by functionalized fullerene materials. *Biomaterials*, 2009, **30**(4), P. 611–621.

[58] Caputo F., De Nicola M., Ghibelli L. Pharmacological potential of bioactive engineered nanomaterials. *Biochemical Pharmacology*, 2014, **92**(1), P. 112–130.

[59] Djordjevic A., Canadanovic Brunet J.M., VojinovicMiloradov M., Bogdanovic G. Antioxidant properties and hypothetic radical mechanism of fullerenol $C_{60}(OH)_{24}$. Oxidation Communications, 2004, **27** (4), P. 806–812.

[60] Kokubo K. WaterSoluble SingleNano Carbon Particles: Fullerenol and Its Derivatives. *InTech*, 2012.

[61] Kato S., Aoshima H., Saitoh Y., Miwa N. Highly hydroxylated or cyclodextrinbicapped Watersoluble derivative of fullerene: the antioxidant ability assessed by electron spin resonance method and carotene bleaching assay. *Bioorganic and Medicinal Chemistry Letters*, 2009, **19**(18), P. 5293–5296.

[62] Ueno H., Yamakura S., et al. Systematic evaluation and mechanistic investigation of antioxidant activity of fullerenols using carotene bleaching assaycarotene bleaching assay. *Journal of Nanomaterials*, 2014, **2014**, P. 802596, P. 7.

[63] Semenov K.N., Charykov N.A., Keskinov V.A., et al. Solubility $C_{60}Br_n$ (n = 6, 8, 24) in organic solvents. *Rus. J. Phys. Chem. A*, 2009, **83**(11), P. 1935–1940.

[64] Semenov K.N., Charykov N.A., Axel'rod B.M. Solubility of Bromderivatives $C_{60}Br_n$ (n = 6, 8, 24) in 1-Chloronaphthalene and 1-Bromonaphthalene In Temperature Range (10 to 60)°C. *J. Chem. Eng. Data.*, 2010, **55**, P. 2373–2378.

[65] Verhulst P.F. Notice sur la loi que la population poursuit dans son accroissement. *Correspondance matématique et physiqu*, 1838, **10**, P. 113–121.

[66] Verhulst P.F. Recherches Mathématiques sur La Loi 'Accroissement de la Population Nouveaux Mémoires de 'Académi Royale des Sciences et Belles-Lettres de Bruxelles, 18, Art. 1, 1-45, 1845 (Mathematical Researches into the Law of Population Growth Increase).

Adsorption and photo catalytic degradation of yellow Auramine–O dye using carbon nano particles

V. Latha

Department of Chemistry, Sri S. Ramasamy Naidu Memorial College, Sattur, India

latha@srnmcollege.ac.in

In this study, Carbon nano particles (C NPs) from neem leaves were synthesized for adsorption and photo catalytic degradation of Auramine–O (Au–O) dye used in paper industries. The synthesized C NPs were characterized by powder X-ray diffraction and scanning electron microscopy. Dye adsorption and photo catalytic properties of C NPs were examined by studying the decolorization of dye Au–O at 5 minutes time interval using a UV-Visible spectrophotometer. The results show that C NPs acts as a better adsorbent even with shorter time and lower concentration than as photocatalysts.

Keywords: Dye degradation, carbon nano particle, adsorption, photo catalytic activity, degradation of Auramine–O dye, X-ray diffraction, photo catalysts.

Received: 15 March 2021

Revised: 16 April 2021

1. Introduction

Synthetic dyes have been widely used in many technological processes such as paints and textiles, as an additive in plastic, paper, leather, cosmetics and rubber industries, and so on [1]. The paper industry is one of the oldest industries in which the extensive use of various dyes has been implemented for ages. There are many variations in the kind of papers produced in paper industry such as writing and printing paper, tissues used as toilet paper, facial tissues or used as paper napkins or towel, copier paper, cover papers, corrugated papers used for packing, handmade paper, lamination paper and the list is endless. For each kind of paper, a different kind of dye is required. The dying process in poly board paper industry involves many dyes such as Acid orange, Brown dye, Red dye, Paper yellow, Methylene Blue, Victoria Pure Blue, Malachite Green Crystals, Rhodamine 6, Methyl Violet, Rhodamine B, Auramine O. Out of these, Auramine–O (Au–O) is a basic yellow dye containing amino and imino groups (Fig. 1). The effluents containing Au–O cause significant health problems. Au–O may bind to hemoglobin, inhibiting the normal uptake of oxygen, leading to methemoglobinemia, cyanosis and breathing difficulties. There is evidence that it may produce eye irritation and eye damage 24 hours or more after instillation. There may be damage to the cornea. Unless treatment is prompt and adequate there may be permanent loss of vision. Inhalation leads to unconscious. Continuous exposure to Au–O causes vomiting and yellowish discoloration of skin [2].
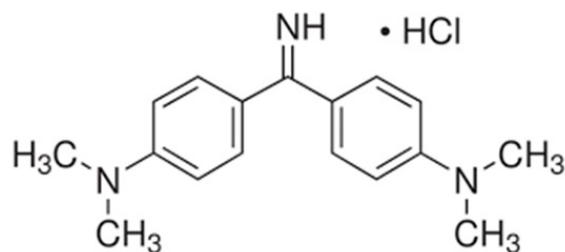

FIG. 1. Structure of Auramine–O

Even at low concentration, the colors of these dyes can be easily observed by water and make it highly injurious effects for an environment and human health. Therefore, significant attention has been drawn to develop a beneficial technology for the removal of these organic pollutants from aqueous solutions. These harmful organic pollutants can be removed by various methods such as precipitation, adsorption, photocatalytic degradation, ion exchange, reverse osmosis, solvent extraction and chlorination. Adsorption of dyes by activated carbon and its composites is one of the simplest and most economical methods for removing dyes from wastewater due to its high adsorption capacity,

high specific surface area, and low selectivity [3–15]. Previous research revealed that photocatalyst had shown a good performance in degrading the persistent organic pollutants with the aid of light absorption in the water [16].

However, the performance does depend not only on the composition, but also on its microstructure, size, and morphology. Smaller nanoparticles could form on active sites of support materials through oxide-support interaction. This could increase the overall surface area of the photocatalyst, and the support materials can act as a sink of electrons. In recent trends, nanomaterials are used as a photocatalyst to degrade organic pollutants. Nanoscale materials have high surface area to volume ratio, making them ideal for use in composite materials, drug delivery, catalysis, sensors, data storage and energy storage. The finite size of material entities as compared to the molecular scale makes nanostructured materials harder, less brittle and mechanically strong. Basically, in nanotechnology, we study materials at nanoscale ($1 \cdot 10^{-9}$ m), materials at bulk scale show different properties and at nanoscale different extraordinary properties, at nanoscale with size their surface to volume ratio increase. This surface to volume ratio property, especially as a catalyst, increases the efficiency by a hundred percent as compared to bulk materials.

Carbon based nanoparticles have application as photocatalysts but there are some limitations, due to which, these were not use commercially. So the present work focussed on the synthesis of carbon nanoparticles from neem leaves and its adsorption and photocatalytic action against Au–O dye.

The neem (Azadirachta indica A. Juss) is a tropical evergreen tree traditionally well known for its medicinal value. Apart from Indian subcontinent, neem is widely used in African countries as therapeutics, preservatives and insecticides. Neem leaves, natural source of flavonoids, polyphenols, isoprenoids, sulfurous and polysaccharides, play important role in free radical scavenging. Neem leaves are used for treating leprosy, eye disorders, bloody nose, intestinal worms, stomach upset, skin ulcers, fever, diabetes, gum disease, and liver problems.

As Au–O dye causes skin coloring, vomiting, unconsciousness, the carbon nanoparticles synthesized from neem leaves may be the best adsorbent.

2. Materials and methods

2.1. Synthesis of carbon nanoparticles

Carbon nanoparticles were synthesized from neem leaves. The fresh neem leaves were collected and then washed with distilled water. Then the washed leaves were soaked in dilute hydrochloric acid for 3–4 hours. After 4 hours the color of the leaves turned black, at which point they were collected and dried at 120°C for 3–5 hours in a hot air oven. The dried mass was collected and stored for application.

2.2. Adsorption

The adsorption performance of carbon nanoparticle was evaluated through the decreased UV absorbency of Au–O solution. The chemical structure of Au–O is shown in Fig. 1. The concentration of Au–O was 5 PPM. 5 mL of the dye solution is sonicated with 20 mg of carbon nanoparticle to get better adsorption activity. The absorbency of the Au–O solution at a wavelength of 435 nm was measured every 10 min by a UV-vis spectrophotometer for 50 minutes.

2.3. Photocatalytic with UV and Visible Sources

Photocatalytic degradation process was also carried out under UV light irradiation. Four fluorescent lamps were used for irradiation of UV light source. 50 mL Au–O dye solution with 5 PPM concentration was sonicated continuously with 20 mg of Carbon nanoparticles in a 100 mL cylindrical Pyrex vessel reactor. The reaction was initiated by switching on the light source. 5 ml of dye solution was taken at the equal intervals of 5 minutes from 0 upto 30 minutes. To examine the degradation of Au–O, the collected solutions were filtered and the UV-Vis absorption spectra were recorded by UV-Vis spectrometer.

2.4. Characterization

Scanning Electron Microscope EVO18 (CARL ZEISS) was used to investigate the surface morphology of carbon nanoparticles. Scanning electron microscopy (SEM) is a widely used method for the high-resolution imaging of surfaces that can also be employed to characterize nanoscale materials. SEM uses electrons for imaging, much as a light microscope uses visible light. The sample were placed in an evacuated chamber and scanned in a controlled pattern by an electron beam. Interaction of the electron beam with specimen produces the SEM images of Carbon NPs.

X-ray diffractometer D8 Advance ECO (Bruker) was used to investigate the grain size. X-ray diffraction (XRD) is one of the most extensively used techniques for the characterization of NPs. Typically, XRD provides information regarding the crystalline structure, nature of the phase, lattice parameters and crystalline grain size. The grain size is
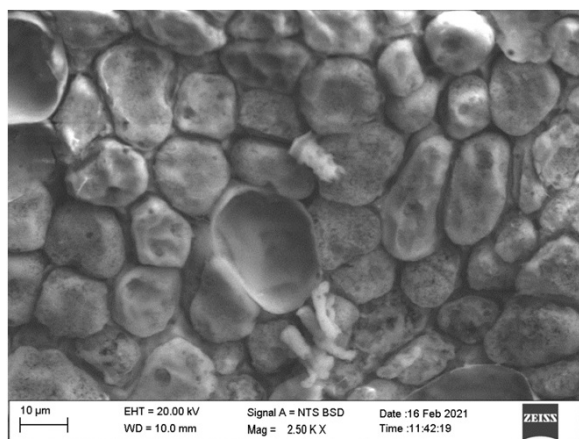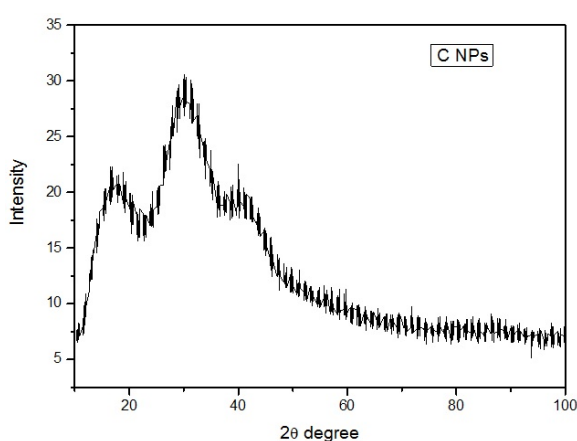
FIG. 2. SEM images of C NPs

FIG. 3. XRD Pattern of Carbon NPs

estimated by using the Scherrer equation using the broadening of the most intense peak of an XRD measurement for a specific sample.

3. Result and Discussion

3.1. Scanning electron microscopic analysis

Morphology of synthesized carbon nanoparticles was characterised by SEM analysis. The SEM images were developed by the interaction of electron beam with carbon nano particles (Fig. 2). The Carbon NPs formed are well dispersed and evenly distributed in all direction. It shows that the Carbon NPs have smooth and uniform surface. It also confirms that there is no contamination with carbon nano particles.

3.2. X-ray diffraction analysis

The XRD pattern of the synthesized C and C–CaO NPs are shown in Fig. 3. It shows that the XRD pattern of the synthesized C NPs observed with 2Θ values 16°58', 18°93', 30°15', 39°96' they are indexed to the 221, 100, 111, 220 crystal planes. The average size of the synthesized C NPs was calculated using Scherrer's equation:

$$D = \frac{k\lambda}{\beta \cos \Theta},$$

where, D – particle in size, k – Scherrer's coefficient, λ – wavelength of X-ray source (1.5406 nm), β – full width half maximum (FWHM) and Θ – diffraction angle.

The average size of carbon nano particle is found to be 6.78 nm. It shows that the synthesized Carbon NPs are spherical.

3.3. Adsorption of dye molecule by Carbon NPs

Adsorption of Au–O dye molecule by Carbon NPs was examined. The adsorption peaks of the synthesized C NPs are depicted in Fig. 4. From the spectra, it is perceived that the intensity of the characteristic peak of Au–O observed at 435 nm decreases with respect to the time for the synthesized C NPs. This reduction in the concentration up to 55% of the initial concentration is due to the adsorption of Au-O dye by adsorption of Carbon nano particle. After 50 minutes, the concentration is reduced to 48% only.

3.4. Photocatalytic degradation of dye molecule by Carbon NPs

The photocatalytic performance of the synthesized C NPs is examined by the degradation of Au–O dye molecules under UV-light irradiation. The photocatalytic degradation peaks of C NPs are depicted in Fig. 5. From the spectra, the intensity of the characteristic peak of Au-O observed at 435 nm decreases with respect to the time for the synthesized C NPs. But the intensity is not that much decreased as in the case of adsorption. This study implies that C NPs are acting as better adsorbents than as photocatalysts.
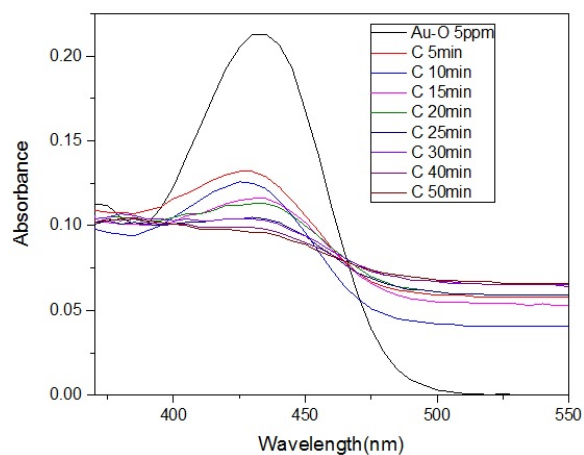
FIG. 4. UV – Visible spectra of Au–O with C NPs at time interval of 5 minutes from 0 to 50 minutes by adsorption studies
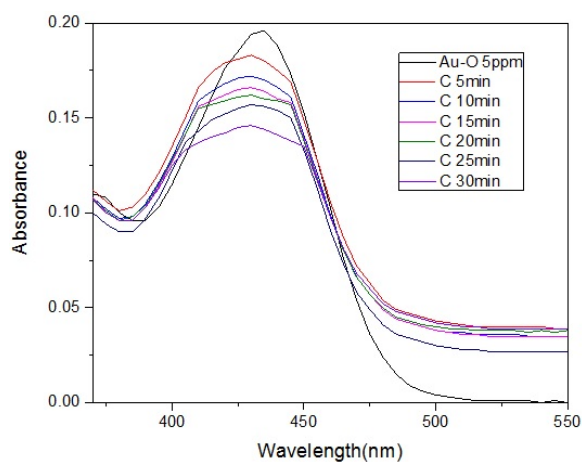

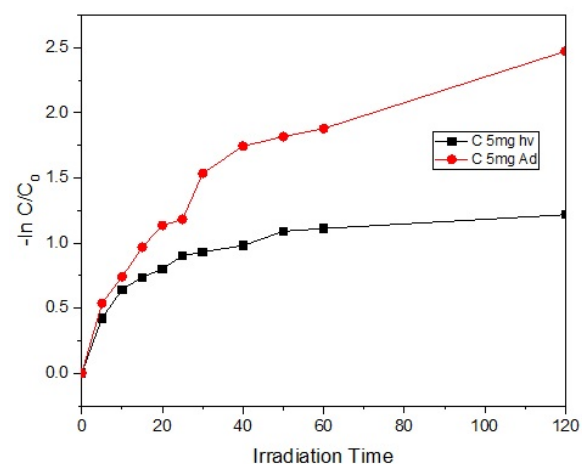FIG. 5. UV – Visible spectra of Au–O with C NPs at time interval of 5 minutes from 0 to 30 minutes

FIG. 6. Time course of Au–O adsorption on C NPs for both adsorption and photocatalytic degradation

3.5. Mechanism for Au–O degradation by Carbon NPs

Fig. 6 depicts the time course of Au–O degradation on C NPs by adsorption and photocatalytic degradation process. Compared to the photocatalytic process, the adsorption process has significantly degraded the Au–O due to C NPs nano size, highly porous structures, in terms of area, pore volume, and pore distribution. The adsorption equilibrium was achieved after 40 min. The graph matches with the physical adsorption curve of Langmuir. But in the photocatalysis process, the low performance of degradation compared to the adsorption process may be due to the rise in temperature by passing the light radiation. This may cause desorption process. Thus, the C NPs act as better adsorbent than photocatalytic degrader.

4. Conclusion

In summary, the carbon nanoparticles were successfully synthesised from neem leaves with smooth and uniform morphology with 6.28 nm grain size. These carbon nanoparticles act as better adsorbents than as photocatalysts. This leads to further study to synthesize composite material with this carbon nano particle to increase their photocatalytic activity.

Acknowledgements

References

[1] K. Hunger *Industrial Dyes: Chemistry, Properties, Applications*. John Wiley & Sons, 2007.

[2] S. Kaja Mohideen, K. Senthil Kumar, D. Pavan Kumar. Cow dung powder poisoning. *Indian Journal of Critical Care Medicine*, 2015, **15**, P. 64–66.

[3] S.K. Giri, N.N. Das, and G.C. Pradhan. Synthesis and characterization of magnetite nanoparticles using waste iron ore tailings for adsorptive removal of dyes from aqueous solution. *Colloid Surface Physicochemal Engineering Aspect*, 2011, **389**, P. 43–49.

[4] P. Hu, Y. Zhang, K. Tong et al. Removal of organic pollutants from red water by magnetic-activated coke. *Desalination and Water Treatment*, 2014, **54**, P. 2710–2722.

[5] T. Jiang, Y.-d. Liang, Y.-j. He, and Q. Wang. Activated carbon/NiFe$_2$O$_4$ magnetic composite: a magnetic adsorbent for the adsorption of methyl orange. *Journal of Environmental Chemical Engineering*, 2015, **3**, P. 1740–1751.

[6] T. Madrakian, A. Afkhami, M. Ahmadi, and H. Bagheri. Removal of some cationic dyes from aqueous solutions using magnetic-modified multi-walled carbon nanotubes. *Journal of Hazardous Materials*, 2011, **196**, P. 109–114.

[7] H.R. Rajabi, H. Arjmand, S.J. Hoseini, and H. Nasrabadi. Surface modified magnetic nanoparticles as efficient and green sorbents: synthesis, characterization, and application for the removal of anionic dye. *Journal of Magnetism and Magnetic Materials*, 2015, **394**, P. 7–13.

[8] N. Yang, S. Zhu, D. Zhang, and S. Xu. Synthesis and properties of magnetic Fe$_3$O$_4$-activated carbon nanocomposite particles for dye removal. *Materials Letters*, 2008, **62**, P. 645–647.

[9] B. Zargar, H. Parham, and A. Hatamie. Fast removal and recovery of amaranth by modified iron oxide magnetic nanoparticles. *Chemosphere*, 2009, **76**, P. 554–557.

[10] A. Latif, S. Noor, Q.M. Sharif, and M. Najeebullah. Different techniques recently used for the treatment of textile dyeing effluents: a review. *Journal of the Chemical Society of Pakistan*, 2010, **32**(1), P. 115–124.

[11] P. Pengthamkeerati, T. Satapanajaru, N. Chatsatapattayakul, P. Chairattanamanokorn, and N. Sananwai. Alkaline treatment of biomass fly ash for reactive dye removal from aqueous solution. *Desalination*, 2010, **261**(1-2), P. 34–40.

[12] Z. Zhang and J. Kong. Novel magnetic Fe$_3$O$_4$@C nanoparticles as adsorbents for removal of organic dyes from aqueous solution. *Journal of Hazardous Materials*, 2011, **193**, P. 325–329.

[13] B. Zargar, H. Parham, and M. Rezazade. Fast removal and recovery of methylene blue by activated carbon modified with magnetic iron oxide nanoparticles. *Journal of the Chinese Chemical Society*, 2011, **58**, P. 694–699.

[14] F. Liu, S. Chung, G. Oh, T.S. Seo. Three-dimensional graphene oxide nanostructure for fast and efficient water-soluble dye removal. *ACS Applied Materials & Interfaces*, 2012, **4**, P. 922–927.

[15] T. Madrakian, A. Afkhami, H. Mahmood-Kashani, and M. Ahmadi. Adsorption of some cationic and anionic dyes on magnetite nanoparticles-modified activated carbon from aqueous solutions: equilibrium and kinetics study. *Journal of the Iranian Chemical Society*, 2013, **10**, P. 481–489.

[16] Pang Y.L., Lim S., Ong H.C., Chong W.T. Synthesis, characteristics and sonocatalytic activities of calcined γ-Fe$_2$O$_3$ and TiO$_2$ nanotubes γ-Fe$_2$O$_3$ magnetic catalysts in the degradation of Orange G. *Ultrason Sonochem*, 2016, **29**, P. 317–327.

Personalized energy systems based on nanostructured materials

A. N. Kovalenko[1], E. A. Tugova[1], V. I. Popkov[1], O. N. Karpov[1], A. I. Klyndyuk[2]

[1]Ioffe Institute, 26 Politekhnicheskaya, St. Petersburg 194021, Russia
[2]Belarusian State Technological University, 13a Sverdlova, Minsk, 220006, Belarus

ras-kan@mail.ru, katugova@inbox.ru, vadim.i.popkov@gmail.com, o_karpov@list.ru, kai_17@rambler.ru

In this paper, the achievements, problems and prospects of creating personalized energy systems based on nanostructured materials are analysed. Various concepts of developing methods and ways of personalized energy provision for autonomous human survival in remote natural habitat, emergency situations of natural disasters and technogenic catastrophes when centralized power supply is unavailable or in an effort to reduce the economic and environmental costs of remote energy production and transportation are also considered. The possibilities and limitations of using traditional and renewable alternative energy sources, processes and devices for extracting, storing and converting their energy into the necessary consumer forms due to fundamental physical laws are discussed as well. The article covers the new nanostructured materials with special functional properties for personalized energy systems development. The mechanisms for formation of the required nanostructures in synthesized materials, especially those with a high content of fractal interfacial formations, are considered as well as methods for studying their structural and phase characteristics that determine the achievability of the specified parameters of model converters and energy storage devices.

Keywords: autonomous energy provision, energy sources, optimization of energy conversion and storage modes, functional materials, nanostructures, fractals, non-autonomous phases .

Contents

1. Introduction

Currrently, two complementary approaches to the development of energy supply systems have been formed: there is a centralized "external" energy industry of large capacity and autonomous distributed, or local "internal" energy industry [1–4]. They differ in various interests of energy producers and consumers, different indicators of energy productivity and energy efficiency, different costs for creation, and operation, energy sources used, technological schemes for converting primary fuel and distributing converted energy flows, and different levels of losses for generating and transporting consumed types of energy. However, this division is rather conditional. As in any complex system, in natural and technical complexes of centralized and autonomous power supply, there are numerous direct and inverse relationships between the selected hierarchical levels, which are based on fundamental and applied scientific achievements of the nineteenth to twenty-first centuries, primarily in the field of thermo- and electrodynamics, hydroaerodynamics, mechanics, heat transfer, atomic physics, chemistry, and materials science.

Centralized energy industry of large capacity (up to 1200 MW in a single at a time when the total installed capacity of all power plants of the Unified Energy System of Russia is over 246 GW as of January 1, 2020) is intended for remote electricity and heat supply through the electric and heat networks of industrial enterprises, public social services and household needs of the population from large generating units of thermal (TPP), nuclear (NPP) and hydro- (HPP) power plants which, respectively, use fossil energy resources of chemical (organic) and nuclear fuel, as well as the energy of nature-renewable movement of large masses of river water. In terms of the unavailability of centralized power supply or in case of attempts to reduce economic and ecological costs of remote production and transport of energy; in order to provide power supply for small industrial and community facilities of different local groups, the autonomous energy industry is used in forms of distributed power installations of low and medium power (5 to 50 MW in a single unit). Along with traditional generation plants, alternative solar, wind, tidal, geothermal, biofuel, thermoelectric and other power units are also used here as well [5–10].

A special area of autonomous energy industry is a personalized energy industry, the power of which is comparable to the power of the human body in the range of its normal and peak loads (about 100 – 1200 W). It is designed in order to maintain the efficiency of individual life support equipment and human survival in remote natural habitat, as well as in terms of emergency situations such as technological catastrophes and natural disasters. This includes provision of food preparation and water supply, housing maintenance, use of tools and devices for personal labor, transport, electronic communication and navigation, medical devices, sports and tourist equipment, personal protective equipment and equipment for rescuers, firefighters, security personnel, emergency medical services and other emergency services. Along with traditional and alternative sources for personalized energy supply, such as, mechanical movement and heat of the human body and environmental objects, as well as the electrical processes occurring in them and accompanying magnetic phenomena, background electromagnetic radiation in the radio and television broadcasting bands, human muscle strength and the strength of domestic animals, secondary energy sources, in the form of agricultural and local industry waste, etc., can be also used [11–13].

Although the development of the scientific and technological base of energy industry in the current understanding dates back about 200 years, the recent problems of depletion of intensively used fossil energy resources, concomitant environmental pollution and attraction of renewable alternative sources stimulate the search for new approaches and solutions in all the energy areas mentioned above. Fundamental and applied physical and chemical problems, as well as the results of such searches, are reflected in numerous original articles published and in a large number of generalizing reviews and monographs [14–20], in which you can find interesting details and additional links. This review is devoted to the consideration of a still poorly presented, but promising and rather intensively developing area of modern research in the field of autonomous personalized energy industry using nanostructured converters. The use of functional materials of such a structure, especially those with a high content of interphase formations of fractal geometry (non-autonomous phases [21–23]), which differ significantly in their properties, structure and composition from the corresponding characteristics of bulk phases, allows us to purposefully influence the processes of energy transformation. In particular, it is possible to develop nonlinear regimes with the so-called exacerbation [24,25], when the effects of local energy concentration appear with their retention for a finite time practically without spreading to other zones. In this case, the change in the space-time structure is not accompanied by a general destruction of the material, in contrast to known examples of thermal explosion, shock wave accumulation, self-focusing of light beams, plasma instability, and other variants of such effects in continuous nonlinear media [26]. Other unusual structural and functional properties of processes in such media (changes in the melting temperature, transport coefficients, etc.) are also found, which are studied in the framework of the theory of dissipative structures and synergetics [27]. They can be used in many applications of physics, biophysics, chemistry, and biology, but they are especially important for solving

problems of personalized energy industry due to the specific requirements for the power of the sources used and their availability, low weight and size characteristics, as well as the unstable operating modes. This review also addresses, as necessary, the main points of research in related areas of energy that are important for the analysis of the topic under consideration. In particular, physical constraints limit the possibilities of converting various forms of energy, the conditions and mechanisms for modes of increasing maximum power and efficiency of these transformations, their thermodynamic stability and regulation of controllability, influence the functional properties of the underlying environments and structures of materials, the development of methods for their synthesis, determining the attainability of the desired properties and the desired intensification of the transformation modes. In this review, these issues are analyzed based on the available literature data, as well as original author's developments.

2. Individual energy needs of the human body and the possibility of sources of additional energy supply in personalized energy industry

Individual energy needs of the body are determined, first of all, by the energy costs of ensuring human's vital activity. This is the maintenance of a constant body temperature, heart and respiratory muscles, the nervous system, physical activity in the processes of work, changes in the structure and physiology of organs in certain age periods. This also includes carrying out functional responses to stressful situations, including the mobilization of all energy and regulatory resources of the body for its survival in the event of sudden changes in the external and internal environment. The physiological source of body energy supply is a combination of metabolic processes as a set of multi-stage biochemical reactions of the exchange of incoming food substances at the tissue and cellular level. Enzymatic self-regulation of the kinetics of these reactions is carried out by the nervous and endocrine systems of the body with the maintenance of hemodynamic balance, indicators of water exchange of biological fluids and gas balance, depending on environmental conditions and internal factors.

According to medical and biological data [26, 28], the individual energy expenditure of an adult of medium build in a temperate climate is 2800 – 3200 kcal/day (11.7 – 13.4 MJ) for men, 2100 – 2300 kcal/day (8.8 – 9.6 MJ) for women, and about 2000 kcal/day (8.4 MJ) for a 10-year-old child. In adults, from 10 to 25 % of energy is spent on the brain, while the brain of a 5–6-year-old child can consume up to 60 % of the body's energy [29]. As the body grows from the age of 20, the energy consumption begins to decrease with a gradual decrease first by 3, then by 7.5, and then by 10 % approximately every 20 years. The intensity of energy consumption depends on the physical activity of the body, slightly different in women and men. Thus, the intensity of energy consumption in light work is 3.5 and 5.3 kcal/min, respectively (which is equivalent to the energy transformation power of 250 – 370 W), in moderate work 5.7 and 8.0 kcal/min (400 – 560 W), in heavy work 7.8 and 11 kcal/min (550 – 770 W). During short-term peak physical activity, energy consumption increases to 14 – 16 kcal/min (980 – 1120 W) or more, while at rest during sleep, energy consumption is only 1 – 1.5 kcal/min (70 – 100 W). These data taken at rest are calculated from the rate of basal exchange, i.e., the formation of heat in the human body. As for various physical activities, these data take into account the additional exchange associated with the intensity of muscle load, when mechanical work is added to the formation of heat and the total energy expenditure increases by 15 – 20 %. The latter means that only about 1/5 of the body's own energy can be spent on transforming the environment in order to improve living conditions. And it may happen only in a time-limited working period within the range of developed power at normal and peak loads (from 100 to 1200 W) in accordance with the physiological capabilities of the body and the rhythms of human life. Approximately the same level of capacity, determined by the density of energy flows in the biochemical reactions of metabolic processes in the human body, is typical for renewable environmental sources as derivatives of solar radiation, which is the main source of renewable energy on the planet's surface. A comparative assessment of the energy capabilities of these sources for additional energy supply in personalized energy systems is given in Table 1 according to the data [6, 30–35]. This includes solar and wind energy, energy of natural magnetic and background electromagnetic fields of anthropogenic nature, thermoelectric materials, including those that convert the heat of the human body, piezoelectric materials that convert the energy of mechanical vibrations, motion or acoustic noise, pyro- and ferroelectric materials that convert radiant energy into high electrical voltage, etc. These sources complement the energy capabilities of the human body discussed above, among which the greatest power density is represented by the thermal energy of the human body (135 mW/cm^3) and the energy of its mechanical movement (800 mW/cm^3).

These indicators are at least one hundred times less than the corresponding indicators of continuous power supply in centralized systems used for covering of general household and industrial needs that are used currently in developed countries (up to 10 or more kW of installed capacity per each resident). According to the materials provided by the academician P. L. Kapitsa in the report "Energy and Physics" at the scientific session in honor of the 250th anniversary of the Academy of Sciences of the USSR [36] and in his Nobel acceptance lecture [37], based on data from the UNO and the International Bank for Reconstruction and Development in the 70s of the last century, which have kept the general trends to the present day, there is a direct proportionality between the cost of gross national (domestic) product

TABLE 1. Comparison of capacities of possible sources and technologies of energy collection in personalized energy systems [6, 30–35]

Harvesting Method	Power density
SOLAR Solar energy – outdoors Solar energy – indoors	15 mW/cm^3 – bright sunny day 0.15 mW/cm^3 – cloudy day 10 – 100 μW/cm^2
MECHANIC (Vibrations) Piezoelectric – shoe inserts Electrostatic conversion Electromagnetic conversion	 330 μW 0.021 μW/mm^3 – 105 Hz 154 μW/cm^3
THERMIC Thermoelectric −5 °C gradient	 40μW/cm^3
PYROELECTRIC Temperature rate of 8.5 °/s	 8.64 μW/cm^3
MAGNETIC Magnetic field energy	 130 μW/cm^3 – 200 μT, 60 Hz
RADIO FREQUENCY GSM 900/1800 MHz WiFi 2.4 GHz	 0.1 μW/cm^2 0.01 μW/cm^2
WIND	380 μW/cm^3 (at the speed of 5 m/s)
ACOUSTIC NOISE	0.96 μW/cm^3 at 100 dB 0.003 μW/cm^3 at 75 dB

produced and energy consumption (Fig. 1). When they decrease, not only the level of well-being falls, but the resulting life expectancy of people in these countries also suffers (Fig. 2).

The report presented by P. L. Kapitsa emphasized not only the fundamentally different level of energy flow density (about 10 MW/m^2) for large-capacity centralized power generation using concentrated fossil energy resources, from the above-mentioned energy flow density for alternative renewable environmental sources (about 100 W/m^2 at the surface to 1.35 kW at the boundary of the Earth's atmosphere), but also noted their relationship with the efficiency (efficiency) of energy transformation processes. These indicators are determined by the fundamental laws of conservation of energy and increasing entropy in transformation processes, which do not allow the creation of "perpetual motion machines" of the 1st and 2nd kind, as well as by the restrictions on the maximum power of its transmission through the material medium by the value of the Umov-Poynting vector $U < \nu F$. Here, ν is the distribution velocity of the medium-deformation, which is usually equal to the speed of sound in gaseous medium, and F is the volume power density of the medium during the transfer of any type of energy (elastic, thermal, electrical, etc.) in it. In stationary processes, the value of $\mathrm{div}\, U$ determines the amount of energy conversion to another type. The example given by P. L. Kapitsa of the effect of this restriction on the parameters of various converters shows that in order to generate 100 MW of power while using the direct conversion of solar energy into electrical energy from a sunlit surface at the usual energy flux density of 100 W per square meter, a working area of 1 km^2 is required. The same working areas of almost impossible dimensions will be needed for the wheel of a wind power plant, for the installation of direct conversion of the chemical energy of hydrogen oxidation into electricity, for an electrostatic generator (Van de Graaff type), thermoelectric generators and similar converters on energy sources with energy flows of similar density.
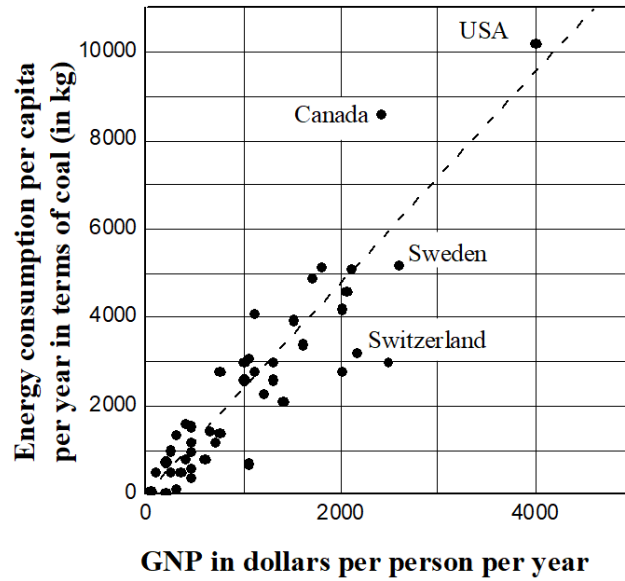
FIG. 1. Dependence of gross national (domestic) product on energy consumption per person per year for different countries of the world [36, 37]
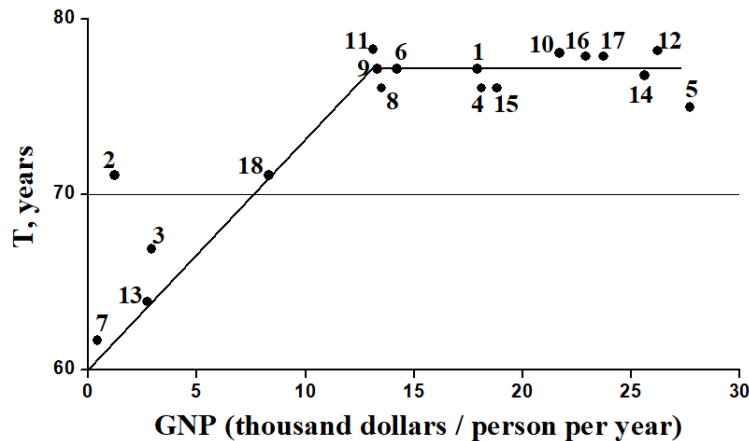
FIG. 2. The dependence of life expectancy in countries of the world on GDP according to the United Nations and the International Bank for Reconstruction and Development (year 2000): 1 – Australia; 2 – Bulgaria; 3 – Brazil; 4 – Great Britain; 5 – Denmark; 6 – Israel; 7 – India; 8 – Ireland; 9 – Spain; 10 – Netherlands; 11 – New Zealand: 12 – Norway; 13 – Russia; 14 – USA; 15 – Finland; 16 – France; 17 – Sweden; 18 – South Korea

Similarly simple estimates show that generating even much smaller capacity by using renewable environmental sources in personalized energy systems will also require quite large converter workspaces. In particular, for an additional external energy supply of a person at the level of capacity at least its peak capacity (about 1 kW) by using solar photovoltaic cells, wind power plants, thermoelectric generators, small water flow energy, etc. if the flow density of the actual power removed in them is about 100 W/m^2, the working area of each of these installations will be required at least 30 – 40 m^2, taking into account the relatively low values of their efficiency of about 25 – 30 %. The increasing of their energy efficiency through the use of new materials, as well as using possible processes of direct (non-thermal) conversion of source energy into electrical energy by the type of fuel cells with an efficiency of 60 – 80 %, allows reducing the weight and size characteristics of such installations. The possibilities of implementing such one-stage transformations are shown in Table 2, presented as a matrix of mutual transformation of various types of energy [38, 39]. As it follows from the the matrix of energy transformations that have practical significance, the possibilities of direct one-stage processes are very limited. A wider choice is provided by the multi-stage organization of sequential transformation of various types of energy with the use of intermediate working bodies. In all cases, it

TABLE 2. Matrix of possible transformations of various types of energy

Type of energy	1	2	3	4	5	6	7	8	9	10
1. Nuclear **PSE, SSE**	(+)	[+]	|+ |	+	[+]	[+]	+	[+]	<+>	[+]
2. Chemical **PSE, SSE, ES**	–	[+]	+	+	+	+	–	(+)	<+>	[+]
3. Electromagnetic **EC**	–	(+)	+	+	+	–	–	(+)	(+)	+
4. Gravistatic **SSE, ES**	–	–	–	[+]	[+]	–	–	+	+	+
5. Elastic **SSE, ES**	–	–	–	[+]	+	[+]	+	[+]	+	(+)
6. Electrostatic **SSE, ES**	–	–	–	+	+	+	+	[+]	+	+
7. Magnetostatic **SSE, ES**	–	–	–	+	+	+	+	+	+	[+]
8. Electric **EC**	–	[+]	+	+	+	+	+	<+>	<+>	<+>
9. Thermal **PSE, SSE, ES**	–	+	+	–	+	–	–	(+)	<+>	<+>
10. Mechanical **PSE, SSE, ES**	–	–	–	+	+	+	+	(+)	(+)	<+>

Designation: " – " – transformation impossible; " + " – transformation is possible, but of no practical interest; \|+ \| – transformation is possible and of practical interest, but not for energy purposes; [+] – the transformation is possible and of practical interest for energy purposes, but so far almost never used; (+) – same as previous but partially already in use; <+> – same as previous but widely used; **PSE** – primary source of energy; **SSE** – secondary source of energy; **ES** – energy storage; energy carrier.

is necessary to ensure the proper level of energy concentration and select working bodies of certain properties for conversion. The simplest, most reliable and promising ways have already been used and can only be improved in the direction of increasing the efficiency of transformations and the specific power of the converter.

Along with the need to increase efficiency, another problem in the development of personalized energy devices is the coordination of energy generation and consumption modes, taking into account the instability of renewable environmental sources and the physiological rhythms of human life. In order to ensure their coordination, well-known electro-galvanic accumulators are used, as well as new types of super-accumulators and double-layer electric accumulators [40–46] with special schemes for their buffer connection (Fig. 3 and Fig. 4), which control the automatic charging of these devices during periods when the amount of incoming energy exceeds the amount of consumed one. Otherwise, accumulated energy is returned to the consumer [9].

A separate extremely important task of personalized energy systems is to ensure a person's potable water requirements in extreme and emergency conditions in the absence of sufficient sources of clean fresh water. The physiological norm of its daily consumption for an adult is considered to be 30 – 40 g per kg of body weight, which on average is about 2.5 liters of water per day, and the same amount is excreted from the body. Under survival conditions, water consumption can be reduced to one quarter of the norm, but its complete absence or replacement with salty seawater leads to rapid dehydration with a fatal outcome in 3 to 5 days [11, 12, 47]. Possible solutions of this problem include distillation methods for cleaning and desalination of existing salty sea and ground waters using energy sources of the environment, primarily solar radiation.

In all these cases, the main criteria for the practical selection of energy sources in personalized energy systems are not only their availability and capacity indicators presented in Table 2 above, but also the possibility of implementing heat and power supply devices based on them as the most used types of energy, taking into account the specific conditions of their operation. In this regard, the mainly solid-state photo- and thermoelectric converters enumerated below, without mechanically moving elements, are considered as very attractive and preferable ones. A special role in solving the problems of their further improvement is assigned to the development of new functional materials for such devices and the identification of optimal modes for regulating the processes of energy conversion in them in terms of specific output power, efficiency and stability of energy transformation.
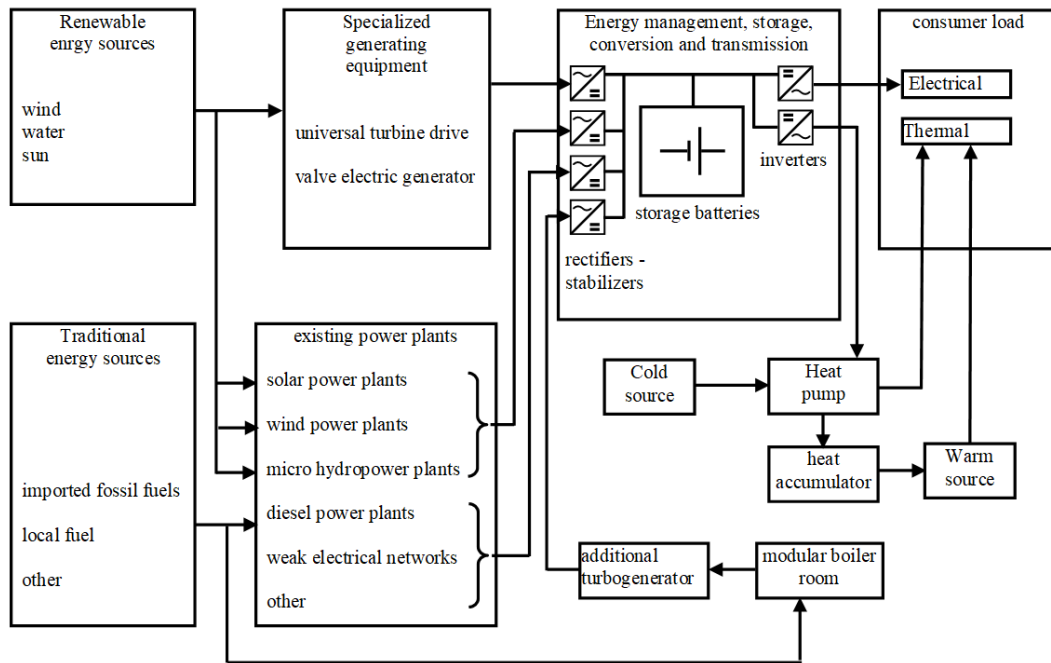
FIG. 3. Autonomous energy system with energy storage buffer
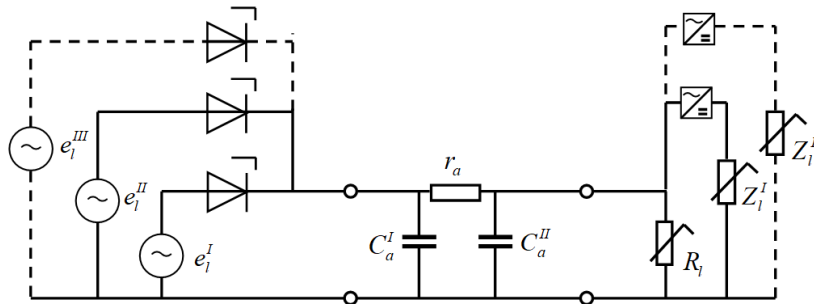
FIG. 4. An equivalent circuit for the calculated replacement of the buffer mode for turning on the drive as part of an autonomous energy system with several energy sources and consumers

3. Regulation of processes and optimization of energy transformation modes in personalized energy systems

3.1. Problems of model description of energy conversion processes in nanostructured media

The problems of optimal regulation of energy conversion processes in terms of specific output power, efficiency and stability in personalized energy systems remain very relevant not only in connection with the above-mentioned instability of its receipt from renewable environmental sources and uneven consumption in the physiological rhythms of human life. It is equally important to set requirements for the development of new materials for such converters, taking into account their operation in variable modes.

In the available works, energy conversion processes are usually considered either in the thermodynamically-equilibrium approximation [48,49] or on models of transport phenomena in non-equilibrium thermodynamic systems, usually applied to problems of continuous media, including not only natural [50–53], but also biological objects [54–56] and even social systems [57]. However, the application of the classical thermodynamic approach to small nanoscale objects requires a certain adjustment of the models used.

The proposed variants of "nanothermodynamics" which are based on the development of classical equilibrium thermodynamics take into account the contribution of surface energy [58], the extension of classical thermodynamics considering "separation energy" – the so-called nanothermodynamics of Hill [59,60], methods of molecular dynamics and Monte Carlo [61], lattice models [62], the van der Waals theory of inhomogeneous media [63], chemical approach

to the description of the nanoparticles as chemical education is a complex of supramolecule [64–66], statistical thermo-dynamics of small systems [67], nonextensive statistical thermodynamics, including the use of Tsalis entropy [68,69], "non-equilibrium" equilibrium thermodynamics with allowance for fluctuation theorems [70–72]. When the material contains a large number of non-autonomous interfacial formations of a fractal nature (non-autonomous phases), which are formed in a limited space between bulk macroscopic phases in the form of intermediate (transient surface or inter-nal) structures, the classical method of J. V. Gibbs is used for thermodynamic description of the system. It reduces the differences in the properties of these structures from the properties of bulk phases to a dedicated conditional tension surface located in the region of the interface [73].

3.2. Principles of thermodynamic extremes in the generalized analysis of energy transformation processes

In non-equilibrium processes, the thermodynamic behavior of non-autonomous phases, as well as the behavior of macroscopic bulk phases, can be conveniently considered based on the analysis of changes in the entropy of the system by using the principles of the extremum of thermodynamic potentials [74]. This approach, as more general in comparison with the Gibbs–Duhem equilibrium relation, is associated with the condition of positivity of internal entropy production due to the irreversibility of the processes [75]. Since the density of flows of various forms of energy increases with increasing nonequilibrium of the system, and the efficiency of their redirected transformation decreases due to the concomitant increase in irreversibility losses, the condition for obtaining the maximum power of energy transformation must correspond to the optimal level of thermodynamic nonequilibrium. Its estimation can be made on the basis of considering the processes of transfer and transformation of one type of energy into another as occurring in a certain volume (Fig. 5). Here, the initial energy type corresponds to the input thermodynamic flow J_1, which, under the action of the conjugate thermodynamic force X_1, is the driving force for the output flow of the converted energy type J_2, induced against the non-conjugate thermodynamic force X_2 [49].
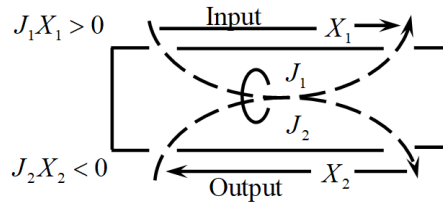
FIG. 5. Generalized energy conversion scheme

The phenomenological connection between thermodynamic flows J_i and the thermodynamic forces X_i in case of deviations from the equilibrium state, in close proximity to it and in stationary processes is described by a linear Onsager relations: $J_i = \sum_{k=1}^{m} L_{ik} X_{ik}$ [76]. Here, L_{ik} means the kinetic coefficients of direct and cross-effects of the transport of converted types of energy, which reveal reciprocity relations $L_{12} = L_{21}$, which are considered a theoretical consequence of the principle of microscopic reversibility of time [75,77], and a consequence of the relationship of convective components of heterogeneous flows at the macro level [78].

Using the Prigogine theorem on the representability of the power source of entropy in the form of a bilinear form of the generalized fluxes and forces,

$$I_S = \sum_i J_i X_i = \sum_i \sum_k L_{ik} X_i X_k = \sum_i \sum_k R_{ik} J_i J_k = \min \geq 0,$$

the number of components, which is equal to the number of degrees of freedom of the system, and stationary stable states correspond to minimum entropy production, and entropy moving from performance to energy, for the value of efficiency as the relationship of output and input power, $\eta = E_2/E_1 = T'' J_2 X_2 / T'' J_1 X_1$ in dimensionless form, we can obtain [49]:

$$W = -T'' J_M X_M = G(\Delta H - T'' \Delta S) = \frac{r(1-r)z}{z+1} L_{11} X_Q^2 = \frac{r(1-r)z}{[1+(1-r)z]^2} R_{11} J_Q^2,$$

$$\eta = \frac{-T'' J_M X_M}{T'' J_Q X_Q} = \frac{G(\Delta H - T'' \Delta S)}{(J_Q - H^\copyright G)\Delta T / T^\copyright} = \frac{r(1-r)z}{1+(1-r)z}.$$

Here, the parameter $r = -(L_{22}/L_{21})(X_2/X_1)$ corresponds to the dimensionless ratio of components in the output energy flow, and the parameter $z = L_{21}^2/(L_{22}L_{11} - L_{21}^2) = R_{21}^2/(R_{22}R_{11} - R_{21}^2)$ corresponds to the dimensionless q-factor of the converter. The inverse values of the conductivity coefficients L_{ik} characterize the transfer resistances of the corresponding energy flows in the system $\Omega_1 = X_1/J_1$ and $\Omega_2 = -X_2/J_2$.

3.3. Modes of energy transformation in non-equilibrium systems

By means of using the standard apparatus of maxima and minima depending on the ratio r and z the main modes of energy transformation are revealed:

- *idle mode and short-circuit mode* with zero output power of the converter; $W_2 = 0$ at $r = 0$ and at $r = 1$;
- *maximum output power mode* $W_{XQ}^{\max} = [(1/4)z/(1 + z)]L_{11}X_Q^2$ at $r = 1/2$ for a fixed power source (DC voltage $X_i = $ const) and $W_{JQ}^{\max} = [(1/4)z/(1 + z)R_{11}J_Q^2]$ for a fixed flow source (DC $J_i = $ const) at $r = (1 + z)(2 + z)$;
- *maximum efficiency mode* with the maximum value of the efficiency of the converter

$$\eta^{\max} = \left(\sqrt{1 + z} - 1\right)/\left(\sqrt{1 + z} + 1\right)$$

at $r = 1 - \left(\sqrt{1 + z} - 1\right)/z$.

As you can see, the maximum power mode is close to the maximum efficiency mode only for low-efficiency installations, with low q-factor at $z \ll 1$ with its increase, all other things being equal, the efficiency and output power increases. However, even for installations with infinitely high q-factor in the maximum output power mode, the efficiency cannot exceed 50 % of its maximum possible value for this type of converter, for example, the Carnot efficiency for heat engines, the Beitz–Zhukovsky coefficient for wind wheels, the Ioffe efficiency index for thermoelectric generators, etc. [79–81]. In the maximum efficiency mode, with an increase in the q-factor of the system, the efficiency value can approach 100 % of the possible efficiency as the limit for reversible equilibrium of the system, however, the output power tends to zero. In order to obtain high output power, high-quality installations with a constant-force power source must have low internal resistance and are poorly adapted to work with high load resistances, and systems with a constant-flow power source must have low internal conductivity and do not work well with high-conductivity loads. At the same time, in modes with zero output power and zero efficiency, energy costs $E_Q = T''R_{11}J_Q^2$ for maintaining the output power at idle are required, at a time when energy costs $E = T''L_{11}X_Q^2$ are required for maintaining the flow of matter at short-circuit mode. The graphical interpretation of the above energy conversion dependences, according to the generalized thermodynamic scheme, is shown in Fig. 6.

The analysis of the given energy characteristics makes it possible to identify the shaded area in Fig. 6 as the most appropriate for creating energy conversion devices, since there is a simultaneous loss in both output power and efficiency beyond its borders. The characteristics of real large-scale power plants presented here show that they are primarily focused on achieving maximum efficiency.
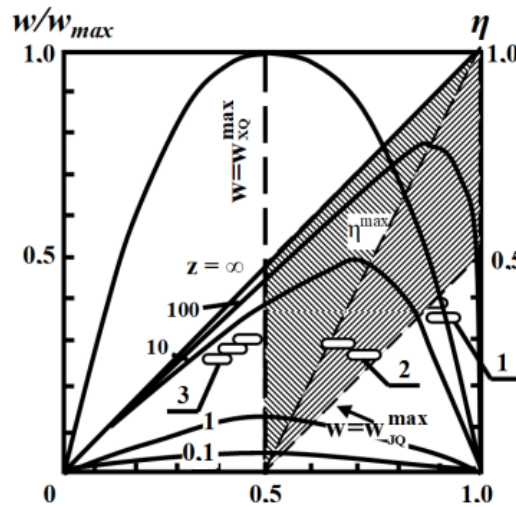

FIG. 6. Generalized characteristics of energy conversion in nonequilibrium thermodynamic systems with conjugate energy flows: 1,2,3-observable data on large-capacity power turbines of thermal power plants, nuclear power plants and gas turbines according to [80, 81]

3.4. Regulation of operating modes of non-equilibrium systems

The possibilities of the considered thermodynamic systems to adapt to work in a wide range of loads are illustrated by the diagram in Fig. 7 [54–56]. It is based on the fact that the linear Onsager equations formally describe the operation of affine transformation of the space of input variables $J_i X_i$ into the space of output variables $J_i X_i$, translating a rectangular coordinate grid into a skew-angular grid with the image of constant load lines in the form of rays coming out of the coordinate center. The examples of transition path from one state (mode) to another shown in the diagram correspond to various output power control programs used in power plants. Thermodynamic expressions for various paths are obtained from ratios that describe the change in output power and efficiency of the converter for the selected method of regulating the power of energy source or load taking into account the boundary flow values, $[J_1], [J_2]$ and forces $[X_1], [X_2]$ that are maximum allowable under the terms of the destruction of the system.
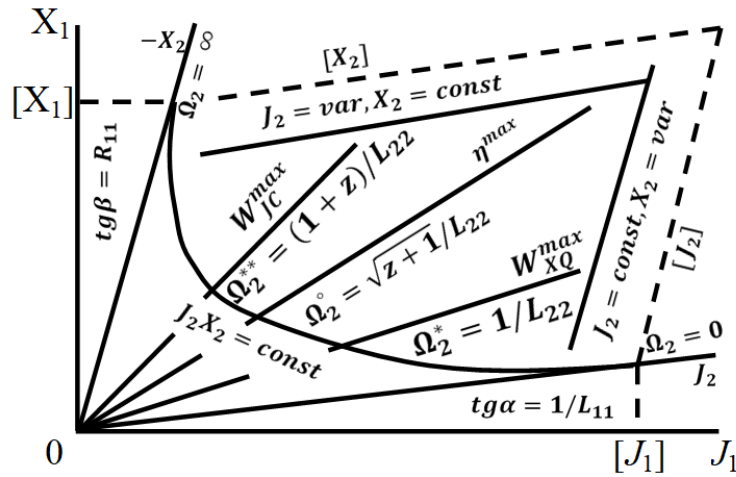

FIG. 7. Load path of energy converters in the input-output space for various control programs

These programs can be implemented by either adjusting the power used by the power source with the converter and load parameters unchanged, or by changing the parameters of the converter and load itself with the input source power unchanged. As can be seen, the greatest thermodynamic gain in efficiency is provided when regulating along the path Ω_2^0, and in terms of output power – along the paths Ω_2^* or Ω_2^{**} depending on the types of energy source discussed above. The control along the path $J_2 X_2 = \text{const}$ ensures constant output power of the converter. The corresponding schemes of serial and parallel regulation are shown in Fig. 8.

3.5. Stability of processes in non-equilibrium systems

The described energy-entropy approach is used in our work in order to analyze the stability of non-equilibrium systems under deterministic and spontaneous fluctuations of thermodynamic quantities with the formation of self-organizing dissipative regimes and structures [80, 81]. The variational synergetic principle of least energy scattering (dissipation) was used as a thermodynamic stability condition, which is equivalent to the theorem of Prigogine on the minimum entropy production in stationary linear systems of the Onsager type, but also allows for the contribution of nonlinear effects. At the same time, a relative non-stationary coefficient of the form $\varepsilon = \langle \dot{E}(J_i X_i) \rangle / \dot{E}(J_{0i} X_{0i})$ is introduced for a general assessment of the influence of dynamic perturbations of flows and forces on changes in entropy production in comparison with their stationary values and determination of self-organization parameters on this basis.

Here, $E(J_{0i} X_{0i}) = T'' S$ is the variable energy dissipation (entropy production). In a system with stationary values of flows and forces, $\langle E(J_i X_i) \rangle$ is the average value of this variable in a system with perturbed flows and forces, determined by the usual averaging rules for both deterministic, for example, harmonic $X_i(\tau) = X_{0i} [1 + n_i \cdot \sin(\omega_i \tau + \nu_i)]$ and random $\bar{E} = \int_{-\infty}^{+\infty} E \cdot \psi(E) \cdot dE$ processes. The value $\varepsilon = 1$ corresponds to a stationary undisturbed state (mode) of a non-equilibrium system; the values $0.5 \leq \varepsilon \leq 1$ correspond increased or decreased dissipative energy losses at various deviations from this mode. The mathematical formulation of the problem of regime stability and energy-entropy self-organization in such a system is reduced to finding the lowest value of entropy generation $\varepsilon = \varepsilon_{\min}$ depending on the perturbation parameters. This is quite valid even
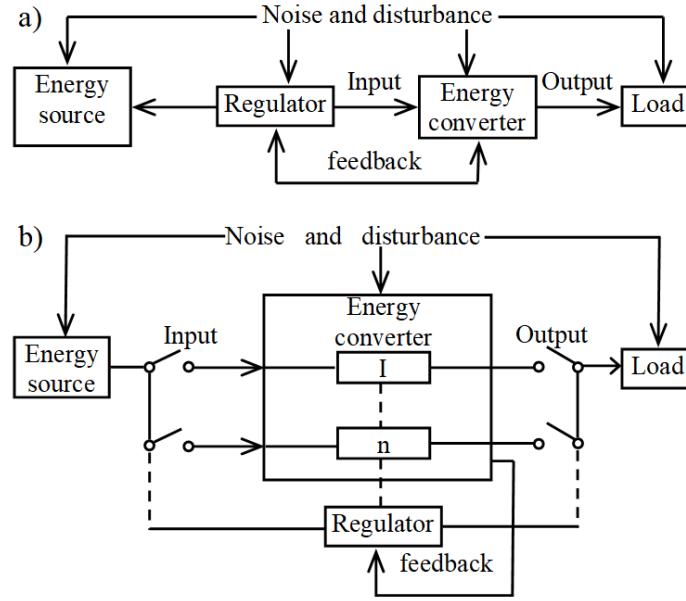
FIG. 8. Schemes of sequential (a) and parallel (b) regulation of input and output power

for systems that allow a linear relationship between thermodynamic flows and forces, $J_K = \sum L_{ki} X_i$, due to the general quadratic (bilinear) function of entropy production from the acting flows and forces. The minimization of the expression in this case

$$\varepsilon = \frac{\left[L_{11}\langle X_1^2 \rangle + 2L_{12}\langle X_1 X_2 \rangle + \langle X_1^2 \rangle \right]}{\left[L_{11}X_{01}^2 + 2L_{12}X_{01}X_{02} + L_{22}X_{02}^2 \right]}$$

leads to the identification of three successive modes of self-organization system, delimited by the roots of the characteristic equation $\dfrac{\partial \varepsilon}{\partial(n_1/n_2)} = 0$ (Fig. 9). As follows from this analysis, a necessary condition for energy-efficient self-organization of the considered thermodynamic systems with the achievement of minimal entropy production $\varepsilon = \varepsilon_{\min}$ in the range $\varepsilon_{\min} \le 1$ is an antiphase $(\nu_1 - \nu_2) = \pi$ feedback between the input and output flows (forces) carried out through direct and cross-coefficients of conductivity L_{ki}.

The explicit form of expressions for flows and forces, as well as for the source of entropy production in the dependencies of the generalized thermodynamic model is determined by comparing the records of the Onsager and Prigogine relations with the results that follow from the generalized Umov–Poynting balance equations

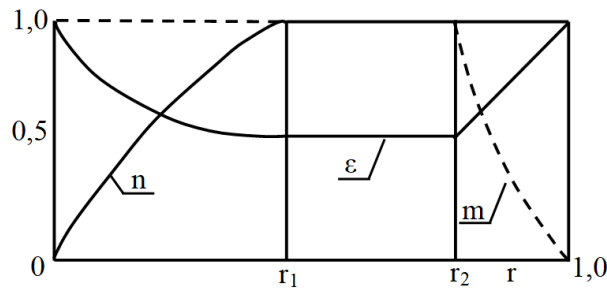$$\rho \frac{dC}{d\tau} + \operatorname{div} J_c = I_c$$

FIG. 9. Change in the relative non-stationarity coefficient ε during self-organization of energy conversion processes for nonequilibrium thermodynamic systems depending on the relative perturbation amplitudes n and m of the acting thermodynamic forces and the ratio of the components of the energy flows r [53]

describing the transfer of an arbitrary substance C (mass, momentum, energy, entropy, etc. in a moving medium), together with the Gibbs relation

$$TdS = dU + pdV + \sum \mu_j dM_j + \sum a_\nu dA_\nu$$

considered for non-equilibrium conditions based on the local equilibrium principle. Here: ρ – medium density, I_C – sources of the target substance, T – temperature, S – entropy, U – internal energy, p – pressure, V – volume, μ_j – chemical potential, M_j – molar mass of substance j in the system.

The central place among these relations belongs to the entropy balance equation, which separates the total change in entropy $dS = d_e S + d_i S$ due to the interaction of the system with the environment $(d_e S)$ and due to the action of an internal source of entropy due to irreversible processes $(d_i S \geq 0)$.

It should be noted that for the first time many historically significant estimates of the specific power and efficiency of energy transformation processes were obtained when solving specific scientific and technical problems of their time, which later determined the directions of modern development of personalized energy considered below. We also note that the use of new nanostructured materials with nonlinear energy transfer effects of various levels expands the nature and areas of manifestation of stability and instability of processes, the possibilities of their regulation and self-organization conditions in thermodynamic systems, where the determining role is played not by entropy production as in linear systems, but by the rate of its change [75].

3.6. Influence of nonlinearities in the structure and properties of the material on the processes of energy transfer and transformation

Non-linearities in the structure and properties of the material are reflected in the processes of energy transfer and transformation in nanostructured converters and storage devices up to the development of modes with aggravation, which express the inertia of transfer processes in a limited part of the medium and local energy concentration with their retention for a finite time practically without spreading to other zones. Such regimes were studied by A. A. Samarsky and other scientists in problems for quasi-linear parabolic equations in continuous media [24, 25]. The analysis of the influence of structural inhomogeneities and functional properties of nanodisperse materials on the nature of the development of such regimes can be carried out on the basis of the modified Fourier–Fick law and the nonlocal transport equation in fractional derivatives with respect to coordinate and time [82–86].

For a general assessment of the influence of metrico-statistical characteristics of the structure of nanodisperse and composite materials on such effects, in particular, manifested in the non-smoothness of the phase paths of solutions of these equations and the stochasticity of their phase attractor up to violations of the ergodicity of the system, fractal analysis methods are used [87, 88]. They consider the self-similarity of different-scale phase formations with a fractional non-Euclidean dependence $M \sim \varepsilon^D$ between the rate of increase in the number of elements considered M and the increase in the scale of their consideration ε based on the generalized Renyi relation

$$D_{Rq} = \lim_{\varepsilon \to 0} \lim_{r \to 0} \lim_{m \to \infty} \left[\frac{1}{1-q} \cdot \frac{\ln I_{Rq}(q, \varepsilon)}{\ln(1/\varepsilon)} \right].$$

Here, $I_{Rq}(q, \varepsilon) = \left[\sum_{i=1}^{M(\varepsilon)} p_i^q(\varepsilon) \right]$ – is the generalized Renyi entropy of order q; $M(\varepsilon)$ – is the minimum number of "measuring" elements with size ε, required for covering of the fractal in the n-dimensional phase coordinate space of the embeddings; p_i – is the probability of visiting the i-th cube by the phase path; m is the number of points used to estimate the dimension [89]. This relation is followed by well-known expressions for the Kolmogorov–Sinai entropy and the Kolmogorov–Hausdorff fractal dimension $(q = 0)$, Shannon entropy and the corresponding information dimension $(q = 1)$, correlation entropy and correlation dimension $(q = 2)$ as special cases for different q [90]. The establishment of these characteristics allows us to link the indicators of structural and phase heterogeneity and their self-organization in the development of new materials with changes in their physical and chemical properties.

The establishment of these characteristics allows us to link the indicators of structural and phase heterogeneity and their self-organization in the development of new materials with changes in their physical and chemical properties.

The characterization of the fractal dimension of nanostructured materials, including micrographs of their chips according to the method discussed in detail in [91], indicates the multifractal nature of their structural-phase inhomogeneity with a whole spectrum of fractal dimensions according to the generalized Renyi ratio, in contrast to the classical regular monofractals of the Sierpinsky structure type [88]. The essential role of fractal structures in regulating the functional properties of such materials is shown for almost all technologies and methods of nanomaterial synthesis [22]. This is determined by the special role of energy and entropy characteristics of non-autonomous phases (interphase layers), the correlation scale of the phenomena of matter and energy transfer in different-sized macro-,

micro- and nano-structural blocks of the material, as well as the tolerance factor of their interface. At the same time, the kinetic and dynamic characteristics of energy-mass transfer and chemical kinetics processes that occur under the conditions of spatial and mass restrictions of non-autonomous interphase formations, where the energy dissipation rate is significantly higher than in macro-volume blocks of matter, change. In particular, the result of changes in the fractal dimension over a layer of strongly micro-homogeneous material may be an unevenness of its thermophysical characteristics, which was experimentally recorded in [92] with the wave-like nature of the temperature distribution characteristic of the acute regime (Fig. 10).
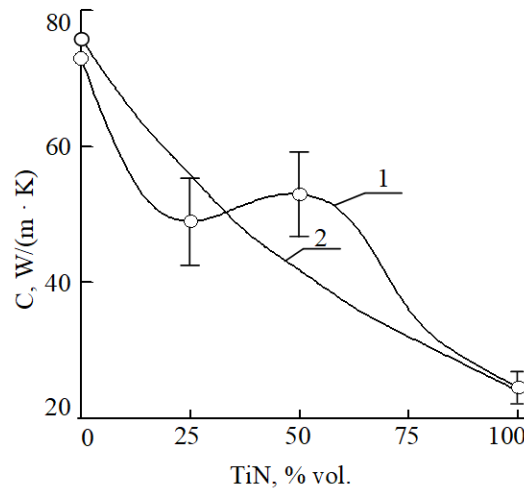

FIG. 10. Comparison of theoretical and measured values of thermal conductivity of the sintered TiN–AlN composite: 1 – thermal conductivity, determined on the basis of the measurement results at $T = 30\,^\circ$C; 2 – theoretical dependence for the "ideal" mixture of non-interacting components [92]

4. Features of energy conversion processes using renewable sources of the environment and the body's own capabilities

4.1. Solar power systems

Solar radiation is the common basis of all the Earth's renewable energy, with an available power of about 100 W/m^2 on a surface illuminated by the Sun. The use of this energy in personalized energy systems can now be carried out by transforming it into the most commonly used electrical and thermal forms using photovoltaic and photochemical generators, as well as heating elements. The first type of generator is based on three types of photo-electric effect (external, internal, and lockable layer), the second – on the photovoltaic effect and solar regenerative fuel cells, and the third – on the effect of thermal accumulation by materials with a high specific heat capacity [93, 94].

In the above-mentioned three types of effects, the liberation of electrons out of a substance by incident light, a significant energy result is only achieved while using semiconductor elements with a locking layers of p-n junctions. The volt-ampere characteristic, or the relationship between the thermodynamic force and the thermodynamic flux in terms of the general energy transformation model, for such a solar cell is the superposition of the Shockley volt-ampere characteristic of an unlit diode $J = J_S\left[\exp(qV/AkT) - 1\right]$ and its light current J_L when the p-n junction is illuminated, as shown in Fig. 11. The latter is characterized by the appearance of a parallel photo-emf on the internal resistance $V_{RS} = (AkT/q)\ln\left[(J - J_L)/J_S + 1\right]$ due to the excitation of light-generated charge carriers of the hole-type in the n-region and the electron type in the p-region [95].

The maximum output power of the photovoltaic transformation of solar radiation energy is determined from the condition $[d(V_R \cdot J_L)/dV_R] = 0$ and is achieved when the internal resistance of the element is optimally matched with the shunt p-n junction external load, amounting to $W_{\max} = J_L^2 R_L F = J_L^2 R_S F M_{opt}$. Here $J_S = AkT/qR$ is the diode saturation current due to the thermal generation of hole and electronic carriers of elementary charge q; A is a dimensionless coefficient depending on the type of semiconductor; k is the Boltzmann constant; T is the temperature; R is the load resistance; F is the illuminated area; $M = R_L/R_S$. This indirectly takes into account the energy contribution of the spectral composition of solar radiation photons, both in the generation of useful power and in the
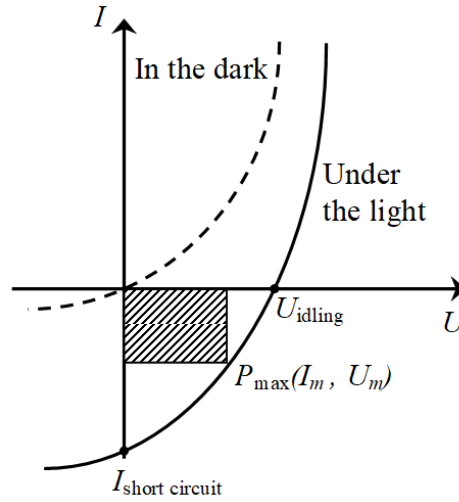
FIG. 11. Current-voltage characteristic of a solar cell based on p-n junction [96]

thermal vibrations of the semiconductor lattice in the form of

$$J_L(E_g) = q \int\limits_{h\nu=E_g}^{\infty} \frac{dn_{ph}}{d(h\nu)} d(h\nu),$$

where E_g is the band gap. The spectral response of the used types of semiconductors is also indirectly taken into account through the dimensionless coefficient A. The optimal load ratio $M_{opt} = R_L/R_S$ can be found graphically from Fig. 11 from the aspect ratio of the shaded rectangle of the maximum area.

The effective efficiency of a solar power generator is determined by the formula

$$\eta_q = \frac{qV}{[(h\nu)(J/J_D)]},$$

where $h\nu$ is the photon energy spent on the formation of a pair of carriers; V is the potential difference, and J/J_D is the ratio of the useful load and diffusion current through the locking layer of the p-n junction due to the uneven distribution of charge carriers over the volume of contacting semiconductors. Although the maximum thermodynamic efficiency of a solar cell in accordance with the Carnot formula $\eta_{\lim} = \dfrac{(T_1 - T_2)}{T_1}$ is estimated at about 95 % when the solar radiation spectrum is approximated by the blackbody radiation spectrum with the emitter temperature $T_1 = 5800$ K and the receiver temperature $T_2 = 300$ K [97], this estimate for the maximum power mode decreases by at least half according to the consequences of the generalized energy transformation model, remaining, however, at a fairly high level of 45 – 48 %.

At the same time, the actual achieved efficiency of solar cells, which has significantly increased from 11 to 15 % for those previously created on the basis of silicon and germanium, currently does not exceed 39 – 41 %, even for a new generation of photovoltaic semiconductor converters. They are developed on the basis of multilayer, for example, AlInGaPAs/GaAs/Si, InGaP, InGaAs and Ge nanoheterostructures of cascade type grown by gas-phase epitaxy from organometallic compounds on silicon and germanium substrates [98–106]. At the same time, an increase in the maximum power of the solar cells is achieved not only by improving the structure of p-n junctions, but also by focusing the sun's rays using mirrors and Fresnel mini-lenses. Experiments show that with increasing intensity (countrywoman) incident flux in 100 – 150 times output power grows 20 – 30-fold, as many times is reduced occupied by the phototransducer working area, however, when increasing concentrations above 4 – 5 W/cm^2, a significant increase in power occurs.

It should be noted that the highest efficiency values of solar photovoltaic cells have been achieved for systems based on A^{III}B^V compounds belonging to straight-band semiconductors, in which direct optical zone-to-zone transitions are allowed, while for other semiconductors the efficiency currently does not exceed 20 – 25 % [107, 108]. In addition, the widespread use of solar cells on inorganic materials is constrained by relatively expensive technology for the production and processing of inorganic semiconductors, which requires high temperatures and high vacuum.

In this regard, to create new types of cheap solar cells, technologies of thin-film (0.5 – 1.0 microns) solar cells based on amorphous hydrogenated silicon (a-Si:H) with a *p–i–n* structure have been developed since the 1970's. They

are obtained by a relatively cheap method of decomposition of SiH_4 monosilane in a glow discharge plasma without the use of expensive silicon substrates or harmful and toxic substances, with a thickness of 300 microns, and they have higher electronic properties and 20 times greater optical absorption compared to single-crystal silicon [109–115]. The proposed *p–i–n* structure makes it possible to create a uniform internal electric field in the entire region of optical light absorption (i-region), which is necessary to provide the film with (a-Si:H) the drift of hole charge carriers with a very small diffusion length ($\sim$ 100 nm), in contrast to crystalline solar cells based on p-n junctions, where charge carriers with a larger diffusion length (100 – 200 microns) reach the electrodes in the absence of an electric field. Such ultra-thin photosensitive semiconductor films on organic and/or polymer substrates of millimeter thickness can be made using roll technology, and they are already competitive in the market of mass power production.

Along with this, there is an increasing interest in organic and hybrid materials, in particular, with the implementation of a bulk heterojunction based on a donor-acceptor composite polymer (donor) with an acceptor material based on fullerene derivatives, polymer and low-molecular acceptors, discussed in detail in the review paper [116–118]. In order to expand the spectral sensitivity of polymer solar cells, it is possible to use narrow-band acceptor components with strong absorption in the region of the optical gap of the conjugated polymer. Such components can be inorganic nanoparticles, for example, quantum dots based on metal chalcogenides stabilized by suitable ligands, as well as core-shell quantum dot structures [119]. The resulting problem of extracting charge carriers from nanoparticles when they are stabilized by organic ligands is solved quite effectively in an electrochemical Gretzel's solar cell [120–123], created on the basis of nanocrystalline titania TiO_2, a metal-complex ruthenium dye and an iodine electrolyte and having an efficiency of up to 11 % (Fig. 12).
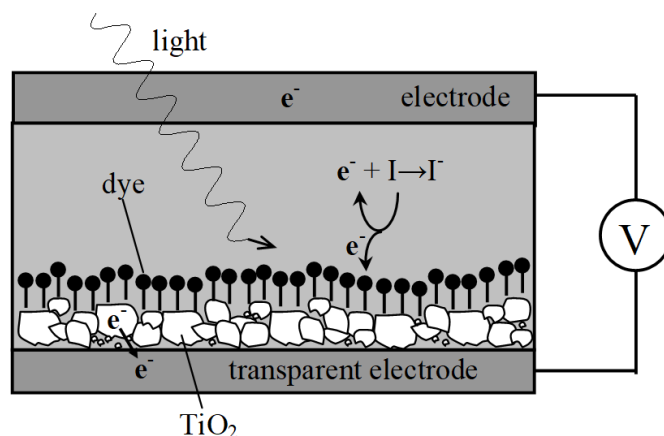

FIG. 12. Gretzel's electrochemical cell [120]

In order to overcome one of the main disadvantages of Gretzel's electrochemical cells associated with the use of a liquid electrolyte that evaporates during long-term operation, the problems of replacing it with a solid electrolyte or eutectic melt are considered [124–134].

Among the chemical methods of solar energy conversion, photochemical, photoelectrochemical (including photoelectrolysis of water into hydrogen and oxygen) and photocatalytic methods are traditionally considered [135, 136], the analysis of which is not included in the tasks of this work. We note only the prospects for using the photocatalytic properties of titania TiO_2, which is widely distributed in nature, not so much for photoenergetic purposes, but for use in water and air purification systems from toxic chemical compounds and disinfection of various types of microorganisms [120–122, 137–139].

Solar radiation, along with the possibility of transformation into an electric current source, can also be easily converted into a heat source [93, 94]. The simplest devices of this type for personalized energy systems are low-temperature heaters in the form of a "hot box". They allow one to obtain the temperature of the intermediate heat carrier circulating inside its pipe system in the range from 55 – 85° with an efficiency of 20 – 40 % to 200 °C at an outdoor temperature of 15 – 20 °C. The physical basis of heating is a local greenhouse or greenhouse effect, which is manifested by the re-emission of heat from the heat-insulated internal volume of the "box" heated by the sun with different transparency of its cover glass (or polyethylene film) in the visible and far infrared ranges. The removed heat can be used not only for heating and cooling of premises, water lifting and drying installations, for cooking, but also for other needs, including desalination of salt sea water. Various designs for the implementation of a solar desalination plant with a specific capacity of 3 – 5 l/m^2 per day have been developed for a long time, including for the crews of aircraft and ships in distress on the high seas [140, 141]. One of the modern versions of such a desalination plant

produced by a German company "Augustin Produktentwicklung" is an inflatable floating shell made of transparent plastic with an inner rim and a blackened bottom strip made of a sponge soaked in sea water (Fig. 13). The water evaporated by the sun's heat condenses when it comes in contact with the cooler sealed sub-cone shell, and the distillate flows down to the lower part of the desalinator. The cone can also be installed on wet ground soaked in salt water. The desalination plant also works at night due to the temperature difference inside and outside the cone.
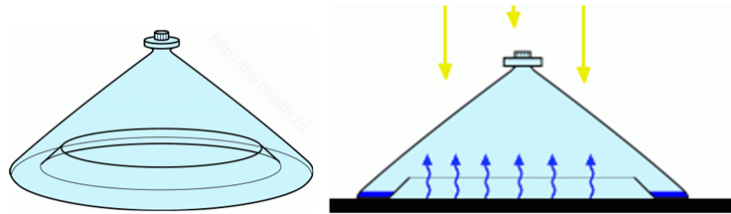

FIG. 13. A desalination solar cone with a base diameter of about 0.8 m and with an optimum 78 degree angle for draining condensed moisture at the apex, providing 40 % efficiency for 1 – 1.15 liters of fresh water per day (URL: http://www.augustin.net/, http://www.watercone.com/)

In principle, it is also possible to recover from the air the moisture always contained in it, for example, by condensing it under strong cooling, which, however, requires excessive energy consumption for each liter of moisture. The proposed cheaper options are based on the phenomenon of intensive absorption of atmospheric moisture by various substances. For example, we can use liquid lithium chloride, followed by the separation of water from the lithium salt by semipermeable membranes due to reverse osmosis. Special nanofabrica "for fog-catching" with alternating nanoporous capillaries and a water-repellent network for collecting absorbed moisture are also proposed.

4.2. Thermoelectric converters

With regard to the problems of heat and power supply as the most used types of energy, this type of solid-state devices without mechanically moving elements can be attributed to the historically first developments in this field, taking into account the specific operating conditions of personalized energy systems. Their characteristics for specific conditions of direct conversion of heat to electricity were first analytically obtained by A. F. Ioffe [142]. This contributed to the widespread use of such devices in the 1940's and 1950's to power battery-operated lamp radio stations and radio receivers up to 10W of power by heating with a kerosene lamp or a fire pot (Fig. 14).

a)   b)   c)
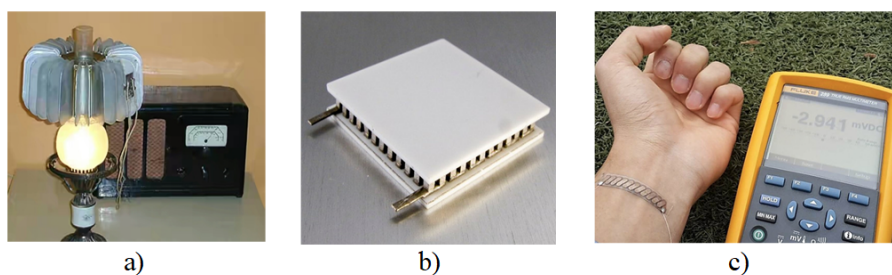
FIG. 14. Museum copy of the thermoelectric generator with a power of 10 W at $\Delta T = 300\,^\circ$C (a) [146] and modern thermoelectric modules of the same power with a size of $40 \times 40 \times 3$ mm at $\Delta T = 170\,^\circ$C (b) [147]; as well as glass fabric (c)

Currently, thermoelectric converters are being improved based on the development of new nanostructured materials, available heat sources and technologies [143, 144], and work is underway to use the existing background electromagnetic radiation in the radio frequency and light range, and even the heat of the human body for similar purposes [145].

The results obtained by A. F. Ioffe [142] and based on the consideration of the Seebeck effect underlying thermoelectric converters for the appearance of a potential difference ΔV at the ends of series-connected dissimilar conductors at different temperatures $\Delta T = T_1 - T_2$ (Fig. 15) specify the above relations of the generalized model in the form of the following dependencies for efficiency and output power.
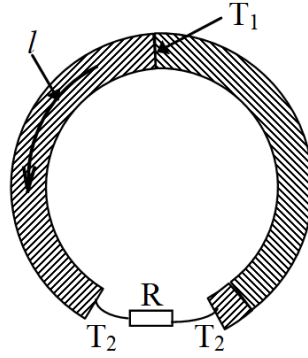
FIG. 15. Scheme of thermoelectric thermogenerator, T_1, T_2 – temperature ($T_1 > T_2$); R –electric load; l – current direction [93, 142]

All in all, the expression for the efficiency of converting thermal energy into electrical energy is given by the formula:

$$\eta = \frac{T_1 - T_2}{T_1} \frac{m/(m+1)}{1 + (kr/\varepsilon^2)(m+1)/T_1 - 0.5\Delta T/T_1(m+1)} = \frac{m/(m+1)}{1 + (m+1)/ZT_1 - 0.5\Delta T/(m+1)}.$$

Here T_1 and T_2 are the temperatures of the hot and cold sides of the thermoelectric converter; $m = R/(r_1 + r_2)$ is the ratio of the resistances of external and internal loads in the circuit of connected conductors;

$$Z = \left[(\varepsilon_1 + \varepsilon_2)^2\right] / \left[\left(\sqrt{\lambda_1 r_1} + \sqrt{\lambda_2 r_2}\right)^2\right]$$

is the total thermoelectric q-factor of the converter, depending on the values of the Seebeck thermoelectric coefficients $\varepsilon = \Delta V/\Delta T$ for the selected p and n-type materials, their thermal conductivity λ_p (λ_n) and resistivity r_p (r_n). We should note that in solids, the thermal conductivity $\lambda = \lambda_l + \lambda_e$ includes the lattice (phonon) (λ_l) and the electronic (λ_e) components, the latter being related to the specific electrical conductivity of the material by the Wiedemann–Franz law $\lambda/\sigma = LT$, with their ratio practically unchanged for different metals at the same temperature $\lambda_e = L\sigma T$, where L is the Lorentz number [148].

Taking into account the value of the current in the circuit $i = \varepsilon\Delta T/(r+R) = \varepsilon\Delta T\left[R(m+1)\right]$ and the magnitude of the generated voltage to an external load equal to the thermo-emf, minus the voltage drop on the internal resistance $U = E - U_r = \varepsilon\Delta T - ir$ the following modes of thermoelectric conversion are determined.

For the mode of maximum electric power $W^{\max} = IU$ at $m = R/t = 1$, the expression efficiency takes the form

$$\eta_{t,N} = \frac{\Delta T}{2(T_1 + 2/z) - (\Delta T/2)},$$

for the mode of maximum efficiency – the form

$$\eta_t^{\max} = \frac{T_1 - T_2}{T_1} \cdot \frac{(M-1)}{M + (T_2/T_1)}$$

at $m_{opt} = (R/r)_{opt} = M\sqrt{1 + 0.5z(T_1 + T_2)}$. As can be seen in mode $\eta_T^{\max}$ the power drops compared to the maximum $w_{\max}$, however, largely reduced the total heat flow through the thermoelectric power source by reducing the Peltier heat taken from the hot junction due to the fall of i in the chain while m-increasing. In this way, an optimal energy balance is achieved.

Ignoring the accounting Joule heat $i^2 r$, we can simplify the expression of the optimal ratio of resistance $M' = \sqrt{1 + zT_1}$ and corresponding optimum efficiency:

$$\eta_t^{\max} = \frac{T_1 - T_2}{T_1} \cdot \frac{\sqrt{1 + zT_1} - 1}{\sqrt{1 + zT_1} + 1}.$$

A graphic illustration of the dependences obtained by A. F. Ioffe with the graphs of the above dependences of energy conversion according to the generalized thermodynamic scheme is shown in Fig. 16.

As it can be seen, the full electromotive difference of potential of the thermoelectric power source $E = \varepsilon\Delta T$ provides the current strength in the electric circuit $i_{sh.c.} = E/r$ when the junctions are short-circuited at $R = 0$ to $i = 0$ when the load resistance is open $R \to \infty$, and in the maximum power mode $i \cong 0.5i_{sh.c.}$. Therefore, one
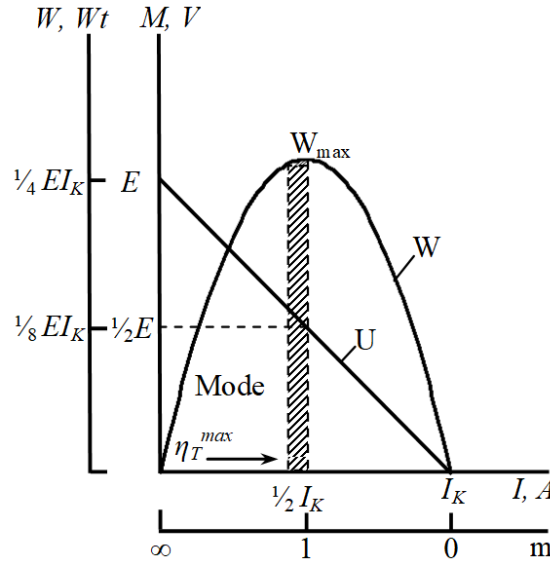
FIG. 16. Characteristics A. F. Ioffe Energy Efficiency Thermoelectric Power Generators [93, 142]

element can only be used with low ohmic loads, but to ensure high-resistance loads, it is necessary to use a system of series-connected elements in a thermal battery with a sufficiently high internal resistance and total efficiency [93]:

$$\eta_\Sigma = \eta_1 + \eta_2(1 - \eta_1) + \eta(1 - \eta_1)(1 - \eta_2) + ... + \eta_n(1 - \eta_1)(1 - \eta_2)...(1 - \eta_{n-1}).$$

The reverse of the Seebeck effect, the Peltier thermoelectric cooling effect is used in solid-state thermoelectric refrigerators that do not have mechanically moving elements, as well as thermal generators. The main energy characteristic of such devices is the cooling coefficient $\eta_c = Q_c/A = Q_c/I\Delta V = Q_c/\varepsilon I\Delta T$, where $\Delta T = (T_1 - T_2)$ is the temperature difference between the hot and cold junctions of dissimilar conductors, and Q_c is the absorbed heat at the cold junction at temperature T_2.

Taking into account the Joule heat release on the internal resistance of the branches of the thermoelement when transferring heat from a cold to a hot junction at a temperature T_1, it is possible to express the efficiency

$$\eta_c = \left(\varepsilon I T_2 - 0.5I^2 R - \lambda \Delta T\right) / \left(I^2 R + \varepsilon I \Delta T\right)$$

and determine its maximum value for the current value [149, 150]:

$$I = (\varepsilon \Delta T) / \left[R(1 + 0.5Z(T_1 + T_2) - 1]^{1/2}.$$

As you can see, the cooling coefficient tends to its maximum value $\eta_c^{\max}$ at $Z \to \infty$, and the maximum cooling capacity $Q_c^{\max}$ is achieved at the maximum operating current $I_{\max}$ with $\eta_c = [T_2 - 2\Delta T/ZT_2]/2T_1$. In this case, the total heat output of the device in this mode will exceed the Joule heating of $0.5I^2 R$ by the variable $Q_h^{\max} = Q_c^{\max} + 0.5I^2 R$, where $Q_X = \eta_X \varepsilon I \Delta T$. This allows it to be used as a heat pump with an efficiency coefficient of $\eta_h = Q_h/I\Delta V = Q_c^{\max} + 0.5I^2 R)/I\Delta V$ [151]. The high functional flexibility of thermoelectric coolers and heat pumps allows somebody easily change their operating mode from the maximum efficiency $\eta_X^{\max}$ up to the maximum thermal power $Q_X^{\max}$ regimes by changing the applied voltage and the q-factor Z of the thermoelectric materials used.

According to A. F. Ioffe [142], the main criteria that must be met by effective thermoelectric materials with high q-factor are: a) the presence of heavy atoms in the material that reduce the lattice thermal conductivity; b) the possibility of deep doping of the matrix to achieve a concentration of charge carriers of the $10^{19} - 10^{20}$ cm^{-3}; c) high values of the Seebeck coefficient ($\varepsilon > 200$ mV/K); d) not too small band gap; e) high effective mass of charge carriers. In this case, solid solutions should have a higher thermoelectric q-factor compared to individual compounds due to lower values of their lattice thermal conductivity due to the disordered nature of one or more sublattices. To a large extent, the functional characteristics of thermoelectrics are determined by the concentration of charge carriers. The electrical conductivity and the electronic component of the thermal conductivity increase with increasing concentration of charge carriers, and the thermo-emf, on the contrary, decreases; the power factor of a thermoelectric material and its thermoelectric q-factor pass through the maximum corresponding to the transition zone between semiconductors and metals, and the thermoelectric converter itself consists of two p- and n-type semiconductor columns (Fig. 17).
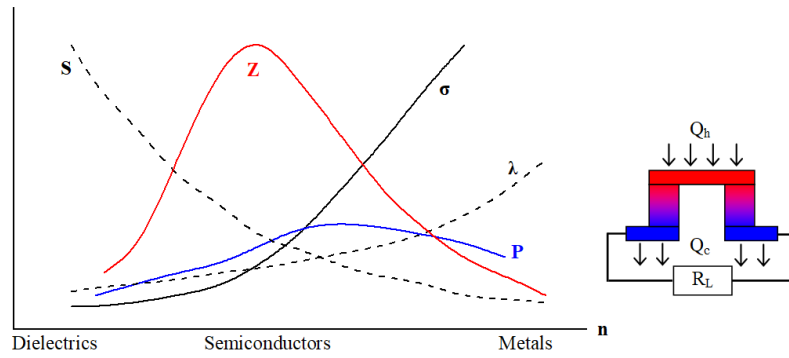
FIG. 17. Concentration dependences of the main characteristics of thermoelectrics. The maximum value of the thermoelectric figure of merit corresponds to a concentration of charge carriers of the order of 10^{19} cm^{-3}

4.3. Background electromagnetic radiation and optical nanoantennas

The targeted application of the fractal organization of nanostructured objects described above creates a possibility for using background electromagnetic radiation, in particular, radio radiation, to power wearable low-power electronic devices in personalized energy systems. Although in the environment, background radio frequency energy has the lowest specific power compared to other alternative sources, such as solar and wind energy, magnetic field energy, thermoelectric materials, including those that convert human body heat, piezoelectric materials that convert the energy of mechanical vibrations, motion or acoustic noise, etc., compared in Table 2 according to [30] and detailed in [32–35], it radiates in a very wide frequency range, independent of the time of day, temperature fluctuations, the presence of noise and vibrations. The beginning of the development of this topic can be considered the simplest detector receivers, which were widely used in the first decades of radio broadcasting, did not need a power source and used exclusively the energy of the received radio signal of the DV and SD bands according to the principle proposed by Nikola Tesla in 1890.

Currently, the power of background radio emission has increased many times (up to 1 mW/cm^3 in total) due to the development of HF and VHF radio broadcasting, analog, digital and satellite television, cellular communications, etc. The energy transmitted by them can be converted into a constant voltage and stored for subsequent power supply of low-power electronic devices by special receivers-microchipsets (energy harvesters with dimensions of about 5×5 mm), developed by various companies [152]. In order to collect this energy, additive antenna technologies with a fractal or fractal-like topology are being developed [153]. Thus, the Institute of Radio engineering and Electronics (IRE named after V. A. Kotelnikov) of the Russian Academy of Sciences proposed broadband fractal antennas (Fig. 18) with a wide absorption band of electromagnetic energy and a wide directional pattern and programmable frequency-selective properties with a transition from 2D to 3D electrodynamic media [154]. They use direct current magnetron sputtering technology and 3d inkjet printing technology with the use of nanoparticles based on metal nanoparticles.

a)   b)   c)
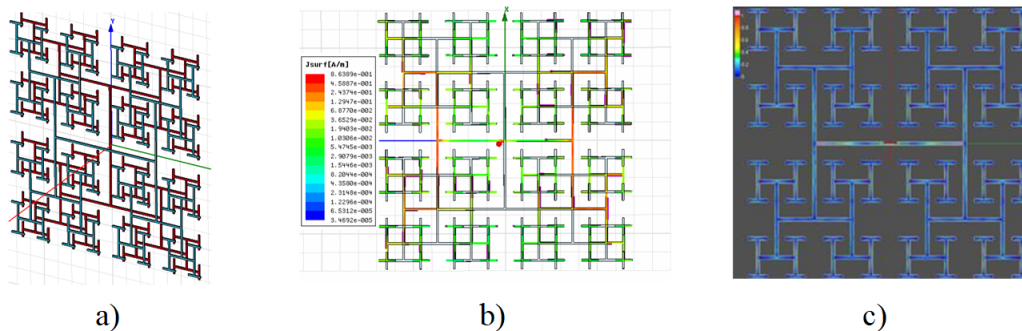
FIG. 18. Antenna plates of fractal frequency-selective surfaces based on the 'Keighley Tree' (a) and current distribution over the surface of fractal structures in normal (b) and inversion (c) color images [154]

Optical nanoantennas are being developed to solve a similar problem of direct collection of the energy of natural electromagnetic radiation from the Sun in the optical range [155].

As in conventional radio antennas, they use the effect of inducing currents by an incident electromagnetic wave with optimization of their spatial distribution. In this case, it is achieved by converting optical frequency radiation from submicron and even nanometer-sized objects into a highly localized electromagnetic field concentrated in a region of small size compared to the wavelength. Nanoparticles, small groups of them, and even individual molecules, atoms, ions, or clusters of them are used as such objects. The spatial spectrum of a concentrated field does not contain uniformly flat transverse waves, but is a superposition of longitudinal evanescent waves whose polarization is directed along their propagation, and the intensity when working with nanometer objects can significantly exceed the intensity of ordinary (transverse) electromagnetic waves. Special cases of nanoantennas are devices that convert light radiation into wave modes of so-called plasmon non-waveguides with sizes much smaller than the optical wavelength based on various spherical, pin-shaped, rhombic, "bow tie" and fractal configurations of metal, semiconductor and dielectric nanoparticles, as well as their hybrid combinations (Fig. 19).
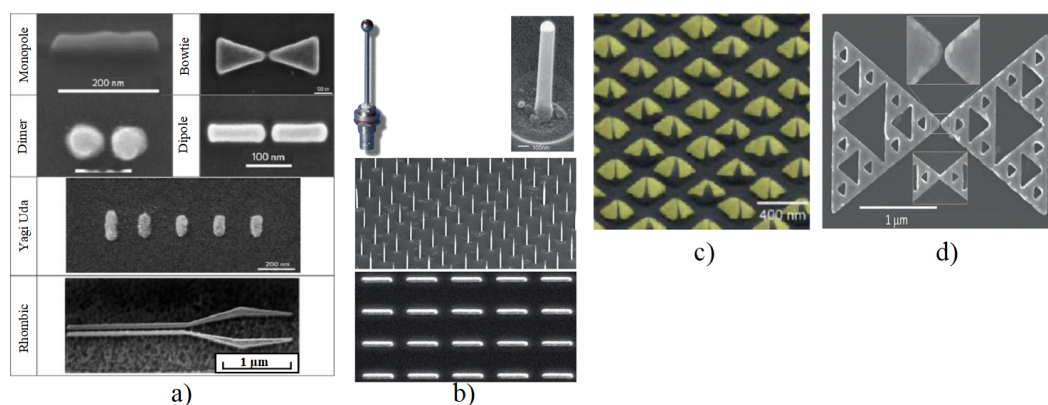

FIG. 19. Main types of optical plasmon nanoantennas (a) [155], their monopole (b) [156–160] and dipole 'bow tie' (c) [161] arrays, including those using Sierpinski fractal structures (d) [162]

Such a wide variety is determined by the various advantages and disadvantages of the presented types of nanoantennas in terms of their broadband, dissipative losses, effective gain, and other parameters, a detailed analysis of which is presented in a large specialized review taking into account various applications [155]. The use of nanoantenn arrays as light-trapping nanostructures for thin-film batteries in photovoltaics promises to realize the mode of localization of incident light inside the sub-wavelength region of an optically thin photosensitive layer. This will allow us to solve the issues of compensation of light reflection and prevent its loss when passing through such a thin film [163, 164].

4.4. Optical communication systems in the ultraviolet range

Among the specific tasks listed in the introduction in personalized energy systems, there is one which corresponds to the increasing of the reliability of wireless mobile communications through a self-organizing information transmission network that is protected from deliberate suppression and interception under the influence of destructive factors of natural and man-made natures. One of the promising directions for solving this problem with the possibility of significantly increasing the bandwidth compared to radio frequency communication systems is the development of optical communication systems based on the use of an ultraviolet channel in the sun-blind range of wavelengths. This range makes it possible to use a huge unlicensed communication spectrum and has good electromagnetic compatibility with various electronic devices. A significant number of scientific articles, in particular, [165–170], as well as numerous patents, for example, [171–176], are devoted to the problems of modeling and experimental research of such communication systems. An important advantage of this channel in comparison with other optical bands is also the ability to provide reliable communication in the absence of line-of-sight (NLOS) in the presence of obstacles between the transmitter (led or laser) and the receiver (photodiode or photoelectric multiplier). The feasibility of communication lines in the ultraviolet range without direct visibility is based on the reception of molecular and aerosol scattering of optical radiation in the atmosphere [177–182].

The calculated and experimental evaluation [183–185] of the pulse characteristics of an optical atmospheric ultraviolet channel with scattering according to a model geometric scheme (Fig. 20) generally indicates the applicability of small-sized semiconductor emitting LEDs based on multilayer semiconductor heterostructures and receiving photodiodes created so far for the UV range as an element base for transmitters and receivers of communication systems. This

is also shown by the results of the first field tests performed at the Institute on Laser physics of the Siberian Branch of the Russian Academy of Sciences in the field of non-line-of-sight ultraviolet communication links, multicast network communications by using a pulsed copper bromine laser as the emitter at the converted wavelength $\lambda = 281.1$ nm and a photoelectronic multiplier FEU-142 as the receiver [186].
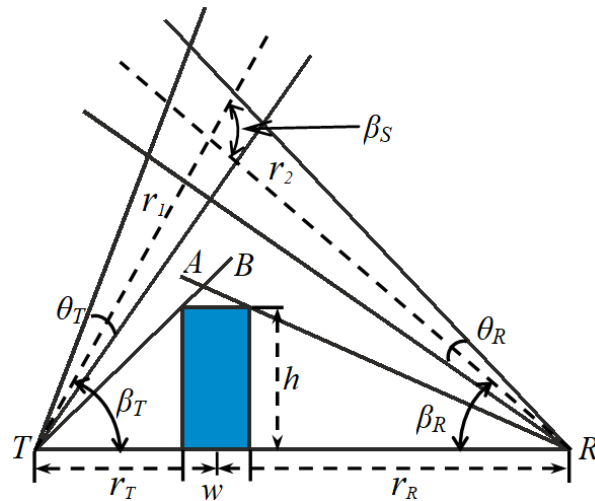

FIG. 20. Model of a UV channel with a line of sight. UV channel model with an obstacle of width [183–185]

4.5. Human muscle power, mini wind- and hydro-electric generators

The above-mentioned energy capabilities of the human body, among which the greatest power density is represented by the thermal energy of the human body (135 mW/cm^3) and the energy of its mechanical movement (800 mW/cm^3), are used in a number of proposed "hiking" tourist solutions for generating electricity through muscle power. The technical basis of these solutions are manual electrodynamic flashlights – "bugs", known since the 1980s with the modern replacement of incandescent lamps with emitting LEDs, bicycle high-speed dynamo-machines that rotate from the side wall of the tire of a moving wheel, and modern bicycle bushing multi-pole generators installed as the wheel axis. The latter provide an electric power output of 3 W at a current of 500 mA and a voltage of 6 V, sufficient for the operation of powerful led lighting and for charging portable electronics at relatively low wheel speeds (160 – 200 rpm). On their basis, compact low-speed wind and hydro-wheel generators are also designed, equipped with blades located directly on the Bicycle spokes, in contrast to the development of bulky wind wheels with a high-speed dynamo-machines. The latter work well at 1500 – 3000 rpm and require a gearbox when using wind or water flow as the driving force. Recently, bladeless non-rotating wind generators have also been proposed [187], based on the effect of frontal wind pressure on a round "sail" that oscillates due to built-in air valves, with further transformation of this movement by hydraulic drive or piezoelectric elements similar to acoustic and thermoauxtic electric generators [188].

In all cases, in order to increase the power and efficiency used in such devices generators with permanent magnets, further development coercivity materials with powerful magnetic induction type known neodymium magnet, consisting of an alloy of rare earth element neodymium, boron and iron with the tetragonal crystal structure of $Nd_2Fe_{14}B$ are required [148].

A historical prototype of power engineering devices using renewable environmental energy without electricity generation can be considered made of wood as a natural nanocomposite wind- and water mills that reached the height of perfection in the 17th century.

5. Development of new functional materials for personalized energy based on nanotechnology approach

5.1. General methods of the nanotechnological approach to the development and synthesis of functional materials

The development of nanostructured materials for working bodies and media of energy converters and storage devices is a developing and very promising area of modern research in the field of autonomous personalized energy industry. The nanotechnology approach involves the creation and use of materials, devices, and technical systems whose

functioning is determined by a nanostructure with ordered structural fragments ranging in size from 1 to 100 nanometers. Features of nanodisperse systems are associated with the manifestation of quantum-dimensional effects, changes in the atomic-crystal structure, and an increase in the proportion of "surface" atoms that are under different conditions compared to the bulk phase atoms. The nonequilibrium state of nanoparticles, which is formed as a result of extreme production conditions, is reflected in the properties of nanomaterials in comparison with massive samples. The use of such materials, whose structure and properties significantly differ from those of a continuous medium, allows us to purposefully influence the energy transformation processes to reduce dissipative losses in various types of generators and converters: thermoelectric, solar and wind generators, fuel cells, batteries and galvanic batteries, supercapacitors and other devices, up to high-temperature superconductivity systems [189–211].

A special influence on the change in the functional properties of a nanostructured material is exerted by the presence of a large number of interphase formations of a fractal nature (so-called non-autonomous phases), which in their properties, structure and composition differ significantly from the corresponding characteristics of bulk phases. These studies were initiated by the works of T. Jung (1805–1807), D. W. Gibbs (1878), and J. D. van der Waals (1908–1912), who considered the properties of surface layers (phases) of finite thickness, as well as the works of R. Defey (1934) and I. R. Prigogine (1947), who defined such formations as "non-autonomous phases" and "non-autonomous state of matter" due to the impossibility of their independent (isolated from bulk phases) existence [21, 50, 51, 75, 212, 213]. New developments in this direction have been made in research on the physicochemistry of surface phenomena and microheterogenic systems [214, 215], as well as intergranular and surface layers at the contact boundaries of solid regions of bulk phases in polycrystalline [216–221].

Current works in the field of development of nanostructured converters and storage devices are mainly focused on the problems of physical and chemical formation of structural and functional characteristics and the development of methods for technological support of the synthesis of nanodisperse and nanoporous materials [222–234]. Also their technological applications in different types of converters, in particular, thermoelectric, solar and wind generators, fuel cells, batteries and galvanic batteries, supercapacitors and other devices, up to systems of high-temperature superconductivity are being discussed [235–248].

To date, plenty of different methods for creating nanostructured materials are known, which can be divided into two large groups according to the type of nanostructure formation.

The "top-down" nanotechnology approach is based on reducing the size of physical bodies up to obtaining objects with nanoscale parameters. When large particles are dispersed to nanoscale sizes, a significant amount of energy must be expended from the outside to dramatically increase the solid-liquid (or gas) interface. In order to do this, we have methods that are conventionally called physical methods which use use low-temperature plasma, cathode sputtering, molecular beams formed by various heating sources, electric explosion, mechanical grinding in its various variants etc. [249]. The extremely fast (extremely non-equilibrium) thermodynamic processes of high-speed phase transitions of the aggregate state of matter through the "solid-liquid-gas", including transitions through the critical point are of particular interest for dispersion [250]. It is the only extremum on the equilibrium curves of the phase diagram that belongs to both a liquid and a vapor, and the approach to it is accompanied by a significant increase in density fluctuations in the micro volumes of matter compared to the regions of existence of metastable states adjacent to the equilibrium curves of the two phases. In case of a sufficiently intensive input of energy, density fluctuations can self-organize, leading to a loss of thermodynamic stability of the substance and the formation of dissipative microstructures. They can serve as "pre-germs" for the subsequent formation of dispersed particles during the destruction of the initial consolidated material and the transfer of part of the energy to the environmental substance. This makes it possible in principle to obtain very small sizes of such particles, up to units of nanometers, in contrast to the observed results of other well-known dispersion mechanisms under mechanical or thermal action, for example, impact grinding of a solid, its melting and crushing of a liquid into droplets, evaporation and subsequent vapor deposition. This significantly increases the energy saturation of nanoparticles, which can cause their unique catalytic, sorbent and other properties, as well as the observed threshold phenomena. For example, the total surface of all particles contained in a metal Ni powder with an average size of 0.1 mm increases by a factor of 1000 when they are dispersed to a size of 100 nm from a consolidated substance in non-equilibrium thermodynamic processes.

In case of the opposite "bottom-up" technology, a nanoobject is "assembled" from individual atoms, molecules, biological cells, etc. The possibility and prospects of this approach were first pointed out by Richard Feynman [251] in a speech at the annual meeting of the American Physical Society in 1959. This process mainly occurs by self-assembly or chemical reactions resulting from the transformation of a precursor compound and subsequent aggregation of molecules or atoms of the reaction product, and therefore these methods are often referred to as chemical [252]. Most technologies for assembling nanomaterials from individual atoms are based on the phenomenon of condensation or chemical deposition from a matrix medium under conditions close to thermodynamic equilibrium. The formation of nanostructures is significantly influenced by clusters of pre-germ micro-formations, as well as spatial restrictions

in the evolution of matter from the formation of pre-germ clusters to the aggregation of nanocrystals in the material of both individual compounds and solid solutions based on them. However, even in this case, a large excess of surface free energy, which is the driving force of spontaneous enlargement of nanoparticles, can also cause their instability and loss of unique properties. To prevent undesirable aggregation and stabilization of nanoparticles, dispersants are used, which are introduced into the medium containing nanoparticles, or the method of so-called matrix isolation of nanoparticles in porous bodies is used, etc.

It should be noted that in the practical implementation of both approaches, both physical and chemical methods can be used, as well as their various combinations. It is fundamentally important that the structure of nanoparticles of the same size obtained by dispersion and construction from atoms may differ. When compact materials are dispersed to nanoscale sizes, the resulting particles usually retain the structure of the original sample. Particles formed by aggregation of atoms may have a different spatial arrangement of the atoms, which affects their electronic structure and the lattice constant.

The choice of specific methods and conditions for the synthesis of nanocomposite materials aimed at use in personalized energy systems is determined by specific requirements for their functional properties noted above, first of all, the efficiency of regulating energy conversion processes in terms of specific output power, efficiency and stability. In particular, according to the results of joint research of the Ioffe Institute and the Belarusian State Technological University have identified advanced technological methods for obtaining basic model compounds with a high content of non-autonomous phases. They are designed to create a new generation of functional nanostructured materials for chemical-catalytic and thermoelectric purposes due to the obvious disadvantages of materials traditionally used for these purposes with a high content of toxic and expensive components.

5.2. Characterization of properties and features of synthesis of new nanostructured thermoelectric materials by "wet chemistry" methods

The development of new classes of thermoelectric materials is based on a number of concepts, one of which is the idea put forward by Slack that a good thermoelectric should be a substance that conducts electric current well ("electron crystal") and poorly conducts heat ("phonon glass"), the so-called PGEC [253]. On the basis of this idea, such classes of thermoelectric materials as filled scutterudites (for example, $Yb_xCo_4Sb_{12}$) [254–257], semiconductor clathrates ($Eu_8Ga_{16}Ge_{30+x}$, etc.) [258, 259], as well as Goisler half-alloys (in particular, $(Zr_{0.7}Hf_{0.3})_{0.7}Ti_{0.3}NiSn$) [260]. The another concept is the idea put forward by Dresselhaus that nanostructuring of thermoelectrics is an effective way to increase their thermoelectric q-factor, due to a sharp decrease in the lattice component of thermal conductivity arising from a decrease in the average free path of phonons [261].

In this regard, the synthesis of nanoceramic materials based on metal oxides such as cobalt and zirconium, in particular, the system of layered calcium cobaltites of the $CaO–CoO_x$ type, is of great interest due to their low cost and high stability at elevated temperatures. At the same time, partial substitution of cobalt with transition or heavy metals, and calcium with rare-earth elements or bismuth can be used to improve their thermoelectric characteristics. The essence of the applied synthesis method consists in the chemical deposition of the hydroxide components of the solution on the solid phase suspended in this solution. $CaCO_3$ suspension in $Co(NO_3)_2$ solution was used as the initial components, and NaOH solution was used as the precipitator. Initial nanopowders in the form of solid solutions of the composition $Ca_{3-x}Bi_xCo_4O_{9+\delta}$ ($0.0 \leq x \leq 1.5$) were obtained by solid-phase reactions from Co_3O_4, Bi_2O_3 and $CaCO_3$. Further high-temperature treatment of the resulting initial mixture was carried out in a muffle furnace aerobically in the temperature range of $400 – 900\,^\circ C$ with an isothermal exposure time of 3 hours.

This method was also used for synthesizing the samples of new materials based on perovskite-like layered compounds in the $Ln_2O_3–MO–Al_2O_3$ system (where Ln = rare earth elements: lanthanum, scandium, yttrium, and lanthanides; M = Mg, Ca, Sr, and Ba) with the structure of the Ruddlesden–Popper phases [262–264]. Using a wide range of physical and chemical analysis methods, the main of which are X-ray fluorescence and X-ray spectral microanalysis, X-ray diffractometry, scanning electron microscopy, synchronous thermal analysis, pycnometry, etc., their physicochemical and functional properties were studied, and their structural features were determined (Fig. 21).

Based on the results of these studies, it was found that the power factor and the thermoelectric q-factor in bismuth-containing ceramics based on layered calcium cobaltite, as well as in polycrystalline substances based on lanthanum-strontium-aluminum oxide, can be significantly improved by creating a chemical [265] or phase inhomogeneity in it [266–269].

The revealed characteristics of these compounds indicate the prospects of their use as p-branches of high-temperature thermoelectric generators of a new generation. Promising materials for the n-branches of thermoelectric generators are perovskite calcium manganites $CaMnO_3$ doped with rare-earth materials [270–276], perovskite plumes of alkaline-earth materials [277–280], and materials based on titanium dioxide and strontium titanate [281–288]. High-density n-type thermoelectric ceramics are produced by the same methods as p-type ceramics, additionally using
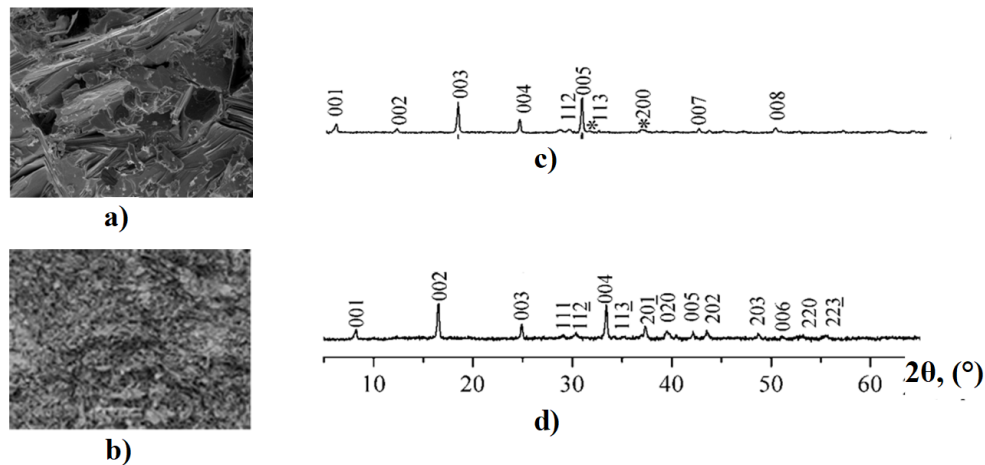
FIG. 21. 50 μm electron micrographs of nanostructured $Ca_{3-x}Co_4O_{9+\delta}$ ceramics at: $x = 0$ (a), $x = 1.5$ (b) and X-ray diffraction patterns of appropriate compositions ceramics (c, d). * marks Co_3O_4 reflections.

annealing in a reducing atmosphere to create the desired level of oxygen sublattice defects that provides the required electrophysical properties [289].

Such complex oxide thermoelectrics can also be used for direct conversion of solar energy into electrical energy [290–292], with higher efficiency than in photovoltaic devices, since the latter allow only UV and part of the visible region to be converted to electricity, while in thermoelectric generators, the entire spectrum of solar radiation is converted.

In order to determine the stability boundaries of complex oxides with the structure of one-layered Ruddlesden–Popper phases, based on the structural-energy approach and taking into account the comparison of geometric tolerance conditions of the perovskite block size parameter with the parameter showing the number (fraction) of compounds from the set of potentially possible [293], the formation of a new $DySrAlO_4$ thermoelectric compound is predicted and synthesized by solid-phase reactions in the temperature range 1300 – 1500 °C. A simplified diagram of the layer coupling mechanism is shown in Fig. 22.

5.3. Features of the implementation of the combustion method of gel-like media in high-speed kinetic mode

The combustion method of gel-like media in high-speed kinetic mode [201, 208, 224, 225, 232, 248, 294] is an alternative to the described synthesis method, which proceeds in a relatively slow diffusion mode [216–221, 262, 293,
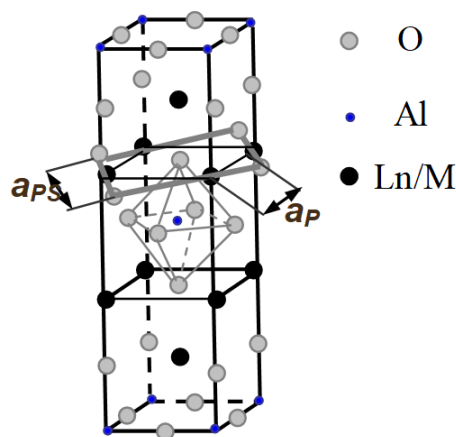

FIG. 22. Scheme of conjugation mechanism of $LnAlO_3$ (P) and rock salt MO (RS) blocks, which form the one-layered Ruddlesden–Popper phases structure. The geometric associativity of P and RS blocks fragments can be estimated by the comparing of these blocks areas sizes or unit cell parameters, in particular, by the size a_P, as shown in the scheme.

295], as well as to the sol-gel and hydrothermal technology with nanopowder deposition from the initial mixture and subsequent dehydration during heat treatment [195, 196, 198, 200, 229, 231, 296–298]. It is used to produce layered calcium cobaltite $Ca_3Co_4O_9$ during the combustion of a glycine-nitrate gel precursor [299–302]. This method provides a higher dispersion and uniformity for the synthesized powders, including stoichiometric composition, which helps to solve the problem of their sinterability, and brings the properties of materials based on them closer to the properties of single-crystal samples. Examples of the structures of highly dispersed $Ca_3Co_4O_9$ samples obtained by this method are shown in Fig. 23.
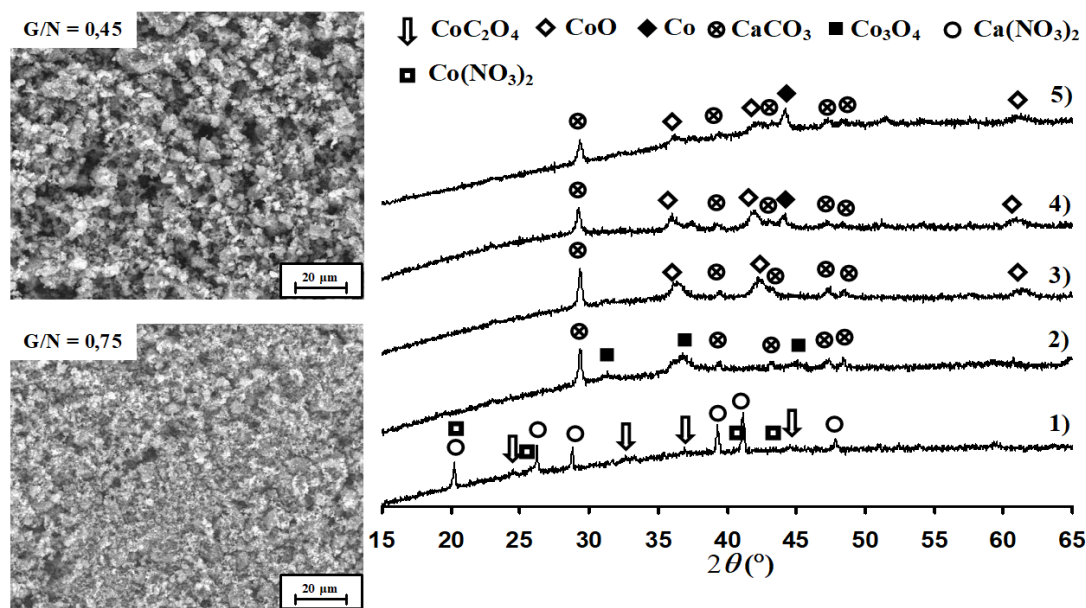

FIG. 23. Electron micrographs of dispersed $Ca_3Co_4O_9$ samples obtained by heat treatment of precursors got at $G/N = 0.45, 0.75$ ratio under $T = 700\ °C$ and X-ray phase analysis data of the initial $Ca_3Co_4O_9$ samples after combustion with different G/N: 1) 0.15, 2) 0.30, 3) 0.45, 4) 0.6, 5) 0.75

Recently, the solution combustion (SCS) method has been used to obtain new nanostructured multiferroic materials with unique magnetic, electrical, and catalytic properties based on rare-earth element (REE) orthoferrites $RFeO_3$ (R = Y, Ln) [194, 207, 231, 297, 303–310] with a perovskite-like structure, combining ferromagnetic and ferroelectric ordering. In some cases, it has been shown that the use of additional heat treatment of solution combustion products and other chemical precursors leads to the formation of metastable forms of REE orthoferrites and a significant change in the functional characteristics of materials based on them [231, 311, 312]. It has been shown that in this case, the chemical and structural background of the precursor exposed to thermal action plays an important role [313–316], while for other systems, for example, KNO_3–$BaTiO_3$-based ferroelectrics, the necessary properties can be achieved by simple mechanical mixing of the components and the background does not play a significant role [317]. Among the oxide magnetic materials that are promising for use in personalized energy devices, it is also worth noting substances with a spinel structure – $Li_{0.5}Fe_{2.5}O_4$, $NiFe_2O_4$, $ZnFe_2O_4$ and others synthesized by solution combustion, successive ionic layer deposition (SILD) (Fig. 24) and plasma-chemical synthesis [318–321]. Their use as the basis for low-coercivity microwave ceramics and corresponding functional devices is also of particular interest [322, 323].

The use of other methods of "wet chemistry", such as hydrothermal synthesis, coprecipitation with subsequent annealing-quenching in a neutral, oxidative or reducing atmosphere, can significantly expand the structural, morphological and disperse characteristics of the resulting nanostructured functional substances and materials [195, 196, 198, 200, 207, 228, 229, 231, 235, 236]. Thus, new oxide materials with high acid-base properties that are of interest in the field of heterogeneous catalysis and new methods of material functionalization have been developed using "wet chemistry" approaches [121–123, 138, 139, 207, 223, 231, 297]. It was shown that, just as in the case of materials for supercapacitors [41, 45, 46, 204, 211], the type and concentration of functional groups on the surface of the substance play a decisive role here. On the other hand, these synthesis methods make it possible to obtain substances in the form of nanocrystals of uniform size and morphology, which can be used as the basis for MRI contrast agents [202, 324–326], catalyst carriers [22, 198, 207, 228, 231], sorbents [45, 115, 116], and other useful materials.
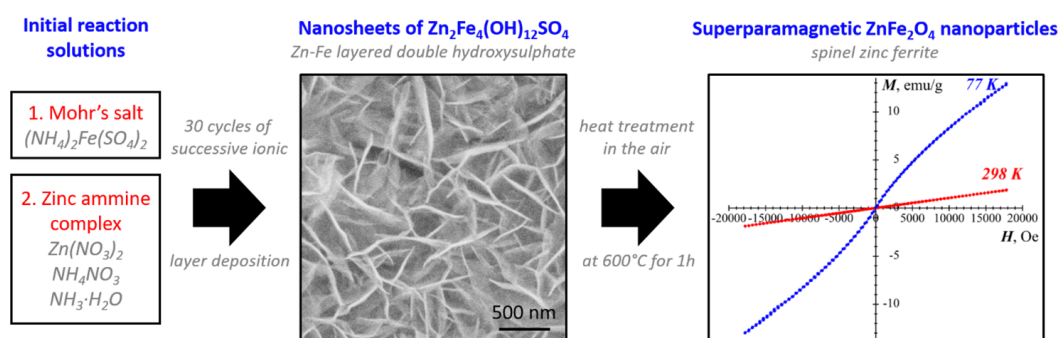
FIG. 24. Synthesis of superparamagnetic $ZnFe_2O_4$ via SILD technique by results of the work [318]

5.4. Characteristics and features of methods for the synthesis of new nanostructured catalysts

Nanostructured catalysts represent a separate area of materials for personalized energy. In this area, effective catalysts based on nanoparticles of d- and f-element oxides and hydroxides have been developed for the electrocatalytic production of hydrogen from water-alcohol solutions [327–331], photocatalysts based on simple and complex oxides [123, 135–139, 233, 332], carbon monoxide oxidation catalysts [333–336], and acid-base *n*-hexane conversion catalysts [337–339]. Obtained in the form of isometric nanoparticles, nanorods, nanoplates, and porous compositions (Fig. 25), these nanostructured catalysts exhibit high catalytic activity and stability compared to materials obtained by using traditional catalytic techniques. Besides, catalytic materials that do not contain expensive metal elements, such as graphite-like carbon nitride or g-C_3N_4, have a great potential for development [328]. This catalytic material can be obtained by simple thermolysis of urea, melamine, and other organic precursors in air and exhibits high, stable catalytic characteristics both in the processes of photocatalytic oxidation of organic substances [340, 341] and in the electrocatalytic release of hydrogen [342].
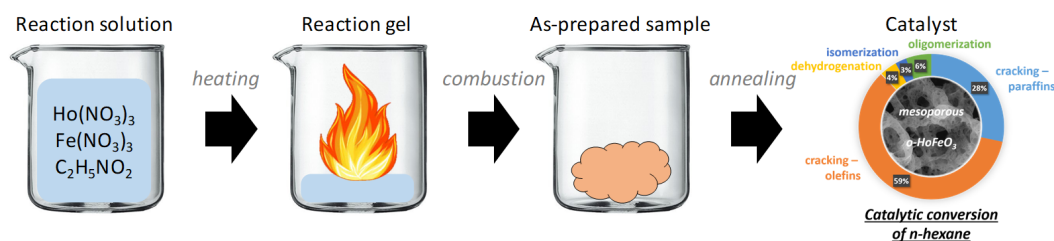

FIG. 25. Synthesis of porous $HoFeO_3$ catalyst via SCS technique (by results of the work [339]

5.5. Features of implementation of high-energy methods for synthesis of nanostructured materials for personalized energy systems

In a number of cases, additional energy effects are used in the synthesis, including sonochemical and microwave synthesis in addition to those mentioned above [343–347]. It is revealed that the size and degree of disorientation of their constituent crystallites have a great influence on the structure and contribution of non-autonomous phases and properties of polycrystalline materials. Depending on the degree of disorientation of the crystallites, the thickness, composition, and structure of the intercrystalline layer change. The ratio of the size of crystallites and the thickness of the intercrystalline layer (non-autonomous surface phase), in turn, determines the volume fractions of crystallites and intercrystalline formations in a polycrystalline material [22, 23, 216–221, 315, 348–351].

As follows from the results of a number of studies on the formation of nanomaterials, in many cases their functional properties are determined by the chemical and thermal prehistory of the initial compositions and the mechanism of their formation [176, 177, 182, 186, 189, 190, 194, 198, 199, 228, 352, 353]. It is also shown that solid-phase reactions are, in a certain sense, liquid-phase, since reactions in a solid system are activated with the transition of two-dimensional non-atomic phases (intergrain formations) to a liquid-like state, when the reaction rate increases sharply [216–221].

Electroexplosive technologies are also being developed for dispersing the initial conducting materials that experience the transition of the aggregate state through the "solid-liquid-gas-plasma" [354–358]. Great prospects for the

development of this direction for obtaining nanoscale metal oxides containing non-autonomous phases are opened when performing an electric explosion of conductors in various chemically active media. In particular, an installation was developed for an electric explosion in a supercritical water fluid with dispersion of the conductor due to the development of thermodynamic instabilities of its physical state in the vicinity of the critical point [250].

The ML-ALD chemical layer deposition method can be used in order to form a molecular or atomic monolayer on complex-shaped substrates without forming three-dimensional "germs" [359]. It is carried out by cyclic alternate supply of gaseous (MOCVD – Metal Organic Chemical Vapor deposition) or liquid (followed by pyrolysis – MOD Metal Organic deposition) reagents – precursors of the buffer layer and the source material to the substrate. In this case, chemical reactions that lead to the growth of films occur only in chemisorbed layers, that is, with the exception of reactions in the gas phase. The specified increase in the thickness of the formed film is easily and very accurately controlled by the number of deposition cycles using the property of self-organization (self-limitation) of surface reactions, which are completed automatically when all reactive areas on the surface are exhausted. In principle, this technology can be implemented by applying atomic layers, for example, by the method of atomic layer deposition (ALD), that was initially proposed by V. B. Aleskovsky in the middle of the twentieth century [360–364].

6. Conclusion

The analysis of the problems of personalized energy supply for autonomous human survival in remote natural habitat, emergency situations of natural disasters and technical catastrophes with the unavailability of centralized power supply indicates a major role in its solution of developments in the field of nanostructured materials with special functional properties. Their application is designed to provide the possibility of preferential use of available renewable energy sources of the environment, processes and devices for extracting, storing and converting their energy into the necessary consumer forms, taking into account specific operating conditions and requirements for power, efficiency, operating modes, and weight and size characteristics. Fundamental restrictions on these indicators are imposed by the characteristics of physical effects associated with these processes and interactions.

The study of these features for various types of such devices by methods of non-equilibrium thermodynamics, chemical kinetics, nonlinear dynamics, fractal analysis, and quantum physics demonstrates the great attractiveness in this regard, primarily for solid-state photo-and thermoelectric semiconductor converters based on a new generation of inorganic compounds that do not have mechanically moving elements. The results of the nanotechnological approach to their development using various technologies and synthesis methods, including "wet chemistry" and solid-phase reactions in diffusion modes, combustion of gel-like media in high-speed kinetic modes, chemical layer deposition and other types of epitaxy, as well as high-energy effects of various types, show the special role of non-autonomous interfacial formations and processes of fractal self-organization in the formation of functional properties of the synthesized materials.

The development of this concept makes it possible to carry out a directed physical and chemical design of new nanostructured materials with an unusual composition, structure, and unique functional behavior as a base for personalized energy systems.

Acknowledgements

References

[1] Fortov V.E., Popel O.S. *Energy in the modern world*. Intellect, Dolgoprudnyy, 2011, 168 p. (In Russian).

[2] Bansal R.C. Dr. Optimization methods for electric power systems: An overview. *International Journal of Emerging Electric Power Systems*, 2005, **2** (1), 1021.

[3] Trukhny A.D., Makarov A.A., Klimenko V.V. *Fundamentals of Modern Energy (in two parts)*. MPEI Publishing House, Moscow, 2002, 368 p. (In Russian).

[4] Danilevich Ya.B., Kovalenko A.N. Energy and its place in the modern world. *Bulletin of the Russian Academy of Sciences, Energetika*, 2004, **6**, P. 20–28 (In Russian).

[5] Alkhasov A.B. *Renewable energy*. Fizmatlit, Moscow, 2010, 255 p. (In Russian).

[6] Twidell J., Weir T. *Renewable energy resources*. Taylor & Francis, London and New-York, 2006, 602 p.

[7] Popel' O.S., Frid S.E., et al. Independent hydrogen power installations with renewable sources of energy. *Thermal Engineering*, 2006, **53**, P. 208–216.

[8] Pozdnyakov B.S., Koptelov E.A. *Thermoelectric power engineering*. Atomizdat, Moscow, 1974, 264 p. (In Russian).

[9] Danilevich Ya.B., Kovalenko A.N., Shilin V.L. Autonomous systems of electric and heat supply with buffer energy storage. *Proceedings of the RAS. Energetika*, 2002, **1**, P. 69–78 (in Russian).

[10] Danilevich Ya.B., Kovalenko A.N. Heat pumps in small energy systems. *Proceedings of the RAS. Energetika*, 2005, **1**, P. 63–69 (in Russian).

[11] Dobarina I.A., Zhigarev O.L. Fundamentals of life safety and first aid. In: *Survival in an autonomous existence*. Ed. R.I. Aizman, S.G. Krivoshchekova, I.V. Omelchenko. Siberian University Press, 2004 (in Russian).

[12] Volovich V.G. *Man in extreme environmental conditions*. Mysl', Moscow, 1983, 197 p. (in Russian).

[13] Davy N., Sezen-Edmonds M., et al. Pairing of near-ultraviolet solar cells with electrochromic windows for smart management of the solar spectrum. *Nat Energy*, 2017, **2**, 17104.

[14] Makarov A.A., Fortov V.E. World energy development trends and energy strategy of Russia. *Herald of the RAS*, 2004, **74** (3), P. 195–208 (in Russian).

[15] Belyaev L. S., Lagerev A. V., Posekalin V. V. *Power Engineering in the 21st Century: Conditions of Evolution, Technologies, Prospects*. Ed. Voropai N.I., Novosibirsk, Nauka, 2004, 386 p. (in Russian).

[16] Bushuev V.V. Prospects for global energy development until 2050. 2010, URL: http://portal-energo.ru/articles/details/id/292.

[17] Olkhovsky G.G. Global Energy Issues. Global energy problems. *Power Technology and Engineering*, 2005, **1**, P. 4–10 (in Russian).

[18] Stennikov V., Voropai N., Barakhtenko E., Sokolov D. Digitalization of integrated energy systems. *Energy Safety and Energy Economy*, 2020, **4** (94), P. 5–10.

[19] Ushakov V.Ya. The main problems of energy and possible solutions. *Bulletin of the Tomsk Polytechnic University*, 2011, **319** (4), P. 5–13 (in Russain).

[20] IEA. *Energy Technology Perspectives 2008: Scenarios and Strategies to 2050*. OECD Publishing, Paris, 2008, 648 p. URL: https://doi.org/10.1787/9789264041431-en.

[21] Defay R., Prigogine I. *Tension superficielle et adsorption*. Editions Desoer, Liege, 1951, 295 p.

[22] Kovalenko A.N., Tugova E.A. Thermodynamics and kinetics of non-autonomous phases formation in nanostructured materials with variable functional properties. *Nanosystems: Phys. Chem. Math.*, 2018, **9** (5), P. 641–662.

[23] Krasnenko T.I., Rotermel M.V., Samigullina R.F. Stabilizing the associated non-autonomous phase upon thermal expansion of $Zn_2V_2O_7$. *Russ. J. Inorg. Chem.*, 2017, **62** (4), P. 413–417.

[24] Samarsky A.A., Galaktionov V.A., Kurdyumov S.P., Mikhailov A.P. *Modes with exacerbation in problems for quasilinear parabolic equations*. Nauka, Moscow, 1987, 480 p. (in Russian).

[25] Akhromeeva T.S., Kurdyumov S.P., Malinetskiy G.G., Samarsky A.A. *Unsteady structures and diffusion chaos*. Nauka, Moscow, 1992, 544 p (in Russian).

[26] Grinchenko V.T., Matsypura V.T., Snarsky A.A. *Introduction to nonlinear dynamics. Chaos and Fractals*. LCI, 2007, 264 p. (in Russian).

[27] Kurdyumov S.P. *New in synergetics: A look into the third millennium. Informatics: unlimited possibilities and possible limitations*. Nauka, Moscow, 2002, 480 p. (in Russian).

[28] Snyder W.S., Cook M. J., et al. *Report of the task group on reference man*. ICRP Publication 23. Pergamon Press, Oxford. 1975, 500 p.

[29] Fokin V.F., Ponomareva N.V. *Neuronergetics and brain physiology*. Antidor, Moscow, 2003, 288 p. (in Russian).

[30] Shaikh F.K., Zeadally S. Energy harvesting in wireless sensor networks: A comprehensive review. *Renewable and Sustainable Energy Reviews*, 2016, **55**, P. 1041–1054.

[31] Yildiz F. Potential ambient energy harvesting sources and techniques. *Journal of Technology Studies*, 2009, **35** (1), P. 40–48.

[32] Jaffe P., McSpadden J. Energy conversion and transmission modules for space solar power. *Proceedings of the IEEE*, 2013, **101** (6), P. 1424–1437.

[33] Siddique A.R., Rabari R., Mahmud Sh. et al. Thermal energy harvesting from the human body using flexible thermoelectric generator (FTEG) fabricated by a dispenser printing technique. *Energy*, 2016, **115** (1), P. 1081–1091.

[34] Leonov V. Thermoelectric energy harvesting of human body heat for wearable sensors. *IEEE Sensors Journal*, 2013, **13** (6), P. 2284–2291.

[35] Turkmen A.C., Celik C. Energy harvesting with the piezoelectric material integrated shoe. *Energy*, 2018, **150**, P. 556–564.

[36] Kapitsa P.L. Energy and Physics. *Bulletin of the USSR Academy of Sciences*, 1976, **46** (1), P. 34–43 (in Russian).

[37] Bekzhanova N.V., Sereda S.B., Sidorenko N.A. *Nobel lectures in Russian translations, 1901–1902: Biobibliographic index*. Academy of Sciences Library, Saint-Petersburg, 2003, 166 p. (in Russian)

[38] Ugarov G.G., Soshinov A.G., Vdovina O.V. *Energy converters*. Volgograd state technical university, Volgograd, 2010, 95 p. (in Russian)

[39] Alekseev G.N. *Forecasting the development of power plants energy conversion*. Nauka, Moscow, 1966, 190 p. (in Russian)

[40] Almyasheva O.V., Gusarov V.V., et al. A new type of super-energy storage based on non-carbon nanomaterials. *Proceedings of the Research Center for Photonics and Optoinformatics*, 2010, **1** (2), P. 187–204. (in Russian)

[41] Rychagov A.Y., Vol'fkovich Y.M., et al. Perspective electrode materials for supercapacitors. *Electrochemical Energetics*, 2012, **11** (4), P. 167–180.

[42] Medvedeva A.E., Pechen L.S., et al. Synthesis and electrochemical properties of lithium-ion battery cathode materials based on $LiFePO_4$–$LiMn_2O_4$ and $LiFePO_4$–$LiNi_{0.82}Co_{0.18}O_2$ composites. *Russ. J. Inorg. Chem.*, 2019, **64** (7), P. 829–840.

[43] Basistaya A.O., Karushev M.P., et al. A new conducting polymer for lithium-ion batteries. *Tech. Phys. Lett.*, 2020, **46** (1), P. 77–79.

[44] Polozhentseva Y.A., Karushev M.P., et al. A lithium-ion supercapacitor with a positive electrode based on a carbon material modified by polymeric complexes of nickel with Schiff bases. *Tech. Phys. Lett.*, 2020, **46** (2), P. 196–199.

[45] Frackowiak E. Carbon materials for supercapacitor application. *Phys. Chem. Chem. Phys.*, 2007, **9**, P. 1774–1785.

[46] Inagaki M., Konno H., Tanaike O. Carbon materials for electrochemical capacitors. *J. Power Sources*, 2010, **195**, P. 7880–7903.

[47] Emerson C. *100 Deadly Skills: The seal operative's guide to eluding pursuers, evading capture, and surviving any dangerous situation*. Atria Books, New York, 2020, 272 p.

[48] Fokin B.S. Optimum values of energy converter efficiency. *J. Eng. Phys. Thermophy*, 2009, **82** (3), P. 598—603.

[49] Tribus M. *Thermostatics and thermodynamics: An introduction to energy, information and states of matter, with engineering applications*. D. Van Nostrand Company Inc., 1961, 649 p.

[50] Glansdorff P., Prigogine I. *Thermodynamic theory of structure, stability and fluctuation*. Wiley-Interscience, New York, 1971, 305 p.

[51] Nicolis G., Prigogine I. *Exploring complexity, an introduction*. W.H. Freedman and Co., New York, 1989, 328 p.

[52] Khvesyuk V.I., Ostanko D.A., et al. Maximum efficiency of thermoelectric heat conversion in high-temperature power devices. *Nauka i Obrazovanie*, 2016, **3**, P. 81–105.

[53] Kovalenko A.N. Study of the characteristics of powerful power plants based on the methods of nonequilibrium thermodynamics. *Proceedings of magnetovitational transport systems and technologies*. Saint-Petersburg, October 29–31, Publishing House PGUPS, 2013, P. 38–42 (In Russian).

[54] Caplan S.R., Essig A. *Bioenergetics and linear nonequilibrium thermodynamics*. Harvard University Press, Cambridge, 1983, 435 p.

[55] Zotin A.I. *The thermodynamic basis of body reactions to external and internal factors*. Nauka, Moscow, 1988, 272 p. (in Russian).

[56] Danilevich Ya.B., Kovalenko A.N., Nosyrev S.P. Irregularity of entropy processes in the body as an indicator of its functional stability. *Doklady Biological Science*, 2009, **429** (1), P. 490–493.

[57] Slovokhotov Y.L. Phase transitions associated with economy and demography. *Computer Research and Modeling*, 2010, **2** (2), P. 209–218.

[58] Delogu F. Thermodynamics on the nanoscale. *J. Phys. Chem. B*, 2005, **109**, P. 21938–21941.

[59] Hill T.L. *Thermodynamics of small systems*. Dover Publication, New-York, 2013, 416 p.

[60] Hill T.L. A Different approach to nanothermodynamics. *Nano Letters*, 2001, **1** (5), P. 273–275.

[61] Babuk V.A., Zelikov A.D., Salimullin R.M. Nanothermodynamics as a tool to describe small objects of nature. *Tech. Phys.*, 2013, **58**, P. 151–157.

[62] Aranson I.S., Gaponov-Grekhov A.V., et al. *Lattice models in the nonlinear dynamics of nonequilibrium media*. Preprint No. 163. IAP Academy of Sciences of the USSR, Gorky, 1987, 24 p. (In Russian).

[63] Rekhviashvili S.Sh., Kishtikova E.V., Rozenberg B.A. Model of a nanoparticle in the theory of inhomogeneous medium. *Technical physics*, 2009, **79** (12), P. 1731–1735.

[64] Rusanov A. Nanothermodynamics. *Russian Journal of Physical Chemistry*, 2003, **77** (10), P. 1558–1563.

[65] Rusanov A.I. Nanothermodynamics: chemical approach. *Russian Chemical Journal*, 2006, **50** (2), P. 145–151. (In Russian)

[66] Rusanov A.I. Surface thermodynamics revisited. *Surface Science Reports*, 2005, **37** (25), P. 111–239.

[67] Rowlinson J.S. Statistical thermodynamics of small systems and interfaces. *Pure and Applied Chemistry*, 1987, **59** (1), P. 15–24.

[68] Shcherbakov L.M. On the statistical assessment of the excess energy of small objects in the thermodynamics of microheterogeneous systems. *Reports of the USSR Academy of Sciences*, 1966, **168** (2), P. 388–391. (In Russian)

[69] Tsallis C. Possible generalization of Boltzmann-Gibbs statistics. *Journal of Statistical Physics*, 1988, **52**(1–2), P. 479–487.

[70] Sevick E.M., Prabhakar R., Williams S.R., Searles D.J. Fluctuation Theorems. *Review of Physical Chemistry*, 2008, **59**, P. 603–633.

[71] Rubi J.M. The non-equilibrium thermodynamics approach to the dynamics of mesoscopic systems. *Journal of Non-Equilibrium Thermodynamics*, 2004, **29**, P. 315–325.

[72] Gemmer J., Michel M., Mahler G. *Quantum thermodynamics. Emergence of thermodynamic behavior within composite quantum systems*. Springer-Verlag Berlin Heidelberg, Berlin, 2009, 346 p.

[73] Jaycock M.J., Parfitt G.D. *Chemistry of Interfaces*. Ellis Horwood Limited, 1981, 279 p.

[74] Gyarmati I. *Non-equilibrium Thermodynamics. Field Theory and Variational Principles*. Springer-Verlag Berlin Heidelberg, Berlin, 1970, 184 p.

[75] Kondepudi D., Prigogine I. *Modern Thermodynamics. From heat engines to dissipative structures*. Wiley, UK, 1998, 506 p.

[76] Onsager L., Hemmer P.C., Holden H. Kjelstrap S. *The collected works of Lars Onsager: with commentary*. World scientific, Singapore, 1996, 1086 p.

[77] Haase R. *Thermodynamics of irreversible processes*. New-York: Dover, 1990, 513 p.

[78] Petrov N., Brankov I. *Modern problems of thermodynamics*. Translation from the Bulgarians. Mir, Moscow, 1989, 385 p. (in Russian)

[79] Etkin V.A. On the origin of Onsager reciprocity relations. *Proceedings of the Siberian Branch of the Academy of Sciences of the USSR, Engineering Sciences*, 1989, **4**, P. 52–57. (In Russian)

[80] Kovalenko A.N. Regulation and thermodynamic stability of non-equilibrium processes of energy conversion of speed. Trudy CKTI, JSC, 1996, **281** (2). (In Russian)

[81] Kovalenko A. Inner nonstationarness of energy conversion in non-equilibrium thermodynamic system. *Proceedings of the fifth Baltic Heat Transfer Conference*, Saint-Petersburg, 21–23 September, SPbGPU, 2009, **1**, P. 446–453.

[82] Paradisi P., Cesari R., Mainardi F., Tampieri F. The fractional Fick's law for non-local transport processes. *Physica A: Statistical Mechanics and its Applications*, 2001, 293 (1), P. 130–142.

[83] Nigmatullin R.R. Fractional integral and its physical interpretation. *Theor. Math. Phys.*, 1992, **90**, P. 242–251.

[84] Marcel O.V. Fractional diffusion equation on fractals: Self-similar stationary solutions in a force field derived from a logarithmic potential. *Chaos, Solutions and Fractals*, 1994, **4** (2), P. 191–199.

[85] Meilanov R.P., Shabanova M.R. The heat equation for media with a fractal structure. *Modern high technology*, 2007, 8, P. 74–75. (In Russian)

[86] Samko S.G., Kilbas A.A., Marichev O.I. *Fractional integrals and derivatives. Theory and Applications*. Gordon and Breach Science Publishers, 1993, 976 p.

[87] Feder J. Fractals. *Physics of Solids and Liquids*. Plenum Press, New York, 1988, 305 p.

[88] Haitun S.D. *From the ergodic hypothesis to the fractal picture of the world*. Moscow URSS, 2007, 251 p. (In Russian).

[89] Rényi A. On a new axiomatic theory of probability. *Acta Mathematica Academiae Scientiarum Hungaricae*, 1955, **6**, P. 285–335.

[90] Klimontovich Yu.L. Entropy and information of open systems. *Progress of physical sciences*, 1999, **169** (4), P. 443–452. (in Russian)

[91] Kovalenko A.N. Fractal characterization of nanostructured materials. *Nanosystems: Phys., Chem., Math.*, 2019, **10** (1), P. 42–49.

[92] Dozhdikova O.L., Zarichnyak Yu.P., et al. Anomalies in the concentration relationship of thermal conductivity of sintered composites with an ultradispersed component in the TiN-AlN system. *Soviet Powder Metallurgy and Metal Ceramics*, 1992, **31** (5), P. 429–433.

[93] Alekseev G.N. *General heat engineering*. Vysshaya shkola, Moscow, 1980, 552 p. (In Russian)

[94] Lee J.-K., Yang M. Progress in light harvesting and charge injection of dye-sensitized solar cells. *Materials Science and Engineering B*, 2011, **176**, P. 1142–1160.

[95] Bonch-Bruevich V.L., Kalashnikov S.G. *Semiconductor Physics*. Nauka, Moscow, 1977, 674 p.

[96] Afanasyev V.P., Terukov E.I., Sherchenkov A.A. *Thin film solar cells based on silicon*, 2nd ed. SPbGETU "LETI", Saint-Petersburg, 2011, 168 p.

[97] Andreev V.M., Griliches V.A., Rumyantsev V.D. *Photoelectric conversion of concentrated solar radiation*. Nauka, Leningrad, 1989, 310 p.

[98] Alferov Zh.I., Andreev V.M., Rumyantsev V.D. *High-Efficient low-cost photovoltaics*. Springer-Verlag, Berlin, Heidelberg, 2009, 227 p.

[99] Sorokin S.V., Avdienko P.S., et al. Molecular beam epitaxy of layered group III metal chalcogenides on GaAs (001) substrates. *Materials*, 2020, **13** (16), 3447.

[100] Kalinovskii V.S., Kontrosh E.V., et al. Development and study of the p-i-n GaAs/AlGaAs tunnel diodes for multijunction converters of high-power laser radiation. *Semiconductors*, 2020, **54**, P. 355–361.

[101] Ivanov S.V., Chernov M.Y., et al. Metamorphic InAs(Sb)/InGaAs/InAlAs nanoheterostructures grown on GaAs for efficient mid-IR emitters. *Prog. Cryst. Growth Charact. Mater.*, 2019, **65** (1), P. 20–35.

[102] Podoskin A.A., Golovin V.S., et al. Properties of external-cavity high-power semiconductor lasers based on a single InGaAs quantum well at high pulsed current pump. *J. Opt. Soc. Am. B-Opt. Phys.*, 2020, **37** (3), P. 784–788.

[103] Andreev V.M., Malevskiy D.A., et al. On the main photoelectric characteristics of three-junction InGaP/InGaAs/Ge solar cells in a broad temperature range (-197°C$\leq T \leq +85^{\circ}$C). *Semiconductors*, 2016, **50**, P. 1356–1361.

[104] Alferov Z.I., Andreev V.M. Rumyantsev V.D. Solar photovoltaics: Trends and prospects. *Semiconductors*, 2004, **38**, P. 899–908.

[105] Antonyshyn I., Wagner F.R., et al. Micro-scale device – an alternative route for studying the intrinsic properties of solid-state materials: The case of semiconducting TaGeI. *Angew.Chem. Int. Ed.*, 2020, **59** (1), P. 1136–11141.

[106] Shpeizman V.V., Nikolaev V.I., et al. The effect of texturing of silicon wafer surfaces for solar photoelectric transducers on their strength properties. *Tech. Phys.*, 2020, **65** (7), P. 1123–1129.

[107] Cahen D. Where are we today in research in photovoltaics? 2007, URL: https://www.scribd.com/document/108703482/123.

[108] Komissarova T.A., Semenov A.N., et al. Peculiarities of the electrophysical properties of InSb/AlInSb/AlSb heterostructures with a high electron concentration in the two-dimensional channel. *Semiconductors*, 2014, **48** (3), P. 338–343.

[109] Joannopoulos J.D., Lucovsky G. *The physics of hydrogenated amorphous silicon I: Structure, Preparation, and Devices*. Springer Berlin Heidelberg, 1984, 290 p.

[110] Joannopoulos J.D., Lucovsky G. *The physics of hydrogenated amorphous silicon II: Electronic and Vibrational Properties*. Springer Berlin Heidelberg 1984. 373 p.

[111] Ken O.S., Andronikov D.A,, et al. Spectral features of the photoresponse of structures with silicon nanoparticles. *Semiconductors*, 2014, **48** (11), P. 1518–1524.

[112] Ayvazov A.A., Budagyan B.G., Vikhrov S.P., Popov A.I. *Disordered semiconductors*. MEI Publishing House, Moscow, 1995, 352 p. (in Russian)

[113] Chopra K.L., Das S.R. *Thin Film Solar Cells*. Springer US, 1983, 607 p.

[114] Spear W.E., LeComber P.G. Investigation of the localised state distribution in amorphous Si films. *J. Non-Cryst. Solids*, 1972, **8–10**, P. 727–738.

[115] Madan A., LeComber P.G., Spear W.E. Investigation of the density of localized states in a-Si using the field effect technique. *J. Non-Cryst. Solids*, 1976, **20**. P. 239–257.

[116] Parashchuk D.Y., Kokorin A.I. Modern photoelectric and photochemical methods of solar power conversion. *Russ. J. Gen. Chem.*, 2009, **79** (11), P. 2543–2555.

[117] Semenov K.N., Charykov N.A., et al. Phase equilibria in fullerene-containing systems as a basis for development of manufacture and application processes for nanocarbon materials. *Russian Chem. Reviews*, 2016, **85** (1), P. 38–59.

[118] Gracheva I.E., Moshnikov V.A., et al. Nanostructured materials obtained under conditions of hierarchical self-assembly and modified by derivative forms of fullerenes. *J. Non-Cryst. Solids*, 2012, **358**, P. 433–439.

[119] Vasiliev R.B., Rumyantseva M.N., et al. Crystallite size effect on the conductivity of the ultradisperse ceramics of SnO_2 and In_2O_3. *Mendeleev Communication*, 2004, **14** (4), P. 167–169.

[120] O'Regan B., Grätzel M. A Low-cost, high-efficiency solar cell based on dye-sensitized colloidal TiO2 films. *Nature*, 1991, **353**, P. 737–740.

[121] Zvereva I.A., Kalinkina L.M., et al. Production of nanocrystalline titanium dioxide photoactive coatings for decomposition of organic water pollutants in a flow reactor. *Glass Physics and Chemistry*, 2012, **38** (6), P. 504–510.

[122] Kozyukhin S.A., Grinberg V.A., et al. Photoelectrochemical cells based on nanocrystalline TiO2 synthesized by high temperature hydrolysis of ammonium dihydroxodilactatotitanate (IV). *Russian Journal of Electrochemistry*, 2013, **49** (5), P. 423–427.

[123] Kovalev I.A., Petrov A.A., et al. New hierarchical titania-based structures for photocatalysis. *Mendeleev Communications*, 2018, **28**, P. 541–542.

[124] Bai Y., Cao Y., et al. High-performance dye-sensitized solar cells based on solvent-free electrolytes produced from eutectic melts. *Nature Materials*, 2008, **7** (8), P. 626–630.

[125] Vildanova M.F., Nikolskaia A.B., et al. Nanostructured ZrO2–Y2O3-based system for perovskite solar cells. *Doklady Physical Chemistry*, 2019, **484** (2), P. 36–38.

[126] Larina L.L., Alexeeva O.V., et al. Very wide-bandgap nanostructured metal oxide materials for perovskite solar cells. *Nanosystems: Phys., Chem., Math.*, 2019, **10** (1), P. 70–75.

[127] Shevaleevskiy O. The future of solar photovoltics: from physics to chemistry. *Pure Appl. Chem.*, 2008, **80**, P. 2079–2089.

[128] Vildanova M.F., Nikolskaia A.B., et al. Potassium doping effect on the photovoltaic performance of perovskite solar cells. *Tech. Phys. Lett.*, 2020, **46**, P. 231–234.

[129] Alexeeva O.V., Kozlov S.S., Larina L.L., Shevaleevskiy O.I. Pt nanoparticle-functionalized RGO counter electrode for efficient dye-sensitized solar cells. *Nanosystems: Phys., Chem., Math.*, 2019, **10** (6), P. 637–641.

[130] Belich N., Udalova N., et al. Perovskite puzzle for revolutionary functional materials. *Front. Chem.*, 2020, **8**, 550625.

[131] Kulova T.L., Semenenko D.A., et al. Cathode materials based on vanadium pentoxide for rechargeable batteries. *Electrochemical Energetics*, 2008, **8** (4), P. 197–201.

[132] Medved'ko A.V., et al. The design and synthesis of thiophene-based ruthenium(II) complexes as promising sensitizers for dye-sensitized solar cells. *Dyes and Pigments*, 2017, **140**, P. 169–178.

[133] Levshanov A.A., Grishina E.P., et al. Ni self-organized balls as a promising energy storage material. *Material J. Phys. Chem. C*, 2016, **120** (30), P. 16453–16458.

[134] Irgashev R.A., Karmatsky A.A., et al. A facile and convenient synthesis and photovoltaic characterization of novel thieno[2,3-b]indole dyes for dye-sensitized solar cells. *Synthetic Metals*, 2015, **199**, P. 152–158.

[135] Zamaraev K.I. *Photocatalytic conversion of solar energy*. Vol. 1, 2. Nauka, Novosibirsk, 1985, 442 p. (in Russian)

[136] Pelizzetti E., Schiavello M. *Photochemical conversion and storage of solar energy*. Kluwer Academic Publishers, Dordrecht, 1991, 660 p.

[137] Zamaraev K.I., Parmon V.N. *Photocatalytic conversion of solar energy. Heterogeneous, homogeneous and molecular structurally organized systems: Collection of scientific papers*, Nauka, Novosibirsk, 1991, 358 p.

[138] Fujishima A., Hashimoto K., Watanabe T. *TiO2 Photocatalysis. Fundamentals and Applications*. BKC, Tokyo, 1999, 176 p.

[139] Rempel A.A., Kuznetsova Y.V., et al. High photocatalytic activity under visible light of sandwich structures based on anodic TiO$_2$/CdS nanoparticles/sol–gel TiO$_2$. *Top Catal.*, 2020, **63**, P. 130–138.

[140] Brdlik P.M. *Testing and calculation of solar desalination plants in collected articles: Using solar energy*, Publishing house Acad. Sciences of the USSR, Moscow, 1957, 248 p.

[141] Gel'dyyev A. *Modern methods of water desalination*. Ilim, Ashgabat, 1967, 181 p.

[142] Ioffe A.F. Semiconductor thermoelements and thermoelectric cooling. London, Infosearch, 1957, 254 p.

[143] Ordin S.V. Achieving the problem of thermoelectricity, 2015, URL: http://www.nanonewsnet.ru/articles/2015/dostizheniya-problemy (in Russian)

[144] Rempel A.A. Nanotechnologies. Properties and applications of nanostructured materials. *Russ. Chem. Rev.*, 2007, **76** (5), P. 435–461.

[145] Glass fabric, URL: https://novate.ru/blogs/201014/28210/.

[146] Daniel-Beck V., Voronin A., Roginskaya N. Thermoelectric generator TGK-3. *Radio Journal*, 1954, **2**, P. 24–25. (in Russian)

[147] Shostakovsky P. Modern solutions of thermoelectric cooling for radio electronic, medical, industrial and household appliances. *Components and technologies*, 2009, **12** (1), P. 40–46. (in Russian)

[148] Postnikov V.S. *Solid state physics and chemistry*. Metallurgiya, 1978, 544 p. (in Russian)

[149] Anatychuk L.I., Bulat L.P. *Semiconductors under extreme temperature conditions*. Nauka, Saint-Petersburg, 2001, 197 p. (in Russian)

[150] Di Cicco A., Filipponi A. Semiconductors under extreme conditions. In: Schnohr C., Ridgway M. (eds) X-*Ray Absorption Spectroscopy of Semiconductors. Springer Series in Optical Sciences*, 2015, **190**, Springer, Berlin, Heidelberg.

[151] Reay D., Macmichael D. *Heat pumps: Design and application*. Pergamon Press, Oxford, 1979, 224 p.

[152] Pinuela M., Mitcheson P.D., Lucyszyn S. Ambient RF energy harvesting in urban and semi-urban environments. *IEEE transactions on microwave theory and techniques*, 2013, **61** (7), P. 2715–2726.

[153] Cansiz M., Altinel D., Kurt G.K. Efficiency in RF energy harvesting systems: A comprehensive review. *Energy*, 2019, **174**, P. 292–309.

[154] Potapov A.A. Fractals, scaling and fractional operators in modern radio engineering and electronics: the current state and development. *J. of Radio Electronics*, 2010, **1**, P. 1–100.

[155] Krasnok A.E., Maksymov I.S., et al. Optical nanoantennas. *Phys. Usp.*, 2013, **56** (6), P. 539–564.

[156] Bharadwaj P., Deutsch B., Novotny L. Optical Antennas. *Advances in Optics and Photonics*, 2009, **1** (3), P. 438–483.

[157] Novotny L., van Hulst N. Antennas for light. *Nature Photonics*, 2011, **5**, P. 83–90.

[158] Giannini V., Fernandes-Dominguez I.A., Heck C.H., Maier S.A. Plasmonic Nanoantennas: Fundamentals and Their Use in Controlling the Radiative Properties of Nanoemitters. *Chem. Rev.*, 2011, **111** (6), P. 3888–3912.

[159] Maksymov I.S., Davoyan A.R., Kivshar Yu.S. Enhanced emission and light control with tapered plasmonic nanoantennas. *Appl. Phys. Lett.*, 2011, **99**, 083304.

[160] Acar H., Coenen T., Polman A., Kuipers L.K. Dispersive ground plane core–shell type optical monopole antennas fabricated with electron beam induced deposition. *ACS Nano*, 2012, **6** (9) P. 8226–8232.

[161] Suh J.Y., Huntigton M.D., et al. Extraordinary nonlinear absorption in 3D bowtie nanoantennas. *Nano Letters*, 2012, **12** (1), P. 269–274.

[162] Rosa L., Sun K., Juodkazis S. Sierpiń´ski fractal plasmonic nanoantennas. *Phys. Status Solidi RRL*, 2011, **5** (5–6), P. 175–177.

[163] Trompoukis C., Daif O.E., et al. Photonic assisted light trapping integrated in ultrathin crystalline silicon solar cells by nanoimprint lithography. *Appl. Phys. Lett.*, 2012, **101**, 103901.

[164] Jeong S., Garnett E.C., et al. Hybrid silicon nanocone-polymer solar cells. *Nano Lett.*, 2012, **12** (6), P. 2971–2976.

[165] Xu Z., Sadler B.M. Ultraviolet communications: potential and state-of-the-art. *IEEE Communications Magazine*, 2008, **46** (5), P. 67–73.

[166] Elshimy M.A., Hranilovic S. Non-line-of-sight single-scatter propagation model for noncoplanar geometries. *J. Opt. Soc. Am. A*, 2011, **28**, P. 420–428.

[167] Shaw G.A., Nischan M.L., et al. NLOS UV communication for distributed sensor systems. *Proc. SPIE*, 2000, **4126**, P. 83–96.

[168] Wang L., Li Y., Xu Z., Sadler B.M. Wireless ultraviolet network models and performance in noncoplanar geometry. *Proceeding of "2010 IEEE Globecom Workshops"*, Miami, FL, USA, 6–10 December, 2010, 1037.

[169] Wang L., Xu Z., Sadler B.M. Non-line-of-sight ultraviolet link loss in noncoplanar geometry. *Opt. Lett.*, 2010, **35** (8), P. 1263–1265.

[170] Wang L., Xu Z., Sadler B.M. An approximate closed-form link loss model for non-line-of-sight ultraviolet communication in noncoplanar geometry. *Opt. Lett.*, 2011, **36** (7), P. 1224–1226.

[171] Wang H., Li J., Qiu K. Ultraviolet communication system in free atmosphere, Patent. CN101986578A China: IPC G02 B 17/06; H04 B 10/07; H04 B 10/11.

[172] Wang H., Li J., Qiu K. Day blind ultraviolet laser communication system in free space, Patent. CN101986579A China: IPC G02 B 27/09; H04 B 10/07; H04 B 10/11.

[173] Zhen H., Binru L., Qiang L., Zhiqin L. Delay transmission system and method for ultraviolet light communications signals, Patent. CN106656338A China: IPC H04 B 10/11; H04 B 10/29; H04 B 10/297; H04 W 84/12.

[174] Bing S. Single-channel ultraviolet (uv) light communication system, Patent CN202918295U China: IPC H04 B 10/11.

[175] Xiaoyi L., Juan Y., Fang Z. Method for optimizing blind ultraviolet non line-of-sight Ad-hoc communication network shared channel, Patent CN103647603B China: IPC G06 N 3/12; H04 B 10/11; H04 L 29/06.

[176] Wang H., Zhao M., Deng Z. Ultraviolet light communication method and transmitter, Patent CN102638309A China: IPC H04 B 10/114; H04 B 10/50.

[177] Pozhidaev V.N. Feasibility of ultraviolet communication links based on the effect of molecular and aerosol scattering in the atmosphere. *Radio Engineering and Electronic Physics*, 1977, **22** (10), P. 2190–2192. (in Russian)

[178] Pozhidaev V.N. Estimation of attenuation and backscattering of millimeter radio waves in meteorological formations. *Journal of Communications Technology and Electronics*, 2010–2011, **55** (11), P. 1223–1230.

[179] Shaw G.A., Siegel A.M., Nischan M.L. Demonstration system and applications for compact wireless ultraviolet communications. *Proc. SPIE*, 2003, **5071**, P. 241–252.

[180] Shaw G.A., Siegel A.M., Model J. Extending the range and performance of non-line-of-sight ultraviolet communication links. *Proc. SPIE*, 2006, **6231**, 62310C.

[181] Xu Zh., Chen G., Abou-Galala, F., Leonardi M. Experimental performance evaluation of non-line-of-sight ultraviolet communication systems. *Proc. SPIE*, 2007, **6709**, 67090Y.

[182] Zhang H., Yin H., et al. Study of effects of obstacle on non-line-of-sight ultraviolet communication links. *Opt. Express*, 2011, **19** (22), P. 21216–21226.

[183] Britvin A.V. The pulse charachteristic estimation of optical atmospheric UV-channel with scattering. *Bulletin of the Novosibirsk state university. Series Physics*, 2010, **5** (2), P. 5–7. (in Russian)

[184] Konstantinov I.S., Vasilyev G.S., et al. Numerical and analytical modeling of wireless UV communication channels for the organization of wireless ad- hoc network. *IJCSNS International Journal of Computer Science and Network Security*, 2018, **18** (8), P. 98–104.

[185] Konstantinov I.S., Vasilyev G.S, et al. Modeling and Analysis of the Characteristics of Ultraviolet Channels under Different Conditions of Radiation Propagation for the Organization of Wireless AD-HOC Network. *J. of Adv. Research in Dynamical and Control Systems*, 2018, **10** (2), P. 1853–1859.

[186] Belov V.V., Abramochkin V.N., et al. Bistatic optoelectronic communication systems: Field experiments in artificial and natural water reservoirs. *Atmos Ocean Opt*, 2017, **30** (2), P. 366–371.

[187] Aouini A. System for converting wind energy, Patent. US20130181458A1 USA: IPC F03 D 9/00.

[188] Vorotnikov G.V. The modeling of the thermoacoustic electric generator by quadrupole approximation approach. *Vestnik of Samara University. Aerospace and Mechanical Engineering*, 2012, **3** (34), P. 191–199.

[189] Almjasheva O.V., Gusarov V.V. Prenucleation formations in control over synthesis of $CoFe_2O_4$ nanocrystalline powders. *Russian Journal of Applied Chemistry*, 2016, **89** (6), P. 851–856.

[190] Lomanova N.A., Tomkovich M.V., Sokolov V.V., Gusarov V.V. Special features of formation of nanocrystalline BiFeO3 via the glycine-nitrate combustion method. *Russian Journal of General Chemistry*, 2016, **86** (10), P. 2256–2262.

[191] Kovalenko A.N. High-temperature superconductivity: From macro- to nanoscale structures, *Nanosystems: Phys., Chem., Math.*, 2016, **7** (6), P. 941–970.

[192] Fedorov P.P. Nanotechnology and material science. *Nanosystems: Phys., Chem., Math.*, 2020, **11** (3), P. 314–315.

[193] Almjasheva O.V., Garabadzhiu A.V., et al. Biological effect of zirconium dioxide-based nanoparticles. *Nanosystems: Phys., Chem., Math.*, 2017, **8** (3), P. 391–396.

[194] Tugova E., Yastrebov S., Karpov O., Smith R. $NdFeO_3$ nanocrystals under glycine nitrate combustion formation. *J. Crystal Growth*, 2017, **467**, P. 88–92.

[195] Proskurina O.V., Tomkovich M.V., et al. Formation of Nanocrystalline BiFeO3 under hydrothermal conditions. *Russian Journal of General Chemistry*, 2017, **87** (11), P. 2507–2515.

[196] Krasilin A.A., Gusarov V.V. Redistribution of Mg and Ni cations in crystal lattice of conical nanotube with chrysotile structure. *Nanosystems: Phys., Chem., Math.*, 2017, **8** (5), P. 620–627.

[197] Lomanova N.A., Tomkovich M.V., Osipov A.V., Ugolkov V.L. Synthesis of nanocrystalline materials based on the Bi_2O_3–TiO_2 system. *Russian Journal of General Chemistry*, 2019, **89** (10), P. 2075–2081.

[198] Zlobin V.V., Krasilin A.A., Almjasheva O.V. Effect of heterogeneous inclusions on the formation of TiO_2 nanocrystals in hydrothermal conditions. *Nanosystems: Phys., Chem., Math.*, 2019, **10** (6), P. 733–739.

[199] Lomanova N.A., Panchuk V.V., et al. Bismuth orthoferrite nanocrystals: magnetic characteristics and size effects. *Ferroelectrics*, 2020, **569**, P. 240–250.

[200] Krasilin A.A., Khrapova E.K., Maslennikova T.P. Cation doping approach for nanotubular hydrosilicates curvature control and related applications. *Crystals*, 2020, **10**, 654.

[201] Tugova E.A., Karpov O.N., Besedina N.A., Yastrebov S.G. Peculiarities of inelastic scattering of light by $Nd_{1-x}Bi_xFeO_3$ nanoclusters. *Nano Express*, 2020, **1** (1), P. 010064–010072.

[202] Shchelokova A., Ivanov V., et al. Ceramic resonators for targeted clinical magnetic resonance imaging of the breast. *Nat Commun.*, 2020, **11**, P. 3840–3846.

[203] Egorysheva A.V., Skorikov V.M. Efficient nonlinear optical material BiB_3O_6 (BIBO). *Inorg Mater.*, 2009, **45** (13), P. 1461–1476.

[204] Sleight Arthur W. Oxide superconductors. *Thermochimica Acta*, 1991, **174**, P. 1–7.

[205] Miyazaki C.M., Riul A. Low-Dimensional Systems: Nanoparticles. *Nanostructures*, 2017, **5**, P. 125–146.

[206] Vance M.E., Kuiken T., et al. Nanotechnology in the real world: Redeveloping the nanomaterial consumer products inventory. *J. Nanotechnol.*, 2015, **6** (1), P. 1769–1780.

[207] Chislova, I.V., Matveeva A.A., Volkova A.V., Zvereva I.A. Sol-gel synthesis of nanostructured perovskite-like gadolinium ferrites. *Glass Phys. Chem.*, 2011, **37** (6), P. 653–660.

[208] Mukasyan A.S., Rogachev A.S. Combustion synthesis: mechanically induced nanostructured materials. *J. Mater. Sci.*, 2017, **52**, P. 11826–11833.

[209] Andrievski R.A. Review of thermal stability of nanomaterials. *J. Mater. Sci.*, 2014, **49** (4), P. 1449–1460.

[210] Tretyakov Yu.D. Self-organisation processes in the chemistry of materials. *Russ. Chem. Rev.*, 2003, **72** (8), P. 651–679.

[211] Kazin P.E., Tretyakov Yu.D. Microcomposites based on superconducting cuprates. *Russ. Chem. Rev.*, 2003, **72** (10), P. 849–865.

[212] Defay R., Prigogine I., Sanfeld A. Surface thermodynamics. *J. Colloid Interface Sci.*, 1977, **58** (3), P. 498–510.

[213] Van-der-Vaal's I.D., Konstamm F. *Kurs termostatiki (Course of Thermostatics).* Moscow, ONTI, 1936, 452 p. (in Russian)

[214] Rusanov A.I. *Phase equilibria and surface phenomena*. Khimiya, Leningrad, 1967, 388 p.

[215] Adamson A.W., Gast A.P. *Physical chemistry of surfaces (six edition)*. John Wiley and Sons, New-York, 1997, 804 p.

[216] Gusarov V.V., Suvorov S.A. Transformations of nonautonomous phases and densification of polycrystalline systems. *Journal of Applied Chemistry of the USSR*, 1992, **65** (7), P. 1227–1235.

[217] Gusarov V.V. Kinetic features of heat effect of melting in polycrystalline systems. *Russ. J. Appl. Chemistry*, 1994, **67** (3), P. 364–366.

[218] Gusarov V.V., Suvorov S.A. Rapid thermal packing of materials. *Russ. J. Appl. Chem.*, 1993, **66** (3), P. 431–437.

[219] Gusarov V.V., Suvorov S.A. Thickness of 2-dimensional nonautonomous phases in local equilibrium polycrystalline systems based on a single bulk phase. *Russ. J. Appl. Chem.*, 1993, **66** (7), P. 1212–1216.

[220] Gusarov V.V., Suvorov S.A. Melting points of locally equilibrium surface phases in polycrystalline systems based on a single volume phase. *J. Appl. Chem. of the USSR*, 1990, **63** (8), P. 1560–1565.

[221] Gusarov V.V., Malkov A.A., Malygin A.A., Suvorov S.A. Thermally activated transformations of 2D nonautonomous phases and contradiction of polycrystalline oxide materials. *Inorganic Materials*, 1995, **31** (3), P. 320–323.

[222] Babaev A.A., Zobov M.E., Terukov E.I., Tkachev A.G. A technology for producing polymeric composites based on carbon nanofibers. *Prot. Met. Phys. Chem. Surf.*, 2020, **56** (4), P. 734–739.

[223] Bespalova Zh.I., Khramenkova A.V. The use of transient electrolysis in the technology of oxide composite nanostructured materials: review. *Nanosystems: Phys., Chem., Math.*, 2016, **7** (3), P. 433–450.

[224] Khaliullin S.M., Bamburov V.G., et al. $CaZrO_3$ synthesis in combustion reactions with glycine. *Doklady Chemistry*, 2015, **461** (2), P. 93–95.

[225] Aruna S.T., Mukasyan A.S. Combustion synthesis and nanomaterials. *Curr. Opin. Solid State Mater. Sci.*, 2008, **12** (3–4), P. 44–50.

[226] Byrappa K., Adschiri T. Hydrothermal technology for nanotechnology. *Progress in Crystal Growth and Characterization of Materials*, 2007, **53**, P. 117–166.

[227] Lee J., Mahendra S., Alvarez P.J.J. Nanomaterials in the construction industry: A Review of their applications and environmental health and safety considerations. *ACS Nano*, 2010, **4** (7), P. 3580–3590.

[228] Vasilevskay A.K., Almjasheva O.V., Gusarov V.V. Peculiarities of structural transformations in zirconia nanocrystals. *J. Nanopart. Res.*, 2016, **18** (7), P. 188–198.

[229] Van Tac D., Mittova V.O., Almjasheva O.V.,Mittova I.Ya. Synthesis and magnetic properties of nanocrystalline $Y_{1-x}Cd_xFeO_{3-\delta}$ ($0 \leq x \leq 0.2$). *Inorg Mater.*, 2011, **47** (10),P. 1141–1146.

[230] Uvarov N.F., Vanek P. Stabilization of new phases in ion-conducting nanocomposites. *Journal of Materials Synthesis and Processing*, 2000, **8** (5/6), P. 319–326.

[231] Nguyen A.T., Nguyen V.Y., et al. Synthesis and magnetic properties of PrFeO3 nanopowders by the co-precipitation method using ethanol. *Nanosystems: Phys., Chem., Math.*, 2020, **11** (4), P. 468–473.

[232] Ostroushko A.A., Russkikh O.V. Oxide material synthesis by combustion of organic-inorganic compositions. *Nanosystems: Phys. Chem. Math.*, 2017, **8** (4), P. 476–502.

[233] Zhukov V.P., Kostenko M.G., Rempel A.A., Shein I.R. Influence of carbon or nitrogen dopants on the electronic structure, optical properties and photocatalytic activity of partially reduced titanium dioxide. *Nanosystems: Phys. Chem. Math.*, 2019, **10** (3), P. 374–382.

[234] Khaliullin Sh.M., Zhuravlev V.D., Bamburov V.G. Solution-combustion synthesis of $MZrO_3$ zirconates (M = Ca, Sr, Ba) in open reactor: thermodynamic analysis and experiment. *International Journal of Self-Propagating High-Temperature Synthesis*, 2017, **26** (2), P. 93–101.

[235] Abryutin V., Nesterov S., Romanko V., Kholopkin A. Application of nanotechnology to create highly efficient thermoelectric materials. *Nanoindustry*, 2010, **1**, P. 24–26.

[236] Ordin S.V., Wang W.N. Thermoelectric effects on micro and nano level. *J. Advances in Energy Research*, 2011, **9**, P. 311–342.

[237] Matsukevich, I.V., Klyndyuk, A.I., et al. Thermoelectric properties of $Ca_{3-x}Bi_xCo_4O_{9+\delta}$ ($0.0 \leq x \leq 1.5$) ceramics. *Inorg Mater.*, 2016, **52** (6), P. 593–599.

[238] Pikalova E.Y., Kolchugin A.A., Bamburov V.G. Ceria-based materials for high-temperature electrochemistry applications. *International Journal of Energy Production and Management*, 2016, **1** (3), P. 272–283.

[239] Almyasheva O.V., Gusarov V.V., et al. Nanocrystals of ZrO_2 as sorption heat accumulators. *Glass Physics and Chemistry*, 2007, **33** (6), P. 587–589.

[240] Chupakhina T.I., Melnikova N.V., et al. Synthesis, structure and dielectric properties of new ceramics with K_2NiF_4-type structure. *J. Eur. Ceram. Soc.*, 2019, **39** (13), P. 3722–3729.

[241] Galakhov V.R., Turkin D.I., et al. Effect of transition metal oxidations state on crystal structure and magnetic ordering in frustrated *ABaM*4O7 systems (*A*=Y, Ca; *M*=Co, Fe): X-ray diffraction, soft X-ray absorption, and magnetization studies. *Current Applied Physics*, 2018, **18**, P. 155–162.

[242] Talanov M.V., Bokov A.A., Marakhovsky M.A. Effects of crystal chemistry and local random fields on relaxor and piezoelectric behavior of lead-oxide perovskites. *Acta Materialia*, 2020, **193**, P. 40–50.

[243] Pikalova E.Y., Bamburov V.G., et al. The development of electrolytes for intermediate temperature solid oxide fuel cells. *WIT Transactions on Ecology and the Environment*, 2014, **190** (1) P. 261–272.

[244] Lim H-D., Lee B., et al. Rational design of redox mediators for advanced Li–O_2 batteries. *Nature Energy*, 2016, **1** (6), 16066.

[245] Zhuk A.Z., Kleymenov B.V., et al. *Aluminum-hydrogen energy*. JIHT RAS, Moscow, 2007, 278 p. (in Russian)

[246] Brusnetsov V.P. *Solid oxide fuel cells: collection of articles. scientific and technical articles*. RFNC-VNIITF Publishing House, Snezhinsk, 2003, 376 p. (in Russian)

[247] Predtechensky M.R., Smal A.N., Nakoryakov V.E., Bobrenok O.F. Fuel cells based on carbonate melts based on electrodes of a new design. *Proceedings of the Institute for Advanced Study*, 2003, **1**, P. 2–13. (in Russian)

[248] Merkulov O.V., Markov A.A., et al. Structural features and high-temperature transport in $SrFe_{0.7}Mo_{0.3}O_{3-\delta}$. *J. Solid State Chem.*, 2018, **258**, P. 447–452.

[249] Lukashin A.V., Eliseev A.A. *Physical methods for the synthesis of nanomaterials*. MSU, Moscow, 2007, 32 p. (in Russian)

[250] Kovalenko A.N., Kalinin N.V. Thermodynamic instability of compound and formation of nanosized particles nearby the critical point of phase generating media. *Nanosystems: Phys., Chem., Math.*, 2014, **5** (2), P. 258–293.

[251] Feynman R.P. There's plenty of room at the bottom. An invitation to enter a new field of physics. *Engineering and Science magazine*, 1960, **23** (5), P. 22–36.

[252] Kolesnik I.V., Eliseev A.A. *Chemical methods for the synthesis of nanomaterials*. Ed. Tretyakov Yu.D. MSU, Moscow, 2011, 41 p. (in Russian)

[253] Rowe D.M. (ed.). *Handbook of Thermoelectrics*. CRC Press, Boca Raton, FL, 1995, 701 p.

[254] Yepremyan A.O., Aroutiounian V.M., Vahanyan A.I. Figure of merit of modern semiconducting thermoelectric materials. *Int. Sci. J. for Alternative Energy and Ecology*, 2005, **5** (25), P. 7–18.

[255] Gridnev S.A., Kalinin Yu.E., Makagonov V.A., Shuvaev A.S. Promising thermoelectric materials. *Int. Sci. J. for Alternative Energy and Ecology*, 2013, **1-2** (118), P. 117–125 (in Russian).

[256] Sherchenkov A.A., Shtern Yu.I., et al. Current state of thermoelectric material science and the search for new effective materials. *Nanotechnologies in Russia*, 2015, **10**(11–12), P. 827–840.

[257] Shevelkov A.V. Chemical aspects of the design of thermoelectric materials. *Russ. Chem. Rev.*, 2008, **77** (1), P. 1–19.

[258] Goldsmid H.J. Bismuth telluride and its alloys as materials for thermoelectric generation. *Materials*, 2014, **7**, P. 2577–2592.

[259] Sootsman J.R., Chung D.Y., Kanatzidis M.G. New and old concept in thermoelectric materials. *Angew. Chem. Int. Ed.*, 2009, **48**, P. 8616–8639.

[260] Populoh S., Aguirre M.H., et al. High figure of merit in (Ti, Zr, Hf) NiSn half-Heusler alloys. *Scripta Materialia*, 2012, **66**, P. 1073–1076.

[261] Minnich A.J., Dresselhaus M.S., Ren Z.F., Chen G. Bulk nanostructured thermoelectric materials: current research and future prospects. *Energy Environ. Sci.*, 2009, **2**, P. 468–479.

[262] Tugova E.A., Klyndyuk A.I., Gusarov V.V. Synthesis of solid solutions of double layered Ruddlesden–Popper phases in the Gd_2O_3–SrO–Fe_2O_3–Al_2O_3 system. *Russian Journal of Inorganic Chemistry*, 2013, **58** (7), P. 848–854.

[263] Tugova E.A. P/RS intergrowth type phases in the Ln_2O_3–MO–Al_2O_3 systems. *Russian Journal of General Chemistry*, 2016, **86** (11), P. 2410–2417.

[264] Zvereva I.A., Tugova E.A., et al. The impact of Nd^{3+}/La^{3+} substitution on the cation distribution and phase diagram in the $La_2SrAl_2O_7$–$Nd_2SrAl_2O_7$ system. *Chimica Techno Acta*, 2018, **5** (1), P. 80–85.

[265] Carvillo P., Chen Y., et al. Thermoelectric performance enhancement of calcium cobaltite through barium grain boundary segregation. *Inorg. Chem.*, 2015, **54**, P. 9027–9032.

[266] Matsukevich I.V., Klyndyuk A.I., et al. Synthesis and properties of materials based on layered calcium and bismuth cobaltites. *Russ. J. Appl. Chem.*, 2015, **88** (8), P. 1241–1247.

[267] Jankowski O., Huber S., et al. Towards highly efficient thermoelectric: $Ca_3Co_4O_{9+\delta} \cdot nCaZrO_3$ composite. *Ceramics – Silikaty*, 2014, **58** (2), P. 106–110.

[268] Gupta R.K., Sharma R., Mahapatro A.K., Tandon R.P. The effect of ZrO_2 dispersion on the thermoelectric power factor of $Ca_3Co_4O_9$. *Physica B*, 2016, **483**, P. 48–53.

[269] Krasutskaya N.S., Klyndyuk A.I., et al. Thermoelectric properties of the ceramics based on the layered calcium cobaltite doped by bismuth oxide. *Refractories and Technical Ceramics*, 2016, **10**, P. 25–29.

[270] Kozhevnikov V.L., Leonidov I.A., et al. High-temperature thermopower and conductivity of $La_{1-x}Ba_xMnO_3$ ($0.02 \leq x \leq 0.35$). *J. Solid State Chem.*, 2003, **172** (1), P. 1-5.

[271] Estemirova, S.K., Yankin A.M., et al. Phase composition and structure of $La_{1-x}Ca_xMnO_{3+\delta}$ ($0 \leq x \leq 0.2$) solid solutions. *Inorg Mater.*, 2008. **44**, P. 1251–1256.

[272] Xu J., Wei C., Jia K. Properties and device of $Ca_{2.7}Sr_{0.3}Co_4O_9$ and $Ca_{0.95}Sm_{0.05}MnO_3$ thermoelectric materials. *J. Chin. Ceram. Soc.*, 2010, **38** (6), P. 1136–1139.

[273] Han L., Jiang Y., et al. High temperature thermoelectric properties and energy transfer devices of $Ca_3Co_{4-x}Ag_xO_9$ and $Ca_{1-y}Sm_yMnO_3$. *J. Alloys Compd.*, 2011, **509**, P. 8970–8977.

[274] Lim C.-H., Choi S.-M., Seo W.-S., Park H.-H. A power-generation test for oxide-based thermoelectric modules using p-type $Ca_3Co_4O_9$ and n-type $Ca_{0.9}Nd_{0.1}MnO_3$ legs. *J. Electron. Mater.*, 2012, **41** (6), P. 1247–1255.

[275] Zhu Y., Wang C., et al. Influence of Dy/Bi dual doping on thermoelectric performance of $CaMnO_3$ ceramics. *Mat. Chem. Phys.*, 2014, **144**, P. 385–389.

[276] Thiel P., Populoh S., Yoon S., Weidenkaff A. Enhancement of redox- and phase-stability of thermoelectric $CaMnO_{3-\delta}$ by substitution. *J. Solid State Chem.*, 2015, **229**, P. 62–67.

[277] Yasukawa M., Murayama N. High-temperature thermoelectric properties of the oxide material: $Ba_{1-x}Sr_xPbO_3$ ($x = 0 — 0.6$). *J. Mat. Sci. Lett.*, 1997, **16** (21), P. 1731–1735.

[278] Yasukawa M., Murayama N. A promising oxide material for high-temperature thermoelectric energy conversion: Ba1-xSrxPbO3 solid solution system. *Mat. Sci. and Eng. B*, 1998, **54**, P. 64–69.

[279] Yasukawa M., Kono T. Preparation of dense $BaPbO_3$-based ceramics by a coprecipitation and their thermoelectric properties. *J. Alloys and Comp.*, 2006, **426**, P. 420–425.

[280] Chizhova E.A., Klyndyuk A.I. Synthesis and thermoelectric properties of ceramics based on barium-strontium metaplumbates. *Glass Physics and Chemistry*, 2013. **39** (4), P. 453–457.

[281] Muta H., Kurosaki K., Yamanaka S. Thermoelectric properties of doped $BaTiO_3$–$SrTiO_3$ solid solution. *J. of Alloys Compd.*, 2004, **368**, P. 22–24.

[282] Ohta H. Thermoelectrics based on strontium titanate. *Mater. Today*, 2007, **10**, P. 44–49.

[283] Ohta H., Sugiura K., Koumoto K. Recent progress in oxide thermoelectric materials: p-type $Ca_3Co_4O_9$ and n-Type $SrTiO_3$. *Inorg. Chem.*, 2008, **47**, P. 8429–8436.

[284] Wang Y.F., Lee K.H., Ohta H., Koumoto K. Fabrication and thermoelectric properties of heavily rare-earth metal-doped $SrO(SrTiO_3)_n$ ($n = 1, 2$) ceramics. *Ceram. Int.*, 2008, **34,** P. 849–852.

[285] Tang J., Wang W., Zhao G.-L., Li Q. Colossal positive Seebeck coefficient and low thermal conductivity in reduced TiO_2. *J. Phys.: Condens. Matter*, 2009, **21**, 205703.

[286] Liu J., Wang H.C., et al. Synthesis and thermoelectric properties of $Sr_{0.95}La_{0.05}TiO_{3-\delta}$–$TiO_2$ solid solutions. *Solid State Sciences*, 2010, **12**, P. 134–137.

[287] Wang H.C., Wang C.L., et al. Enhancement of thermoelectric figure of merit by doping Dy in $La_{0.1}Sr_{0.9}TiO_3$ ceramic. *Mat. Res. Bull.*, 2010, **45**, P. 809–812.

[288] Zhang Y., Feng B., et al. Thermoelectric phase diagram of the $SrTiO_3$–$SrNbO_3$ solid solution system. *J. Appl. Phys. Lett.*, 2017, **121**, 185102.

[289] Boston R., Schmidt W.L., et al. Protocols for the fabrication, characterization, and optimization of n-type thermoelectric ceramic oxides. *Chem. Mater.*, 2017, **29** (1), P. 265–280.

[290] Robert R., Bocher L., et al. Ni-doped cobaltates as potential materials for high temperature solar thermoelectric converters. *Progr. Solid State Chem.*, 2007, **35**, P. 447–455.

[291] Tomeš P., Trottmann M., et al. Thermoelectric Oxide Modulus (TOMs) for the Direct Conversion of Stimulated Solar Radiation into Electrical Energy. *Materials*, 2010, **3**, P. 2801–2814

[292] Suter C., Tomeš P., Weidenkaff A., Steinfeld A. Heat transfer and geometrical analysis of thermoelectric converters driven by concentrated solar radiation. *Materials*, 2010, **3**, P. 2735–2752.

[293] Tugova E.A. New $DySrAlO_4$ compound synthesis and formation process correlations for $LnSrAl_O4$ (Ln = Nd, Gd, Dy) series. *Acta Metallurgica Sinica (English Letters*, 2016, **29** (5), P. 450–456.

[294] Semenov N.N. Thermal theory of combustion and explosions. III Theory of normal flame propagation. *Progress of Physical Science (USSR)*, 1940, **24** (4) 80 p.

[295] Tretyakov Yu.D., Lukashin A.V., Eliseev A.A. Synthesis of functional nanocomposites based on solid-phase nanoreactors. *Russ. Chem. Rev.*, 2004, **73** (9), P. 899–923.

[296] Shaporev A.S., Zeng H., Ivanov V.K. Tret'yakov Yu.D. Mechanism of formation of finely dispersed zinc oxide in homogeneous hydrolysis of zinc nitrate in the presence of hexamethylenetetramine. *Dokl. Chem.*, 2009, **426** (1), P. 101–104.

[297] Tugova E.A., Zvereva I.A. Formation mechanism of GdFeO$_3$ nanoparticles under the hydrothermal conditions. *Nanosystems: Phys., Chem., Math.*, 2013, **4** (6), P. 851–856.

[298] Al'myasheva, O.V., Korytkova, E.N., Maslov, A.V. Gusarov V.V. Preparation of nanocrystalline alumina under hydrothermal conditions. *Inorg. Mater.*, 2005, **41** (5), P. 460–467.

[299] Klyndyuk A., Chizhova E., Matsukevich I., Tugova E. Thermoelectric properties of inhomogeneous ceramics based on the layered calcium cobaltate. *Universal Journal of Materials Science*, 2019. **7** (4), P. 43–53.

[300] Wu N.Y., Holgate T.C., et al. High temperature thermoelectric properties of Ca$_3$Co$_4$O$_{9+\delta}$ by auto-combustion synthesis and spark plasma sintering. *Journal of the European Ceramic Society*, 2014, **34** (4), P. 925–931.

[301] Agilandeswari K., Ruban Kumar A. Synthesis, characterization, temperature dependent electrical and magnetic properties of Ca$_3$Co$_4$O$_9$ by a starch assisted sol–gel combustion method. *Journal of Magnetism and Magnetic Materials*, 2014, **364**, P. 117–124.

[302] Sotelo A., Rasekh Sh., et al. Effect of synthesis methods on the Ca$_3$Co$_4$O$_9$ thermoelectric ceramic performances. *Journal of Solid State Chemistry*, 2015, **221**, P. 247–254.

[303] Zaboeva E.A., Izotova S.G., Popkov V.I. Glycine-nitrate combustion synthesis of CeFeO$_3$-based nanocrystalline powders. *Russian J. of Appl. Chem.*, 2016, **89** (8), P. 1228–1236.

[304] Bachina A.K., Ivanov V.A., Popkov V.I. Peculiarities of LaFeO$_3$ nanocrystals formation via glycine-nitrate combustion. *Nanosystems: Phys., Chem., Math.*, 2017, **8** (5). P. 647–653.

[305] Martinson K.D., Kondrashkova I.S., Popkov V.I. Synthesis of EuFeO3 nanocrystals by glycine-nitrate combustion method. *Russ. J. Appl. Chem.*, 2017. **90** (8), P. 980–985.

[306] Kondrashkova I.S., Martinson K.D., Zakharova N.V., Popkov V.I. Synthesis of nanocrystalline HoFeO$_3$ photocatalyst via heat treatment of products of glycine-nitrate combustion. *Russ. J. Gen. Chem.*, 2018, **88** (12), P. 2465–2471.

[307] Martinson K.D., Ivanov V.A., et al. Facile combustion synthesis of TbFeO$_3$ nanocrystals with hexagonal and orthorhombic structure. *Nanosystems: Phys., Chem., Math.*, 2019, **10** (6), P. 694–700.

[308] Komova O.V., Simagina V.I., et al. A modified glycine-nitrate combustion method for one-step synthesis of LaFeO$_3$. *Adv. Powder Technol.*, 2016, **27** (2), P. 496–503.

[309] HaoX., Zhang Y. Low temperature gel-combustion synthesis of porous nanostructure LaFeO$_3$ with enhanced visible-light photocatalytic activity in reduction of Cr(VI). *Mater. Lett.*, 2017, **197**, P. 120–122.

[310] Salehabadi A., Salavati-Niasari M., Gholami T., Khoobi A. Dy$_3$Fe$_5$O$_{12}$ and DyFeO$_3$ nanostructures: Green and facial auto-combustion synthesis, characterization and comparative study on electrochemical hydrogen storage. *Int. J. Hydrog. Energy*, 2018, **43** (20), P. 9713–9721.

[311] Popkov V.I., Almjasheva O.V., Gusarov V.V. The investigation of the structure control possibility of nanocrystalline yttrium orthoferrite in its synthesis from amorphous powders. *Russ. J. Appl. Chem.*, 2014, **87** (10), P. 1417–1421.

[312] Popkov V.I., Tugova E.A., Bachina A.K., Almjasheva O.V. The formation of nanocrystalline orthoferrites of rare-earth elements XFeO$_3$ (X = Y, La, Gd) via heat treatment of coprecipitated hydroxides. *Russ. J. Gen. Chem.*, 2017, **87** (11), P. 1771–1780.

[313] Popkov V.I., Almjasheva O.V., et al. The role of pre-nucleus states in formation of nanocrystalline yttrium orthoferrite. *Doklady Chem.*, 2016, **471** (4), P. 439–443.

[314] Popkov V.I., Almjasheva O.V., et al. Effect of spatial constraints on the phase evolution of YFeO$_3$-based nanopowders under heat treatment of glycine-nitrate combustion products. *Cer. Intern.*, 2018, **44** (17), P. 20906–20912.

[315] Almjasheva O.V., Lomanova N.A., et al. The minimum size of oxide nanocrystals – phenomenological thermodynamic vs crystal-chemical approaches. *Nanosystems: Phys., Chem., Math.*, 2019, **10** (4), P. 428–437.

[316] Kopeychenko E.I., Mittova I.Ya., et al. Nanocrystalline heterogeneous multiferroics based on yttrium ferrite (core) with calcium zirconate (titanate) shell. *Russ. J. Gen. Chem.*, 2020, **90**, P. 1030–1035.

[317] Alekseeva O.A., Naberezhnov A.A., Stukova E.V., Popkov V.I. The effect of barium titanate admixture on the stability of potassium nitrate ferroelectric phase in $(1 - x)$KNO$_3$ + (x)BaTiO$_3$ composites. *St. Petersburg Polytechnical University Journal: Physics and Mathematics*, 2015, **1** (3), P. 229–234.

[318] Popkov V.I., Tolstoy V.P., Semenov V.G. Synthesis of phase-pure superparamagnetic nanoparticles of ZnFe$_2$O$_4$ via thermal decomposition of zinc-iron layered double hydroxysulphate. *Journal of Alloys and Compounds*, 2020, **813**, 152179.

[319] Gusev A.I., Rempel A.A. *Nanocrystalline Materials*. Cambridge International Science Publishing, 2004, 351 p.

[320] Martinson K.D., Sakhno D.D., et al. Synthesis of Ni0.4Zn0.6Fe2O4 spinel ferrite and microwave adsorption of related polymer composite. *Nanosystems: Phys., Chem., Math.*, 2020, **11** (5), P. 595–600.

[321] Rempel A.A. Hybrid nanoparticles based on sulfides, oxides, and carbides. *Russian Chemical Bulletin*, 2013, **62** (4), P. 857–868.

[322] Martinson K.D., Kozyritskaya S.S., Panteleev I.B., Popkov V.I. Low coercivity microwave ceramics based on LiZnMn ferrite synthesized via glycine-nitrate combustion. *Nanosystems: Phys., Chem., Math.*, 2019, **10** (3), P. 313–317.

[323] Shevchenko E.V., Charnaya E.V., et al. Superconductivity in a Ga–Ag nanocomposite with dendritic morphology. *Physica C*, 2020, **574**, 1353666.

[324] Albadi Y., Popkov V.I. Dual-modal contrast agent for magnetic resonance imaging based on gadolinium orthoferrite nanoparticles: synthesis, structure and application prospects. *Medicine: theory and practice*, 2019, **4**, P. 35–36.

[325] Pinho S.L.C., Amaral J.S., et al. Synthesis and characterization of rare-earth orthoferrite LnFeO$_3$. *Nanoparticles for Bioimaging*, 2018, **38**, P. 3570–3578.

[326] Albadi Y., Martinson K.D., et al. Synthesis of GdFeO$_3$ nanoparticles via low-temperature reverse co-precipitation: the effect of strong agglomeration on the magnetic behavior. *Nanosystems: Phys., Chem., Math.*, 2020, **11** (2), P. 252–259.

[327] Dmitriev D.S., Popkov V.I. Layer by layer synthesis of zinc-iron layered hydroxy sulfate for electrocatalytic hydrogen evolution from ethanol in alkali media. *Nanosystems: Phys., Chem., Math.*, 2019, **10** (4), P. 480–487.

[328] Chebanenko M.I., Lobinsky A.A., Nevedomskiy V.N., Popkov V.I. NiO-decorated graphitic carbon nitride toward electrocatalytic hydrogen production from ethanol. *Dalton Trans.*, 2020, **49**, P. 12088–12097.

[329] Kodintsev I.A., Martinson K.D., Lobinsky A.A., Popkov V.I. SILD synthesis of the efficient and stable electrocatalyst based on CoO–NiO solid solution toward hydrogen production. *Nanosystems: Phys., Chem., Math.*, 2019, **10** (6), P. 681–685.

[330] Belmesov A.A., Baranov A.A., Levchenko A.V. Anodic Electrocatalysts for Fuel Cells Based on Pt/Ti$_{1-x}$Ru$_x$O$_2$. *Russ. J. Electrochem.*, 2018, **54**, P. 493–499.

[331] Voloshin Y.Z., Buznik V.M., Dedov A.G. New types of the hybrid functional materials based on cage metal complexes for (electro) catalytic hydrogen production. *Pure Appl. Chem.* 2019, **92** (7), P. 1159–1174.

[332] Semishchenko K., Tolstoy V., Lobinsky A. A novel oxidation-reduction route for layer-by-layer synthesis of TiO$_2$ Nanolayers and investigation of its photocatalytical properties. *J. Nanomater.*, 2014, **10**, P. 1–7.

[333] Cam T.S., Vishnievskaia T.A., Popkov V.I. Catalytic oxidation of CO over CuO/CeO$_2$ nanocomposites synthesized via solution combustion method: effect of fuels. *Reviews on Advanced Materials Science*, 2020, **59**, P. 1–13.

[334] Sheshko T.F., Sharaeva A.A., et al. Carbon oxide hydrogenation over GdBO$_3$ (B = Fe, Mn, Co) complex oxides: Effect of carbon dioxide on product composition. *Pet. Chem.*, 2020, **60**, P. 571–576.

[335] Cam T.S., Vishnevskaya T.A., et al. Urea–nitrate combustion synthesis of CuO/CeO$_2$ nanocatalysts toward low-temperature oxidation of CO: the effect of Red/Ox ratio. *J. Mater. Sci.*, 2020, **55**, P. 11891–11906.

[336] Kryuchkova T.A., Kost V.V., et al. Effect of cobalt in GdFeO$_3$ catalyst systems on their activity in the dry reforming of methane to synthesis gas. *Petroleum Chemistry*, 2020, **60** (5), P. 609–615.

[337] Cam T.S., Petrova A.E., et al. On the SCS approach to the CeO$_2$/CuO nanocomposite: thermochemical aspects and catalytic activity in n-hexane conversion. *Russ. J. Inorg. Chem.*, 2020, **65** (5), P. 725–732.

[338] Shamanaeva I.A., Yu Zh., et al. Role of texture and acidity of SAPO-34 in methanol to olefins conversion. *Pet. Chem.*, 2020, **60**, P. 471–478.

[339] Martinson K.D., Kondrashkova I.S., et al. Magnetically recoverable catalyst based on porous nanocrystalline HoFeO$_3$ for processes of n-hexane conversion. *Advanced Powder Technology*, 2020, **31** (1), P. 402–408.

[340] Chebanenko M.I., Zakharova N.V., Popkov V.I. Synthesis and visible-light photocatalytic activity of graphite-like carbon nitride nanopowders. *Russian Journal of Applied Chemistry*, 2020, **94** (4), P. 490–497.

[341] Shcherban N.D., Mäki-Arvela P., et al. Melamine-derived graphitic carbon nitride as a new effective metal-free catalyst for Knoevenagel condensation of benzaldehyde with ethylcyanoacetate. *Catal. Sci. Technol.*, 2018, **8**, P. 2928–2937.

[342] Chebanenko M.I., Zakharova N.V., Lobinsky A.A., Popkov V.I. Ultrasonic-assisted exfoliation of graphitic carbon nitride and its electrocatalytic performance in process of ethanol reforming. *Semiconductors*, 2019, **53** (16), P. 28–33.

[343] Ivanov V.K., Baranchikov A.E., et al. Effect of hydrothermal and ultrasonic/hydrothermal treatment on the phase composition and micromorphology of yttrium hydroxocarbonate. *Russ. J. Inorg. Chem.*, 2007, **52** (9), P. 1321–1327.

[344] Ivanov V.K., Kopitsa, G.P., et al. Mesostructure of hydrated hafnia xerogels. *Dokl. Chem.*, 2009, **427** (1), P. 160–163.

[345] Rutberg F.G., Gusarov V.V., et al. Analysis of physicochemical properties of nanoparticles obtained by pulsed electric discharges in water. *Tech. Phys.*, 2012, **57** (12), P. 1641–1645.

[346] Rutberg F.G., Kolikov V.A., et al. Phase composition and magnetic properties of iron oxide nanoparticles obtained by impulse electric discharge in water. *High Temperature*, 2016, **54** (2), P. 170–174.

[347] Wu J., Shen X., et al. Solvothermal synthesis and characterization of sandwich-like grafen/ZnO nanocomposite. *Appl. Surface Sci.*, 2010, **256**, P. 2826–2830.

[348] Andrievski R.A. Size-dependent effects in properties of nanostructured materials. *Rev. Adv. Mater. Sci.*, 2009, **21**, P. 107–133.

[349] Tananaev I.V., Fedorov V.B, Morokhov I.D., Malyukova L.V. Fundamentals of physical chemistry of substances in a metastable ultradispersed state and prospects for their use. *Inorg. Mater.*, 1984, **20** (6), P. 1026–1033. (in Russian)

[350] Tananaev I.V., Fedorov V.B., et al. Characteristic peculiarities of ultrafine structures, *Dokl. Akad. Nauk USSR*, 1985, **283** (6), P. 1364–1368. (in Russian)

[351] Gleiter H. Nanostructured material: basic concepts and microstructure. *Acta Mater.*, 2000, **48** (1), P. 1–29.

[352] Golovin Y.I. Nanoindentation and mechanical properties of materials at submicro- and nanoscale levels: recent results and achievements. *Phys. Solid State*, 2021, **63**, P. 1–41.

[353] Schoonman J. Nanostructured materials in solid state ionics. *Solid State Ionics*, 2000, **135**, P. 5–19.

[354] Burtsev V.A., Kalinin N.V., Luchinsky A.V. *Electrical explosion of conductors and its application in electrophysical installations*. Energoatomizdat, Moscow, 1990, 288 p.

[355] Oreshkin V.V., Sedoi V.S., Chemezova L.I. Application of electrical explosion of wires to obtain nanoscale powders. *Applied Physics*, 2001, **3**, P. 94–102. (in Russian)

[356] Kotov Yu.A., Ivanov V.V. Powder nanotechnology to create functional materials and devices for electrochemical energy. *Herald of the RAS*, 2008, **78** (9), P. 777–787. (in Russian)

[357] Bulgakov A.V., Bulgakova N.M., Burakov I.M. *Synthesis of nanoscale materials under the influence of powerful energy flows on matter*. IT SB RAS, Novosibirsk, 2009, 462 p. (in Russian)

[358] Ilyin A.P. Development of electroexplosive technology for producing nanopowders in the Research Institute of high voltage at the Tomsk Polytechnic University. *Bulletin of the Tomsk Polytechnic University*, 2003, **306** (1), P. 133–139.

[359] Gusarov V.V., Almjasheva O.V. The role or status of substances in the formation of structure and properties of materials. In: *Nanomaterials: properties and applications*. Scientific world, Moscow, 2014, 456 p. (in Russian)

[360] Aleskovskiy V.B. Chemistry and technology of solid substances. *J. Appl. Chem. USSR*, 1974, **47**, P. 2145–2156. (in Russian)

[361] Aleskovskiy V.B. Chemical Assembly materials. *Bulletin of the USSR Academy of Sciences*, 1975, **45**, P. 48–51. (in Russian)

[362] Malygin A.A. The molecular layering nanotechnology: basis and application *J. Ind. Eng. Chem.*, 2006, **12** (1), P. 1–11.

[363] Malygin A.A., Drozd V.E., Malkov A.A., Smirnov V.M. From V. B. Aleskovskii's "Framework" Hypothesis to the Method of Molecular Layering/Atomic Layer Deposition. *Chem. Vap. Deposition*, 2015, **21**, P. 216–240.

[364] Malygin A.A., Malkov A.A., Sosnov E.A. Structural dimensional effects and their application in the 'core-nanoshell' systems synthesized by the molecular layering. *Russian Chemical Bulletin, International Edition*, 2017, **66** (11), P. 1939–1962.

NANOSYSTEMS:

PHYSICS, CHEMISTRY, MATHEMATICS

INFORMATION FOR AUTHORS

The journal publishes research articles and reviews, and also short scientific papers (letters) which are unpublished and have not been accepted for publication in other magazines. Articles should be submitted in English. All articles are reviewed, then if necessary come back to the author to completion.

The journal is indexed in Web of Science Core Collection (Emerging Sources Citation Index), Chemical Abstract Service of the American Chemical Society, Zentralblatt MATH and in Russian Scientific Citation Index.

Author should submit the following materials:

1. Article file in English, containing article title, the initials and the surname of the authors, Institute (University), postal address, the electronic address, the summary, keywords, MSC or PACS index, article text, the list of references.
2. Files with illustrations, files with tables.
3. The covering letter in English containing the article information (article name, MSC or PACS index, keywords, the summary, the literature) and about all authors (the surname, names, the full name of places of work, the mailing address with the postal code, contact phone number with a city code, the electronic address).
4. The expert judgement on possibility of publication of the article in open press (for authors from Russia).

Authors can submit a paper and the corresponding files to the following addresses: nanojournal.ifmo@gmail.com, popov1955@gmail.com.

Text requirements

Articles should be prepared with using of text editors MS Word or LaTex (preferable). It is necessary to submit source file (LaTex) and a pdf copy. In the name of files the English alphabet is used. The recommended size of short communications (letters) is 4-6 pages, research articles– 6-15 pages, reviews – 30 pages.

Recommendations for text in MS Word:

Formulas should be written using Math Type. Figures and tables with captions should be inserted in the text. Additionally, authors present separate files for all figures and Word files of tables.

Recommendations for text in LaTex:

Please, use standard LaTex without macros and additional style files. The list of references should be included in the main LaTex file. Source LaTex file of the paper with the corresponding pdf file and files of figures should be submitted.

References in the article text are given in square brackets. The list of references should be prepared in accordance with the following samples:

[1]   Surname N. *Book Title*. Nauka Publishing House, Saint Petersburg, 2000, 281 pp.
[2]   Surname N., Surname N. Paper title. *Journal Name*, 2010, **1** (5), P. 17-23.
[3]   Surname N., Surname N. Lecture title. In: Abstracts/Proceedings of the Conference, Place and Date, 2000, P. 17-23.
[4]   Surname N., Surname N. Paper title, 2000, URL: http://books.ifmo.ru/ntv.
[5]   Surname N., Surname N. Patent Name. Patent No. 11111, 2010, Bul. No. 33, 5 pp.
[6]   Surname N., Surname N. Thesis Title. Thesis for full doctor degree in math. and physics, Saint Petersburg, 2000, 105 pp.

Requirements to illustrations

Illustrations should be submitted as separate black-and-white files. Formats of files – jpeg, eps, tiff.

NANOSYSTEMS:

PHYSICS, CHEMISTRY, MATHEMATICS